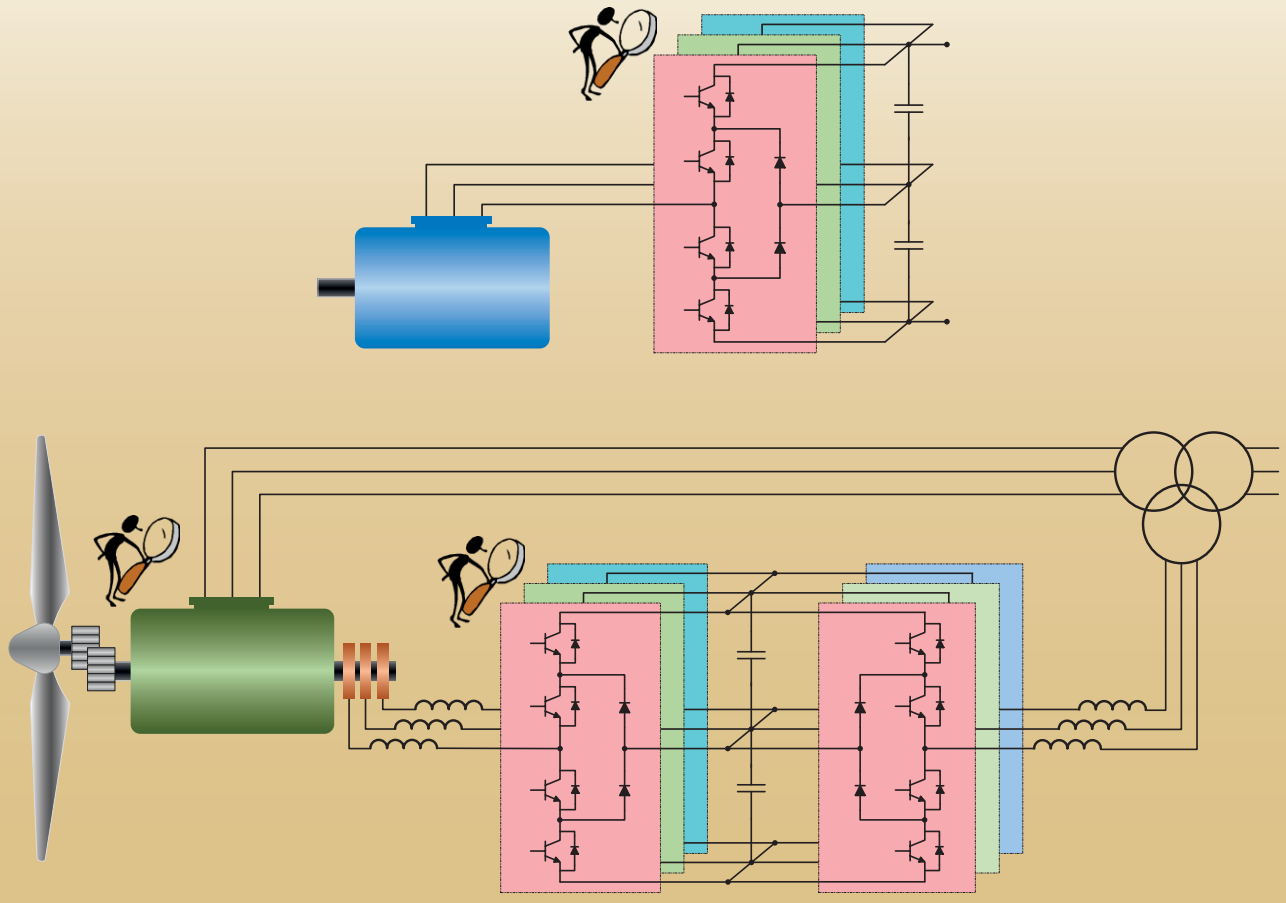

Mohsen Bandar Abadi

FAULT DIAGNOSIS IN AC DRIVES AND WIND TURBINE DOUBLY-FED INDUCTION GENERATORS BASED ON THREE-LEVEL NPC CONVERTERS

PhD Thesis in Electrical and Computer Engineering, specialization in Energy, supervised by Professor Sérgio Manuel Ângelo da Cruz and Professor André Manuel dos Santos Mendes, submitted to the Department of Electrical and Computer Engineering of the Faculty of Sciences and Technology of the University of Coimbra

October 2017

· U C ·

Universidade de Coimbra

Mohsen Bandar Abadi

Fault Diagnosis in AC Drives and Wind Turbine Doubly-Fed Induction Generators Based on Three-Level NPC Converters

PhD Thesis in Electrical and Computer Engineering, specialization in Energy, supervised by Professor Sérgio Manuel Ângelo da Cruz and Professor André Manuel dos Santos Mendes, submitted to the Department of Electrical and Computer Engineering of the Faculty of Sciences and Technology of the University of Coimbra

October 2017

UNIVERSIDADE DE COIMBRA

This work was supported by the Portuguese Foundation for Science and Technology (FCT) under project nº SFRH/BD/101111/2014.

Dedication

To my parents, for their love, encouragements and endless support.

To my greatest blessing, my wife, the most decent and loving person I've ever known.

To my little angel, Hilda, who brings so much love, happiness & joy to my life.

Acknowledgments

I am deeply indebted to my supervisor Prof. Dr. Sérgio Manuel Ângelo da Cruz from the University of Coimbra for giving me the opportunity to join his research group as well as for his scientific supports and encouragements during past years to accomplish my Ph.D. degree. Moreover, I would like to thank my co-supervisor Prof. Dr. André Manuel dos Santos Mendes from the University of Coimbra who was leading me patiently and actively in these years through his valuable hints, interest, and support.

I would like to thank my colleagues and friends Bruno Baptista, Pedro Gonçalves, André Gonçalves, Hazem Hadla, Luís Caseiro, Emanuel Marques, Rui Ventura and our mentors from the University of Tehran: Prof. Dr. Javad Faiz, Dr. Mohammad Moosavi and Mehran Keravand for their friendship, support, and collaborations.

I must appreciate Instituto de Telecomunicações (IT) and its members for their generous support on my project during these years.

This dissertation has been financially supported, in part, by EnDiPrev Lda. Therefore, I express my gratitude to this company, especially to Eng. André Ribeiro who was supporting and managing my project.

I would like to acknowledge the collaboration of Bobinadora BJS S.A. in the preparation of the test machine.

I would like to acknowledge the financial support of the Portuguese Foundation for Science and Technology (FCT) under fellowship SFRH/BD/101111/2014.

I also would like to thank my kind parents for their endless love and support from many kilometers away.

And, last but not least, I must thank my wife, Homa, whose patient love, compassion and motivation were priceless to start this incredible journey.

Mohsen Bandar Abadi

Abstract

Currently, wind energy conversion systems based on doubly-fed induction generators (DFIGs) are the most popular configuration in the wind energy market due to their advantages such as reduced converter cost, variable speed operation and control capability.

On the other hand, multilevel converters have become an attractive alternative, especially in high-power wind turbines, as they are able to meet the increasing demand for higher power ratings in this type of application. Amongst the different multilevel converters topologies, three-level neutral-point-clamped (3LNPC) converters are highly popular. Although they have been extensively used in medium-voltage AC motor drives, the large number of switches and gate drivers used in this converter topology increases the probability of the occurrence of a fault. Therefore, the use of reliable real-time diagnostic systems is able to improve the availability of the power converter and of the drive system as a whole.

In addition, inter-turn short-circuit (ITSC) faults in the stator and rotor windings of DFIGs are one of the most common types of faults reported in the literature. To avoid unscheduled downtimes and to minimize the maintenance costs associated with wind turbines, it is imperative to implement reliable diagnostic systems for the detection of this type of faults as well.

Having this in mind, the main goals of this thesis are twofold: the diagnosis of faults in 3LNPC converters used in different applications and the diagnosis of faults in the stator and rotor windings of DFIGs used in wind energy conversion systems.

Regarding the first goal, open-circuit (OC) faults in 3LNPC converters, used in induction motor (IM) drives and DFIG systems, were investigated. For the case of IM drives, three novel real-time diagnostic approaches for the detection and identification of power switch OC faults in 3LNPC inverters were developed. The first approach is based on the average current Park's Vector (ACPV) and has the capability of pinpointing the exact location of the faulty IGBT. The second diagnostic approach has the ability to detect and identify multiple OC IGBT faults in 3LNPC inverters. This

approach is based on the average values of the positive and negative parts of the output currents. The third diagnostic approach relies on the analysis of the pole voltages of the inverter and is able to detect and identify multiple OC faults in the IGBTs as well as OC fault in the clamp-diodes of 3LNPC inverters. The significant advantages of this new technique, which makes it superior to their counterparts reported in the literature, are the independence of the diagnostic process with regard to the operating conditions of the system and a fast diagnosis, both in steady-state and in transient conditions.

With regard to DFIG systems, their performance under different semiconductor OC faults in the rotor-side converter was investigated and a diagnostic approach with the capability of detecting and locating OC faults in the IGBTs as well as in the clamp-diodes of the converter was developed. This diagnostic approach is similar to the third diagnostic method proposed for IM drives but constitutes a simplified version of it, with a smaller number of diagnostic variables. This approach provides very fast and reliable diagnostic results for all operating conditions of the DFIG system, including operation in the subsynchronous and supersynchronous regions.

As for the second main goal of this thesis, ITSC faults in the stator and rotor windings of the DFIG were investigated and an approach towards the detection and quantification of these types of faults was introduced. The diagnostic approach proposed is based on the spectrum analysis of the stator instantaneous reactive power. In addition, for each type of fault, a severity factor was defined that indicates the extension of the fault. In order to conduct a detailed analysis of the DFIG system, a mathematical model of the DFIG, based on the modified winding function approach (MWFA), was developed and implemented in Matlab/Simulink environment. This model allows the introduction of ITSC faults in the stator and rotor windings of the DFIG and includes phenomena such as the effects of the linear rise of magnetomotive force (MMF) across the slots, stator and rotor slotting, and magnetic saturation.

The diagnostic methods proposed for semiconductor faults and for DFIG windings faults can easily be integrated into the control system of the DFIG, thus increasing their availability and reducing its maintenance cost. They can easily be applied in real wind generation systems, having a high potential for commercialization and large scale production.

Resumo

Atualmente, os sistemas de conversão de energia eólica baseados em máquinas de indução duplamente alimentadas (MIDAs) são a configuração mais popular no mercado da energia eólica devido às suas vantagens, tais como um custo reduzido do conversor de potência, capacidade de operação a uma velocidade variável e grande capacidade de controlo.

Por outro lado, os conversores multinível tornaram-se uma alternativa atraente, especialmente em turbinas eólicas de grande potência, sendo capazes de atender à procura crescente de geradores com uma potência nominal cada vez maior neste tipo de aplicação. Entre as diferentes topologias de conversores multinível, os conversores de três níveis na configuração NPC (3LNPC) são bastante populares. Embora os conversores 3LNPC sejam amplamente utilizados em acionamentos elétricos baseados em motores de indução de média tensão, o número elevado de semicondutores de potência e circuitos de comando usados nesta topologia de conversor de potência aumenta a probabilidade de ocorrência de uma falha. Por conseguinte, o uso de sistemas de diagnóstico em tempo real fiáveis permite o aumento da disponibilidade do conversor de potência e do acionamento elétrico como um todo.

Adicionalmente, os curtos-circuitos entre espiras nos enrolamentos do estator e do rotor da MIDA são um dos tipos mais comuns de falhas relatados na literatura publicada neste domínio. De modo a evitar paragens não programadas e a minimizar os custos de manutenção associados às turbinas eólicas, é imperativo implementar sistemas de diagnóstico fiáveis também para a deteção deste tipo de falhas.

Tendo isto em mente, os objetivos desta tese são duais: (i) o diagnóstico de falhas em conversores 3LNPC usados em diferentes aplicações e (ii) o diagnóstico de falhas nos enrolamentos do estator e do rotor da MIDA, usada em sistemas de conversão de energia eólica.

Relativamente ao primeiro objetivo, foram investigadas falhas de circuito aberto em conversores 3LNPC usados em acionamentos elétricos baseados no motor de indução trifásico

(MIT) e em sistemas de conversão de energia eólica baseados na MIDA. Para o caso dos acionamentos baseados no MIT, foram desenvolvidas três novas estratégias de diagnóstico em tempo real para a deteção e identificação de falhas de circuito aberto em inversores 3LNPC. A primeira estratégia é baseada no Vetor de Park dos valores médios das correntes (ACPV), tendo esta estratégia a capacidade de localizar com exatidão o IGBT em falha. A segunda estratégia de diagnóstico tem a capacidade de detetar e identificar falhas múltiplas de circuito aberto em IGBTs usados em inversores 3LNPC. Esta segunda abordagem baseia-se na análise dos valores médios das alternâncias positiva e negativa das correntes de saída do inversor. A terceira estratégia de diagnóstico baseia-se na análise das tensões polares do inversor e é capaz de detetar e identificar falhas múltiplas de circuito aberto nos IGBTs bem como falhas de circuito aberto nos díodos de fixação usados nos inversores 3LNPC. As principais vantagens desta nova estratégia de diagnóstico, que a tornam superior às suas concorrentes relatadas na literatura, são a independência do processo de diagnóstico relativamente às condições de funcionamento do sistema e um diagnóstico extremamente rápido, quer em regime permanente quer em regime transitório.

No que diz respeito aos sistemas de conversão de energia eólica baseados na MIDA, foi investigado o seu desempenho na presença de diferentes falhas de circuito aberto no conversor de potência do lado do rotor, tendo sido desenvolvida uma nova estratégia de diagnóstico com a capacidade de detetar e localizar falhas de circuito aberto nos IGBTs e nos díodos de fixação desse conversor. Esta estratégia de diagnóstico é bastante semelhante à terceira estratégia proposta para os acionamentos baseados no MIT, constituindo uma versão simplificada da mesma dado recorrer a um menor número de variáveis de diagnóstico. Esta abordagem fornece resultados de diagnóstico muito rápidos e fiáveis para todas as condições de funcionamento da MIDA, incluindo o funcionamento nas regiões subsíncrona e supersíncrona.

Relativamente ao segundo grande objetivo desta tese, foi investigada a ocorrência de curtos-circuitos entre espiras nos enrolamentos do estator e do rotor da MIDA, tendo ainda sido introduzida uma estratégia de diagnóstico com o objetivo de detetar e quantificar este tipo de falhas. A estratégia de diagnóstico proposta baseia-se na análise espetral da potência reativa instantânea total do estator, tendo ainda, para cada tipo de falha, sido definido um fator de severidade que indica a extensão da falha. Para realizar uma análise detalhada do comportamento da MIDA, foi desenvolvido e implementado em ambiente Matlab/Simulink, um modelo

matemático da MIDA, baseado no uso da função de enrolamento modificada. Este modelo permite a introdução de falhas nos enrolamentos do estator e rotor da MIDA e inclui fenómenos tais como o aumento linear da força magnetomotriz ao longo das ranhuras da máquina, efeitos das ranhuras do estator e rotor, e saturação magnética.

Os métodos de diagnóstico propostos para as falhas nos semicondutores de potência e falhas nos enrolamentos da MIDA podem ser facilmente integrados no sistema de controlo da mesma, aumentando desta forma a sua disponibilidade e reduzindo os respetivos custos de manutenção. Eles poderão portanto ser aplicados em sistemas de geração eólica reais, tendo um elevado potencial de comercialização e utilização em grande escala.

Contents

List of figures

List of figures

List of figures

List of figures

List of figures

List of figures

List of figures

List of tables

List of tables

List of symbols

α_i	Bandwidth of the rotor current control loops	Hz
γ_x	Diagnostic variable	
δ_x	Diagnostic variable	
$\varepsilon_x^+, \varepsilon_x^-, \varepsilon_x^z, \varepsilon_x^o$	Diagnostic variables	
θ	Angular rotor position	rad
θ_C	Ceil sample position	rad
θ_F	Floor sample position	rad
θ_g	Angle of the fundamental component of the grid voltages	rad
θ_s	Angle of *d*-axis of the synchronous reference frame	rad
$\theta_{s.av}$	Angle of the average current Park's vector	deg
μ	Magnetic permeability of the material used in the magnetic circuit	Hm^{-1}
μ_0	Magnetic permeability of free space	Hm^{-1}
ρ	Angular position in the stator frame	rad
ρ_N	Angle resolution	rad
σ	leakage coefficient of the machine	
τ_r	Angle corresponding to the rotor slot pitch	rad
τ_s	Angle corresponding to the stator slot pitch	rad
ϕ_i	Magnetic flux in tooth *i* of the machine	Wb
ψ_{dr}, ψ_{qr}	Direct and quadrature components of the rotor flux	Wb
ψ_{ds}, ψ_{qs}	Direct and quadrature components of the stator flux	Wb

List of symbols

$\underline{\psi}_s$	Stator flux space vector	Wb
ω_m	Electrical rotor angular speed	rad/s
ω_r	Rotor angular frequency	rad/s
ω_s	Stator angular frequency	rad/s
Ω_m	Mechanical rotor angular speed	rad/s
B	Magnetic flux density	T
B_m	Viscous friction coefficient	N.m.s/rad
CS	Control state	
d_x	Diagnostic variable	
e_x	Diagnostic variable	
$e_x^+,\ e_x^-$	Diagnostic variables	
F_{de}	Faulty device	
F_{gr}	Faulty group	
F_{leg}	Faulty leg	
F_{pair}	Faulty IGBT pair	
f_r	Rotor frequency	Hz
f_s	Stator frequency	Hz
F_{switch}	Faulty switch	
F_T	Time of occurrence of the fault	s
f_x	Diagnostic variable	
g	Air-gap length	m
g^{-1}	Inverse air-gap length	m^{-1}
H	Magnetic field intensity	A/m
$i_a,\ i_b,\ i_c$	Rotor currents	A
$i_A,\ i_B,\ i_C$	Stator currents	A
i_{dr}, i_{qr}	Direct and quadrature components of the rotor currents	A
i_{ds}, i_{qs}	Direct and quadrature components of the stator currents	A

List of symbols

$\underline{i}_{s.av}$	Park's Vector of the mean value of the inverter currents	A
i_x	Inverter output current of leg x	A
$i_{x.n}$	i_x normalized	
$i_{x.n}^{+}$	Positive part of $i_{x.n}$	
$i_{x.n}^{-}$	Negative part of $i_{x.n}$	
$i_{x.n.av}^{+}$	Average value of $i_{x.n}^{+}$	
$i_{x.n.av}^{-}$	Average value of $i_{x.n}^{-}$	
j_x	Diagnostic variable	
J_m	Moment of inertia	Kg.m^2
l	Rotor stack length	m
L_{lr}	Rotor leakage inductance	H
L_{ls}	Stator leakage inductance	H
L_m	Magnetizing inductance	H
L_r	Rotor inductance	H
L_s	Stator inductance	H
N_{SC}	Number of short-circuited turns	
p	Number of pole-pairs	
P_{Cu}	Power copper losses	W
P_r	Rotor active power	W
P_s	Stator active power	W
Q_r	Rotor reactive power	VAr
Q_s	Stator reactive power	VAr
r	Rotor radius	m
R_n	Region number	
R_r	Resistance of the rotor windings	Ω
R_s	Resistance of the stator windings	Ω
R_{sc}	Short-circuit resistance	Ω

List of symbols

s	Rotor slip	
SF_{rf}	Severity factor for rotor ITSC faults	%
SF_{sf}	Severity factor for stator ITSC faults	%
Sg_n	Segment number	
S_n	Sector number	
S_r	Number of rotor slots	
S_s	Number of stator slots	
t	Time	s
T_{em}	Electromagnetic torque	N.m
$T_{i.s}$	Period of the fundamental component of the motor line currents	s
T_L	Mechanical torque	N.m
T_s	Sampling period	s
T_{sw}	Converter switching period	s
u	Stator/rotor turns ratio	
v_{dr}, v_{qr}	Direct-axis and quadrature-axis components of the rotor voltages	V
v_{ds}, v_{qs}	Direct-axis and quadrature-axis components of the stator voltages	V
$\underline{v}_g$	Grid voltage space vector	V
v_{xz}	Pole voltage of inverter leg x	V
$v_{xz.n}$	Normalized value of v_{xz}	

List of abbreviations

3LNPC	Three-level neutral-point-clamped
AC	Alternating current
ACPV	Average current Park's Vector
ADC	Analog to digital conversion
CHB	Cascaded H-bridge
DC	Direct current
DFIG	Doubly-fed induction generator
EPVA	Extended Park's Vector Approach
FC	Flying capacitor
IGBT	Insulated-gate bipolar transistor
IRFOC	Indirect rotor field oriented control
IM	Induction motor
IPR	Increased phase resistance
ITSC	Inter-turn short-circuit
MLC	Multilevel converters
MMF	Magnetomotive force
MWFA	Modified winding function approach
NPC	Neutral-point-clamped
OC	Open-circuit
PI	Proportional-integral
PLL	Phase locked loop
PMSG	Permanent magnet synchronous generator

PWM	Pulse width modulation
RMS	Root mean square
rpm	Revolutions per minute
SC	Short-circuit
SCIG	Squirrel cage induction generator
SCIM	Squirrel cage induction motor
SPWM	Sinusoidal pulse width modulation
STATCOM	Static compensator
SVM	Space vector modulation
THIPWM	Third harmonic injection pulse width modulation
VSI	Voltage source inverter
WRIG	Wound rotor induction generator
WRIM	Wound rotor induction machine
WRSG	Wound rotor synchronous generator
WT	Wavelet transform
ZOH	Zero-order hold

Chapter 1

Introduction

1.1 Overview and problem motivation

A large number of power generation systems based on renewable energy sources such as wind, solar, geothermal and biomass are currently being developed and installed. Among all renewable energy sources, wind energy is drawing a growing interest and becoming competitive with conventional sources of energy [1-3].

The global cumulative installed wind capacity for the years 2000-2015 is presented in Fig. 1.1, which reveals that the total wind power capacity installed by the end of 2015 has increased to 432.4 GW [4]. Also, total wind power capacity installed in the European Union by the end of 2015 has increased to 141.6 GW [5]. Fig. 1.2 shows a general view of the top 10 wind markets in the European Union by the end of 2015 [5] which is an evidence about the importance of wind energy in the European energy market. Additionally, the European Commission stated that wind power would be capable of contributing with up to 20% of the European Union electricity by 2020 and as much as 33% by 2030 and 50% by 2050 [6].

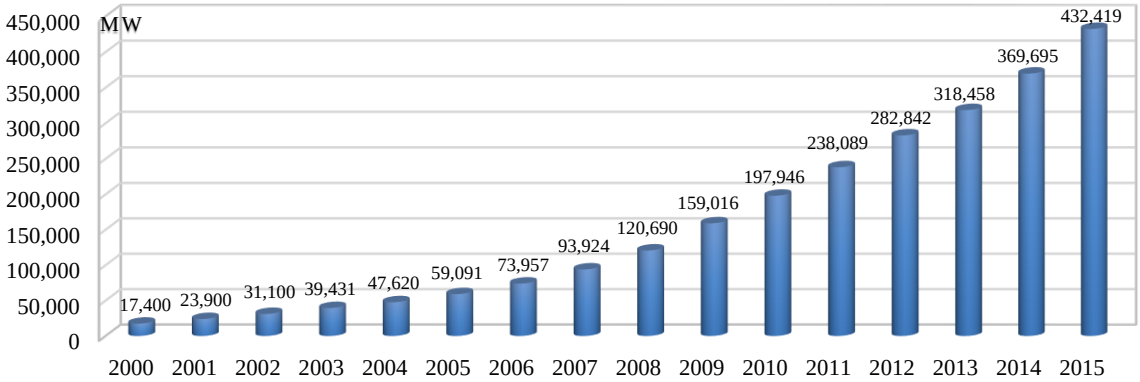

Fig. 1.1. Global cumulative installed wind capacity 2000-2015 [4].

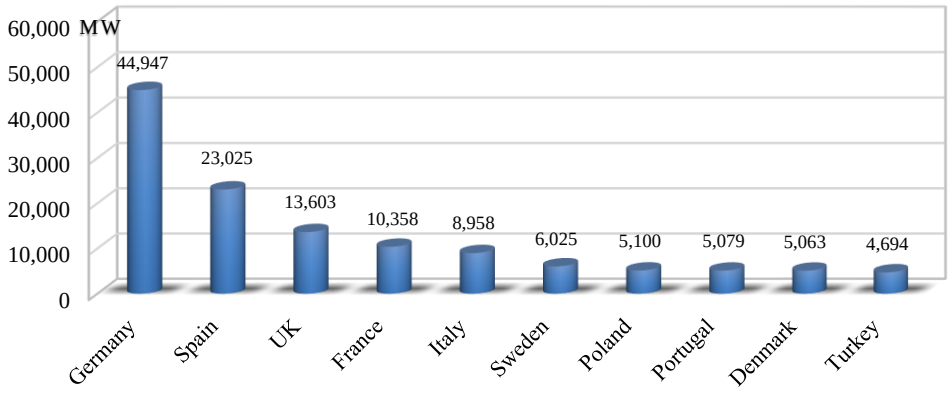

Fig. 1.2. Top 10 wind markets in the European Union by the end of 2015 [5].

There are four different dominating concepts of wind turbines in the global market [7]. These concepts are introduced in the following.

- **Type *A*: Fixed speed wind turbines**

This concept of wind turbines is based on a squirrel cage induction generator (SCIG), its rotor is driven by the turbine and its stator directly connected to the grid. A capacitor bank provides reactive power compensation and the grid connection is facilitated using a soft-starter (Fig. 1.3) [3, 7, 8]. Due to its direct grid connection, its rotation speed can only vary slightly (between 1% and 2%). The only speed control is through pole changing which leads to two rotation speeds. The advantages of this concept of wind turbines are its low cost, simplicity and robustness. However,

there are some limitations associated with this concept of wind turbines, *i.e.* uncontrollable reactive power consumption, higher mechanical stresses and poor power quality [3, 7, 8].

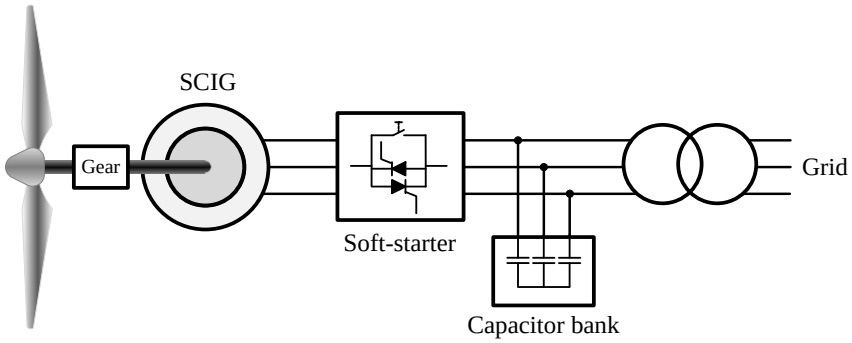

Fig. 1.3. Type *A* wind turbine configuration: fixed speed.

- **Type *B*: Variable speed wind turbines with variable rotor resistance**

The principle of this concept of wind turbines is the same as Type *A*. However, in Type *B*, instead of a SCIG, a wound rotor induction generator (WRIG) with external rotor resistances is used (Fig. 1.4). This allows variable speed operation in a limited range of 10% above synchronous speed [3, 7, 8]. As a drawback, herein, the external resistances increase the ohmic losses in the system.

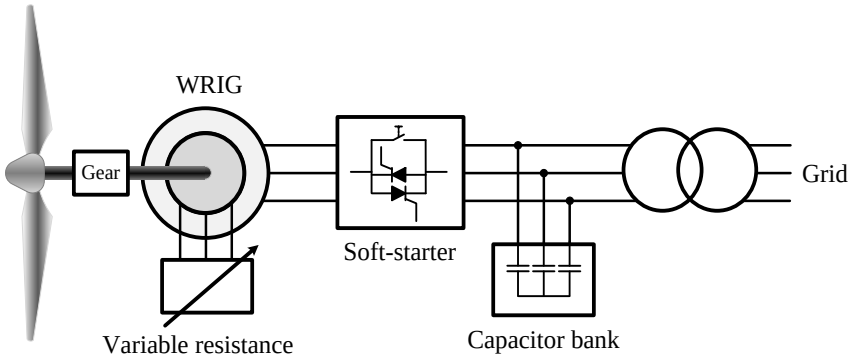

Fig. 1.4. Type *B* wind turbine configuration: limited variable speed.

- **Type *C*: Partial-scale power converter with doubly-fed induction generator**

Currently, the most common configuration of variable-speed wind turbine systems is the partial-scale power converter with a doubly-fed induction generator (DFIG). As shown in Fig. 1.5,

the stator windings of the DFIG are directly connected to the grid while the rotor windings are connected to the grid through a back-to-back converter [3, 7-9].

The DFIG provides variable speed operation by means of a partial-scale frequency converter feeding the rotor circuit. In general, the nominal power of the converter is about 30% of the wind turbine nominal power, allowing a rotor speed variation in the range of about ±30% around the synchronous speed. This leads to a reduction of the scale and cost of the power electronic converter [8, 10]. Moreover, as the converter system provides a reactive power compensation and a smooth grid connection, this type of wind turbines needs neither a soft-starter nor a reactive power compensator [8].

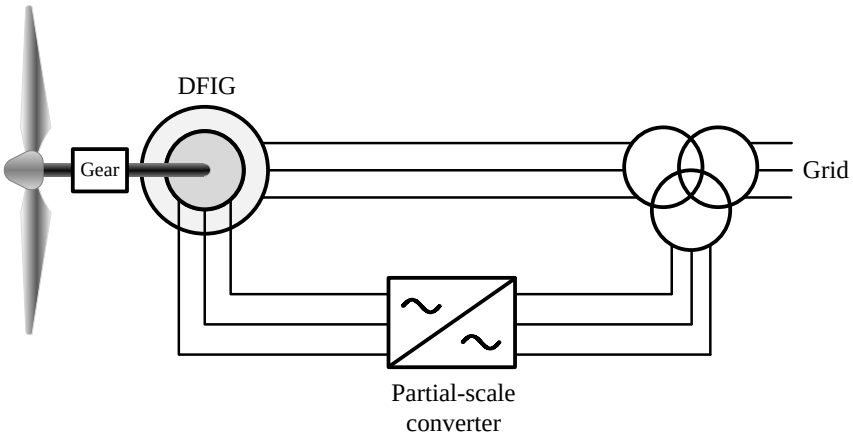

Fig. 1.5. Type *C* wind turbine configuration: partial-scale power converter with DFIG.

- **Type *D*: Variable speed wind turbines with full-scale frequency converter**

In type *D* wind turbines, the stator is connected to the grid via a full-power electronic converter (Fig. 1.6). The full-scale frequency converter provides variable speed operation over the entire speed range of the generator [3, 7]. Different types of generator, namely induction generator (IG), wound rotor synchronous generator (WRSG) and permanent magnet synchronous generator (PMSG) are proper candidates to be used [9]. If a synchronous generator with a very high number of poles is used, the gearbox can be omitted (see the dotted gearbox in Fig. 1.6). Since the power converter must be rated for 100% of the generator power, the size, cost and complexity of the overall system increases [3].

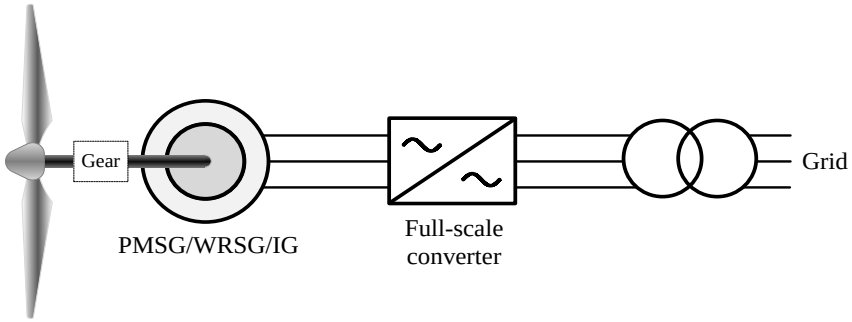

Fig. 1.6. Type *D* wind turbine configuration: full-scale power converter.

Some examples of commercial wind turbines are listed in Table 1.1 [3]. Wind turbines based on the DFIG are the most popular configuration of wind turbines in European Union countries, representing around 55% of the installed wind turbines [6]. For this reason, this turbine concept is the focus of studies in the present thesis.

Table 1.1. Commercial wind turbines.

Type	Manufacturer, name and rated power of wind turbines
A	Siemens SWT-4-130 (4 MW), Vestas V136 (3.45 MW),
B	Suzlon Energy S88 (2.1 MW), Vestas V66 (2.0 MW),
C	Acconica AW-100/3000 (3 MW), Alstom ECO 122/2700 (3.0 MW), Bard 5.0 (5 MW), Gamesa G132 (3.3 MW), GE's 3.4-137 (3.4 MW), Nordex N131/3300 (3.3 MW) Repower 6M (6.0 MW), Senvion 6.2M152 (6.1 MW), Vestas V90 (2.0 MW and 3.0 MW)
D	Enercon E126 (7.5 MW), Eno energy eno 126 (3.5 MW), Gamesa G132 (5 MW), Multibrid M5000 (5 MW), Siemens SWT-7-154 (7 MW), Vestas V112 (3 MW)

The power converter is a fundamental element in modern wind turbines, acting as an interface between the electric generator and the power grid [9]. Multilevel converters (MLC) are more appropriate than conventional two-level converters for utilization in large-scale wind turbines due to their ability to meet the increasing demand for high power ratings in large-scale wind turbines

[11-13]. The main advantages of multilevel converters, when compared to conventional two-level converters, are their higher voltage capability, reduction of the harmonic content, lower switching losses, the accomplishment of higher power quality waveforms and lower *dv/dt* [14-16]. The most common MLCs are the neutral-point-clamped (NPC) [17], flying capacitor (FC) [18], and cascaded H-bridge (CHB) topologies [19]. Among all types of multilevel converters, three-level neutral-point-clamped (3LNPC) converters are particularly verified to be used in high-power wind turbines [20, 21]. 3LNPC converters require a relatively small DC-link capacitor and a have simple power circuit topology. Additionally, 3LNPC converters have the highest converter efficiency compared to other MLC topologies [22, 23]. The application of 3LNPC converter for DFIG wind turbines is reported in [24-30]. Also, 3LNPC inverters are used more extensively in the medium-voltage induction motor (IM) drive market compared to other MLC topologies [31].

By increasing the number of installed wind turbines, it becomes mandatory to force wind power generation to be a reliable source of energy. Also, the reliability increase of wind turbines is identified as a specific objection inside the Horizon 2020 work program 2016-2017 of the European Union [32].

Wind turbines are usually erected in mountainous or offshore regions with harsh environmental conditions. The different parts of a wind turbine system such as rotors and blades, gearboxes, yaw systems, generators, converters, and electrical controls are exposed to various types of faults [33-35]. In order to avoid unscheduled downtimes and to minimize the maintenance costs associated with wind turbines, it is imperative to implement reliable fault diagnostic systems, able to provide the maintenance personnel with information about the working conditions of the different components of wind turbines.

Fig. 1.7 shows the percentage of downtime for different components of wind turbines in Swedish wind power plants between 2000-2004 [36]. As shown in this figure, 8.9% of the downtime of wind turbines was due to generator faults. The database used in [36] contains old and small turbines. Therefore, their fault rates may be different from those obtained from modern MW-scale turbines.

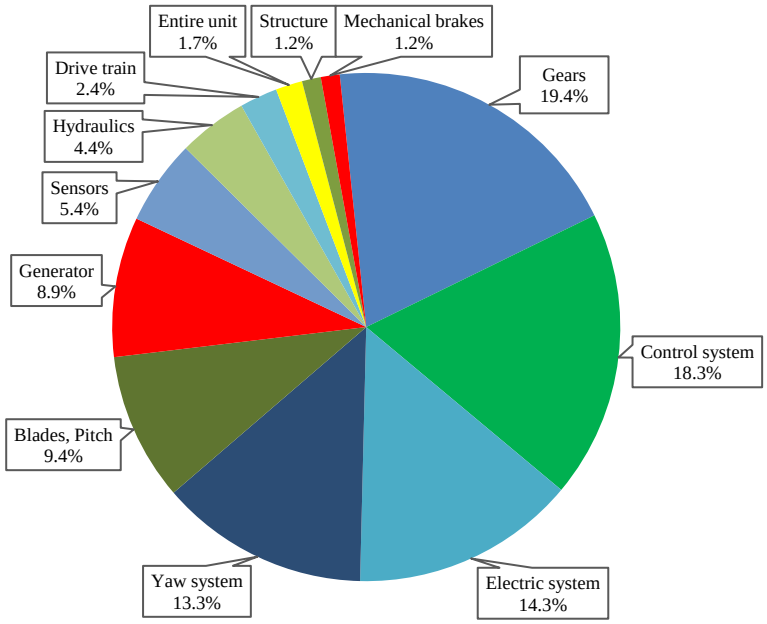

Fig. 1.7. Percentage of downtime due to the fault in different components of wind turbines in Swedish wind power plants between 2000-2004.

In [37], a statistical data analysis for the Vestas V90-2MW wind generator (2MW DFIG) has been conducted based on fault data from 57 wind turbines located in Germany, in the period 2004–2008 (Fig. 1.8). According to this report, 24% of the wind turbines downtime was due to generator and converter faults. As reported in [38], considering only generator faults, DFIGs have around 40% more faults than PMSGs.

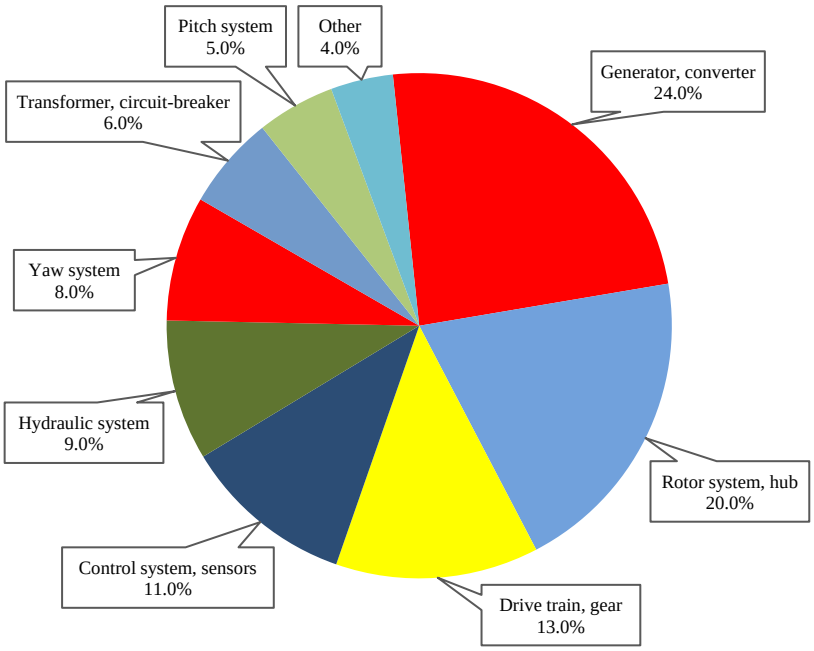

Fig. 1.8. Percentage of downtime due to the fault in different components of DFIG wind turbines between 2004-2008.

Generally, generator faults can be categorized into 1) mechanical faults such as bearing faults [39] and eccentricity faults [40]; 2) electrical faults such as inter-turn short-circuit (ITSC) faults in the stator and rotor windings of generators [41]. ITSC faults in the stator and rotor windings are one of the most common fault modes in the generators used in WTs, being caused by many reasons such as high temperature in the windings or core, mechanical stress, insulation damage and transient overvoltages [42, 43]. ITSC faults normally begin with undetected turn-to-turn faults which then extend to more serious faults. Although a wide range of diagnostic techniques for this type of the fault has been proposed in the literature, the reliability of those techniques was not fully accessed yet for all conditions under which a DFIG operates in an actual wind turbine.

On the other hand, power electronic converters contribute to ~13% of the wind turbine fault rate and ~ 18% of the downtime [44]. Due to the complexity of the topology and the high number of power semiconductor devices and gate drivers, the probability of the occurrence of faults in 3LNPC converters is even more likely. One common type of fault in the power switches of a converter is an IGBT open-circuit (OC) fault. This type of fault mostly arises due to the lifting of wire bond in a power module upon thermal stresses. The gate driver unit or the gate firing hardware faults are also common OC fault sources [45, 46]. If the OC fault is not detected and the protection system does not actuate, the converter will continue running for long period of time, which may lead to secondary faults and high repairing costs [47]. Since commercial IGBT drivers have only short-circuit (SC) protection (OC fault detection features are not included) [48], the use of a real-time OC fault diagnostic algorithm is required to avoid the aforementioned problems. This diagnostic system can also be utilized for the inclusion of fault tolerant control strategies [49-54]. Additionally, in high-power applications where discrete IGBT modules are used, the identification of the faulty IGBT by the diagnostic system reduces the inverter repair time and the associated repair cost. The literature shows a significant lack of investigations on techniques for detection of OC faults in the 3LNPC converters used in DFIG systems.

It should be noted that 3LNPC inverters are also being used extensively in the medium-voltage IM drive market compared to other MLC topologies [31]. However, fault diagnostic methods reported so far in the literature are not mature enough and more studies must be conducted with this regard in order to fully address reliable methods for the diagnosis of faults in IM drives.

Therefore, fault diagnosis for IM drives based on 3LNPC converters is also one of the topics addressed in this thesis.

Considering all the above mentioned facts, the global objective of this thesis is to develop some innovative real-time diagnostic approaches for the detection of faults in 3LNPC converters employed in IM drives and DFIG systems as well as for the detection of faults in the windings of the DFIG.

1.2 Main contributions

In this thesis, three novel real-time diagnostic approaches for the detection and identification of power switch OC faults in 3LNPC converter of an IM drive are developed. The first approach is based on the average current Park's Vector (ACPV) and has the capability of pinpoint the exact faulty IGBT after the occurrence of an OC fault in the 3LNPC inverter. The second approach has the capability to detect and identify of multiple OC IGBT faults in 3LNPC inverters. This approach is based on the average values of the positive and negative parts of the output currents. The third approach relies on the analysis of the pole voltages of the inverter and has the capability to detect and identify of multiple OC IGBT faults as well as OC clamp-diode faults in 3LNPC inverters.

As far as the converter of DFIG systems is concerned, a fault diagnostic approach with the ability to detect and locate of OC faults in the IGBTs as well as in the clamp-diodes of the rotor-side 3LNPC converter was developed. This diagnostic approach is basically an improved version of the method proposed for IM drives (the third approach).

Regarding the diagnosis of fault in the DFIG, a novel approach for the detection and quantification of ITSC faults in the stator and rotor windings of a DFIG was developed. The diagnostic approach is based on the spectrum analysis of the stator instantaneous reactive power. Moreover, for each type of fault, a severity factor that indicates the extension of the fault was defined.

Based on the obtained results, three journal papers [55-57] and three conference paper [58-60] were prepared and published.

1.3 Thesis outline

Following this introductory chapter, Chapter 2 presents the configuration of the 3LNPC converter and its application in an IM drive. This chapter starts with a general overview of multilevel converters, followed by the presentation of the configuration of the 3LNPC converter. Later in Chapter 2, different modulation strategies for 3LNPC converters are presented. Finally, an IM drive system based on the 3LNPC inverter is presented.

In Chapter 3, three novel approaches are developed for fault diagnosis in 3LNPC inverters. The chapter starts with a literature review on approaches for OC fault diagnosis in 3LNPC inverters, providing the state-of-the-art on this subject. Then, the behavior of the 3LNPC converters under different faulty conditions is analyzed. The theoretical principles of three novel diagnostic approaches are then presented for the real-time fault diagnosis in 3LNPC inverters. These approaches are appropriately tested and validated through laboratory experiments.

The simulation model of a WRIM based on the use of the modified winding function approach (MWFA) is discussed in Chapter 4. In this chapter, firstly, the basic theoretical background of the MWFA is presented. Then, the implementation of the model of the WRIM using MWFA presented. This model includes several phenomena namely the effects of the linear rise of magnetomotive force (MMF) across the slots, stator, and rotor slotting, and magnetic saturation. Furthermore, the model is developed to allow the capability of introducing ITSC faults in the stator and rotor windings of DFIGs. Finally, the simulation model is validated experimentally.

Chapter 5 is devoted to the control of the DFIG system. The steady-state operation of DFIG system is presented at first. Then, the space vector model of the DFIG system is outlined. Later on in this chapter, the employed control strategy for the DFIG system is presented.

Diagnosis of faults in the windings of the DFIG is developed and discussed in Chapter 6. The chapter starts with a literature review on the approaches used for the detection of ITSC faults in the stator and rotor windings of DFIGs. Then, the theoretical principles behind the proposed approach for the detection and quantification of ITSC faults in the stator and rotor windings of DFIGs are presented. The proposed approach is entirely tested and validated through several simulation and experimental tests.

Chapter 7 is devoted to the diagnosis of faults in the rotor-side converter of the DFIG system. The applicability and performance of the proposed diagnostic approach are demonstrated by

simulation and experimental results obtained for different operating conditions of the DFIG system.

Finally, Chapter 8 provides a summary of the main conclusions of this thesis. Some topics for possible future research work in the field and potential for the extension the work here reported are included at the end of this chapter.

Chapter 2

Three-level neutral-point-clamped converter

2.1 Introduction

Power electronic converters are important components for the integration of wind power into power systems, in order to control voltage, frequency, active and reactive powers, guarantee fault ride-through capabilities, control the voltage and current harmonics, *etc*.

The power rating achieved by today's multi-MW wind turbines are best handled at the medium-voltage level (3.3, 4.16, 6.9, 13.8 kV) compared to low-voltage level (690 V). At higher voltages, the current levels are lower. Hence, power losses in the generator, in the converter and in the cables are minimized [61].

Multilevel converters are one of the most important medium-voltage converter technologies, especially for medium-voltage applications like wind turbine systems [14]. The structures of one leg of the most common types of multilevel converters are schematically illustrated in Fig. 2.1.

The CHB multilevel converter uses multiple H-bridge power cells connected in series. H-bridge cells have the advantages of modularity and independence the switching frequency of each module [19, 62]. However, each H-bridge cell requires an isolated voltage source which increases the complexity and cost of the converter [63].

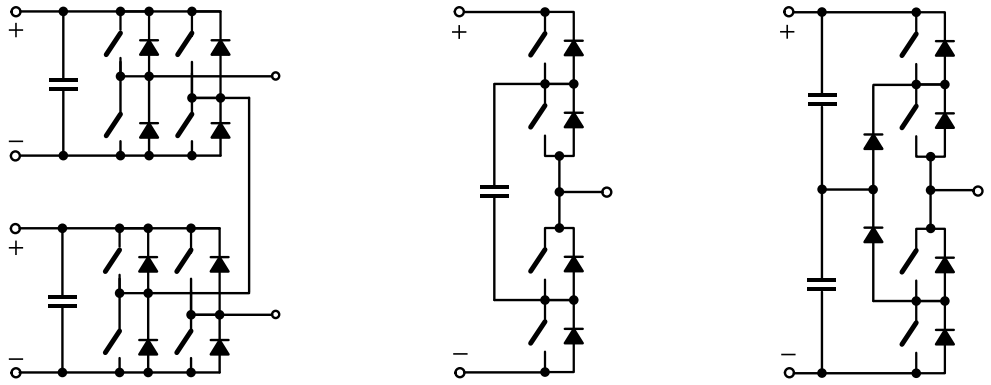

(a) Three-level CHB converter (b) Three-level FC converter (c) Three-level NPC converter

Fig. 2.1. Schematic representation of one leg of three common types of MLCs.

A three-level FC converter contains a total of 12 unidirectional active switches with antiparallel diodes and three flying capacitors. The general concept of operation is that each flying capacitor is charged to half of the DC-link voltage. It can be connected in series with the phase to add or subtract this voltage to the DC-link voltage [18].

3LNPC converters are used more extensively in the medium-voltage AC drive market compared to other MLC topologies [22, 31]. 3LNPC converters use a relatively small DC-link capacitor. Additionally, 3LNPC converters have the highest converter efficiency compared to other MLC topologies [22, 23]. Wind energy conversion systems [64-69], photovoltaic systems [70-72], DC-DC converters [73], multiphase AC drives [74-76], and static compensator (STATCOM) [77] are some of the applications of 3LNPC converters.

2.2 3LNPC converter configuration

Fig. 2.2 shows the topology of a three-phase, 3LNPC converter. It contains three legs, each one with four active switches, labeled S_{x1}, S_{x2}, S_{x3} and S_{x4}, four free-wheeling diodes labeled D_{x1}, D_{x2}, D_{x3} and D_{x4}, and two clamp-diodes labeled D_{x5} and D_{x6} (x means leg A, B or C). Each leg includes 2 IGBT pairs, P_{x1} and P_{x2} as shown in Fig. 2.2. Moreover, in this work, S_{x1} and S_{x4} of each leg will be designated by outer switches while S_{x2} and S_{x3} are the inner switches. The DC-bus includes two identical capacitors, series-connected. The middle point of the DC-bus is called the neutral point "z".

Each converter leg is characterized by three switching states, in this work designated by 1, 0 and -1, according to the information listed in Table 2.1. For example, if the switching state of the converter is "10-1" that means the output terminal of leg *A* is connected to the positive terminal of the DC-bus through S_{A1} and S_{A2}, the output terminal of leg *B* is connected to the DC-bus middle point *z* through S_{B2} and S_{B3} and the output terminal of leg *C* is connected to the negative terminal of the DC-bus through S_{C3} and S_{C4}. In this switching state, the leg output pole voltages v_{Az}, v_{Bz} and v_{Cz} are $+V_{DC}/2$, 0, and $-V_{DC}/2$, respectively

For each leg, there are 6 available current paths according to the current direction and coverter switching state, as shown in Fig. 2.3 and summarized in Table 2.1 [78]. This figure shows that current paths 1, 2, 5 and 6 involve IGBTs while current paths 3 and 4 use the free-wheeling diodes.

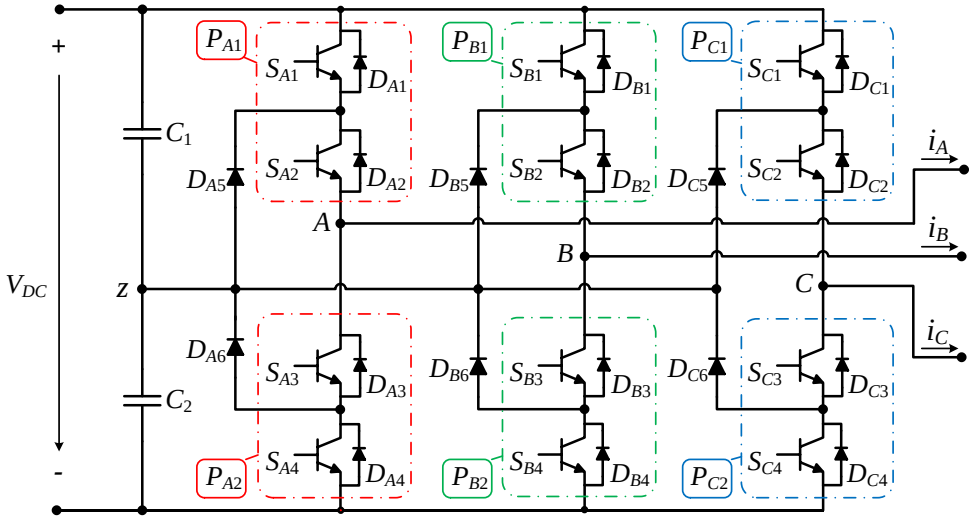

Fig. 2.2. Schematic representation of a 3LNPC converter.

Table 2.1. State of leg *x* and corresponding pole voltage and current path.

State of leg *x*	IGBTs states				Pole voltage (v_{xz})	Current path (Fig. 2.3)	
	S_{x1}	S_{x2}	S_{x3}	S_{x4}		i_x>0	i_x<0
1	on	on	off	off	$+V_{DC}/2$	1	4
0	off	on	on	off	0	2	5
-1	off	off	on	on	$-V_{DC}/2$	3	6

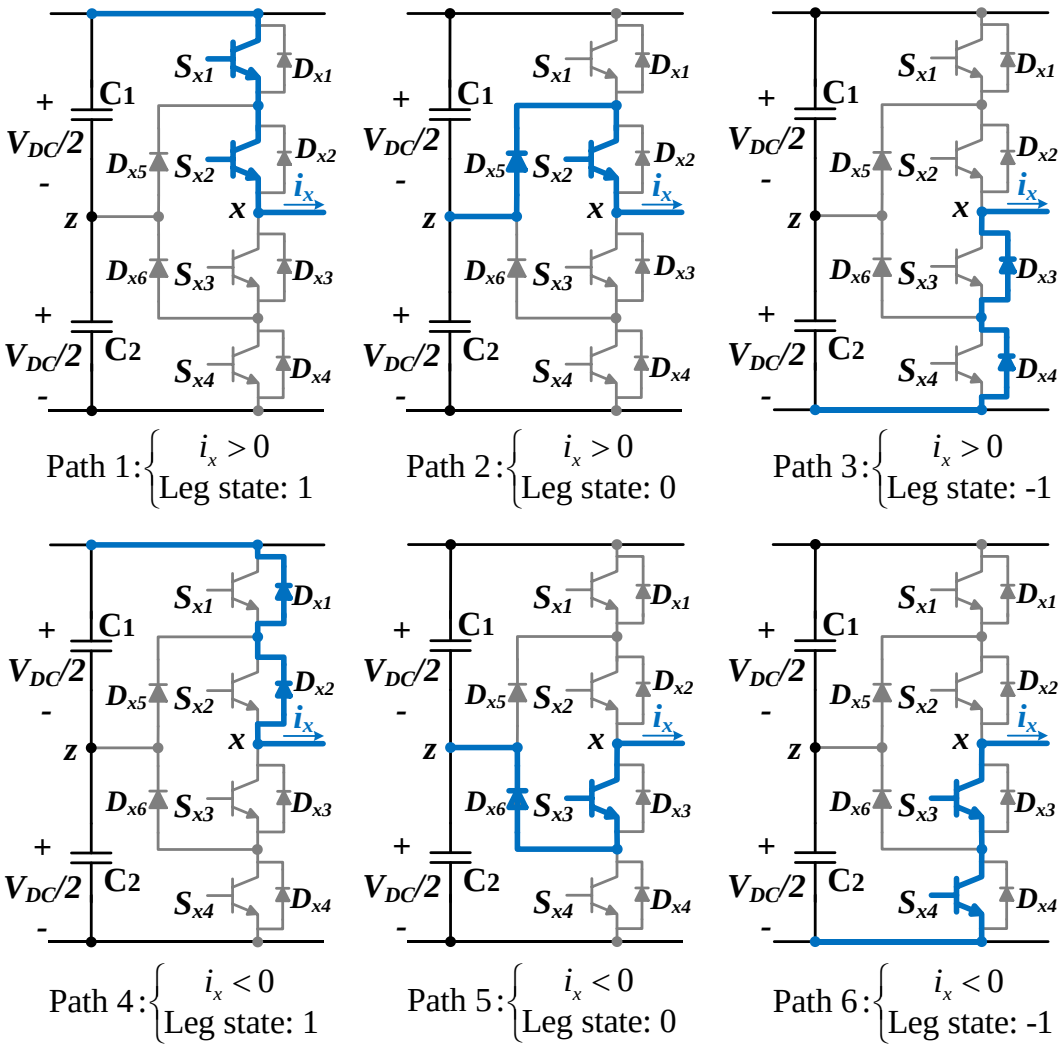

Fig. 2.3. Current paths according to the leg current direction and leg state.

2.3 Modulation schemes

Regarding the modulation techniques, several options are available for 3LNPC converters. The most popular ones are sinusoidal pulse width modulation (SPWM) and space vector modulation (SVM) [22, 79].

2.3.1 Sinusoidal pulse width modulation

The principle behind SPWM methods is based on the comparison of a sinusoidal modulation signal with a high-frequency carrier waveform to generate the gating signals. Fundamental component of the converter output voltage is controlled by varying the amplitude and frequency of the modulation signal [80, 81]. As shown in Fig. 2.4, for 3LNPC converters, two triangle carrier

waveforms with a unitary peak-to-peak amplitude (the positive CW^{+} and the negative CW^{-}) are needed.

The normalized reference voltage for leg *x* is defined by [82]

$$v_{x.n}^{*} = \frac{2v_{x}^{*}}{V_{DC}}, \tag{2.1}$$

where *x* is the leg index and v_{x}^{*} is the reference voltage for leg *x*, given by

$$v_{x}^{*} = v_{x.\max}^{*} \sin\left(\omega_1 t\right), \tag{2.2}$$

where $v_{x.\max}^{*}$ and ω_1 are the peak value and the fundamental angular frequency of the reference voltage.

According to (2.3), the control state of leg *x* $\left(CS_x\right)$ is given by the comparison of the normalized reference voltage of leg *x* with the two carrier waveforms, as shown in Fig. 2.4 [15, 81, 82].

$$CS_x = \begin{cases} 1 \Leftarrow & v_{x.n}^{*} > \mathrm{CW}^{+} \\ 0 \Leftarrow & \mathrm{CW}^{-} \le v_{x.n}^{*} \le \mathrm{CW}^{+} \\ -1 \Leftarrow & v_{x.n}^{*} < \mathrm{CW}^{-}. \end{cases} \tag{2.3}$$

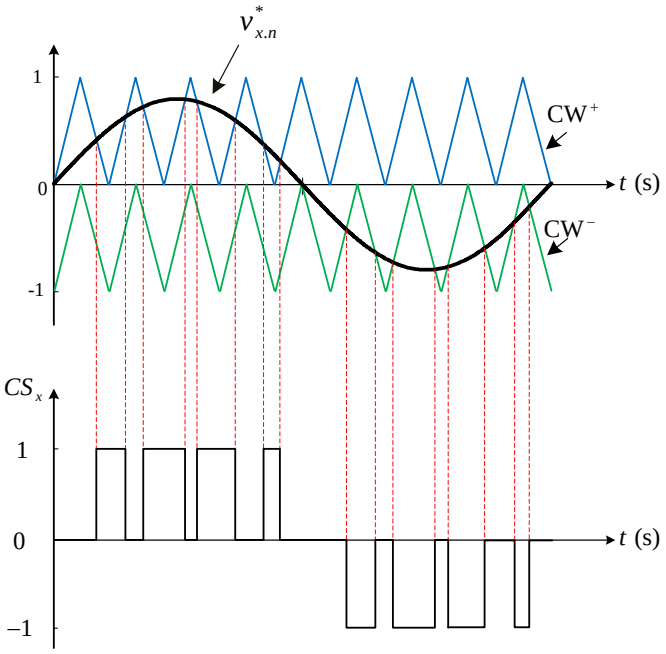

Fig. 2.4. Three-level sinusoidal pulse-width modulation.

Referring to (2.1), the maximum achievable output voltage amplitude of the 3LNPC converter by using the SPWM technique is $V_{DC}/2$.

The maximum achievable output voltage amplitude of converter can be enhanced by adding a third harmonic component to the sinusoidal modulating voltage. This modulation technique is known as third harmonic injection PWM (THIPWM) [83, 84].

In this technique, the modulating wave of leg *x* is given by

$$v_{x.THI}^{*} = v_{x}^{*} + v_{x3}^{*}, \tag{2.4}$$

where v_{x3}^{*} is the third harmonic added to the reference voltage of leg *x*, given by

$$v_{x3}^{*} = v_{x3.\max}^{*} \sin\left(3\omega_1 t\right), \tag{2.5}$$

where $v_{x3.\max}^{*}$ is the peak value of the third harmonic added to the reference voltage of leg *x*.

The principle of the THIPWM technique is shown in Fig. 2.5, where the modulating wave $v_{x.THI}^{*}$ is composed of a fundamental component v_{x}^{*} and a third harmonic component v_{x3}^{*} [83, 84].

As shown in this figure, the amplitude of $v_{x.THI}^{*}$ is smaller than the amplitude of v_{x}^{*} which makes it possible to increase the maximum achievable amplitude of the output voltage. The maximum achievable amplitude of the output voltage for THIPWM technique is $V_{DC}/\sqrt{3}$ which is almost 1.15 times greater than the SPWM technique.

However, when the peak value of the reference voltage is always lower than $V_{DC}/2$, both modulation techniques can be used without the problems caused by overmodulation.

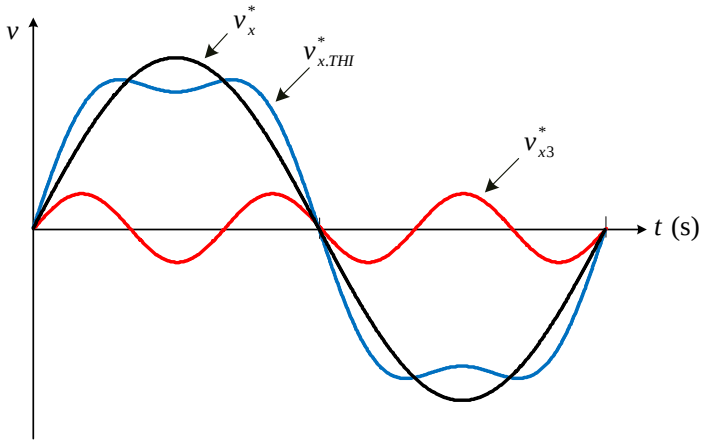

Fig. 2.5. Third harmonic injection to the reference voltage.

2.3.2 Space vector modulation

SVM is one of the preferred real-time modulation techniques and is widely used in digital control systems of multilevel converters [14, 83, 85]. In this modulation strategy, instead of using a separate modulator for each converter leg, a complex reference voltage vector is processed as a whole. The SVM has the advantage of easily balancing the voltages of the DC-link capacitors [85, 86].

Several SVM schemes were proposed for 3LNPC converters [87-91]. In this work, a conventional SVM technique for 3LNPC converters with the mechanism of even-order harmonic elimination [83, 91] was employed in the control system of the IM drive, as this modulation scheme eliminates even-order harmonics of the converter output voltages.

The space vector diagram and the division of the complex plane into sectors and regions, underlying the use of the SVM technique in a 3LNPC converter is shown in Fig. 2.6 [83]. As can be seen, there are 6 triangular sectors $(S_1 \text{ to } S_6)$, each one with 6 regions $(R_1 \text{ to } R_6)$. Taking all three phases into account, the converter has a total of 27 possible switching states that are listed in Table 2.2. These 27 switching states correspond to 19 voltage vectors ($\underline{v}_0$ to $\underline{v}_{18}$) than can be seen in Fig. 2.6 and Table 2.2.

The converter output voltage can be adjusted by choosing the reference voltage vector $\underline{v}^* = \left| \underline{v}^* \right| e^{j\theta_v}$. The SVM algorithm for a 3LNPC converter is based on a volt-second balancing principle, that is, the product of the reference voltage $\underline{v}^*$ by the switching period T_{sw} equals the sum of each voltage vector to be used by the SVM algorithm multiplied by the time during each one of these vectors is applied. For a given length and position in space, $\underline{v}^*$ can be approximated by three nearby stationary vectors. Based on the chosen stationary vectors, switching states are selected, and gate signals are generated. As an example, when $\underline{v}^*$ falls into region 4 of sector 1, as shown in Fig. 2.7, the three nearest vectors are $\underline{v}_1$, $\underline{v}_7$ and $\underline{v}_2$, from which [91, 92]

$$\underline{v}^* T_{sw} = \underline{v}_1 T_a + \underline{v}_7 T_b + \underline{v}_2 T_c, \tag{2.6}$$

$$T_{sw} = T_a + T_b + T_c \ , \tag{2.7}$$

where T_a, T_b and T_c are the dwell times for $\underline{v}_1$, $\underline{v}_7$ and $\underline{v}_2$, respectively. T_a, T_b and T_c are different values, depending on the reference voltage $\underline{v}^*$, being calculated by the relations in Table 2.3 [83].

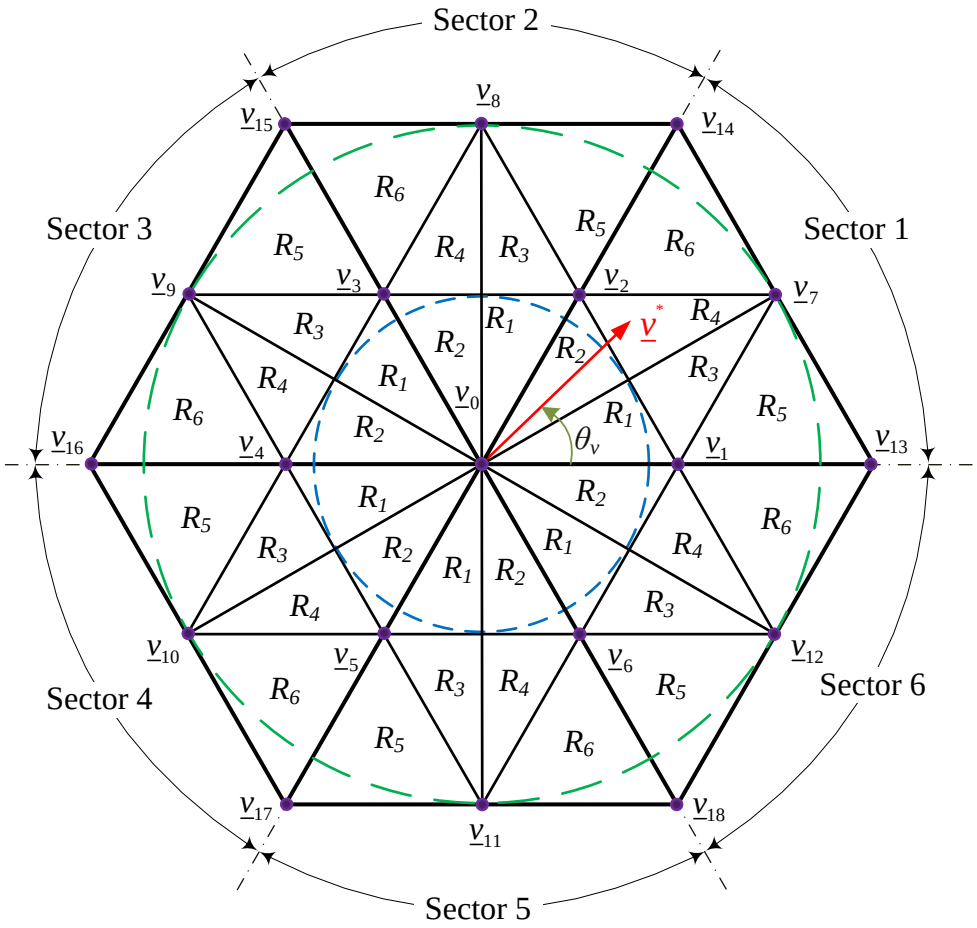

Fig. 2.6. Space vector diagram and division of the complex plane into sectors and regions in a 3LNPC converter.

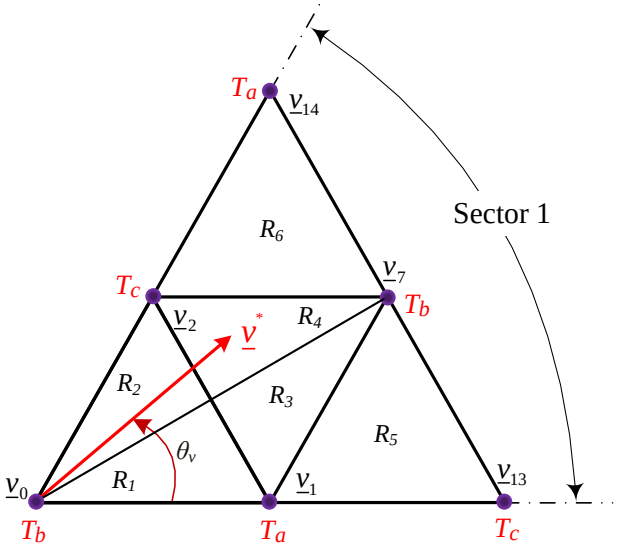

Fig. 2.7. Division of sector 1 into 6 regions.

Table 2.2. Voltage vectors and switching states of a 3LNPC converter [83].

Space vector		**Switching state**		**Vector classification**	**Vector magnitude**
$\underline{v}_0$		[111], [000], [-1-1-1]		Zero Vector	0
		P-type	**N-type**	Small vector	$\frac{1}{3}V_{DC}$
$\underline{v}_1$	$\underline{v}_{1P}$	[100]			
	$\underline{v}_{1N}$		[0-1-1]		
$\underline{v}_2$	$\underline{v}_{2P}$	[110]			
	$\underline{v}_{2N}$		[00-1]		
$\underline{v}_3$	$\underline{v}_{3P}$	[010]			
	$\underline{v}_{3N}$		[-10-1]		
$\underline{v}_4$	$\underline{v}_{4P}$	[011]			
	$\underline{v}_{4N}$		[-100]		
$\underline{v}_5$	$\underline{v}_{5P}$	[001]			
	$\underline{v}_{5N}$		[-1-10]		
$\underline{v}_6$	$\underline{v}_{6P}$	[101]			
	$\underline{v}_{6N}$		[0-10]		
$\underline{v}_7$		[10-1]		Medium vector	$\frac{\sqrt{3}}{3}V_{DC}$
$\underline{v}_8$		[01-1]			
$\underline{v}_9$		[-110]			
$\underline{v}_{10}$		[-101]			
$\underline{v}_{11}$		[0-11]			
$\underline{v}_{12}$		[1-10]			
$\underline{v}_{13}$		[1-1-1]		Large vector	$\frac{2}{3}V_{DC}$
$\underline{v}_{14}$		[11-1]			
$\underline{v}_{15}$		[-11-1]			
$\underline{v}_{16}$		[-111]			
$\underline{v}_{17}$		[-1-11]			
$\underline{v}_{18}$		[1-11]			

Table 2.3. Calculation of dwell times.

Region number	Dwell time		
	T_a	T_b	T_c
1, 2	$T_{sw}[2m_a \sin\left(\frac{\pi}{3} - \beta_v\right)]$	$T_{sw}[1-2m_a \sin(\frac{\pi}{3} + \beta_v)]$	$T_{sw}[2m_a \sin(\beta_v)]$
3, 4	$T_{sw}[1-2m_a \sin(\beta_v)]$	$T_{sw}[2m_a \sin\left(\frac{\pi}{3} + \beta_v\right) - 1]$	$T_{sw}[1-2m_a \sin\left(\frac{\pi}{3} - \beta_v\right)]$
5	$T_{sw}[2-2m_a \sin\left(\frac{\pi}{3} + \beta_v\right)]$	$T_{sw}[2m_a \sin(\beta_v)]$	$T_{sw}[2m_a \sin\left(\frac{\pi}{3} - \beta_v\right) - 1]$
6	$T_{sw}[2m_a \sin\left(\beta_v\right) - 1]$	$T_{sw}[2m_a \sin\left(\frac{\pi}{3} - \beta_v\right)]$	$T_{sw}[2-2m_a \sin\left(\frac{\pi}{3} + \beta_v\right)]$

In all equations shown in Table 2.3, m_a is the modulation index, given by

$$m_a = \sqrt{3}\frac{\left|\underline{v}^*\right|}{V_{DC}} \tag{2.8}$$

and β_v is the angle of $\underline{v}^*$ inside each sector, being given by

$$\beta_v = \theta_v - \left[\frac{\pi}{3}\left(S_n - 1\right)\right], \tag{2.9}$$

where θ_v is the angle of $\underline{v}^*$ and S_n is the sector number where $\underline{v}^*$ is located.

Referring to (2.8), the maximum achievable amplitude of the output voltage using this modulation technique is $V_{DC}/\sqrt{3}$.

As an example, when $T_{sw} = 1$ ms, $V_{DC} = 200$ V, $\left|\underline{v}^*\right| = 70$ V and $\theta_v = 45$, $\underline{v}^*$ falls into region 4 of sector 1 (Fig. 2.7) and the values of the modulation index and the dwell times for $\underline{v}_1$, $\underline{v}_7$ and $\underline{v}_2$ are calculated as $m_a = 0.606$, $T_a = 0.143$ ms, $T_b = 0.171$ ms and $T_c = 0.686$ ms.

In order to implement the even-order harmonic elimination, the switching sequence in each T_{sw} should be divided into 7 segments $\left(Sg_1 \text{ to } Sg_7\right)$. Table 2.4 shows the dwell times for the seven segments which will define the final switching sequence for the 3LNPC converter. All switching sequences for a reference voltage vector positioned in any region of any sector are summarized in Table 2.5-Table 2.10 [83].

For the implementation of the modulation, the following three variables are calculated: sector number (S_n), region number (R_n) and segment number (Sg_n). A global schematic of the algorithm for the SVM of the 3LNPC converter is shown in Fig. 2.8. As can be observed in this figure, to obtain the required IGBT pulses corresponding to a specific $\underline{v}^*$, it is necessary to calculate S_n, R_n and Sg_n. After that, by using the lookup tables (Table 2.5-Table 2.10), the corresponding phases states are obtained.

Table 2.4. Dwell times for the seven segments.

Segment number		1	2	3	4	5	6	7
Dwell time	For odd regions	$\frac{T_a}{4}$	$\frac{T_b}{2}$	$\frac{T_c}{2}$	$\frac{T_a}{2}$	$\frac{T_c}{2}$	$\frac{T_b}{2}$	$\frac{T_a}{4}$
	For even regions	$\frac{T_c}{4}$	$\frac{T_b}{2}$	$\frac{T_a}{2}$	$\frac{T_c}{2}$	$\frac{T_a}{2}$	$\frac{T_b}{2}$	$\frac{T_c}{4}$

Table 2.5. Switching states of the converter when $\underline{v}^*$ is located in sector 1.

Segment number	Region number					
	1	2	3	4	5	6
1	100	00-1	100	00-1	100	00-1
2	000	000	10-1	10-1	10-1	10-1
3	00-1	100	00-1	100	1-1-1	11-1
4	0-1-1	110	0-1-1	110	0-1-1	110
5	00-1	100	00-1	100	1-1-1	11-1
6	000	000	10-1	10-1	10-1	10-1
7	100	00-1	100	00-1	100	00-1

Table 2.6. Switching states of the converter when $\underline{v}^*$ is located in sector 2.

Segment number	Region number					
	1	2	3	4	5	6
1	00-1	010	00-1	010	00-1	010
2	000	000	01-1	01-1	01-1	01-1
3	010	00-1	010	00-1	11-1	-11-1
4	110	-10-1	110	-10-1	110	-10-1
5	010	00-1	010	00-1	11-1	-11-1
6	000	000	01-1	01-1	01-1	01-1
7	00-1	010	00-1	010	00-1	010

Table 2.7. Switching states of the converter when $\underline{v}^*$ is located in sector 3.

Segment number	Region number					
	1	2	3	4	5	6
1	010	-100	010	-100	010	-100
2	000	000	-110	-110	-110	-110
3	-100	010	-100	010	-11-1	-111
4	-10-1	011	-10-1	011	-10-1	011
5	-100	010	-100	010	-11-1	-111
6	000	000	-110	-110	-110	-110
7	010	-100	010	-100	010	-100

Table 2.8. Switching states of the converter when $\underline{v}^*$ is located in sector 4.

Segment number	Region number					
	1	2	3	4	5	6
1	-100	001	-100	001	-100	001
2	000	000	-101	-101	-101	-101
3	001	-100	001	-100	-111	-1-11
4	011	-1-10	011	-1-10	011	-1-11
5	001	-100	001	-100	-111	-1-11
6	000	000	-101	-101	-101	-101
7	-100	001	-100	001	-100	001

Table 2.9. Switching states of the converter when $\underline{v}^*$ is located in sector 5.

Segment number	Region number					
	1	2	3	4	5	6
1	001	0-10	001	0-10	001	0-10
2	000	000	0-11	0-11	0-11	0-11
3	0-10	001	0-10	001	-1-11	1-11
4	-1-10	101	-1-10	101	-1-10	101
5	0-10	001	0-10	001	-1-11	1-11
6	000	000	0-11	0-11	0-11	0-11
7	001	0-10	001	0-10	001	0-10

Table 2.10. Switching states of the converter when $\underline{v}^*$ is located in sector 6.

Segment number	Region number					
	1	2	3	4	5	6
1	0-10	100	0-10	100	0-10	100
2	000	000	1-10	1-10	1-10	1-10
3	100	0-10	100	0-10	1-11	1-1-1
4	101	0-1-1	101	0-1-1	101	0-1-1
5	100	0-10	100	0-10	1-11	1-1-1
6	000	000	1-10	1-10	1-10	1-10
7	0-10	100	0-10	100	0-10	100

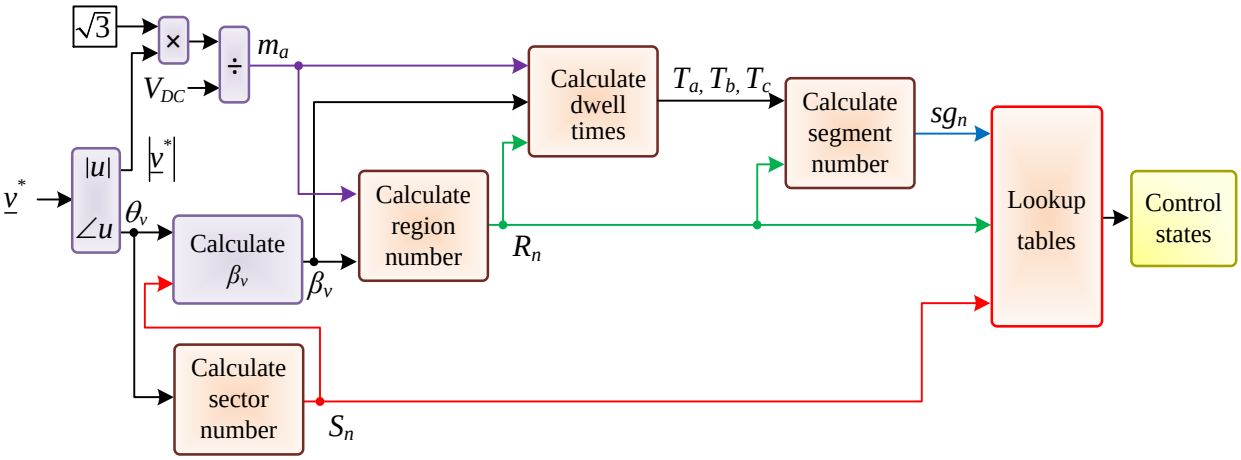

Fig. 2.8. Schematic diagram for the implementation of the SVM.

2.4 IM drives based on 3LNPC inverters

The IM drive used in this work comprises an IM fed by the 3LNPC inverter, subjected to an indirect rotor field oriented control (IRFOC) strategy [93, 94].

The IRFOC strategy is based on the decomposition of the stator currents into two components: a flux-producing component and a torque-producing component. The *d*-axis component of the stator currents is proportional to the rotor flux while the *q*-axis component is proportional to the electromagnetic torque. These two components are then controlled separately [83, 93].

This control strategy has its foundations in a dynamic model of the IM in a synchronous reference frame with the *d*-axis aligned with the rotor flux space vector, as detailed below.

The rotor flux-orientation is schematically represented in Fig. 2.9, where $\underline{\psi}_r$ is the rotor flux space vector, $\underline{i}_s$ is the stator currents space vector, θ_{rf} is the rotor flux angle, ω_s is the instantaneous angular supply frequency and ω_m is the electrical rotor angular speed [83, 93].

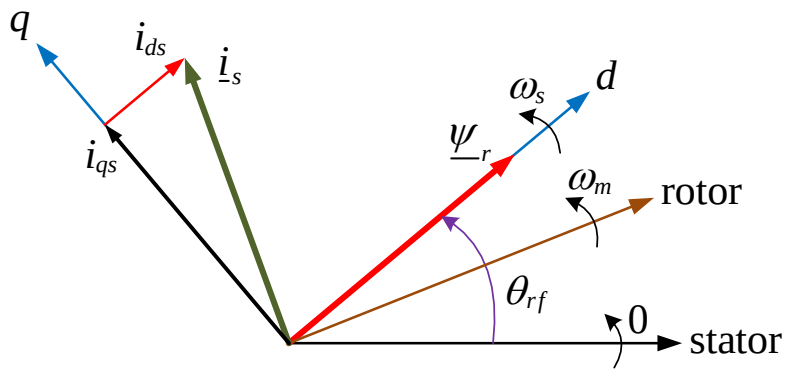

Fig. 2.9. Reference frame orientation. Rotor flux-orientation.

In a synchronous reference frame with the *d*-axis aligned with the rotor flux space vector, the *dq*-axes components of the rotor flux, referred to the stator side, are given by [83]

$$\begin{cases} \psi'_{dr} = L'_r i'_{dr} + L_m i_{ds} = \left|\underline{\psi}'_r\right| \\ \psi'_{qr} = L'_r i'_{qr} + L_m i_{qs} = 0, \end{cases} \tag{2.10}$$

where i'_{dr} and i'_{qr} are the *dq*-axes components of the rotor currents, referred to the stator side, i_{ds} and i_{qs} are the *dq*-axes components of the stator currents, $\left|\underline{\psi}'_r\right|$ is the magnitude of the rotor flux space vector referred to the stator side, L_m is the magnetizing inductance and L'_r is the rotor inductance referred to the stator side, according to

$$L'_r = L'_{lr} + L_m, \tag{2.11}$$

where L'_{lr} is the rotor leakage inductance referred to the stator side.

From (2.10), the relationship between the stator and rotor current components is given by

$$\begin{cases} i'_{dr} = \dfrac{\left|\underline{\psi}'_r\right|}{L'_r} - \dfrac{L_m}{L'_r} i_{ds} \\ i'_{qr} = -\dfrac{L_m}{L'_r} i_{qs}. \end{cases} \tag{2.12}$$

The *dq*-axes components of the rotor voltages in the synchronous reference frame, referred to the stator side, are given by [83]

$$\begin{cases} v'_{dr} = R'_r i'_{dr} + \dfrac{d}{dt}\psi'_{dr} - \omega_r \psi'_{qr} = 0 \\ v'_{qr} = R'_r i'_{qr} + \dfrac{d}{dt}\psi'_{qr} + \omega_r \psi'_{ds} = 0, \end{cases} \tag{2.13}$$

where R'_r is the rotor resistance, referred to the stator side and ω_r is the rotor angular slip frequency, given by

$$\omega_r = \omega_s - \omega_m. \tag{2.14}$$

Combining (2.13) with (2.12), one has

$$\begin{cases} \dfrac{R'_r}{L'_r}\left|\underline{\psi}'_r\right| - \dfrac{R'_r L_m}{L'_r} i_{ds} + \dfrac{d}{dt}\left|\underline{\psi}'_r\right| = 0 \\ -\dfrac{R'_r L_m}{L'_r} i_{qs} + \omega_r \left|\underline{\psi}'_r\right| = 0. \end{cases} \tag{2.15}$$

Based on the first equation in (2.15), the relationship between the rotor flux reference $\left|\underline{\psi}'^{*}_r\right|$ and *d*-axis component of stator current reference i^*_{ds} is given by

$$i^*_{ds} = \frac{1}{L_m}\left|\underline{\psi}'^{*}_r\right| + \frac{L'_r}{R'_r L_m}\frac{d}{dt}\left|\underline{\psi}'^{*}_r\right|. \tag{2.16}$$

Since $\left|\underline{\psi}'^{*}_r\right|$ is normally constant in amplitude, the derivative of $\left|\underline{\psi}'^{*}_r\right|$ is zero and therefore, (2.16) is simplified to

$$i^*_{ds} = \frac{1}{L_m}\left|\underline{\psi}'^{*}_r\right|. \tag{2.17}$$

Based on the second equation in (2.15), the rotor angular slip frequency is given by

$$\omega_r = \frac{R'_r L_m}{L'_r}\frac{i^*_{qs}}{\left|\underline{\psi}'^{*}_r\right|}. \tag{2.18}$$

In general, the electromagnetic torque of induction machines is given by [83]

$$T_{em} = \frac{3}{2} p \frac{L_m}{L'_r} (\psi'_{dr} i_{qs} - \psi'_{qr} i_{ds}), \tag{2.19}$$

where p is the number of pole-pairs of the machine.

In a synchronous reference frame with the d-axis aligned with the rotor flux space vector, the electromagnetic torque is given by

$$T_{em} = \frac{3}{2} p \frac{L_m}{L'_r} |\underline{\psi}'_r| i_{qs}. \tag{2.20}$$

From (2.20), the q-axis current reference i^*_{qs} is given by

$$i^*_{qs} = \frac{2}{3} \frac{L'_r}{pL_m |\underline{\psi}'^*_r|} T_{em}{}^*. \tag{2.21}$$

The equations (2.17) and (2.21) show that under the IRFOC strategy, the rotor flux and electromagnetic torque can be controlled independently by i^*_{ds} and i^*_{qs}, respectively.

The entire control system of the IM drive is schematically illustrated in Fig. 2.10. The implementation of this control system involves the measurement of the stator currents, DC-bus voltage and motor rotor speed.

The rotor flux angle θ_{rf} needed for the transformations of the stator currents to a synchronous reference frame is obtained by [83, 94]

$$\theta_{rf} = \int (\omega_m + \omega_r) dt. \tag{2.22}$$

This control system comprises one outer control loop to control the rotor speed and two inner current control loops to control the stator currents. The reference value of the rotor speed is compared with the measured rotor speed and the error is passed through the PI speed controller whose output gives the reference value of the q component of the stator currents in a synchronous reference frame (i^*_{qs}). Referring to (2.17), i^*_{ds} is obtained by dividing the reference value of the rotor flux by the motor magnetizing inductance. The values of the i^*_{ds} and i^*_{qs} are compared with the values of i_{ds} and i_{qs} and the errors are passed through the PI current controllers. The outputs

of these two controllers generate the references stator voltages in the synchronous frame (v_{ds}^{*} and v_{qs}^{*}). Using the *dq/αβ* transformation block, these voltages are transformed to *αβ*-axes and with the aid of the SVM modulation, the gate signals of the IGBTs are finally generated.

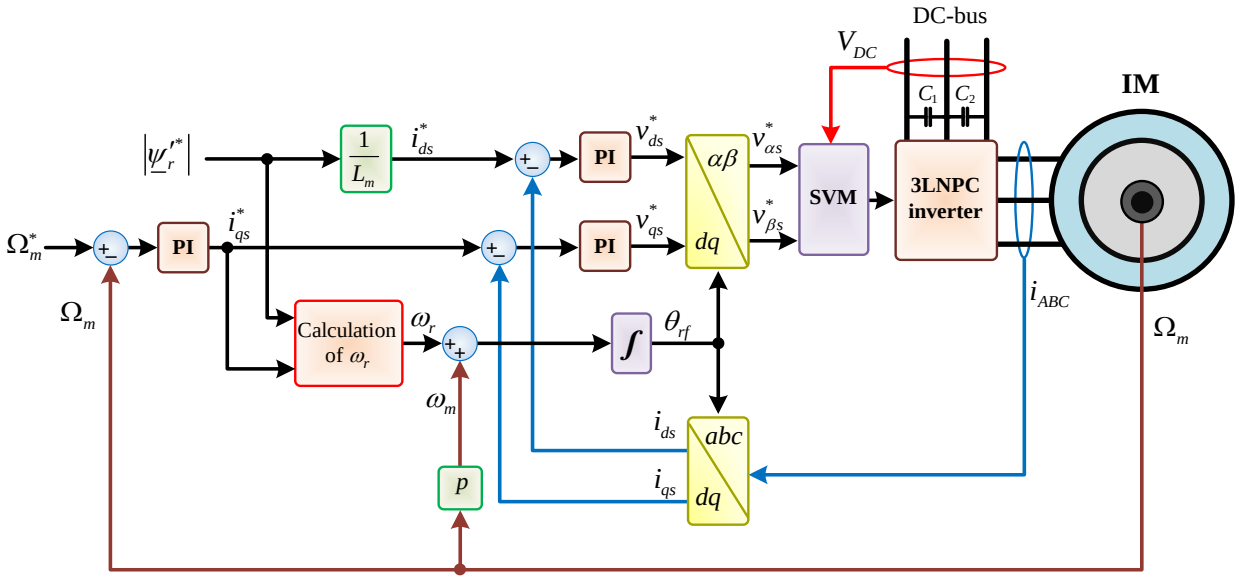

Fig. 2.10. IRFOC control system of an IM drive.

Chapter 3

Fault diagnosis in IM drives based on 3LNPC inverters

3.1 Introduction

Nowadays, important aspects for power converters, particularly the ones used in the high-power range and critical applications are fault detection and protection. Fault detection for 3LNPC converters is even more critical because of their complex topology, associated with a large number of devices and other components used in the converter, increasing the probability of the occurrence of a fault [95]. In order to select the best fault tolerant strategy, it is necessary to identify first the faulty switch.

Several diagnostic approaches for 3LNPC inverters have been proposed in the literature. In [96], the error between the output voltage of each inverter leg and the corresponding reference value is used for the OC fault detection. This diagnostic algorithm only has the capability of detecting the upper or lower IGBT faulty pair. For a correct identification of the faulty IGBT, it is necessary to stop the normal IGBT control pulses and send appropriate test pulses for the IGBTs of the faulty leg. The technique suggested in [78] is based on the measurement of the pole voltages and their duration time. This method, however, is only able to identify the faulty leg and not to discriminate the faulty switch among the four candidates. The implementation of the approaches proposed in [78, 96] needs extra voltage sensors which increase the cost of the system.

In [97], an approach for fault detection and identification of the faulty switch in 3LNPC inverters by measuring the clamp-diode legs currents has been introduced. This method needs 6 Rogowski coils positioned in each clamp-diode leg, in addition to the three current sensors usually located in the output phases of the inverter. By knowing the values of the output currents of the inverter and the currents in each Rogowski coil, together with the control pulses of the IGBTs, it is possible to identify the faulty switch.

An approach to identify the location of a faulty switch in a grid connected 3LNPC inverter is proposed in [98]. According to this approach, the fault detection and identification of the faulty pair is based on the analysis of the radius of the output line current space vector locus. If an OC fault occurs, the angle of the current patterns obtained is measured. After identification of the faulty pair, the location of a faulty switch is met by adding an extra switching scheme to the conventional method.

In [99], the effects of OC faults in a 3LNPC back-to-back converter used in PMSG wind turbines are investigated. Furthermore, a fault detection method based on the slope method is proposed. For the 3LNPC rectifier, the faulty switch can be identified using the slope method. However, in the case of the 3LNPC inverter, this approach is only able to identify the faulty pair (two upper switches or two lower switches of each leg).

Although several techniques for diagnosis of this type of the fault have been proposed in the literature, the implementation of the majority of them needs extra sensors which increase the cost of the system. Only the technique proposed in [98] has the capability to detect and identify OC IGBT faults in 3LNPC inverters without using extra sensors. What's more, the reliability of those techniques was not evaluated for 3LNPC inverters operating under transient operating conditions.

Except for the two diagnostic approaches presented in this chapter, all diagnostic approaches proposed in the literature for 3LNPC inverters have only considered the occurrence of single IGBT faults without having the capability to identify simultaneous faults. For the identification of multiple OC faults in two-level inverters, several approaches have been proposed, which indicate the importance of this topic [100-103]. Due to the high number of power semiconductor devices and gate drivers, the probability of the occurrence of multiple faults in 3LNPC inverters is more significant than in two-level inverters.

To overcome these limitations, three novel real-time diagnostic methods are developed and implemented, which allow the detection and location of the faulty power switches in 3LNPC inverters. The performance of the 3LNPC inverter under different faulty conditions is assessed. Then, the proposed diagnostic approaches along with the corresponding experimental results supporting their applicability are reported.

3.2 IM drives based on 3LNPC inverters under OC faults

3.2.1 Analysis of OC faults in a 3LNPC inverter

In order to develop an approach for fault diagnosis, it is important to know in advance how the system behaves under the presence of a fault. The behavior of the 3LNPC inverter under different faulty conditions is analyzed.

Under an inverter OC fault, the faulty IGBT is unable to commutate in agreement with the output pulses generated by the modulator and remains in an off-state permanently, thus eliminating some current paths available before [104]. Table 3.1 shows the unavailable current paths for 12 different fault combinations. In this table, condition 1 is for the healthy operation, conditions 2 to 5 are for single IGBT faults, conditions 6 to 11 are for double IGBT faults, and conditions 12 and 13 are for clamp-diode faults. This table shows that when an OC fault occurs in one of the outer switches (S_{x1} and S_{x4}) as well as in the clamp-diodes, one current path is not available and if an OC fault occurs in an inner IGBT (S_{x2} and S_{x3}), two current paths are not available.

For each faulty condition, according to the control state of leg x (CS_x) and the current direction, the current may flow through an available alternative path. These available alternative paths are listed in Table 3.1 according to CS_x and the current direction . For example, if an OC fault occurs in S_{x1} (condition 2 in Table 3.1), the current path number 1 is not available. In this case, when CS_x is 1 and $i_x > 0$, i_x can flow through current path number 2 as an alternative to path number 1. Thus, i_x will have a small positive amplitude value when compared to the normal operation. In this case, the output of leg x is connected to the middle point z. If an OC fault occurs in S_{x2} (condition 3 in Table 3.1), the current paths numbers 1 and 2 are not available. In this case, for the circulating of a positive value of i_x, only the current path number 3 is available. An analogous analysis can be performed for other faulty conditions.

Table 3.1. Inverter leg situation after OC fault(s) in leg x.

Condition number	Condition of IGBTs and diodes located in leg x						Unavailable current path(s)	Available current paths					
								CS_x=1		CS_x=0		CS_x=-1	
	S_{x1}	S_{x2}	S_{x3}	S_{x4}	D_{x5}	D_{x6}		i_x>0	i_x<0	i_x>0	i_x<0	i_x>0	i_x<0
1	ok	ok	ok	ok	ok	ok	---	1	4	2	5	3	6
2	OC	ok	ok	ok	ok	ok	1	2	4	2	5	3	6
3	ok	OC	ok	ok	ok	ok	1, 2	3	4	3	5	3	6
4	ok	ok	OC	ok	ok	ok	5, 6	1	4	2	4	3	4
5	ok	ok	ok	OC	ok	ok	6	1	4	2	5	3	5
6	OC	OC	ok	ok	ok	ok	1, 2	3	4	3	5	3	6
7	OC	ok	OC	ok	ok	ok	1, 5	2	4	2	4	3	4
8	OC	ok	ok	OC	ok	ok	1, 6	2	4	2	5	3	5
9	ok	OC	OC	ok	ok	ok	1, 2, 5, 6	3	4	3	4	3	4
10	ok	OC	ok	OC	ok	ok	1, 2, 6	3	4	3	5	3	5
11	ok	ok	OC	OC	ok	ok	5, 6	1	4	2	4	3	4
12	ok	ok	ok	ok	OC	ok	2	1	4	3	5	3	6
13	ok	ok	ok	ok	ok	OC	5	1	4	2	4	3	6

3.2.2 Experimental results

In order to perform the experimental tests for fault diagnosis in IM drives, a test rig of an IM drive based on a 3LNPC inverter was prepared. It comprises an IM fed by the 3LNPC inverter prototype (Appendix *A*), subjected to an IRFOC strategy. The motor line currents, the inverter pole voltages, the DC-bus voltage, the mechanical torque and the rotor speed were measured by the sensors installed in the test rig. Further details about the test rig of the IM drive are presented in Appendix *B*. In the experiments, the OC fault was introduced by sending a zero gate signal to a specific IGBT.

Fig. 3.1 shows the experimental results for the IM drive operating at a rotor speed of 750 rpm and a mechanical torque of 7 Nm with an OC fault in S_{A1}, introduced at t=1 s (indicated by the vertical line F_T). According to Table 3.1, for this faulty condition, the inverter current path number 1 in Fig. 2.3 is not available. In this case, when CS_A is 1 and $i_A > 0$, i_A can flow through current path number 2. Consequently, the output of leg *A* is connected to the middle point *z* and not to the positive terminal of the DC-bus.

As shown in Fig. 3.1(a), after the occurrence of the OC fault in S_{A1}, the pole voltage of leg *A* does not follow the control state. When the fault is introduced at *t*=1 s the positive part of i_A is affected as shown in Fig. 3.1(b) and it will have small positive values when compared to a normal operation of the inverter.

Fig. 3.2 shows the experimental results for the IM drive operating with an OC fault in S_{A2} (condition 3 in Table 3.1), introduced at *t*=1 s. After the occurrence of this fault, the current paths number 1 and 2 in Fig. 2.3 are not available. In this case, when CS_A is 1 and $i_A > 0$, i_A can flow through the current path number 3. Consequently, the output of leg *A* is connected to the negative terminal of the DC-bus and i_A decreases to zero. During this process, the pole voltage of the faulty leg changes to $-V_{DC}/2$, until the current of the faulty leg reaches zero. After that, the output pole voltage of the faulty leg is defined by the operating condition of the healthy phases, while the current of the faulty leg is zero.

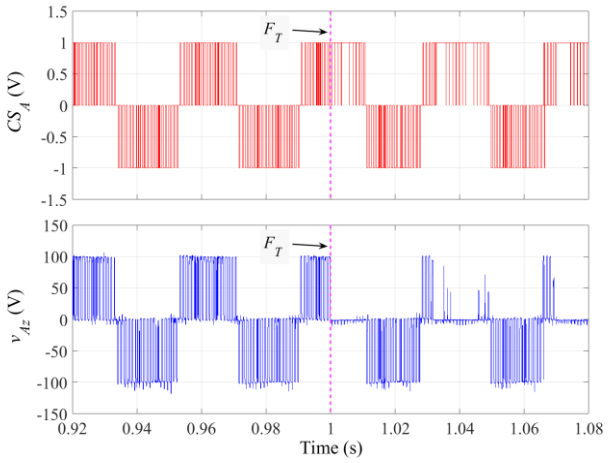

(a) Control state and pole voltage of the inverter leg *A*

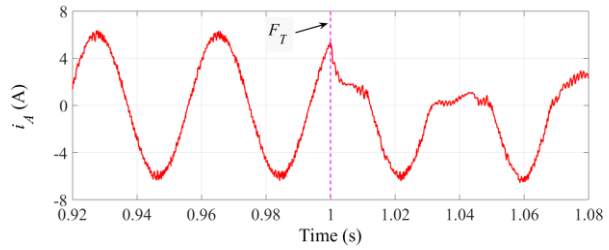

(b) Output current of the inverter leg *A*

Fig. 3.1. Results for the 3LNPC inverter operating in healthy conditions ($t < 1$ s) and with an OC fault in S_{A1} ($t \geq 1$ s).

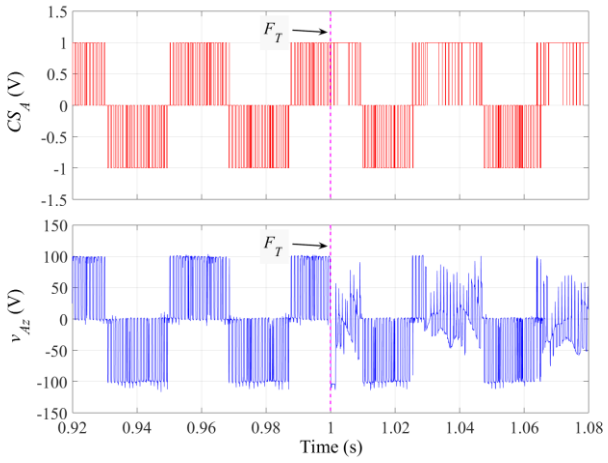

(a) Control state and pole voltage of the inverter leg *A*

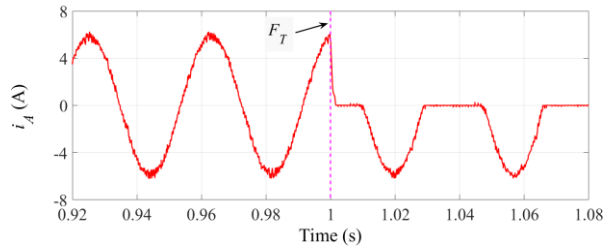

(b) Output current of the inverter leg *A*

Fig. 3.2. Results for the 3LNPC inverter operating in healthy conditions ($t < 1$ s) and with an OC fault in S_{A2} ($t \geq 1$ s).

The results presented in Fig. 3.1(b) and Fig. 3.2(b) show that the behavior of the positive current values of i_A depends on the condition whether the fault occurs in an outer IGBT (small positive current values available) or inner IGBT (no positive current values available). A similar analysis can be done for the behavior of the negative current values of i_A for a fault in an inner IGBT (no negative current values available) or outer IGBT (small negative current values available).

3.3 Average Current Park's Vector

This section presents the ACPV approach as a novel technique for the diagnosis of IGBT OC faults in a 3LNPC inverter. This technique was firstly presented in [58] and modified in [55].

3.3.1 Approach description

The ACPV approach was applied in two-level inverters and first presented in [105]. With the ACPV diagnostic technique, the detection of an OC fault and the localization of the faulty semiconductor is accomplished by examining the magnitude and position of the Park's vector of the average value of each inverter output line current.

To implement this method, first, the average value of each motor line current is calculated by

$$i_{x.av}[k] = \frac{1}{N} \sum_{i=k-N}^{k} i_{x,k}[i], \tag{3.1}$$

where k is the sample index, x is the leg index and N is the number of samples in one electric period, given by

$$N = \left\lfloor \frac{T_{i.s}}{T_s} \right\rfloor, \tag{3.2}$$

where $T_{i.s}$ is the of the motor line currents period and T_s is the sampling period.

Afterwards, the Park's Vector transformation is applied to those values, in order to obtain the average motor line current Park's Vector $\underline{i}_{s.av}$, characterized by a magnitude $|\underline{i}_{s.av}|$ and a phase angle $\theta_{s.av}$, given by [105]

$$\underline{i}_{s.av}[k] = i_{\alpha.av}[k] + j i_{\beta.av}[k] = \left|\underline{i}_{s.av}[k]\right| \angle \theta_{s.av}, \tag{3.3}$$

where $i_{\alpha.av}$ and $i_{\beta.av}$ are α and β components of $\underline{i}_{s.av}$, given by

$$\begin{cases} i_{\alpha.av}[k] = \dfrac{2}{3} i_{A.av}[k] - \dfrac{1}{3}\left(i_{B.av}[k] + i_{C.av}[k]\right) \\ i_{\beta.av}[k] = \dfrac{1}{\sqrt{3}}\left(i_{B.av}[k] - i_{C.av}[k]\right). \end{cases} \tag{3.4}$$

Under inverter normal operation, the average value of each motor line current is almost zero and consequently $\left|\underline{i}_{s.av}\right|$ is also nearly zero. However, if an IGBT OC fault occurs, $\left|\underline{i}_{s.av}\right|$ will increase and assume a value higher than a predefined threshold value (near zero) allowing the fault detection. Afterwards, the faulty IGBT is identified by reading the value of $\theta_{s.av}$.

The same ACPV approach was applied to a 3LNPC inverter in [58]. However, taking into account that each half of each inverter leg has two semiconductors, the diagnostic technique introduced in [105] is unable to locate the faulty IGBT.

Considering the fundamentals of the ACPV diagnostic technique, a new method suitable to perform a complete diagnosis of IGBTs OC faults in a 3LNPC inverter is proposed in this section.

The block diagram of the proposed diagnostic technique is shown in Fig. 3.3. In this figure, the block diagram is divided into three subsystems, corresponding to different tasks of the fault diagnostic algorithm. Subsystem 1 is used to calculate the Park's vector modulus of the motor line currents that is used to obtain normalized instantaneous values of the motor line currents and also to normalize the ACPV magnitude $\left|\underline{i}_{s.av.n}\right|$ in order to obtain a diagnostic method independent of the load level and system rated power. Subsystem 2 in Fig. 3.3 is responsible for the algorithms of fault detection and faulty pair identification, whereas Subsystem 3 is responsible for the faulty switch identification.

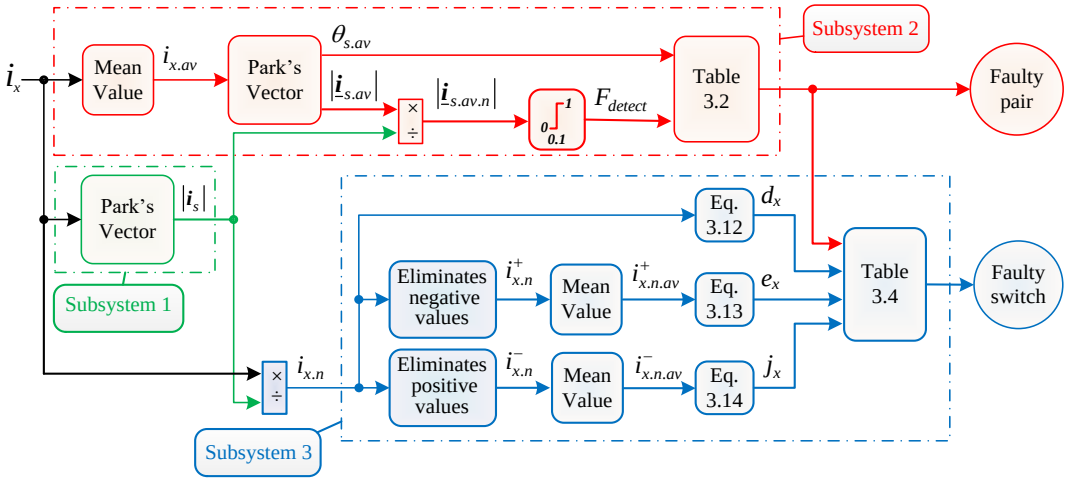

Fig. 3.3. Block diagram of the diagnostic technique based on the ACPV.

The motor line current Park's vector $\underline{i}_s$ is calculated from the motor line currents by (3.5).

$$\begin{cases} \underline{i}_s[k] = i_{\alpha.s}[k] + j i_{\beta.s}[k] = |\underline{i}_s[k]| \angle \theta_s \\ i_{\alpha.s}[k] = \frac{2}{3} i_A[k] - \frac{1}{3}(i_B[k] + i_C[k]) \\ i_{\beta.s}[k] = \frac{1}{\sqrt{3}}(i_B[k] - i_C[k]). \end{cases} \tag{3.5}$$

The normalized motor line currents $i_{x.n}$ are obtained by (3.6) and the normalized ACPV magnitude $|\underline{i}_{s.av.n}|$ is obtained by (3.7).

$$i_{x.n}[k] = \frac{i_x[k]}{|\underline{i}_s[k]|}. \tag{3.6}$$

$$|\underline{i}_{s.av.n}[k]| = \frac{|\underline{i}_{s.av}[k]|}{|\underline{i}_s[k]|}. \tag{3.7}$$

The value of $|\underline{i}_{s.av.n}|$ is used to detect the faulty IGBT. As shown in Subsystem 2, when $|\underline{i}_{s.av.n}|$ is higher than a predefined threshold value $I_{s.av}^{th}$, a fault alarm corresponding to a fault detection is generated by the diagnostic algorithm (F_{detect} signal).

To identify the faulty pair, the angle $\theta_{s.av}$ is used. Under normal operating conditions, the value of $\theta_{s.av}$ is a mathematical indetermination since the ACPV $\alpha\beta$ components are both zero. However, the experimental results show that in practice, these $\alpha\beta$ components are nearly zero and angle $\theta_{s.av}$

is changing between 0º and 360º. Nevertheless, the exact angle value is not important before fault detection. When an IGBT OC fault occurs, the angle $\theta_{s.av}$ will present an almost constant value belonging to a predefined range, characteristic for each faulty IGBT pair. The relation between the value of $\theta_{s.av}$ and the faulty IGBT is shown in Table 3.2. After fault detection, this lookup table allows the identification of the faulty pair and faulty leg, corresponding to the output of Subsystem 2.

Table 3.2. Lookup table to find the faulty pair and faulty leg.

$\theta_{s.av}$	Faulty switch	Faulty pair		Faulty leg
		Number	Label	
$150^o \le \theta_{s.av} < 210^o$	S_{A1} or S_{A2}	1	P_{A1}	*A*
$-30^o \le \theta_{s.av} < 30^o$	S_{A3} or S_{A4}	2	P_{A2}	
$270^o \le \theta_{s.av} < 330^o$	S_{B1} or S_{B2}	3	P_{B1}	*B*
$90^o \le \theta_{s.av} < 150^o$	S_{B3} or S_{B4}	4	P_{B2}	
$30^o \le \theta_{s.av} < 90^o$	S_{C1} or S_{C2}	5	P_{C1}	*C*
$210^o \le \theta_{s.av} < 270^o$	S_{C3} or S_{C4}	6	P_{C2}	

To complete the fault diagnostic process, after fault detection and identification of both the faulty leg and the faulty pair, it is necessary to identify the faulty IGBT, which can be accomplished by the algorithm illustrated by Subsystem 3 in Fig. 3.3. As can be observed, the normalized current $i_{x.n}$ is split into two parts, one with positive instantaneous values $i_{x.n}^{+}$ and the other with negative instantaneous values $i_{x.n}^{-}$ that are determined by (3.8) and (3.9), respectively.

$$i_{x.n}^{+}[k] = \begin{cases} i_{x.n}[k] \Leftarrow & i_{x.n}[k] > 0 \\ 0 \quad\;\; \Leftarrow & i_{x.n}[k] \le 0. \end{cases} \tag{3.8}$$

$$i_{x.n}^{-}[k] = \begin{cases} 0 \quad\;\; \Leftarrow & i_{x.n}[k] \ge 0 \\ i_{x.n}[k] \Leftarrow & i_{x.n}[k] < 0. \end{cases} \tag{3.9}$$

Thus, the average values of $i_{x.n}^{+}$ and $i_{x.n}^{-}$ are calculated by (3.10) and (3.11), respectively, where *N* is the number of samples in one electric period (given by (3.2)), *k* is the index of a sample and *x* is the inverter leg index.

$$i^{+}_{x.n.av}[k] = \frac{1}{N}\sum_{i=k-N}^{k} i^{+}_{x.n}[i]. \tag{3.10}$$

$$i^{-}_{x.n.av}[k] = \frac{1}{N}\sum_{i=k-N}^{k} i^{-}_{x.n}[i]. \tag{3.11}$$

As $i^{+}_{x.n}$ and $i^{-}_{x.n}$ are signals which are equivalent to a half-wave rectified signal, when all IGBTs are healthy, the normalized current average values are $i^{+}_{x.n.av} \approx 0.318$ and $i^{-}_{x.n.av} \approx -0.318$. If these variables present values different from those, then an OC fault exists in an outer or inner IGBT, as discussed below.

To implement the fault diagnostic algorithm in a digital controller, the diagnostic variables d_x, e_x and j_x are used, as illustrated by Subsystem 3 in Fig. 3.3. The diagnostic variable d_x is obtained from the comparison between $i_{x.n}$ and the threshold values I^{th}_{pos} and I^{th}_{neg}. The diagnostic variables e_x and j_x are obtained from the comparison of $i^{+}_{x.n.av}$ and $i^{-}_{x.n.av}$ with the threshold values I^{th+}_{av} and I^{th-}_{av}, respectively.

The considered threshold values are listed in Table 3.3. These values were determined based on several experimental tests and are suitable to work under steady-state as well as under transient load conditions.

Table 3.3. Thresholds values used in the ACPV system.

Threshold label	Value	Description	Application
$I^{th}_{s.av}$	0.1	Threshold value for $\lvert i_{s.av.n}\rvert$	Fault detection
I^{th+}_{av}	0.05	Threshold value for $i^{+}_{x.n.av}$	Calculation of e_x
I^{th-}_{av}	-0.05	Threshold value for $i^{-}_{x.n.av}$	Calculation of j_x
I^{th}_{pos}	0.15	Positive threshold value for $i_{x.n}$	Calculation of d_x
I^{th}_{neg}	-0.15	Negative threshold value for $i_{x.n}$	

The diagnostic variables d_x, e_x and j_x are defined by (3.12), (3.13) and (3.14), respectively.

$$d_x[k] = \begin{cases} 1 \Leftarrow & i_{x.n}[k] \geq I^{th}_{pos} \\ 0 \Leftarrow & I^{th}_{neg} < i_{x.n}[k] < I^{th}_{pos} \\ -1 \Leftarrow & i_{x.n}[k] \leq I^{th}_{neg}. \end{cases} \tag{3.12}$$

$$e_x[k]=\begin{cases} 1 \Leftarrow i^{+}_{x.n.av}[k] \le I^{th+}_{av} \\ 0 \Leftarrow i^{+}_{x.n.av}[k] > I^{th+}_{av}. \end{cases} \tag{3.13}$$

$$j_x[k]=\begin{cases} 1 \Leftarrow i^{-}_{x.n.av}[k] \ge I^{th-}_{av} \\ 0 \Leftarrow i^{-}_{x.n.av}[k] < I^{th-}_{av}. \end{cases} \tag{3.14}$$

The variable d_x is used to identify an outer faulty IGBT in leg x (S_{x1} or S_{x4}), the variable e_x is used to identify faulty IGBT S_{x2} in leg x and variable j_x is used to identify faulty IGBT S_{x3} in leg x. Under inverter normal operating conditions, the variable d_x is changing between -1 and 1, while the variables e_x and j_x present null values. After the appearance of the IGBT OC fault, the values of these variables are dependent on the faulty switch.

As can be seen in Fig. 3.3, to identify the faulty switch, it is necessary to use these diagnostic variables together with the number of the faulty pair. Based on Table 3.4 the faulty switch is isolated. In this table, the symbol "--" means that the variable value is irrelevant for the diagnosis.

The flowchart of the proposed diagnostic technique is shown in Fig. 3.4.

Table 3.4. Lookup table for identification of the faulty IGBT.

Faulty pair	Diagnostic variables									Faulty switch	
	d_A	d_B	d_C	e_A	e_B	e_C	j_A	j_B	j_C	Number	Label
P_{A1}	1	--	--	0	--	--	--	--	--	1	S_{A1}
	0	--	--	1	--	--	--	--	--	2	S_{A2}
P_{A2}	0	--	--	--	--	--	1	--	--	3	S_{A3}
	-1	--	--	--	--	--	0	--	--	4	S_{A4}
P_{B1}	--	1	--	--	0	--	--	--	--	5	S_{B1}
	--	0	--	--	1	--	--	--	--	6	S_{B2}
P_{B2}	--	0	--	--	--	--	--	1	--	7	S_{B3}
	--	-1	--	--	--	--	--	0	--	8	S_{B4}
P_{C1}	--	--	1	--	--	0	--	--	--	9	S_{C1}
	--	--	0	--	--	1	--	--	--	10	S_{C2}
P_{C2}	--	--	0	--	--	--	--	--	1	11	S_{C3}
	--	--	-1	--	--	--	--	--	0	12	S_{C4}

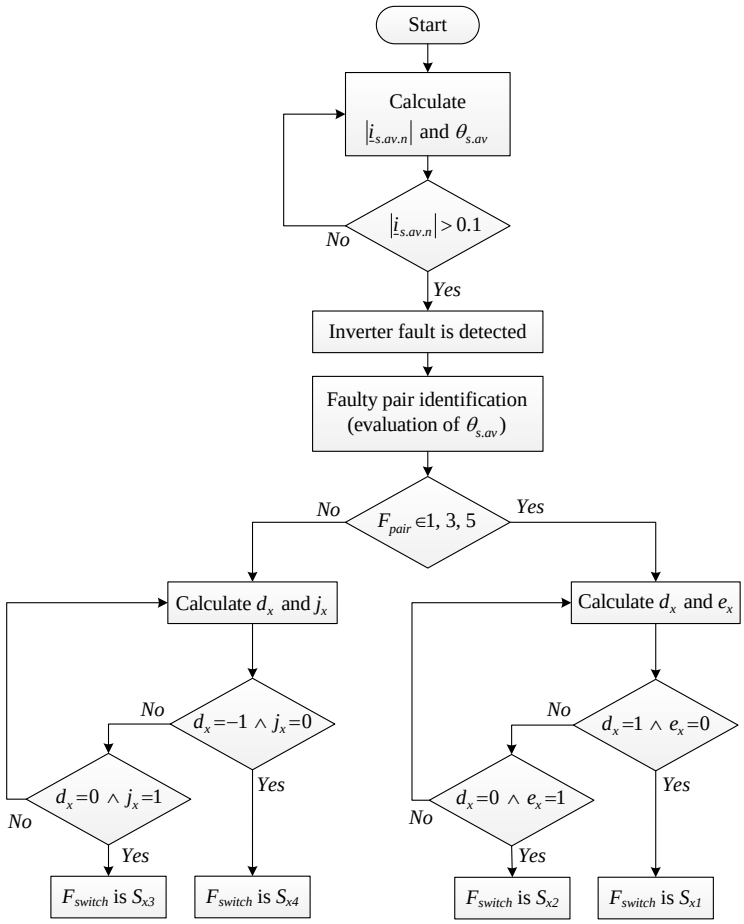

Fig. 3.4. Flowchart of the diagnostic technique based on the ACPV.

3.3.2 Experimental validation

This subsection presents fault diagnostic results obtained for some IGBT OC faults in a single inverter leg. Similar results were obtained for the other inverter legs. Considering the schematic representation shown in Fig. 2.2, a 3LNPC inverter has six IGBT pairs, each one with an inner and outer IGBT. The inverter legs *A*, *B* and *C* have upper pairs of IGBTs identified with the numbers 1, 3 and 5, and lower IGBT pairs identified with the numbers 2, 4 and 6, respectively.

As presented before (Fig. 3.3), the fault diagnostic algorithm is developed in two steps. In the first step, the OC fault is detected and the faulty pair is isolated. When the first step is completed, it is necessary to know the diagnostic variable values listed in Table 3.4 in order to identify the faulty IGBT.

3.3.2.1 Results for steady-state operation

The results shown in this subsection are for the steady-state condition of the IM drive with a reference speed of 750 rpm and a mechanical torque of 7 Nm.

Fig. 3.5(a) and Fig. 3.5(b) show the behavior of motor speed and mechanical torque when an OC fault affects IGBTs S_{A1} and S_{A2}, respectively. These figures show that the motor is operating with a mechanical speed of 750 rpm and a mechanical torque of 7 Nm when the fault occurs at t=1 s. After this moment, the motor is unable to follow the speed reference of 750 rpm and torque oscillations are generated, particularly for the OC fault in IGBT S_{A2}, as illustrated in Fig. 3.5(b).

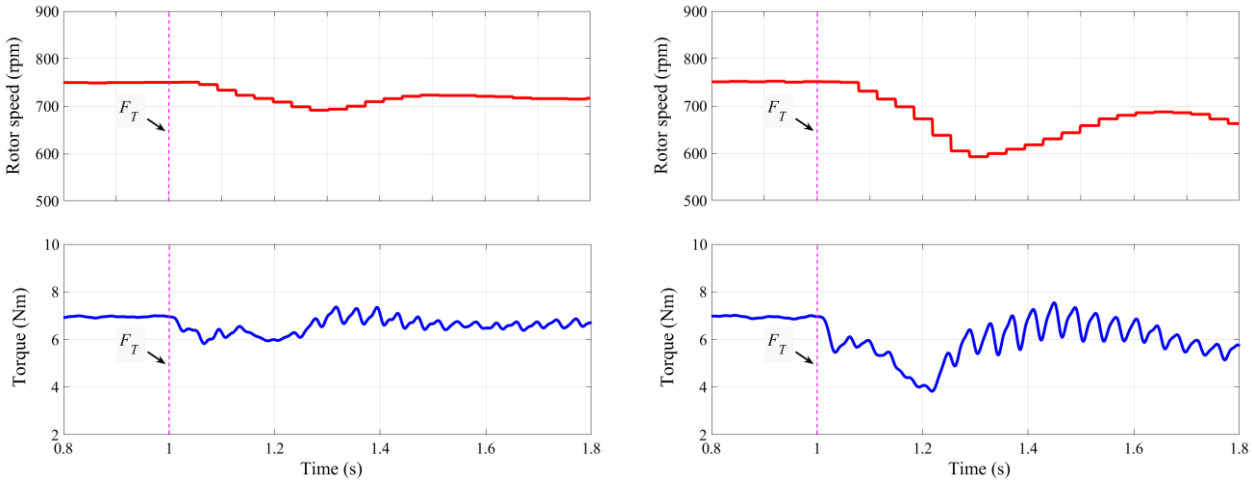

(a) OC fault in S_{A1} (b) OC fault in S_{A2}

Fig. 3.5. Operation of the IM drive before and after an OC fault.

Fig. 3.6 and Fig. 3.7 show the diagnostic results for an OC fault in IGBT S_{A1} and S_{A2}, respectively. The motor mechanical behavior is also accompanied with motor line currents oscillations and current profile changes after the fault as can be observed in Fig. 3.6(a) for the OC fault in S_{A1}. These oscillations that appear after t=1 s are the result of inverter operation with a permanent switch-off state in one IGBT of inverter leg *A*.

As shown in Fig. 3.6(a), before the fault, the current i_A presents an almost sinusoidal shape with a fundamental period around 39 ms. When the fault is introduced at t=1 s the positive part of i_A is affected. Therefore, as can be observed in Fig. 3.6(b), after the fault, $|i_{s.av.n}|$ starts increasing from nearly zero, and 6 ms later this value is higher than the threshold value $I_{s.av}^{th} = 0.1$ which

triggers the fault detection. At the same instant, Fig. 3.6(b) shows that $\theta_{s.av} = 204^{o}$. Based on Table 3.2, this angle allows identifying the faulty pair number 1, that belongs to the inverter leg *A*.

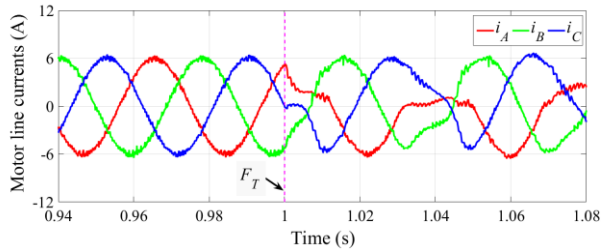

(a) Motor line current waveforms

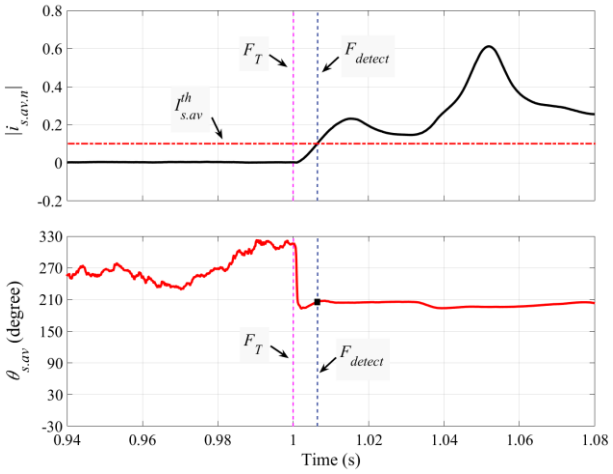

(b) Magnitude and angle of ACPV

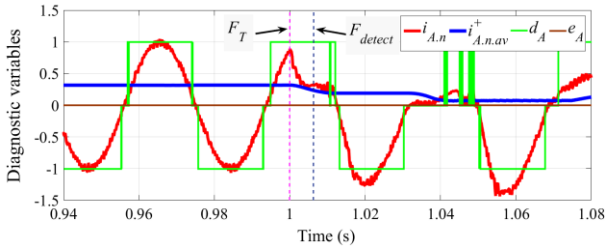

(c) Diagnostic variables

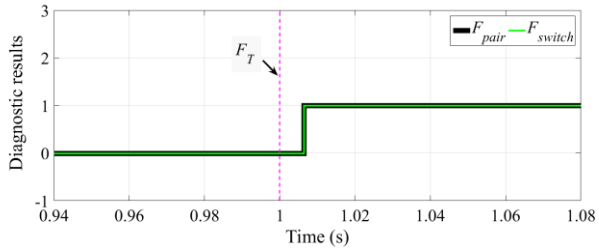

(d) Diagnostic result

Fig. 3.6. Diagnostic results for the IM drive operating with an OC fault in S_{A1}.

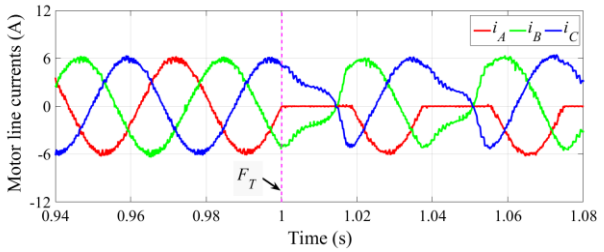

(a) Motor line current waveforms

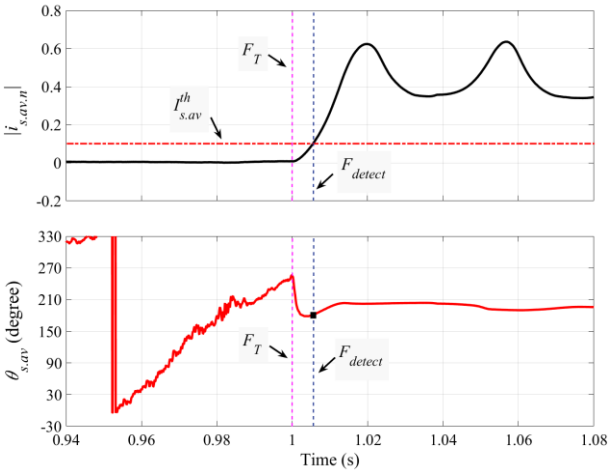

(b) Magnitude and angle of ACPV

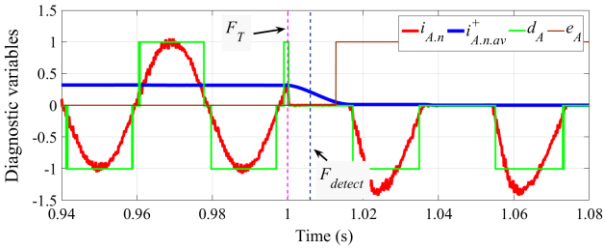

(c) Diagnostic variables

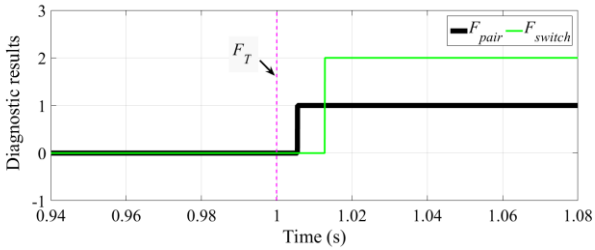

(d) Diagnostic result

Fig. 3.7. Diagnostic results for the IM drive operating with an OC fault in S_{A2}.

Based on Fig. 3.6(c) it can be observed that for the corresponding instant of faulty pair detection (Fig. 3.6(b)) the condition $i_{A.n} > I_{pos}^{th}$ is verified and consequently $d_A = 1$. At the same instant, the condition $i_{A.n.av}^{+} > I_{av}^{th+}$ is verified which leads to $e_A = 0$. Taking into account that $F_{pair} = 1$, $d_A = 1$ and $e_A = 0$, the diagnostic result is shown in Fig. 3.6(d), which shows that the faulty pair is the number 1 and the faulty IGBT is also number 1, which corresponds to S_{A1} (according to Table 3.4). The fault detection and identification is accomplished in 6 ms.

The motor line currents presented in Fig. 3.7(a) correspond to a different faulty IGBT. After the introduction of the fault at *t*=1 s, the motor line current i_A starts decreasing to zero. The corresponding $|\underline{i}_{s.av.n}|$ and $\theta_{s.av}$ values are represented in Fig. 3.6(b). As can be noticed, the fault is detected when $|\underline{i}_{s.av.n}| > 0.1$ which occurs at $t = 1.006$ s. At this instant, the angle $\theta_{s.av} = 181^{o}$, which in conjunction with Table 3.2 leads to $F_{pair} = 1$.

After knowing the faulty pair, it is necessary to identify the faulty IGBT. As observed in Fig. 3.7(c), after fault detection, the condition $i_{A.n} < I_{pos}^{th}$ is confirmed thereby imposing a value 0 to the diagnostic variable d_A which, according to Table 3.4, none IGBT can be identified as the faulty one. Thus, in these cases, it is necessary to verify if the condition $i_{A.n.av}^{+} \leq I_{av}^{th+}$ is met which happens at $t = 1.013$ s and consequently $e_A = 1$. Knowing that $F_{pair} = 1$, $d_A = 0$ and $e_A = 1$, Table 3.4 lets to identify S_{A2} as the faulty IGBT. Fig. 3.7(d) resumes the timeline corresponding to the diagnostic result where the IGBT pair number 1 is detected at *t*=1.006 s, and the faulty IGBT number 2 is isolated at *t*=1.013 s.

3.3.2.2 Results for transient conditions

To evaluate the performance of the proposed diagnostic approach under transient conditions, several load and speed variations were tested. The results presented in this subsection are for a predefined reference speed profile, starting with 500 rpm. Then, an acceleration ramp until 800 rpm is imposed during 5 s. Thereafter, the speed reference used was 800 rpm during 1 s followed by a deceleration ramp until 500 rpm.

The behavior of motor speed and mechanical torque under this transient condition and when an OC fault affects IGBTs S_{A1} and S_{A2} are shown in Fig. 3.8(a) and Fig. 3.9(a), respectively. As shown in these figures, the load torque starts with 5 Nm and then changes during the transient, proportionally to speed. After *t*≥9 s, both results show that the motor is unable to follow the speed

reference and the mechanical torque has oscillations. It was verified that with a S_{A2} OC fault, there are larger mechanical speed and torque oscillations than with a S_{A1} OC fault.

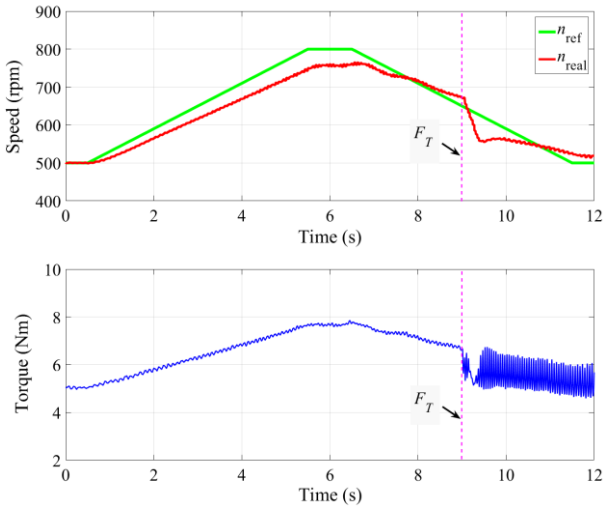

(a) Reference and mechanical motor speeds and mechanical torque

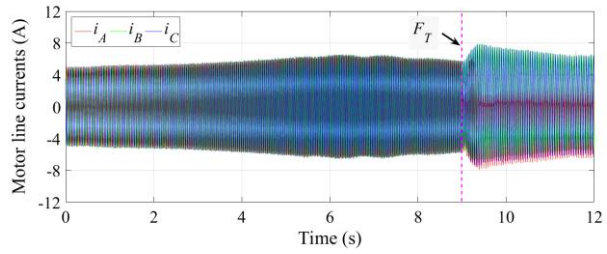

(b) Motor line current waveforms

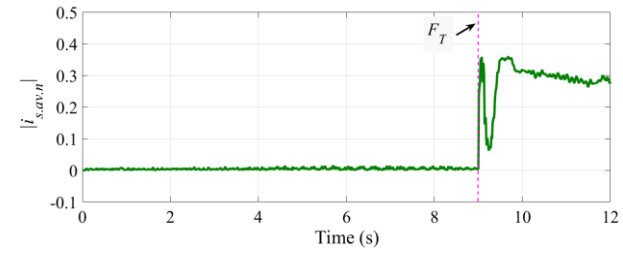

(c) ACPV magnitude

Fig. 3.8. Transient operation of the IM drive under speed and torque variations, without any fault ($t < 9$ s) and after OC fault in S_{A1} ($t \geq 9$ s).

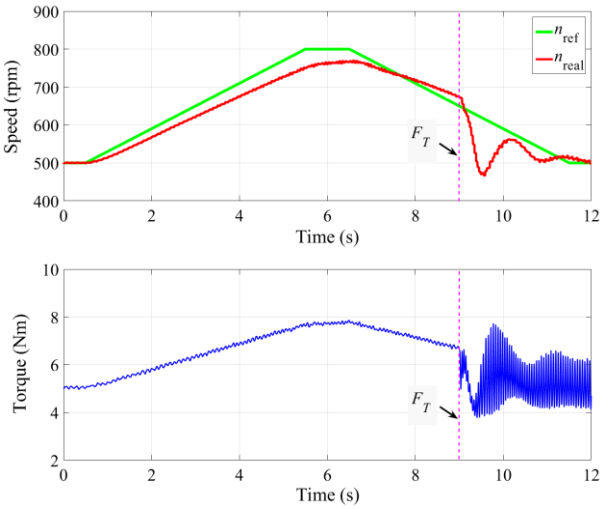

(a) Reference and mechanical motor speeds and mechanical torque

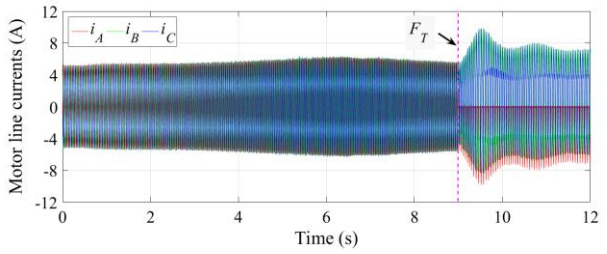

(b) Motor line current waveforms

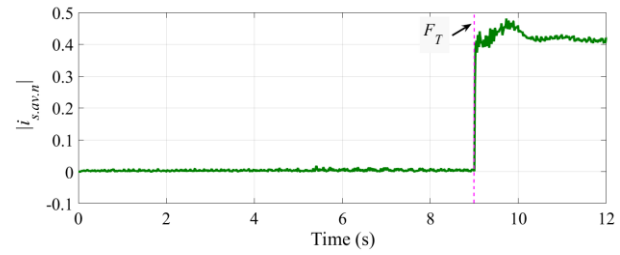

(c) ACPV magnitude

Fig. 3.9. Transient operation of the IM drive under speed and torque variations, without any fault ($t < 9$ s) and after OC fault in S_{A2} ($t \geq 9$ s).

The motor line current waveforms with an OC fault in the IGBTs S_{A1} and S_{A2} are represented in Fig. 3.8(b) and Fig. 3.9(b), respectively. As can be observed in these figures, the oscillations of the motor line current waveforms due to S_{A2} fault are larger than those with S_{A1} fault.

Despite this dynamic speed profile, until fault occurrence at *t*=9 s, no false fault detection was triggered as can be observed in Fig. 3.8(c) and Fig. 3.9(c) where the normalized modulus of the average output current Park's Vector is represented. Until the fault occurrence, the value of $|\underline{i}_{s.av.n}|$ is near zero, but after that instant, its value increases above the threshold $I_{s.av}^{th}$ allowing the fault detection.

Fig. 3.10 and Fig. 3.11 show the diagnostic results for these two faulty conditions. A zoom of the motor supply currents centered at *t*=9 s for an OC fault in IGBT S_{A1} and S_{A2} are shown in Fig. 3.10(a) and Fig. 3.11(a), respectively. As shown in Fig. 3.10(b) and Fig. 3.11(b), when $|\underline{i}_{s.av.n}|$ is higher than the threshold value 0.1, the fault is detected (*t*=9.006 s) and at the same instant, the values of $\theta_{s.av}$ for both tests are within the range 150-210º which corresponds to IGBT pair 1 (see Table 3.2).

As mentioned before, to identify the faulty IGBT of pair 1, the diagnostic variables d_A and e_A should be evaluated. From Fig. 3.10(c) and Fig. 3.11(c) it can be observed that after fault occurrence $i_{A.n}$ presents a different behavior. In Fig. 3.10(c), $i_{A.n}$ has the half positive waveform affected, with only a few positive values while the half negative waveform is almost normal. In Fig. 3.11(c) the motor supply current waveform $i_{A.n}$ has no positive values and the half negative waveform is also almost normal. Therefore, after the faulty pair identification, Fig. 3.10(c) shows that $i_{A.n} < I_{pos}^{th}$ and thus $d_A = 0$, but a few milliseconds later $i_{A.n} > I_{pos}^{th}$ and consequently $d_A = 1$.

Fig. 3.11(c) shows that after the faulty pair identification, the condition $i_{A.n} < I_{pos}^{th}$ is always verified and subsequently $d_A = 0$. With $F_{pair} = 1$ and $d_A = 0$ it is not possible to identify the faulty IGBT. For this case is necessary to confirm if the condition $i_{A.n.av}^{+} \le I_{av}^{th+}$ is met which happens at $t = 9.013$ s and, as a consequence, $e_A = 1$.

Based on these two working conditions, Fig. 3.10(d) and Fig. 3.11(d) indicate the final diagnostic results. Fig. 3.10(d) shows that both fault detection and faulty pair 1 are reached at *t*=9.006 s and the faulty IGBT 1 is isolated at *t*= 9.013 s. Fig. 3.11(d) shows that both fault detection and faulty pair 1 occurs at t=9.006 s and the faulty IGBT 2 is isolated at *t*= 9.014 s.

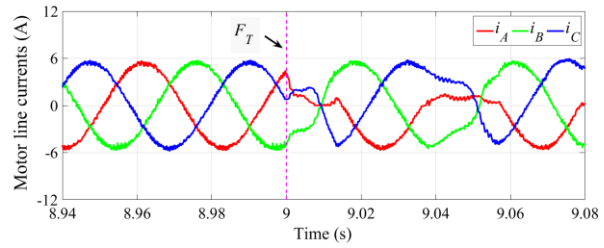

(a) Motor line current waveforms

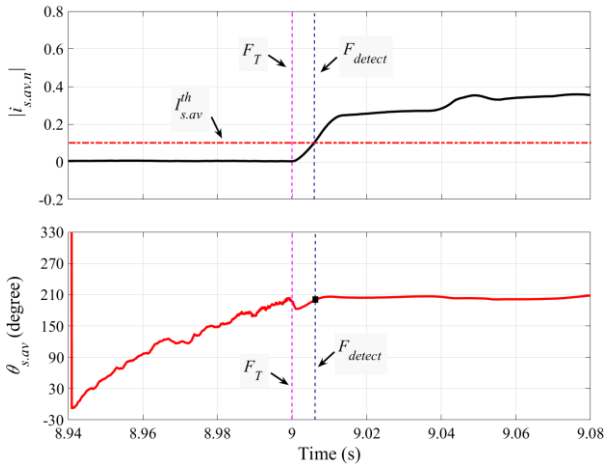

(b) ACPV magnitude and angle

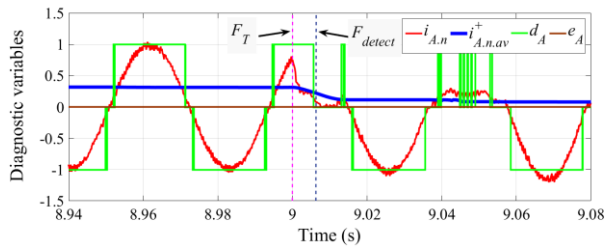

(c) Diagnostic variables

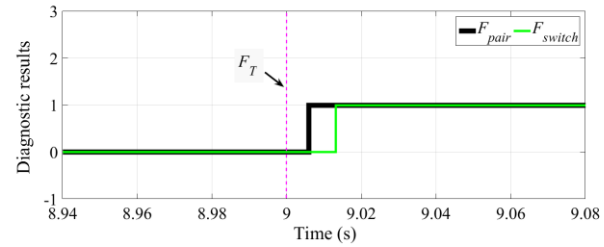

(d) Diagnostic result

Fig. 3.10. Diagnostic results for the IM drive operating with an OC fault in S_{A1}.

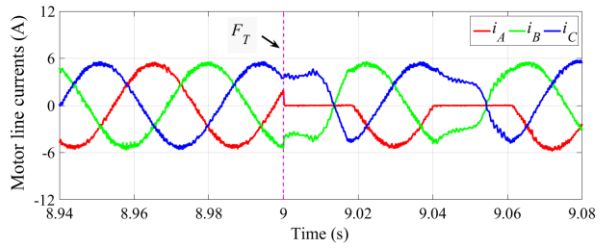

(a) Motor line current waveforms

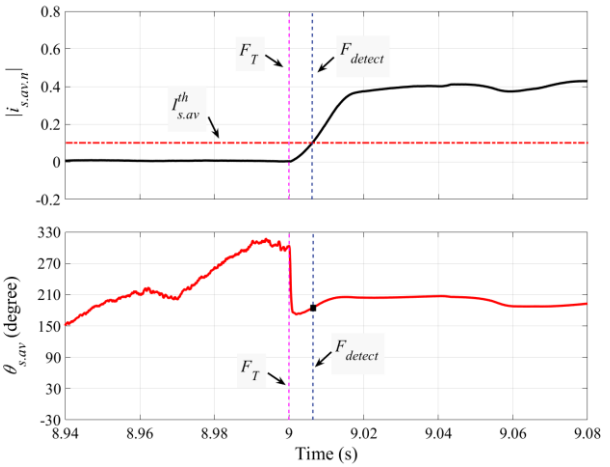

(b) ACPV magnitude and angle

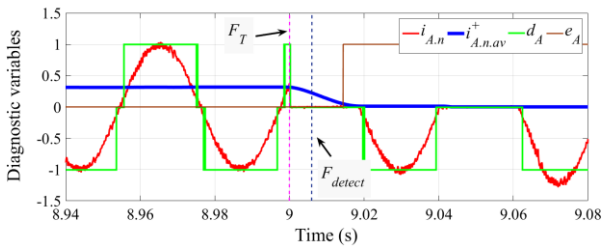

(c) Diagnostic variables

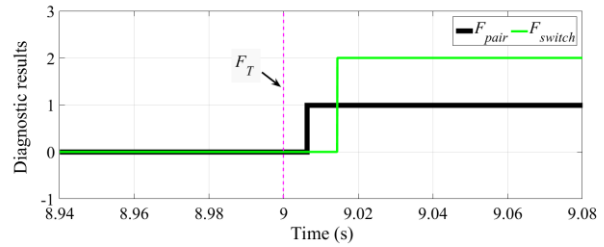

(d) Diagnostic result

Fig. 3.11. Diagnostic results for the IM drive operating with an OC fault in S_{A2}.

Compared with the fundamental current period of 39 ms, these fault diagnostic times are less than half period. The time taken by the diagnostic algorithm to identify the faulty pair and faulty IGBT $\left(T_{pair} \text{ and } T_{switch}\right)$ in the experimental tests is summarized in Table 3.5. As can be seen, for all faulty operating conditions, the diagnostic is performed within half period of the fundamental motor line currents $\left(T_{i.s}\right)$.

Table 3.5. Diagnostic times for the diagnostic approach based on the ACPV.

Faulty IGBT(s)	$T_{i.s}$	Identification time after OC fault occurrence			
		Faulty pair		Faulty switch	
		T_{pair}	$\frac{T_{pair}}{T_{i.s}}$	T_{switch}	$\frac{T_{switch}}{T_{i.s}}$
S_{A1} (Steady-state)	39 ms	6 ms	0.15	6 ms	0.15
S_{A2} (Steady-state)	39 ms	6 ms	0.15	13 ms	0.33
S_{A1} (Transient)	45 ms	6 ms	0.13	13 ms	0.29
S_{A2} (Transient)	45 ms	6 ms	0.13	14 ms	0.31

3.4 Average value of positive and negative parts of inverter output currents

According to the previous diagnostic approach, the normalized modulus and the phase angle of the average output current Park's Vector was used for the detection of an OC fault and identification of the faulty pair, respectively. Then, the average value of the positive and negative parts of the inverter output currents along with the normalized inverter output currents were used for the identification of the faulty IGBT. This approach is very useful and reliable for the identification of a single IGBT OC fault in the 3LNPC inverter, but it has a limitation to identify the faulty pairs (and consequently faulty IGBTs) after the occurrence of double IGBT OC faults.

To overcome this limitation, this section presents a fault diagnostic approach that allows the detection and location of multiple OC faults in all IGBTs [56]. On the contrary to the approach based on the ACPV, this new approach uses the average values of the positive and negative parts of the inverter output currents for the detection of IGBT OC faults and identification of the faulty pair.

3.4.1 Approach description

Similarly to the previous approach, the inverter output currents are normalized and the normalized values are split into positive and negative parts ($i_{x.n}^{+}$ and $i_{x.n}^{-}$). Thus, the average values of the positive and negative parts ($i_{x.n.av}^{+}$ and $i_{x.n.av}^{-}$) are calculated.

As mentioned before, under healthy conditions, $i_{x.n.av}^{+} \approx 0.318$ and $i_{x.n.av}^{-} \approx -0.318$. After the occurrence of an OC fault in one of the IGBTs located in P_{x1} (S_{x1} or S_{x2}), $i_{x.n.av}^{+}$ decreases. In the presence of an OC fault in one of the IGBTs located in P_{x2} (S_{x3} or S_{x4}), $i_{x.n.av}^{-}$ increases. Hence, the evolution of $i_{x.n.av}^{+}$ and $i_{x.n.av}^{-}$ under IGBT OC faults can be used for fault detection and identification of the faulty pair.

The diagnostic variables e_x^{+} and e_x^{-} are obtained by comparing $i_{x.n.av}^{+}$ and $i_{x.n.av}^{-}$ with the corresponding threshold values I_{av}^{th1+}, I_{av}^{th2+}, I_{av}^{th1-} and I_{av}^{th2-}, according to (3.15) and (3.16). The diagnostic variable f_x is obtained by comparing $i_{x.n}$ with the threshold values I^{th+} and I^{th-} according to (3.17).

$$e_x^{+}[k] = \begin{cases} 0 \Leftarrow i_{x.n.av}^{+}[k] > I_{av}^{th1+} \\ 1 \Leftarrow I_{av}^{th2+} < i_{x.n.av}^{+}[k] \le I_{av}^{th1+} \\ 2 \Leftarrow i_{x.n.av}^{+}[k] \le I_{av}^{th2+} \end{cases} \tag{3.15}$$

$$e_x^{-}[k] = \begin{cases} 0 \Leftarrow i_{x.n.av}^{-}[k] < I_{av}^{th1-} \\ 1 \Leftarrow I_{av}^{th1-} \le i_{x.n.av}^{-}[k] < I_{av}^{th2-} \\ 2 \Leftarrow i_{x.n.av}^{-}[k] \ge I_{av}^{th2-} \end{cases} \tag{3.16}$$

$$f_x[k] = \begin{cases} 1 \Leftarrow & i_{x.n}[k] \ge I^{th+} \\ 0 \Leftarrow & I^{th+} > i_{x.n}[k] > I^{th-} \\ -1 \Leftarrow & i_{x.n}[k] \le I^{th-} \end{cases} \tag{3.17}$$

According to (3.15) and (3.16), if the inverter operates with no faults the diagnostic variables e_x^{+} and e_x^{-} present null values. Also, in normal conditions, the variable f_x is changing between 1, 0 and -1.

Details of the threshold values used in this approach are listed in Table 3.6. For fault detection and identification of the faulty pair, $i_{x.n.av}^{+}$ and $i_{x.n.av}^{-}$ are compared with two threshold values $I_{av}^{th1+} = 0.1$ and $I_{av}^{th1-} = -0.1$, respectively. These threshold values represent 31% of the values of

$i^{+}_{x.n.av}$ and $i^{-}_{x.n.av}$ under healthy conditions. Therefore, there is a sufficient safety margin to avoid false alarms due to more severe or unusual working conditions such as during transient operation or unbalanced load conditions.

For discrimination between the outer and inner IGBT faults in an IGBT pair, $i_{x.n}$ is compared with two threshold values $I^{th+}=0.1$ and $I^{th-}=-0.1$ (10% of the maximum value of $i_{x.n}$ under healthy conditions), while $i^{+}_{x.n.av}$ and $i^{-}_{x.n.av}$ are compared with two threshold values $I^{th2+}_{av}=0.01$ and $I^{th2-}_{av}=-0.01$ (3.1% of the values $i^{+}_{x.n.av}$ and $i^{-}_{x.n.av}$, under healthy conditions).

Since $i_{x.n}$, $i^{+}_{x.n.av}$ and $i^{-}_{x.n.av}$ are normalized values, the employed threshold values are independent of the operating conditions of the inverter and do not need to be adjusted for each specific operating condition.

Table 3.6. Thresholds values used in the diagnostic approach based on the average value of the positive and negative parts of inverter output currents.

Threshold label	Value	Description	Application
I^{th1+}_{av}	0.1	First threshold value for $i^{+}_{x.n.av}$	Calculation of e^{+}_{x}
I^{th2+}_{av}	0.01	Second threshold value for $i^{+}_{x.n.av}$	
I^{th1-}_{av}	-0.1	First threshold value for $i^{-}_{x.n.av}$	Calculation of e^{-}_{x}
I^{th2-}_{av}	-0.01	Second threshold value for $i^{-}_{x.n.av}$	
I^{th+}	0.1	Positive threshold value for $i_{x.n}$	Calculation of f_x
I^{th-}	-0.1	Negative threshold value for $i_{x.n}$	

In order to address the detection and identification of the faulty pair, the values of e^{+}_{x} and e^{-}_{x} are used, as presented in Table 3.7. If any of the variables e^{+}_{x} or e^{-}_{x} presents a value higher than 1, a fault is detected and both the faulty pair and the faulty leg are immediately identified. The symbol "--" in Table 3.7 means that the variable value is irrelevant for the diagnostic process.

After the faulty pair identification, the faulty pair number together with the values of f_A, e^{+}_{x} and e^{-}_{x} are necessary to identify F_{switch} number, as shown in Table 3.8. For example, if a fault occurs in the IGBT pair P_{A1}, based on Table 3.8, the values of f_A and e^{+}_{x} are necessary to identify F_{switch}. If f_A takes the value 1, then $F_{switch}=S_{A1}$, and if e^{+}_{x} takes the value 2, $F_{switch}=S_{A2}$.

Table 3.7. Lookup table for the fault detection and faulty pair identification.

Diagnostic variables						Faulty pair		Faulty leg	
e_A^+	$e_{\bar{A}}^-$	e_B^+	$e_{\bar{B}}^-$	e_C^+	$e_{\bar{C}}^-$	Number	Label	Number	Label
≥1	--	--	--	--	--	1	P_{A1}	1	*A*
--	≥1	--	--	--	--	2	P_{A2}		
--	--	≥1	--	--	--	3	P_{B1}	2	*B*
--	--	--	≥1	--	--	4	P_{B2}		
--	--	--	--	≥1	--	5	P_{C1}	3	*C*
--	--	--	--	--	≥1	6	P_{C2}		

Table 3.8. Lookup table for identification of the faulty IGBT(s).

Faulty pair	Diagnostic variables									Faulty switch	
	f_A	e_A^+	$e_{\bar{A}}^-$	f_B	e_B^+	$e_{\bar{B}}^-$	f_C	e_C^+	$e_{\bar{C}}^-$	Number	Label
P_{A1}	1	--	--	--	--	--	--	--	--	1	S_{A1}
	--	2	--	--	--	--	--	--	--	2	S_{A2}
P_{A2}	--	--	2	--	--	--	--	--	--	3	S_{A3}
	-1	--	--	--	--	--	--	--	--	4	S_{A4}
P_{B1}	--	--	--	1	--	--	--	--	--	5	S_{B1}
	--	--	--	--	2	--	--	--	--	6	S_{B2}
P_{B2}	--	--	--	--	--	2	--	--	--	7	S_{B3}
	--	--	--	-1	--	--	--	--	--	8	S_{B4}
P_{C1}	--	--	--	--	--	--	1	--	--	9	S_{C1}
	--	--	--	--	--	--	--	2	--	10	S_{C2}
P_{C2}	--	--	--	--	--	--	--	--	2	11	S_{C3}
	--	--	--	--	--	--	-1	--	--	12	S_{C4}

The block diagram and flowchart of the proposed OC fault diagnostic procedure are shown in Fig. 3.12 and Fig. 3.13, respectively.

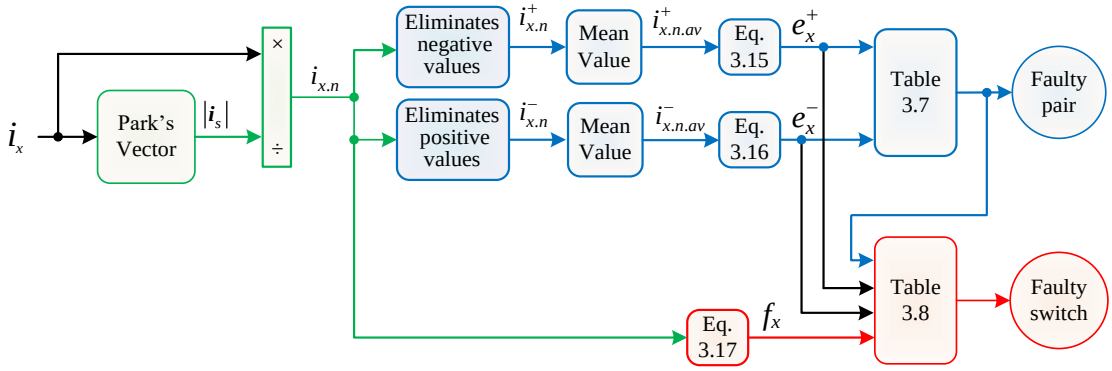

Fig. 3.12. Block diagram of the diagnostic technique based on the average values of the positive and negative parts of the inverter output currents.

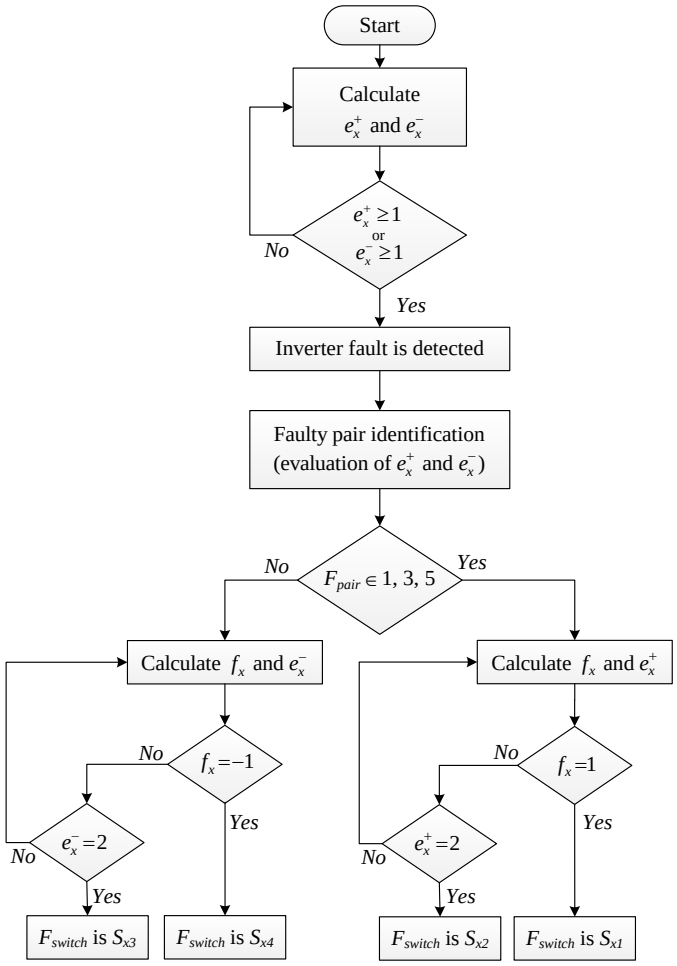

Fig. 3.13. Flowchart of the diagnostic technique based on the average values of the positive and negative parts of the inverter output currents.

3.4.2 Experimental validation

To evaluate the performance of the proposed diagnostic approach, several IGBT OC faults were introduced in the inverter. In this subsection, results for different inverter faulty conditions, with single and double IGBT OC faults are presented.

3.4.2.1 Results for a single IGBT OC fault

Results for two different single IGBT OC faults are analyzed in this subsection. The employed reference speed profile of the IM drive for these tests is shown in Fig. 3.14. In both tests, at *t*=3 s, an OC fault is introduced in the inverter. In the first test, an OC fault is introduced in IGBT S_{A1}. In the second test, the fault is introduced in IGBT S_{A2}.

The motor speed for these faulty conditions is shown in Fig. 3.15. As can be noticed, before the fault occurrence, the motor speed follows the reference value closely. After *t*=3 s, the motor speed is unable to follow the reference value and exhibits oscillations. This figure also shows that the oscillations of the motor speed due to the S_{A2} fault are higher than those with a S_{A1} fault.

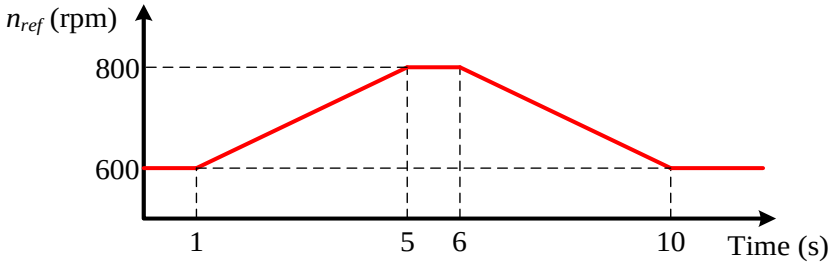

Fig. 3.14. The used profile of the reference speed.

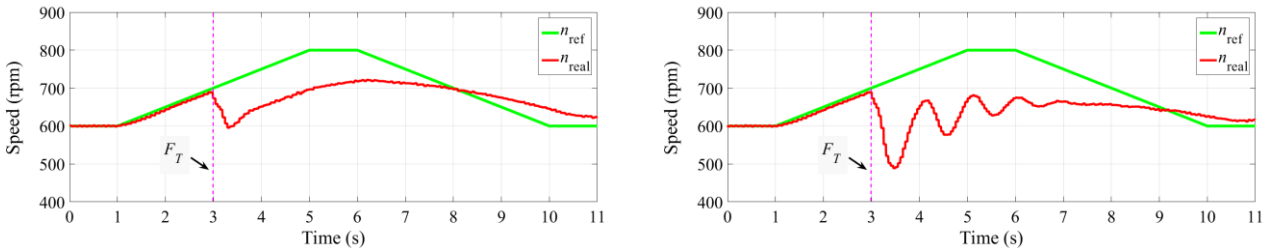

(a) with OC fault in S_{A1}.

(b) with OC fault in S_{A2}.

Fig. 3.15. IM drive speed variations.

The diagnostic results for an OC fault in IGBT S_{A1} and S_{A2} are shown in Fig. 3.16 and Fig. 3.17, respectively. The motor line current waveforms for the IM drive operating with an OC fault in S_{A1} are shown in Fig. 3.16(a). Fig. 3.16(b) shows the normalized current of leg *A* together with the average values of positive and negative parts of the normalized current of leg *A*. As can be noticed, before the fault occurrence, $i_{A.n}$ has a sinusoidal shape with an amplitude of 1 and therefore $i^{+}_{A.n.av} \approx 0.318$ and $i^{-}_{A.n.av} \approx -0.318$. After the appearance of the fault, almost all positive values of $i_{A.n}$ are eliminated and the value of $i^{+}_{A.n.av}$ decreases. When $i^{+}_{A.n.av}$ is below the threshold value I^{th1+}_{av} (Fig. 3.16(b)), e^{+}_{A} takes the value 1 (at *t*=3.0115 s) as shown in Fig. 3.16(c). Considering these results, Table 3.7 allows the identification of the $F_{leg} = 1$ and $F_{pair} = 1$.

Knowing that F_{pair}=1, based on Table 3.8, the values of e^{+}_{A} and f_A are necessary to identify the faulty switch. The first time that f_A takes the value 1 after the faulty pair 1 identification, Table 3.8 allows identifying S_{A1} as the faulty IGBT. As can be seen in the diagnostic timeline represented in Fig. 3.16(d), the IGBT pair number 1 (P_{A1}) and the faulty switch number 1 (S_{A1}) are identified by the diagnostic algorithm.

For the second test with an OC in S_{A2}, the motor line current waveforms are shown in Fig. 3.17(a). The results for $i_{A.n}$, $i^{+}_{A.n.av}$, and $i^{-}_{A.n.av}$ are shown in Fig. 3.17(b). After the fault occurrence at *t*=3 s, the positive part of $i_{A.n}$ is completely eliminated and therefore, $i^{+}_{A.n.av}$ decreases to zero. As observed in Fig. 3.17(b), $i^{+}_{A.n.av}$ decreases to a value below I^{th1+}_{av} at *t*=3.0115 s. At this point $e^{+}_{A}[k] = 1$ (Fig. 3.17(c)) and the fault is detected. Using these diagnostic variable values as entries in Table 3.7, the identification of the faulty pair as the number 1 is met (Fig. 3.17(d)). After fault detection, considering that $F_{pair} = P_{A1}$, to identify the faulty IGBT is necessary to check the values of e^{+}_{A} and f_A. Fig. 3.17(c) shows that after fault occurrence, f_A is changing between -1 and 0 and e^{+}_{A} assumes the value 2 at *t*=3.0175 s. Considering these values, Table 3.8 allows the identification of S_{A2} as the faulty IGBT. The timeline of the diagnostic process is shown in Fig. 3.17(d).

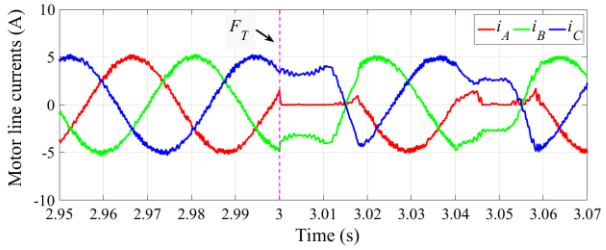

(a) Motor line currents

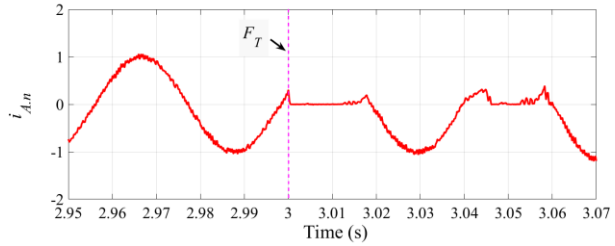

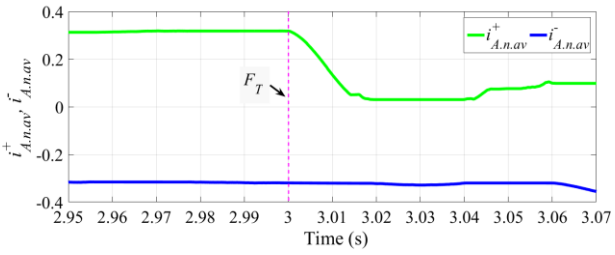

(b) Normalized and average currents of leg *A*

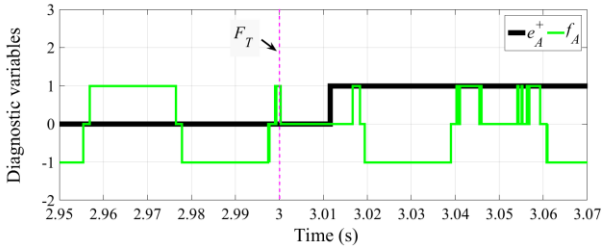

(c) Diagnostic variables of leg *A*

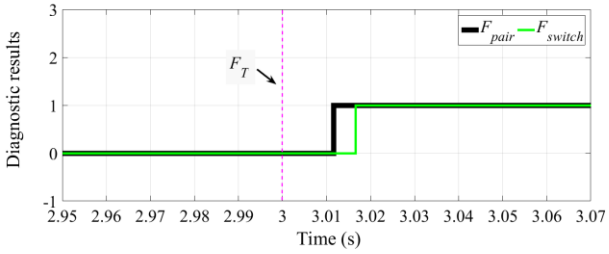

(d) Final diagnostic result.

Fig. 3.16. Diagnostic results for the IM drive operating with an OC fault in S_{A1}.

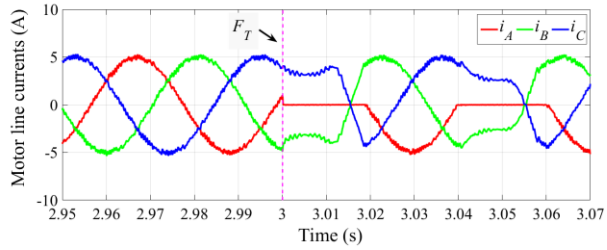

(a) Motor line currents

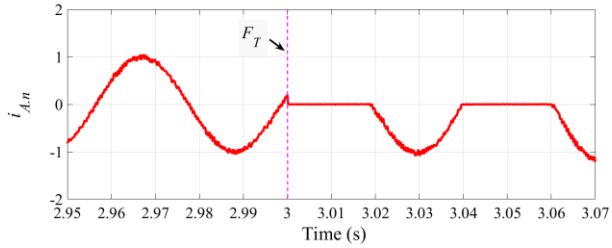

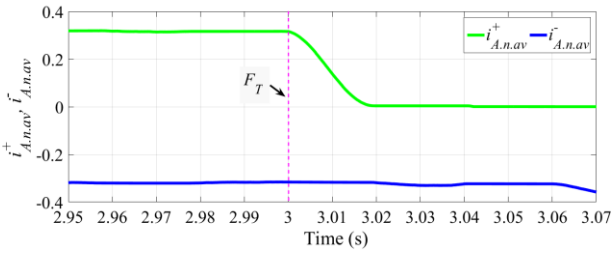

(b) Normalized and average currents of leg *A*

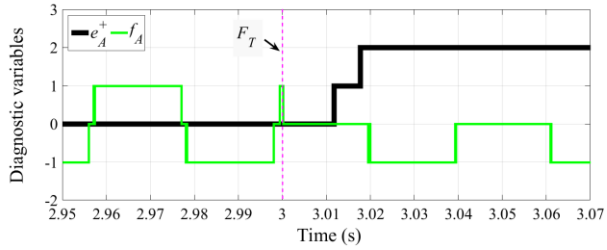

(c) Diagnostic variables of leg *A*

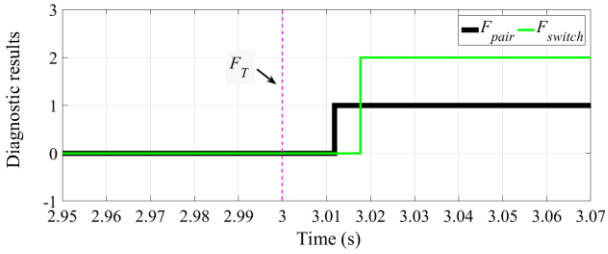

(d) Final diagnostic result

Fig. 3.17. Diagnostic results for the IM drive operating with an OC fault in S_{A2}.

3.4.2.2 Results for multiple IGBT OC faults

Several tests were also conducted for different combinations of double OC faults. Results for two different double IGBT OC faults under transient operating conditions are presented. The employed reference speed profile for all the results represented in this subsection is similar to the one already shown in Fig. 3.14.

In the first test, the first OC fault is applied to IGBT S_{A4} at *t*=8 s and the second one is applied to IGBT S_{C1} at *t*=8.01 s. The motor line current waveforms are shown in Fig. 3.18(a). Two vertical lines labeled F_T^1 and F_T^2 indicate the instants in time when the faults in S_{A4} and S_{C1} are introduced.

For the OC fault in leg *A*, $i_{A.n}$, $i_{A.n.av}^{+}$ and $i_{A.n.av}^{-}$ are shown in Fig. 3.18(b). Following the procedures mentioned before, at *t*=8.0115 s, $e_A^- = 1$ (Fig. 3.18(c)) which allows the identification of the faulty pair P_{A2}. Fig. 3.18(c) also shows that after fault detection, f_A takes the value -1 at *t*=8.012 s. With these collected values for the faulty pair and f_A, the identification of S_{A4} is accomplished.

For the OC fault in leg *C*, $i_{C.n}$, $i_{C.n.av}^{+}$ and $i_{C.n.av}^{-}$ are shown in Fig. 3.18(d). Fig. 3.18(e), shows that at *t*=8.017 s e_C^+ takes the value 1 and Table 3.7 allows the identification of $F_{pair} = P_{C1}$. Since at the fault detection moment $f_C = 1$, S_{C1} is identified as the second faulty IGBT.

Now, a different combination of double OC faults is analyzed. The first OC fault is applied to S_{A4} at *t*=8 s (similarly to the previous example) and the second one is applied to S_{C2} at *t*=8.01 s. The motor line current waveforms are shown in Fig. 3.19(a).

The procedure to identify the first faulty IGBT is similar to the previous example. To analyze the second OC fault, $i_{C.n}$, $i_{C.n.av}^{+}$ and $i_{C.n.av}^{-}$ are shown in Fig. 3.19(d). This figure shows that after the fault in S_{C2}, $i_{C.n.av}^{+}$ decreases bellow I_{av}^{th1+} at *t*=8.017 s. Therefore, e_C^+ takes the value 1 and Table 3.7 allows the identification of P_{C1} as the second faulty pair. To identify the IGBT in OC, e_C^+ and f_C are shown in Fig. 3.19(e), at the moment that e_C^+ takes the value 2 (*t*=8.023 s), Table 3.8 give the results of S_{C2} as the second faulty IGBT. Fig. 3.19(f) represents the summary of diagnostic result for this double OC fault.

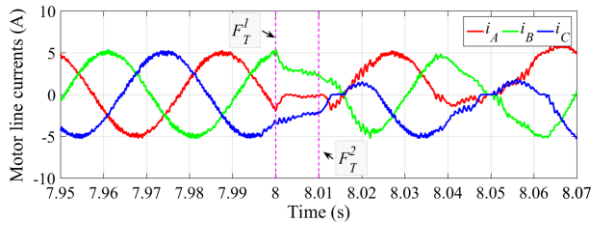

(a) Motor line currents

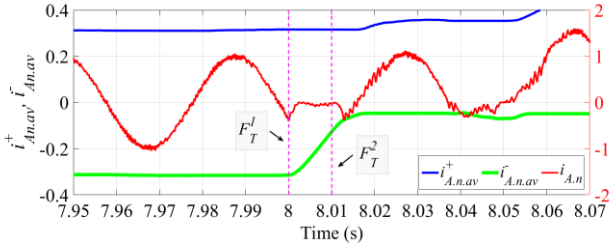

(b) Normalized and average currents of leg *A*

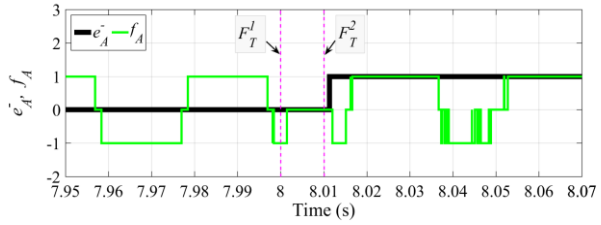

(c) Diagnostic variables of leg *A*

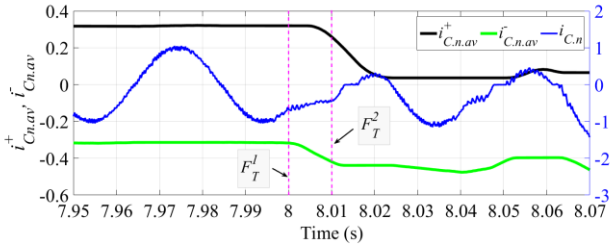

(d) Normalized and average currents of leg *C*

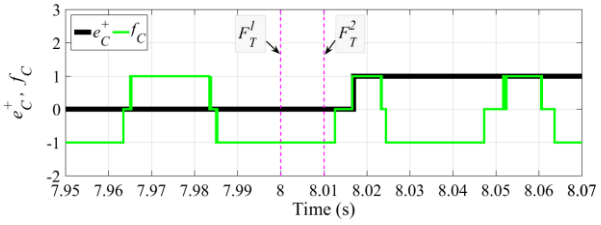

(e) Diagnostic variables of leg *C*

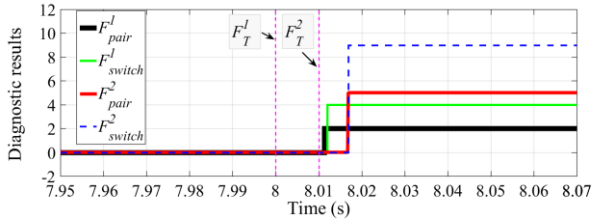

(f) Final diagnostic results

Fig. 3.18. Diagnostic results for the IM drive operating with two OC faults in S_{A4} and S_{C1}.

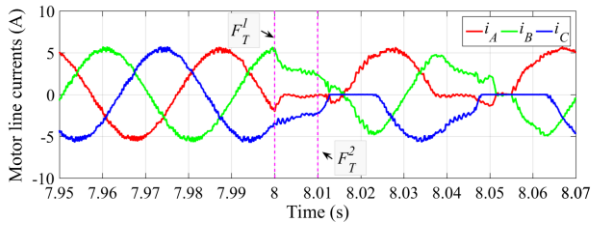

(a) Motor line currents

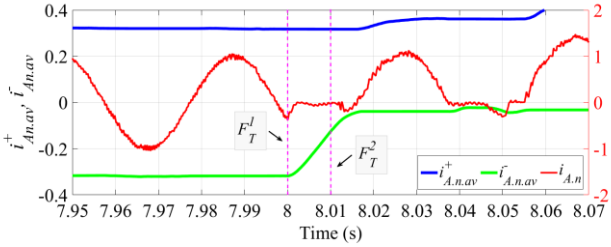

(b) Normalized and average currents of leg *A*

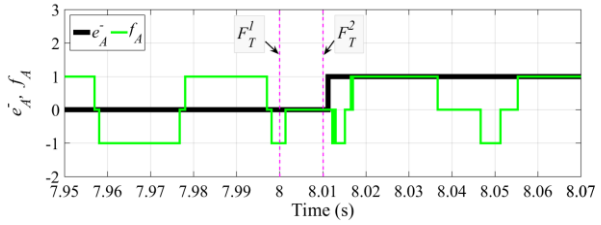

(c) Diagnostic variables of leg *A*

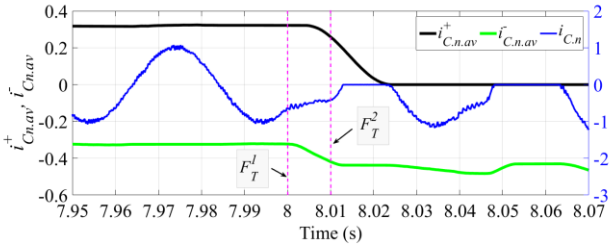

(d) Normalized and average currents of leg *C*

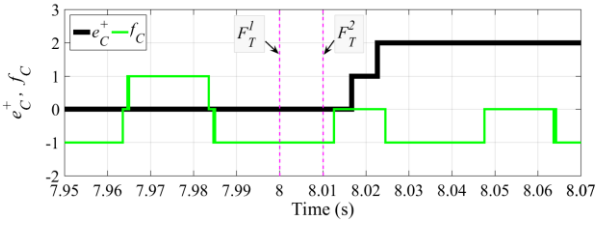

(e) Diagnostic variables of leg *C*

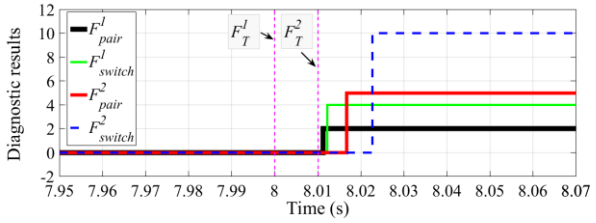

(f) Final diagnostic results

Fig. 3.19. Diagnostic results for the IM drive operating with two OC faults in S_{A4} and S_{C2}.

Table 3.9 summarizes the time taken by the diagnostic algorithm to detect and identify the faulty IGBTs in the experimental tests. As can be seen, for all faulty conditions, the diagnostic process was performed within half the period of the fundamental motor line currents.

Table 3.9. Diagnostic times for the diagnostic approach based on the average values of the positive and negative parts of the inverter output currents.

Faulty IGBT(s)	$T_{i.s}$	Identification time after OC fault(s) occurrence							
		First faulty pair		First faulty switch		Second faulty pair		Second faulty switch	
		T_{pair}	$\frac{T_{pair}}{T_{i.s}}$	T_{switch}	$\frac{T_{switch}}{T_{i.s}}$	T_{pair}	$\frac{T_{pair}}{T_{i.s}}$	T_{switch}	$\frac{T_{switch}}{T_{i.s}}$
S_{A1}	42 ms	11.5 ms	0.27	16.6 ms	0.4	---	---	---	---
S_{A2}	42 ms	11.5 ms	0.27	17.5 ms	0.42	---	---	---	---
S_{A4}, S_{C1}	42 ms	11.5 ms	0.27	12 ms	0.29	7 ms	0.17	7 ms	0.17
S_{A4}, S_{C2}	42 ms	11.5 ms	0.27	12 ms	0.29	7 ms	0.17	13 ms	0.31

3.5 Pole voltages analysis

The diagnostic approaches presented in the previous subsections are only able to diagnose OC faults in the IGBTs of the 3LNPC inverter but they are unable to diagnose OC faults in the clamp-diodes.

Moreover, as it will be shown in this section, when the 3LNPC inverter operates with a low modulation index, the effects of the fault in an outer IGBT (S_{x1} or S_{x4}) is almost imperceptible in the inverter output currents. This makes impractical to use diagnostic approaches based on the analysis of the output currents of the inverter (including the two approaches presented in the previous sections) to detect OC faults in the outer IGBTs if the inverter is operating with a low modulation index.

This section presents a novel fault diagnostic approach that allows the detection and location of multiple OC faults in all IGBTs as well as in all clamp-diodes of a 3LNPC inverter in an IM drive [57]. This method is also able to detect and identify OC faults in the outer IGBTs under inverter operating conditions with very low modulation indexes.

3.5.1 Approach description

This approach is based on the deviation between the real inverter output pole voltage of each leg and the corresponding reference voltage imposed by the respective leg control state. Therefore, three inverter output pole voltages measured between the inverter terminals *A*, *B*, *C* and the DC-bus middle point "z" (v_{Az}, v_{Bz} and v_{Cz}) are required.

For the explanation of the proposed diagnostic approach, the components of each 3LNPC inverter leg are classified into four groups g_{x1}, g_{x2}, g_{x3} and g_{x4}, as shown in Fig. 3.20.

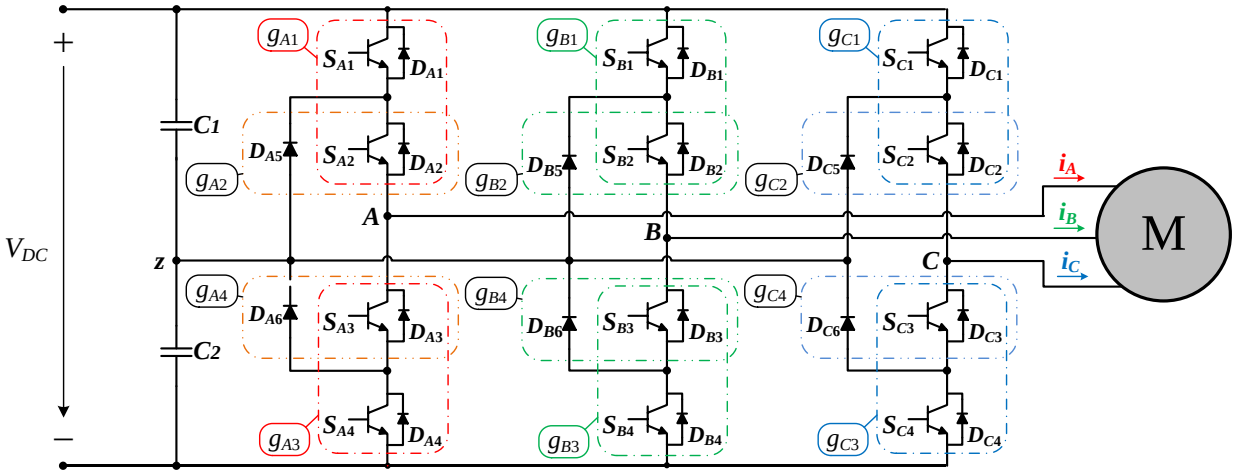

Fig. 3.20. Schematic representation of a 3LNPC IM drive.

To obtain a diagnostic approach independent of V_{DC}, the sample values of the output pole voltages v_{xz} are normalized according to (3.18).

$$v_{xz.n}[k] = \frac{v_{xz}[k]}{V_{DC}/2},\ x \in \{A, B, C\} \tag{3.18}$$

The diagnostic variables LS_x are defined by (3.19). These variables are defined to identify the range of the normalized real pole voltage. Considering the possible V_{DC} variations and to clearly identify the output pole voltages range, some threshold values are used.

$$LS_x[k] = \begin{cases} 1 \Leftarrow\ v_{xz.n}[k] > 0.7 \\ 0 \Leftarrow\ |v_{xz.n}[k]| < 0.05 \\ -1 \Leftarrow\ v_{xz.n}[k] < -0.7 \\ 2 \Leftarrow 0.05 \le |v_{xz.n}[k]| \le 0.7. \end{cases} \tag{3.19}$$

In the experimental tests, the measured pole voltage signal and the corresponding control state have a delay equal to one sampling period (in this tests $T_s = 50\ \mu s$). Therefore, to compensate this delay, the normalized pole voltage of leg *x* at sample k ($v_{xz.n}[k]$) should be compared to the control state of leg *x* at sample $k-1$ ($CS_x[k-1]$).

Under healthy operating conditions, $LS_x[k]$ is equal to $CS_x[k-1]$. With an OC fault in one of the IGBTs or clamp-diodes, $LS_x[k]$ will no longer be identical to $CS_x[k-1]$. The group where the faulty power device is located will depend not only on the value of $CS_x[k-1]$ but also on the value $LS_x[k]$:

$CS_x[k-1]=1$ and $LS_x[k]\neq 1 \Rightarrow$ there is a fault in g_{x1}.

$CS_x[k-1]=0$ and $LS_x[k]=-1 \Rightarrow$ there is a fault in g_{x2}.

$CS_x[k-1]=0$ and $LS_x[k]=1 \Rightarrow$ there is a fault in g_{x4}.

$CS_x[k-1]=-1$ and $LS_x[k]\neq -1 \Rightarrow$ there is a fault in g_{x3}.

Diagnostic variables ε_x^+, ε_x^- and δ_x are now defined in (3.20)-(3.22).

$$\varepsilon_x^+[k]=\begin{cases} -1 \Leftarrow CS_x[k-1]\neq 1 \\ 0 \Leftarrow LS_x[k]=1 \ \wedge \ CS_x[k-1]=1 \\ 1 \Leftarrow LS_x[k]\neq 1 \ \wedge \ CS_x[k-1]=1. \end{cases} \tag{3.20}$$

$$\varepsilon_x^-[k]=\begin{cases} -1 \Leftarrow CS_x[k-1]\neq -1 \\ 0 \Leftarrow LS_x[k]=-1 \ \wedge \ CS_x[k-1]=-1 \\ 1 \Leftarrow LS_x[k]\neq -1 \ \wedge \ CS_x[k-1]=-1. \end{cases} \tag{3.21}$$

$$\delta_x[k]=\begin{cases} 0 \Leftarrow \ CS_x[k-1]\neq 0 \\ 0 \Leftarrow LS_x[k]=0 \ \wedge CS_x[k-1]=0 \\ 1 \Leftarrow LS_x[k]=1 \ \wedge CS_x[k-1]=0 \\ -1 \Leftarrow LS_x[k]=-1 \wedge CS_x[k-1]=0. \end{cases} \tag{3.22}$$

The diagnostic process is developed in two steps. The first step involves the OC fault detection and faulty group identification. Table 3.10 shows how the faulty group and the potential faulty devices can be identified using the diagnostic variables. Moreover, in this table, the symbol "--" means that the variable is irrelevant for the diagnostic process.

The variables ε_x^+ and ε_x^- show the condition of the power devices located in groups g_{x1} and g_{x3}, respectively. The variables δ_x indicate the condition of the power devices in groups g_{x2} and g_{x4}. When the inverter operates in healthy conditions, ε_x^+ and ε_x^- change between -1 and 0 while δ_x presents a null value.

Table 3.10. Lookup table for identification of the faulty group(s).

Diagnostic variables									Faulty leg	Faulty group		Faulty devices
ε_A^+	ε_A^-	δ_A	ε_B^+	ε_B^-	δ_B	ε_C^+	ε_C^-	δ_C		Name	Number	
1	--	--	--	--	--	--	--	--	*A*	g_{A1}	1	S_{A1} or S_{A2}
--	--	-1	--	--	--	--	--	--		g_{A2}	2	S_{A2} or D_{A5}
--	1	--	--	--	--	--	--	--		g_{A3}	3	S_{A3} or S_{A4}
--	--	1	--	--	--	--	--	--		g_{A4}	4	S_{A3} or D_{A6}
--	--	--	1	--	--	--	--	--	*B*	g_{B1}	5	S_{B1} or S_{B2}
--	--	--	--	--	-1	--	--	--		g_{B2}	6	S_{B2} or D_{B5}
--	--	--	--	1	--	--	--	--		g_{B3}	7	S_{B3} or S_{B4}
--	--	--	--	--	1	--	--	--		g_{B4}	8	S_{B3} or D_{B6}
--	--	--	--	--	--	1	--	--	*C*	g_{C1}	9	S_{C1} or S_{C2}
--	--	--	--	--	--	--	--	-1		g_{C2}	10	S_{C2} or D_{C5}
--	--	--	--	--	--	--	1	--		g_{C3}	11	S_{C3} or S_{C4}
--	--	--	--	--	--	--	--	1		g_{C4}	12	S_{C3} or D_{C6}

In the second step, to identify the faulty power device among the two potential candidates given by Table 3.10, additional variables ε_x^z and γ_x are needed, being defined by (3.23) and (3.24).

$$\varepsilon_x^z[k]=\begin{cases}-1 \Leftarrow CS_x[k-1]\neq 0\\ 0 \Leftarrow LS_x[k]=0 \wedge CS_x[k-1]=0\\ 1 \Leftarrow LS_x[k]\neq 0 \wedge CS_x[k-1]=0\end{cases} \tag{3.23}$$

$$\gamma_x[k]=\begin{cases}1 \Leftarrow i_x[k]\geq 0.1\\ 0 \Leftarrow -0.1<i_x[k]<0.1\\ \text{-}1 \Leftarrow i_x[k]\leq -0.1\end{cases} \tag{3.24}$$

The variables γ_x indicate the direction of the motor line currents i_x. $\gamma_x = 1$ indicates a positive current while $\gamma_x = -1$ indicates a negative current i_x. Considering the existence of noise in the current measurements, the threshold values of -0.1 and 0.1 are used in (3.24).

The faulty power device(s) can now be finally identified based on the knowledge of the faulty group provided by Table 3.10 and the values of the diagnostic variables, according to Table 3.11.

Table 3.11. Lookup table for the identification of the faulty power device(s).

Faulty group	Diagnostic variables												Faulty device	
	ε_A^z	γ_A	ε_A^+	ε_A^-	ε_B^z	γ_B	ε_B^+	ε_B^-	ε_C^z	γ_C	ε_C^+	ε_C^-	Name	number
g_{A1}	0	1	--	--	--	--	--	--	--	--	--	--	S_{A1}	1
	1	--	--	--	--	--	--	--	--	--	--	--	S_{A2}	2
g_{A2}	--	--	1	--	--	--	--	--	--	--	--	--	S_{A2}	2
	--	1	0	--	--	--	--	--	--	--	--	--	D_{A5}	5
g_{A3}	1	--	--	--	--	--	--	--	--	--	--	--	S_{A3}	3
	0	-1	--	--	--	--	--	--	--	--	--	--	S_{A4}	4
g_{A4}	--	--	--	1	--	--	--	--	--	--	--	--	S_{A3}	3
	--	-1	--	0	--	--	--	--	--	--	--	--	D_{A6}	6
g_{B1}	--	--	--	--	0	1	--	--	--	--	--	--	S_{B1}	7
	--	--	--	--	1	--	--	--	--	--	--	--	S_{B2}	8
g_{B2}	--	--	--	--	--	--	1	--	--	--	--	--	S_{B2}	8
	--	--	--	--	--	1	0	--	--	--	--	--	D_{B5}	11
g_{B3}	--	--	--	--	1	--	--	--	--	--	--	--	S_{B3}	9
	--	--	--	--	0	-1	--	--	--	--	--	--	S_{B4}	10
g_{B4}	--	--	--	--	--	--	--	1	--	--	--	--	S_{B3}	9
	--	--	--	--	--	-1		0	--	--	--	--	D_{B6}	12
g_{C1}	--	--	--	--	--	--	--	--	0	1	--	--	S_{C1}	13
	--	--	--	--	--	--	--	--	1	--	--	--	S_{C2}	14
g_{C2}	--	--	--	--	--	--	--	--	--	--	1	--	S_{C2}	14
	--	--	--	--	--	--	--	--	--	1	0	--	D_{C5}	17
g_{C3}	--	--	--	--	--	--	--	--	1	--	--	--	S_{C3}	15
	--	--	--	--	--	--	--	--	0	-1	--	--	S_{C4}	16
g_{C4}	--	--	--	--	--	--	--	--	--	--	--	1	S_{C3}	15
	--	--	--	--	--	--	--	--	--	-1	--	0	D_{C6}	18

A summary of the implementation process and the flowchart of this new diagnostic technique are shown in Fig. 3.21 and Fig. 3.22, respectively.

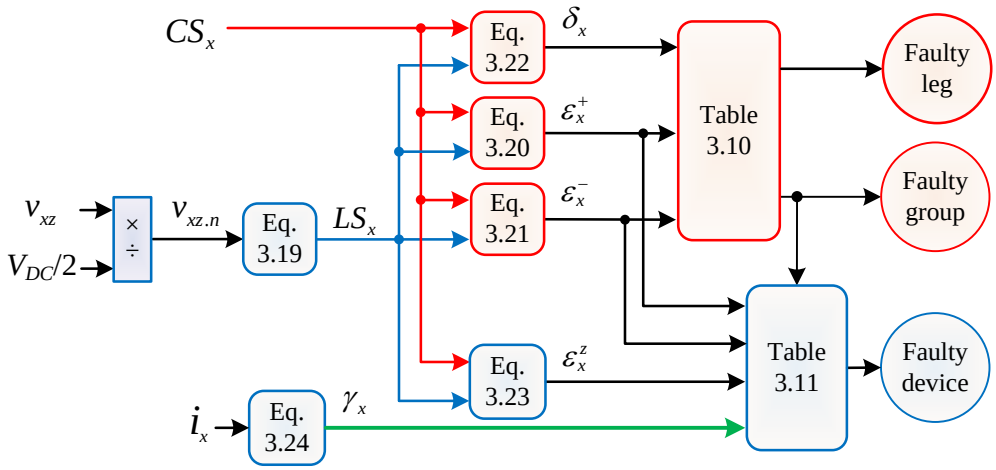

Fig. 3.21. Block diagram of the diagnostic technique based on the pole voltage analysis.

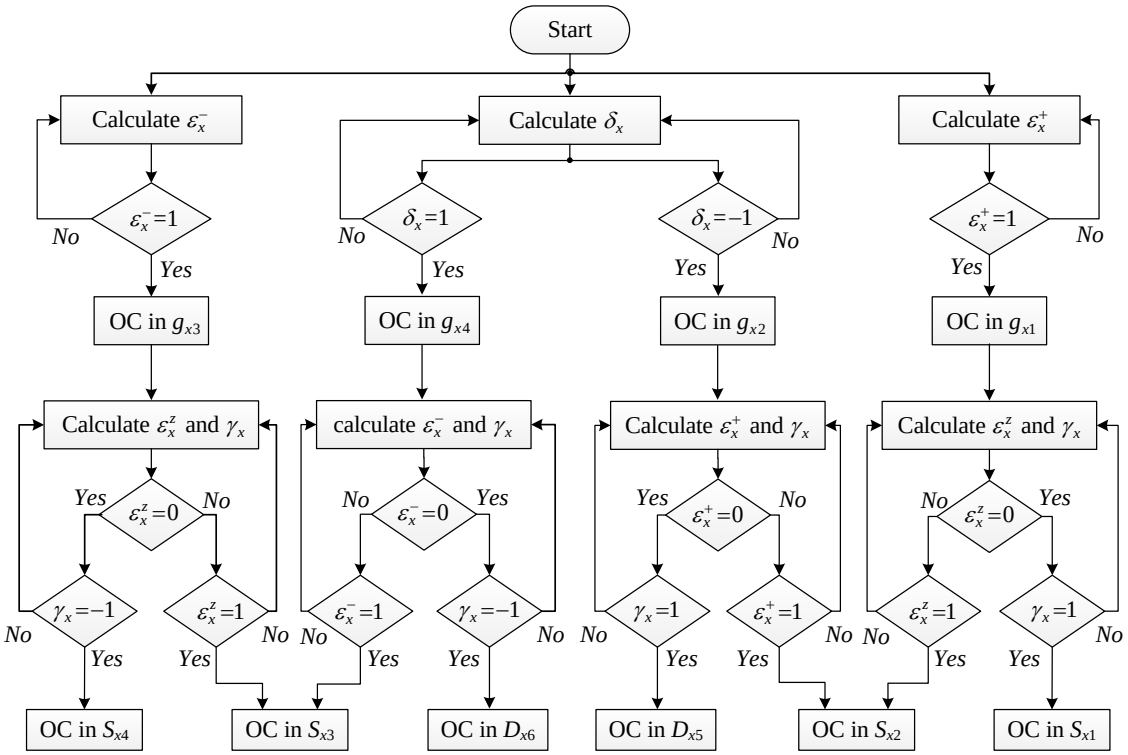

Fig. 3.22. Flowchart of the diagnostic technique based on the pole voltage analysis.

3.5.2 Experimental validation

To evaluate the proposed diagnostic approach, several OC faults in the IGBTs and clamp-diodes were introduced individually and simultaneously in the 3LNPC inverter. The results are presented in three subsections. Subsection 3.5.2.1 shows the results for two different conditions of single OC faults. Subsection 3.5.2.2 presents the results for double OC faults. Finally, the results for OC fault in a clamp-diode are presented in Subsection 3.5.2.3. All results presented in this subsection are obtained under transient operating conditions.

3.5.2.1 Results for a single IGBT OC faults

The diagnostic results obtained for two different single IGBT OC faults in leg *A* are shown in Fig. 3.23 and Fig. 3.24.

The first test is performed with the system operating under transient conditions with an OC fault in S_{A1} introduced at *t*=3 s. The reference speed profile, the real motor rotor speed and the inverter modulation index are shown in Fig. 3.23(a). The motor line current waveforms (inverter output currents) are shown in Fig. 3.23(b).

In this test, the inverter is operating with a low modulation index. Under these conditions, the switching state zero is applied most of the time, while the leg switching states 1 and -1 are applied only for very short periods of time. Hence, the leg current, most of the time, is flowing through current paths 2 and 5 (see Fig. 2.3). As all power switches involved in these paths are healthy, the effect of the fault in S_{A1} is almost imperceptible in the motor currents.

The control state of leg *A* and the normalized pole voltage are shown in Fig. 3.23(c). The diagnostic variables ε_A^+, ε_A^z, δ_A, and γ_A are shown in Fig. 3.23(d). As shown in these figures, after the occurrence of the fault, the positive parts of $v_{Az.n}$ and CS_A are different and this difference is reflected in ε_A^+ (ε_A^+ changed to 1). The first time that ε_A^+ takes value 1 (*t*=3.00005 s), Table 3.10 allows the identification of the faulty group as g_{A1}.

In the next step, knowing that the faulty device is located in g_{A1}, according to Table 3.11, it is necessary to read the value of ε_A^z and γ_A, presented in Fig. 3.23(d). Since the faulty device is located in g_{A1} and $\gamma_A = 1$, the first time that $\varepsilon_A^z = 0$ (*t*=3.0002 s), Table 3.11 allows to identify S_{A1} as the faulty device. The diagnostic timeline presented in Fig. 3.23(e) shows that the algorithm identifies the faulty group number 1 and the faulty device number 1.

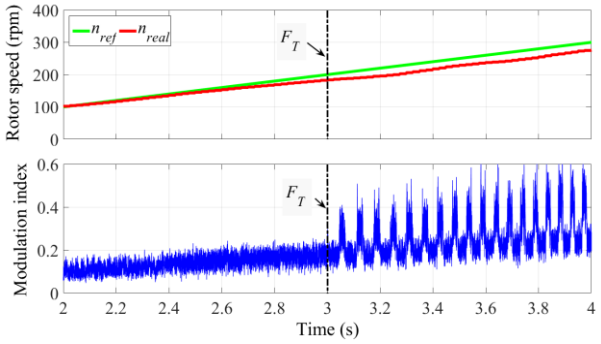

(a) Rotor speed and inverter modulation index

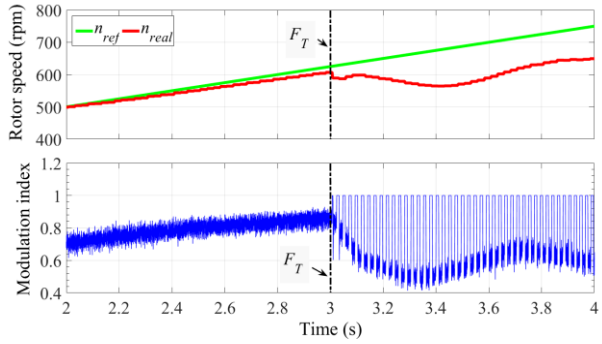

(a) Rotor speed and inverter modulation index

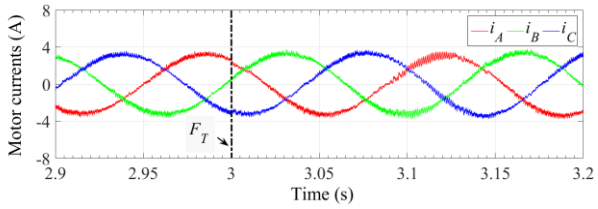

(b) Motor line current waveforms

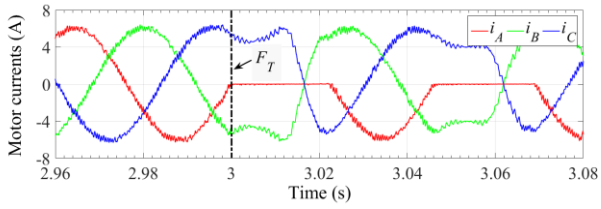

(b) Motor line current waveforms

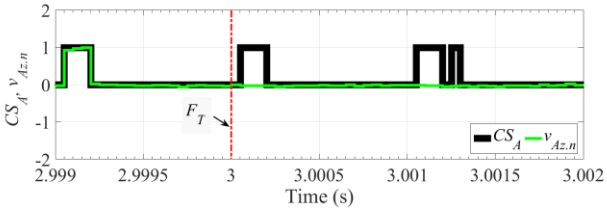

(c) Normalized pole voltage and control state of leg *A*

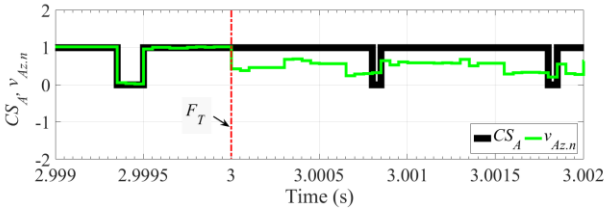

(c) Normalized pole voltage and control state of leg *A*

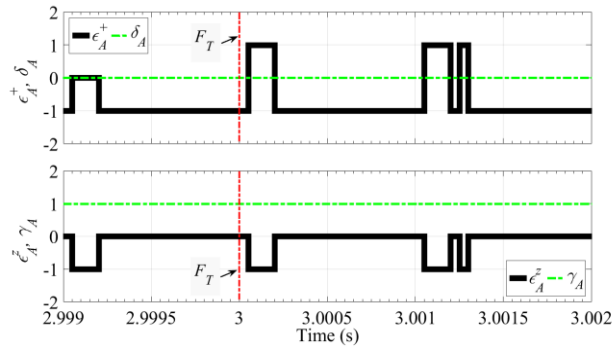

(d) Diagnostic variables of leg *A*

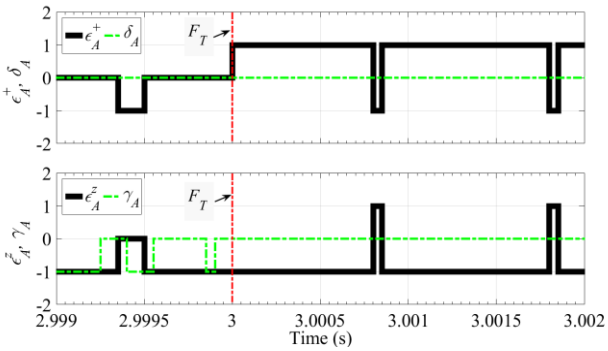

(d) Diagnostic variables of leg *A*

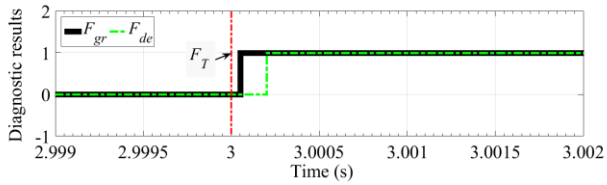

(e) Diagnostic results

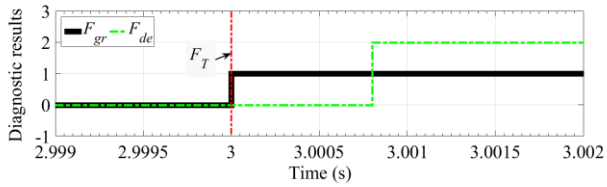

(e) Diagnostic results

Fig. 3.23. Results under normal ($t < 3$ s) and faulty operation ($t \geq 3$ s) with an OC fault in S_{A1}.

Fig. 3.24. Results under normal ($t < 3$ s) and faulty operation ($t \geq 3$ s) with an OC fault in S_{A2}.

Another faulty condition was carried out at a high value of the modulation index and with an OC fault in S_{A2}, introduced at *t*=3 s. The evolution of the reference and actual motor speeds, as well as the modulation index for this faulty condition are shown in Fig. 3.24(a). The fault was applied when the inverter modulation index was about 0.85. Fig. 3.24(b) shows the motor line currents waveforms, which demonstrates that after the fault occurrence at *t*=3 s, the positive part of i_A is completely eliminated.

As presented in Fig. 3.24(c), after the fault, $v_{Az.n}$ is different from CS_A. This difference is shown by ε_A^+, presented in Fig. 3.24(d). The first time that ε_A^+ takes value 1 (*t*=3 s), the faulty group is identified as g_{A1} from Table 3.10. Taking into account that the faulty device is located in g_{A1}, the first time that ε_A^z takes value 1 (*t*=3.0008 s), Table 3.11 allows to identify S_{A2} as the faulty device, as shown in Fig. 3.24(e).

3.5.2.2 Results for multiple IGBTs OC faults

Several tests were also conducted for different combinations of double OC faults. Results for two different combinations of double IGBT OC faults are shown in Fig. 3.25 and Fig. 3.26.

The first OC fault is applied to IGBT S_{A1} at *t*=3 s and the second one is applied to IGBT S_{B3} at *t*=3.001 s, being these time instants labeled as F_T^1 and F_T^2. The motor line current waveforms for this faulty condition are represented in Fig. 3.25(a) which shows that after the occurrence of the faults some positive values of i_A and all negative values of i_B are eliminated.

The control state and the normalized inverter pole voltage and the diagnostic variables of leg *A* are shown in Fig. 3.25(b) and Fig. 3.25(c), respectively.

Considering the results of the first fault (Fig. 3.25(c)), the first time that ε_A^+ takes value 1 (*t*=3.0004 s), Table 3.10 allows to identify the first faulty group as g_{A1}. Then, knowing that the faulty device is located in g_{A1}, it is necessary to know ε_A^z. As shown in Fig. 3.25 (c), while $\gamma_A = 1$, $\varepsilon_A^z = 0$ at *t*=3.00065 s. Thus, Table 3.11 allows identifying S_{A1} as the first faulty device.

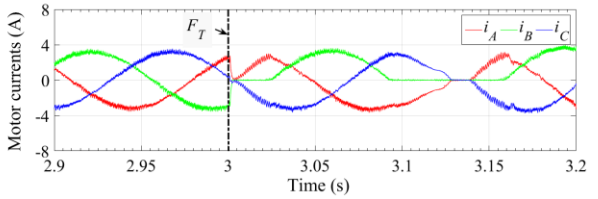

(a) Motor line current waveforms

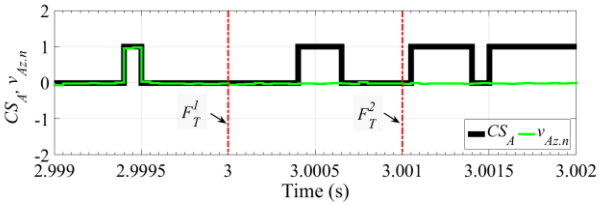

(b) Normalized pole voltage and control state of leg *A*

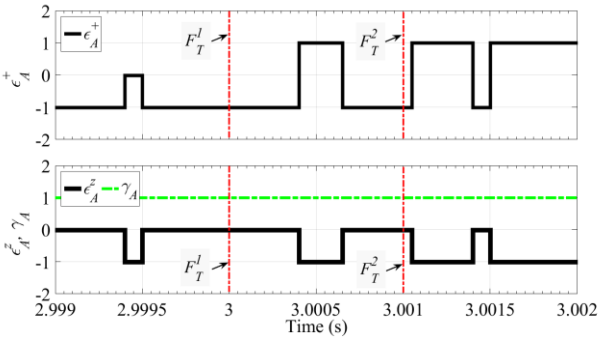

(c) Diagnostic variables of leg *A*

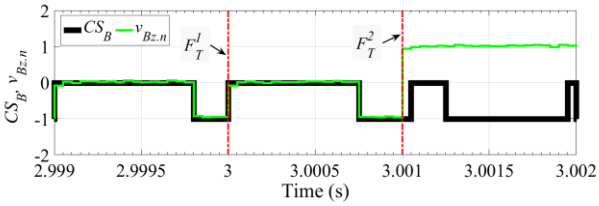

(d) Normalized pole voltage and control state of leg *B*

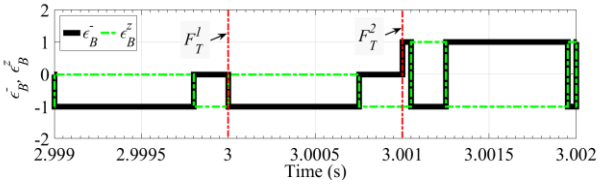

(e) Diagnostic variables of leg *B*

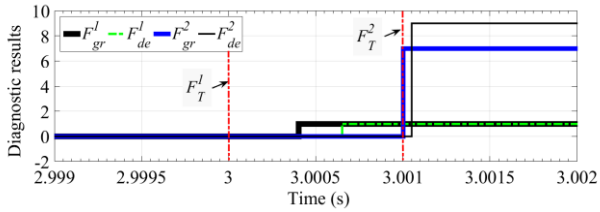

(f) Final diagnostic results

Fig. 3.25. Results for the IM drive operating with an OC in S_{A1} and S_{B3}.

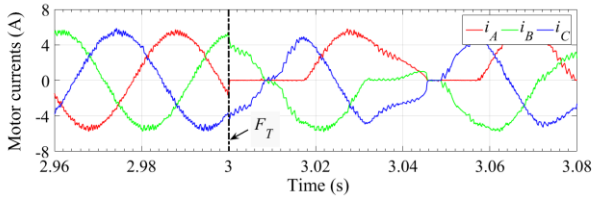

(a) Motor line current waveforms

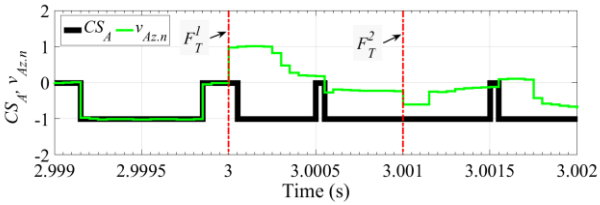

(b) Normalized pole voltage and control state of leg *A*

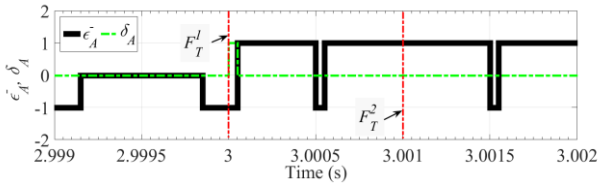

(c) Diagnostic variables of leg *A*.

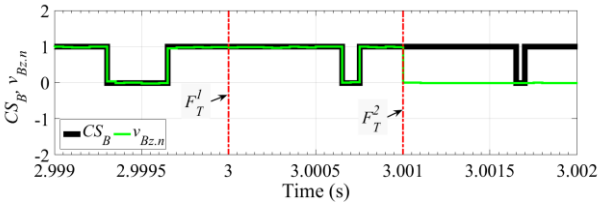

(d) Normalized pole voltage and control state of leg *B*

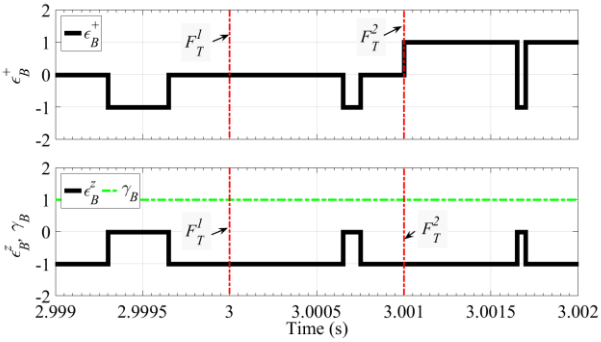

(e) Diagnostic variables of leg *B*

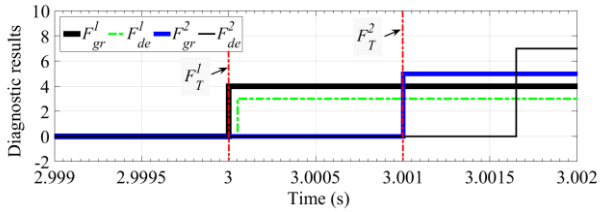

(f) Final diagnostic results

Fig. 3.26. Results for the IM drive operating with an OC in S_{A3} and S_{B1}.

The control state and the normalized inverter pole voltage and the diagnostic variables of leg *B* are shown in Fig. 3.25(d) and Fig. 3.25(e), respectively. Looking now to the second fault, Fig. 3.25(e) shows the first time that ε_B^- takes value 1 is at *t*=3.001 s. Using this value in Table 3.10, it is possible to identify the second faulty group as g_{B3}. Afterwards, combining this information with the fact that at *t*=3.00105 s $\varepsilon_B^z = 1$, and using Table 3.11, it is possible to identify S_{B3} as the second faulty device.

The diagnostic timeline is shown in Fig. 3.25(f), where the diagnostic algorithm identifies the first faulty group as number 1, the first faulty device as number 1, the second faulty group as number 7 and the second faulty device as number 9.

Fig. 3.26 shows the results for another example of double OC faults, applied to S_{A3} at *t*=3 s and to S_{B1} at *t*=3.001 s. In this situation, the reference speed was initially set to 800 rpm, then decreased to 600 rpm following a deceleration ramp with a duration of 2 s. The inverter modulation index before the first fault was about 0.85.

As observed in Fig. 3.26(a), after the occurrence of the faults, all negative values of i_A and some positive values of i_B are eliminated. The control state and the normalized pole voltage of legs *A* and *B* are shown in Fig. 3.26(b) and Fig. 3.26(d), respectively. As observed in Fig. 3.26(b), after the occurrence of the fault in leg *A* at *t*= 3 s, $v_{Az.n}$ is different from CS_A. The same behavior is observed in Fig. 3.26(d) for the faulty IGBT located in leg *B*, after *t*= 3.001 s.

The diagnostic variables δ_A, ε_A^-, ε_B^+, ε_B^z and γ_B, defined for legs *A* and *B*, are shown in Fig. 3.26(c) and Fig. 3.26(e), respectively. As represented in Fig. 3.26(c), the first time that δ_A takes value 1 (*t*=3 s), the first faulty group is identified as g_{A4}, according to Table 3.10. Then, the first time that $\varepsilon_A^- = 1$ (*t*=3.00005 s), Table 3.11 allows to identify S_{A3} as the first faulty device.

The same procedure is applied to Fig. 3.26(e). When ε_B^+ takes value 1 (*t*=3.001 s), g_{B1} is identified as the second faulty group. In Fig. 3.26(e), it is observed that $\varepsilon_B^+ = 0$ while $\gamma_B = 1$ at *t*=3.00165 s. This result and Table 3.11 allows to identify S_{B1} as the second faulty device.

The diagnostic timeline is shown in Fig. 3.26(f), where the diagnostic algorithm identifies the first faulty group as number 4, the first faulty device as number 3, the second faulty group as number 5 and the second faulty device as number 7.

3.5.2.3 Results for clamp-diode OC fault

The diagnostic results obtained for an OC fault in clamp-diode D_{A5} are shown in Fig. 3.27. To introduce OC faults in the clamp-diodes, extra mechanical switches were connected in series with these power switches.

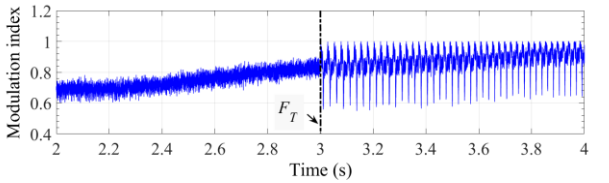

(a) Inverter modulation index

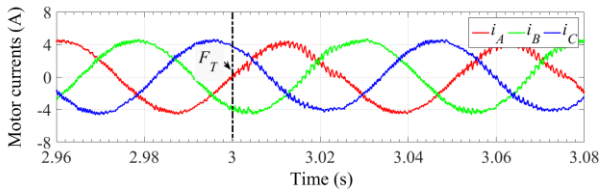

(b) Motor line current waveforms

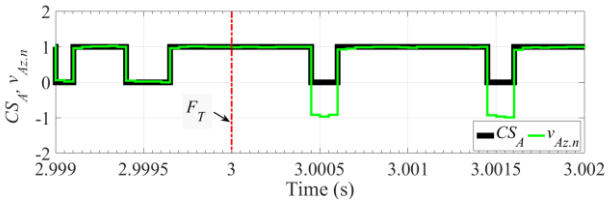

(c) Normalized pole voltage and control state of leg *A*

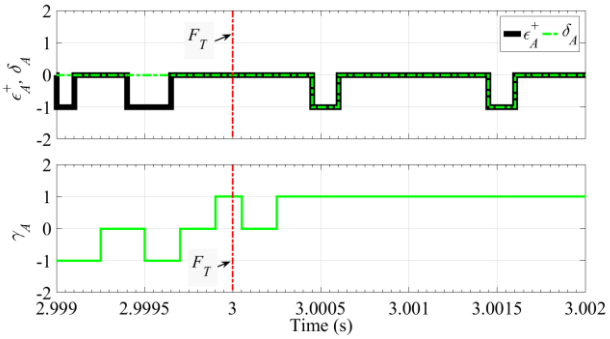

(d) Diagnostic variables of leg *A*

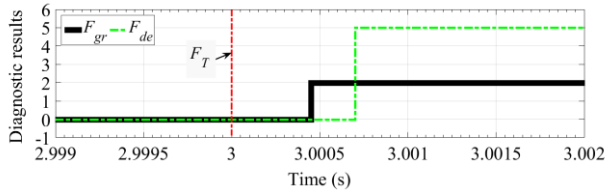

(e) Diagnostic results

Fig. 3.27. Results for the IM drive operating with an OC in D_{A5}.

When the inverter operates with a high modulation index, the dwell time of states 1 and -1 is higher than the dwell time of state 0, and the leg current most of the time flows through current paths 1 and 6 (see Fig. 2.3). Therefore, the effect of the OC fault in the clamp-diodes under such operating conditions is insignificant.

The motor line current waveforms are shown in Fig. 3.27(b). As can be observed, the positive part of i_A is slightly affected by the OC fault in D_{A5}. To analyze the fault, CS_A and $v_{Az.n}$ are shown in Fig. 3.27(c). As shown in this figure, after the occurrence of the fault, the zero parts of CS_A and $v_{Az.n}$ are different and this difference is reflected in δ_A, presented in Fig. 3.27(d). The first time that δ_A takes value -1 (t=3.00045 s), Table 3.10 allows the identification of g_{A2} as the faulty group.

In the next step, since the faulty device is located in g_{A2}, the first time that $\varepsilon_A^+ = 0$ while $\gamma_A = 1$ (t=3.0006 s), Table 3.11 allows to identify the faulty device as D_{A5} (Fig. 3.27(d)). As shown in the diagnostic timeline presented in Fig. 3.27(e), the faulty group number 2 and the faulty device number 5 are identified by the diagnostic algorithm.

A summary of the diagnostic process time is presented in Table 3.12.

Table 3.12. Diagnostic times for the diagnostic approach based on the pole voltages analysis.

Faulty device(s)	Identification time after the OC fault(s)			
	First faulty group	First faulty device	Second faulty group	Second faulty device
S_{A1}	0.05 ms	0.2 ms	---	---
S_{A2}	0	0.8 ms	---	---
S_{A1}, S_{B3}	0.4 ms	0.65 ms	0	0.05 ms
S_{A3}, S_{B1}	0	0.05 ms	0	0.65 ms
D_{A5}	0.45 ms	0.6 ms	---	---

3.6 Final remarks

In this chapter, an extensive literature survey on fault diagnostic approaches for 3LNPC inverters was presented. The behavior of the IM drive operating with IGBT OC faults was investigated and three novel real-time diagnostic approaches were developed and implemented, which allow the detection and identification of the faulty power switches in the 3LNPC inverter.

The first approach is based on the ACPV and has the capability to detect and identify single OC IGBT faults in 3LNPC inverters. The second one is based on the average values of the positive and negative parts of the normalized inverter output currents. The approach is able to diagnose multiple OC faults in all IGBTs of the inverter. The implementation of the first and second approaches only requires the inverter output currents already used by the IM drive controller, thus guaranteeing a low implementation cost and easiness of integration into the motor drive control system. Typically, in both approaches, the faulty IGBT is identified within half of the fundamental inverter output period. However, the required time for detection of the fault and identification of the faulty pair for the approach based on the ACPV is smaller than the second one.

The third approach is based on the deviation of the normalized real pole voltages of each inverter leg and the corresponding reference leg states, which means that its implementation requires the measurement of each inverter leg pole voltage. The capability of the detection and identification of multiple OC fault in all IGBTs and clamp-diodes, the capability of the detection and identification of OC faults in outer IGBTs under operating conditions with very low modulation indexes as well as a quick and reliable performance are the main advantages of the third approach. Typically, the faulty IGBT can be identified within one modulation period (1 ms in this work).

These three diagnostic approaches present independence to the system operating conditions and reliable performance under transient working conditions. Their implementation requires basic mathematical operations and there is no need to use complex algorithms such as pattern recognition. Therefore, they are suitable to be easily integrated into the drive control system without great effort.

All developed approaches were tested and validated through various experimental tests. The experimental results show that the diagnostic approaches work well under all conditions without any incorrect result.

The main features of the fault diagnostic approaches proposed in this chapter are compared with the state-of-the-art in this field and the results are summarized in Table 3.13.

Table 3.13. Comparison of the proposed fault diagnostic approaches with others available in the bibliography.

Ref.	System Operating condition	Extra hardware	Application	Capabilities		
				Identification of faulty switch	Identification of double faults	Identification of clamp-diode faults
[96]	Steady-state	3 voltage sensors	IM drive	yes	no	no
[78]	Steady-state	3 voltage sensors	RL load	no	no	no
[97]	Steady-state	6 current sensors	IM drive	yes	no	yes
[98]	Steady-state	--	RL load	yes	no	no
			Grid-connected	yes	no	no
[99]	Steady-state	--	PMSG	no	no	no
Approach 1 [55]	Transients	--	AC drive	yes	no	no
Approach 2 [56]	Transients	--	AC drive	yes	yes	no
Approach 3 [57]	Transients	3 voltage sensors	AC drive	yes	yes	yes

Chapter 4

Modeling of a wound rotor induction machine

4.1 Introduction

With the aim of performing a detailed analysis of the DFIG system, it is necessary to develop and implement a suitable mathematical model of the WRIM that allows to characterize its behavior and analyze different quantities both in healthy and in faulty conditions.

Electric fault diagnosis often requires analysis of harmonics in several machine quantities like line currents, flux, torque, or speed. One possible way to analyze these signatures is to obtain the electromagnetic field distribution inside the machine with field solvers, which is time-consuming [106].

The modified winding function approach (MWFA) provides another way of obtaining the operating characteristics of the machine. The MWFA provides way to effective calculate the inductances of the machine windings. With the MWFA, the non-sinusoidal distribution of the windings can easily be considered, and the effects of space harmonics can easily be taken into account. Even slotting and magnetic saturation can be modeled by suitably modifying the air-gap permeance. The analysis of internal faults such as rotor eccentricity and inter-turn short-circuits (ITSCs) is also possible using this method [106].

In this chapter, a simulation model of a WRIM using the MWFA, is developed and implemented in Matlab/Simulink environment. The model includes phenomena such as the effects of the linear rise of magnetomotive force (MMF) across the slots, stator and rotor slotting, and magnetic

saturation. Furthermore, the model was developed to allow the introducing of ITSC faults in the stator and rotor windings of the machine.

The following assumptions were initially made for the development of the model:

- The eddy currents and hysteresis effects in the magnetic materials were neglected.
- The magnetic flux lines are considered to cross the air-gap radially.
- The capacitive coupling between the windings was neglected.
- Skin effect was not considered in the model.
- As the stator and rotor slots of the machine employed in the experimental tests are straight, the stator and rotor skewing was not considered in the model.

4.2 Basic concepts of modified winding function approach

The fundamentals of the MWFA are given in [106]. We will start by considering an elementary WRIM as shown in Fig. 4.1. The machine contains two windings in the stator (winding *A* and winding *B*) and two windings in the rotor (winding *a* and winding *b*). The quantities ρ and θ are the angular position in a stator reference frame and the angular position of the rotor with respect to the stator axis S_{ref}, respectively.

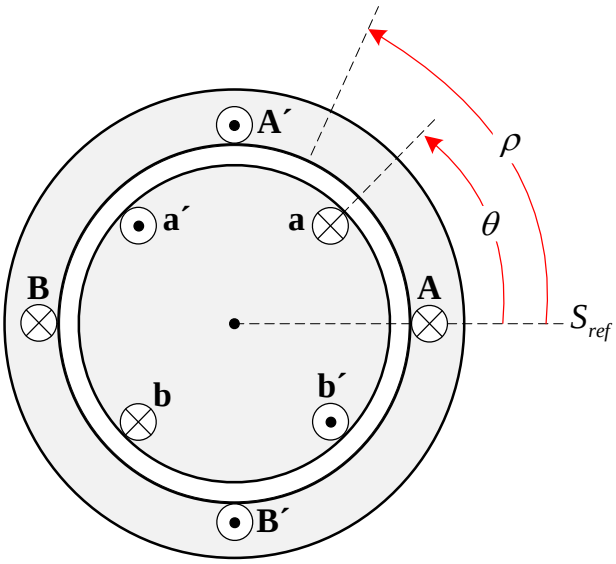

Fig. 4.1. Elementary WRIM.

The function $n(\rho,\theta)$ is called the turns function and represents the number of turns of the winding at the angular position ρ in the stator frame. In general, for a stationary coil, the turns function is only a function of ρ while for a rotating coil it is a function of ρ and θ.

The function $g^{-1}(\rho,\theta)$ is the inverse air-gap function of the machine and represents the inverse of the air-gap length at an angular position ρ in the stator frame. Ignoring slotting of the rotor and stator, the function $g^{-1}(\rho,\theta)$ is constant. Taking into account the stator and rotor slotting, $g^{-1}(\rho,\theta)$ becomes a function of ρ and θ.

The modified winding function is the MMF drop across the air-gap for a current circulating in the winding, being defined as [106]

$$M(\rho,\theta) = n(\rho,\theta) - \langle M(\rho,\theta) \rangle, \tag{4.1}$$

where $\langle M(\rho,\theta) \rangle$ is the average value of the modified winding function, defined as

$$\langle M(\rho,\theta) \rangle = \frac{1}{2\pi \langle g^{-1}(\rho,\theta) \rangle} \int_0^{2\pi} n(\rho,\theta) g^{-1}(\rho,\theta) d\rho \tag{4.2}$$

and $\langle g^{-1}(\rho,\theta) \rangle$ is the average value of the inverse air-gap function, defined as

$$\langle g^{-1}(\rho,\theta) \rangle = \frac{1}{2\pi} \int_0^{2\pi} g^{-1}(\rho,\theta) d\rho \,. \tag{4.3}$$

The mutual inductance between windings B and A is defined as [106]

$$L_{BA} = \mu_0 r l \int_0^{2\pi} n_B(\rho,\theta) M_A(\rho,\theta) g^{-1}(\rho,\theta) d\rho, \tag{4.4}$$

where μ_0, r and l are the free space permeability, stator inner radius and axial stack length of the machine, respectively.

Replacing $(M_A(\rho,\theta))$ in (4.4) by its definition given by (4.1) leads to [106]

$$L_{BA} = \mu_0 r l \int_0^{2\pi} n_B(\rho,\theta) \left(n_A(\rho,\theta) - \langle M_A(\rho,\theta) \rangle \right) g^{-1}(\rho,\theta) d\rho, \tag{4.5}$$

which is equivalent to

$$L_{BA} = \mu_0 rl\left[\int_0^{2\pi} n_B(\rho,\theta) n_A(\rho,\theta) g^{-1}(\rho,\theta) d\rho - \int_0^{2\pi} n_B(\rho,\theta)\left\langle M_A(\rho,\theta)\right\rangle g^{-1}(\rho,\theta) d\rho\right]. \quad (4.6)$$

In (4.6), $\left\langle M_A(\rho,\theta)\right\rangle$ is a constant and therefore, it is taken outside the integral, thus obtaining

$$L_{BA} = \mu_0 rl\left[\int_0^{2\pi} n_B(\rho,\theta) n_A(\rho,\theta) g^{-1}(\rho,\theta) d\rho - \left\langle M_A(\rho,\theta)\right\rangle \int_0^{2\pi} n_B(\rho,\theta) g^{-1}(\rho,\theta) d\rho\right], \quad (4.7)$$

which is equivalent to

$$L_{BA} = \mu_0 rl\left[\int_0^{2\pi} n_B(\rho,\theta) n_A(\rho,\theta) g^{-1}(\rho,\theta) d\rho - 2\pi\left\langle M_B(\rho,\theta)\right\rangle\left\langle M_A(\rho,\theta)\right\rangle\left\langle g^{-1}(\rho,\theta)\right\rangle\right]. \quad (4.8)$$

4.3 Development of the machine model

In this subsection, the implementation of the simulation model of the machine that will be used later on in the experimental tests is discussed. The details of the machine can be found in Appendix *C*.

The developed model takes into account phenomena such as the linear rise of the MMF across the slots, stator and rotor slotting effects and magnetic saturation in the machine core.

The subscripts used in the turns function and inductances are *A*, *B*, *C* for the three windings of the stator while *a*, *b* and *c* refer to the three windings of the rotor.

The equations (4.1)-(4.8) consider the continuous variations of the signals. However, for the computer implementation, it is necessary to discretize these equations. Therefore, it is considered a finite number of samples and, for that purpose, the stator frame is divided into *N* sections (in this study *N*=720). It will give an angular resolution of

$$\rho_N = \frac{2\pi}{N}. \quad (4.9)$$

With the aim of implementing the model, the turns functions and the inverse air-gap function are discretized. Then, the rectangular integration is used to calculate the inductances.

4.3.1 Turns and winding functions

The distribution of the stator and rotor windings are presented in Fig. 4.2 and Fig. 4.3, respectively. Each phase of the stator windings has 6 series-connected coils with a total of 180 turns per phase (each coil of the stator windings has 30 turns). Each phase of the rotor windings has 4 series-connected coils with a total of 108 turns per phase (each coil of the rotor windings has 27 turns). Fig. 4.4 shows the layout of the stator and rotor windings of the WRIM at $\theta = 0$ rad (θ is the angle between the rotor axis and the stator axis S_{ref}).

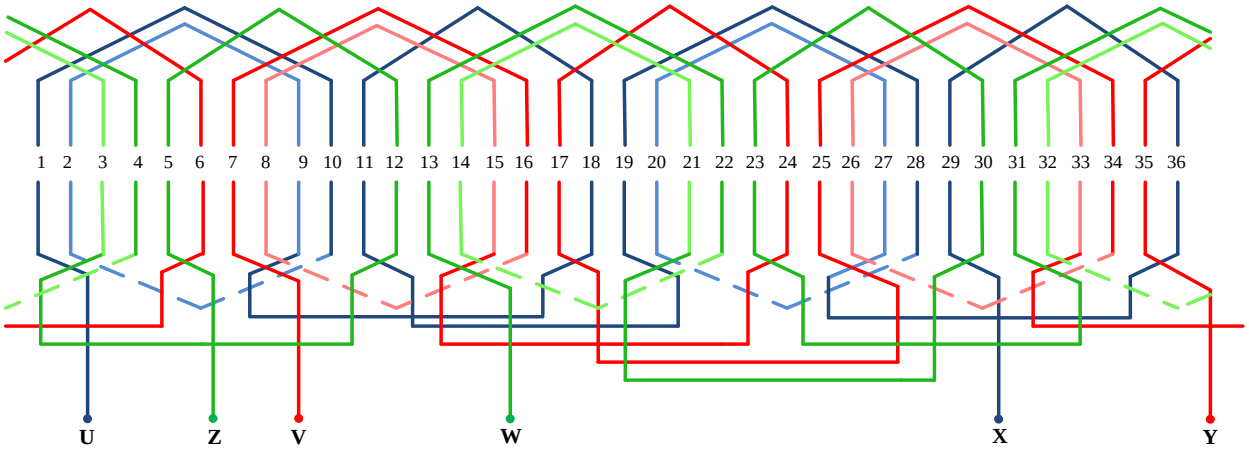

Fig. 4.2. Stator winding distribution of the WRIM.

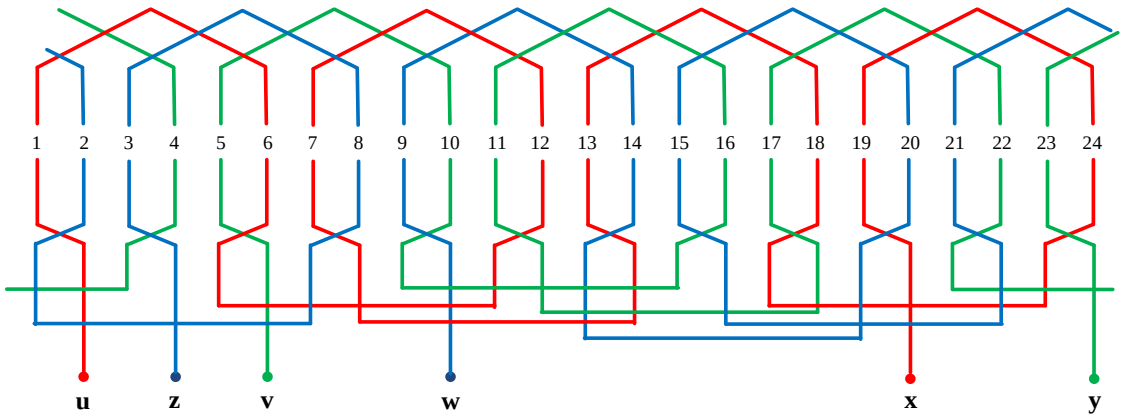

Fig. 4.3. Rotor winding distribution of the WRIM.

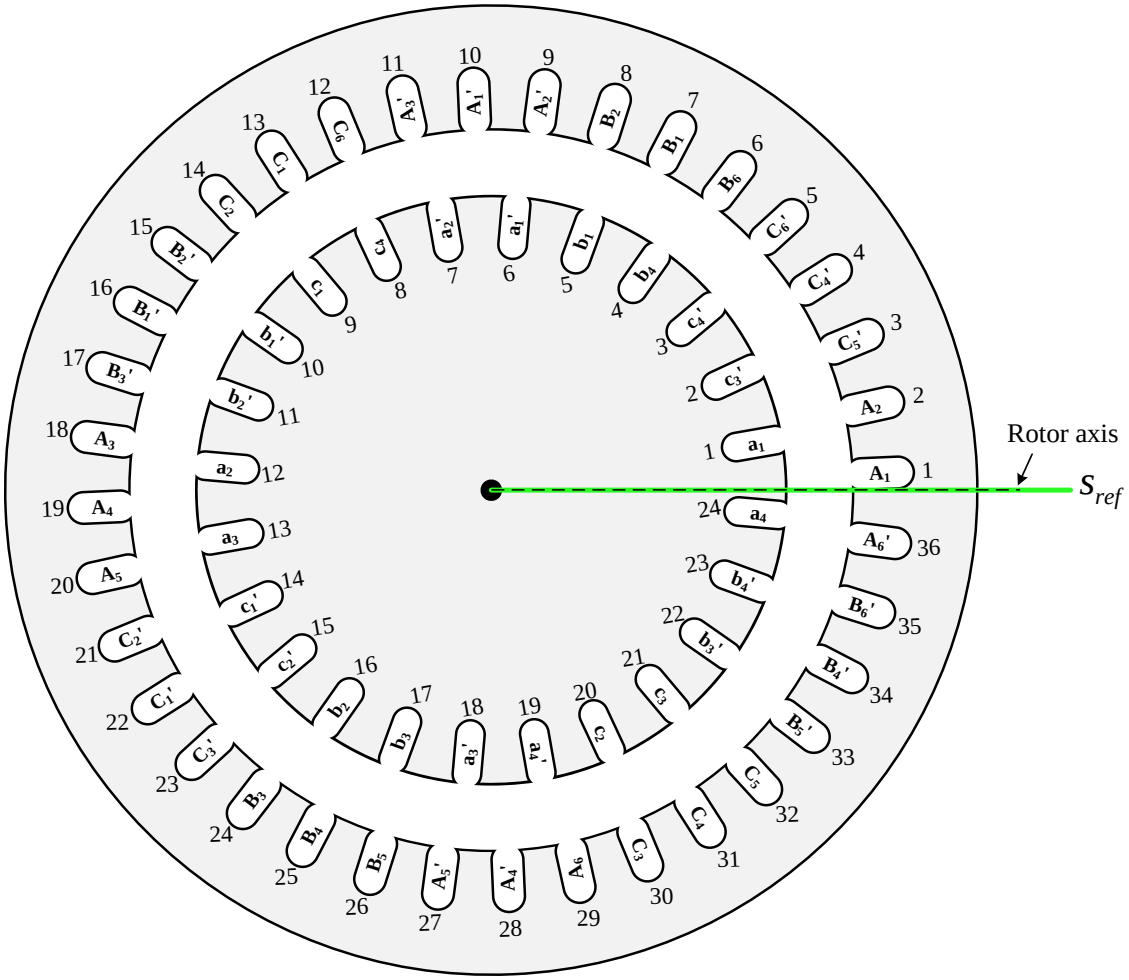

Fig. 4.4. Layout of the windings in the stator and rotor of the WRIM (at $\theta = 0$ rad).

The turns functions of the stator windings $(n_A(\rho),\ n_B(\rho)$ and $n_C(\rho))$ are only a function of ρ while those for the rotor windings $(n_a(\rho,\theta),\ n_b(\rho,\theta)$ and $n_c(\rho,\theta))$ are a function of ρ and θ.

From the windings arrangements of the machine, presented in Fig. 4.2, Fig. 4.3 and Fig. 4.4, the turns function of the three windings of the stator and rotor are illustrated in Fig. 4.5 and Fig. 4.6, respectively. As can be seen in these figures, the effects of the linear rise of the MMF across the slots are included in the turns functions.

Fig. 4.7 shows the winding functions of the stator winding *A* and the rotor winding *a*.

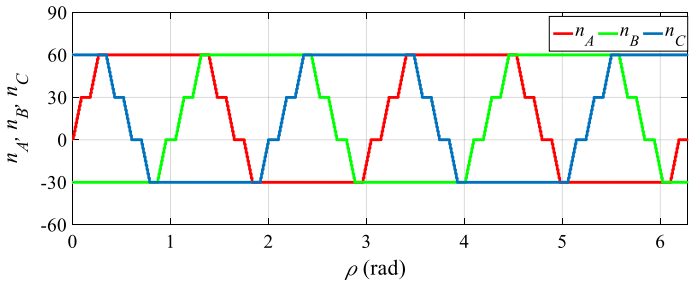

Fig. 4.5. Turns function of the stator windings.

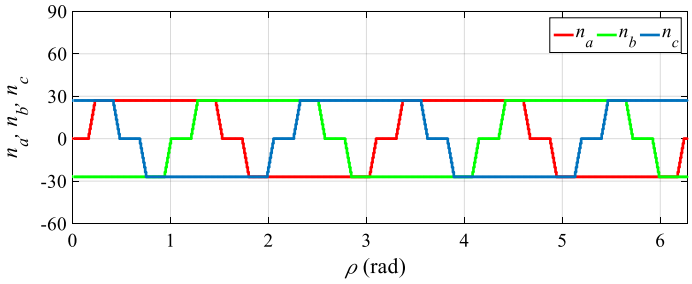

Fig. 4.6. Turns function of the rotor windings (at $\theta = 0$ rad).

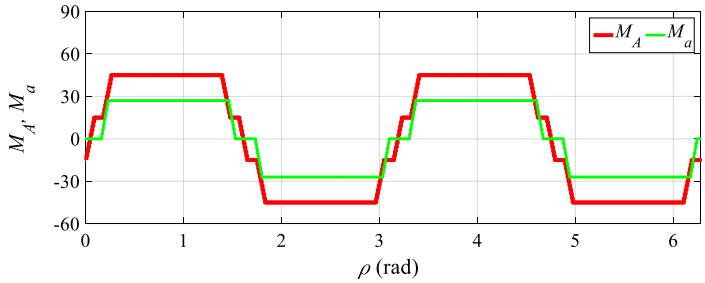

Fig. 4.7. Winding functions of phase A of stator and phase a of the rotor windings (at $\theta = 0$ rad).

4.3.2 Inverse air-gap function

The position of the stator and rotor slots when θ=0 rad is shown in Fig. 4.8, where g_0 is the minimum value of the air-gap of the machine, and h_s and h_r are the stator and rotor teeth height, respectively. τ_s and τ_r are the angles corresponding to the stator and rotor slot pitch and are given by

$$\begin{cases} \tau_s = \dfrac{2\pi}{S_s} \\ \tau_r = \dfrac{2\pi}{S_r}, \end{cases} \tag{4.10}$$

where $S_s = 36$ is number of the stator slots and $S_r = 24$ is number of the rotor slots.

Initially, for the definition of the air-gap function, the real dimensions of the stator and rotor slots (h_s=20 mm and h_r=18 mm) and the real value of the air-gap (g_0=0.6 mm) were considered in the model. However, the simulation results were not in agreement with the experimental results because the slotting effect was too pronounced.

In order to have a better matching between the simulation and experimental results, it was necessary to consider a smoother variation of the air-gap in the model. Therefore, using a trial and error procedure, the effective depths of the stator and rotor slots are obtained, as marked in Fig. 4.8. The minimum value of the air-gap is also considered as g_0=1.1 mm. With these modifications, the simulation results were in agreement with the experimental ones, thus improving this modeling procedure.

The stator air-gap function $g_s(\rho)$, which is the distance between the effective depth of the stator slots and the stator surface, is independent of the rotor position. The rotor air-gap function $g_r(\rho,\theta)$, which is the distance between the effective depth of the rotor slots and the rotor surface, rotates with the rotor.

The total air-gap function is defined as

$$g(\rho,\theta) = g_0 + g_s(\rho) + g_r(\rho,\theta). \tag{4.11}$$

The inverse air-gap function is given by

$$g^{-1}(\rho,\theta) = \frac{1}{g(\rho,\theta)}. \tag{4.12}$$

Fig. 4.9 shows the values of $g_s(\rho)$, $g_r(\rho,\theta)$, $g(\rho,\theta)$ and $g^{-1}(\rho,\theta)$ at $\theta = 0$ rad. As can be seen in Fig. 4.9, $g_s(\rho)$ and $g_r(\rho,\theta)$ are a periodic function of ρ with a repetition period of one stator slot pitch (0.1745 rad) and one rotor slot pitch (0.2618 rad), respectively. Therefore, the repetition period of the total air-gap function is 0.5236 rad (the least common multiple of 0.1745 and 0.2618).

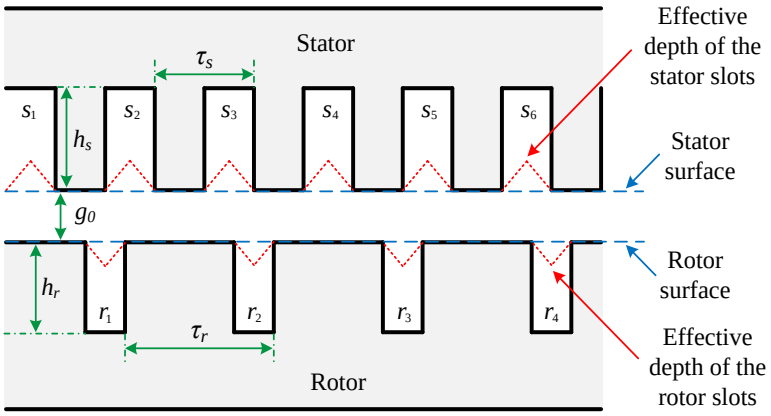

Fig. 4.8. Position of the stator and rotor slots at $\theta = 0$ rad.

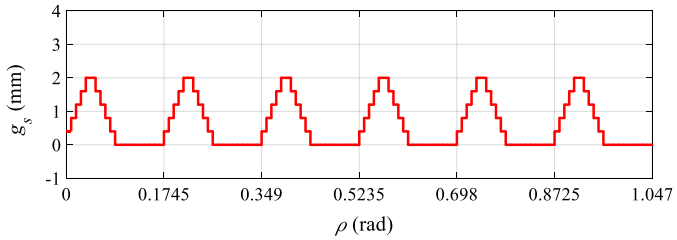

(a) Stator air-gap function

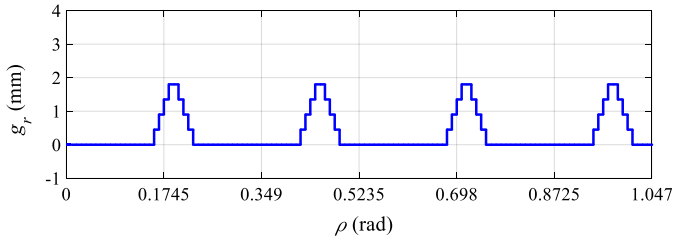

(b) Rotor air-gap function

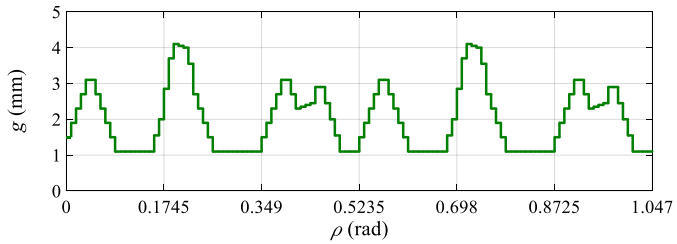

(c) Total air-gap function, considering g_0=1.1 mm

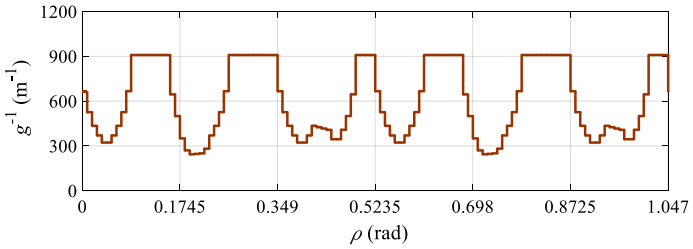

(d) Inverse air-gap function

Fig. 4.9. Effective air-gap and inverse air-gap functions at $\theta = 0$ rad.

4.3.3 Inclusion of magnetic saturation

Until this point, the magnetic permeability of the iron was considered infinity. Therefore the effects of magnetic saturation were ignored.

The non-linear behavior of the magnetic circuit influences the amplitude of currents drawn by the machine and produces additional currents and torque harmonics [107]. In order to improve the accuracy of the obtained simulation results, the magnetic saturation was included in the developed model.

In the model, it is assumed that the stator and rotor teeth have reluctance. This magnetic reluctance changes with the magnetic saturation. Hence, the saturation is emulated by a proper decrease of the height of the teeth which results in an increase of the air-gap length in front of the teeth. This procedure is equivalent to consider the teeth with infinite permeability and introduce a proper increase of the air-gap length in front of the teeth [108].

In a first step, the magnetic flux in all stator and rotor teeth should be calculated. In this work, for the calculation of the magnetic flux in the teeth, a single-turn open-circuit search coil was added around each stator and rotor tooth. The mutual inductances between these search coils and the stator and rotor windings are calculated using the MWFA. The magnetic flux crossing the search coil in tooth *i* is calculated by

$$\phi_i = \left[\left[L_{is} \right] \vdots \left[L_{ir} \right] \right] \left[\begin{matrix} \left[I_s \right] \\ \hdashline \left[I_r \right] \end{matrix} \right]^{1}, \tag{4.13}$$

where

$$\left[I_s \right] = \left[i_A \quad i_B \quad i_C \right]^T \tag{4.14}$$

$$\left[I_r \right] = \left[i_a \quad i_b \quad i_c \right]^T \tag{4.15}$$

$$\left[L_{is} \right] = \left[L_{iA} \quad L_{iB} \quad L_{iC} \right] \tag{4.16}$$

$$\left[L_{ir} \right] = \left[L_{ia} \quad L_{ib} \quad L_{ic} \right], \tag{4.17}$$

[1] As the search coil has only one turn, flux and flux linkage associated for the search coils is identical.

where L_{iA}, L_{iB} and L_{iC} are the mutual inductances between the search coil of tooth *i* and the three stator windings and L_{ia}, L_{ib} and L_{ic} are the mutual inductances between the search coil and the three rotor windings.

The flux density in tooth *i* is calculated by

$$B_i = \frac{\phi_i}{A_i}, \tag{4.18}$$

where A_i is cross-section of tooth *i*.

The magnetic permeability of tooth *i* is calculated by

$$\mu_i = \frac{B_i}{H_i}, \tag{4.19}$$

where H_i is the magnetic field intensity of tooth *i*, which is obtained from the magnetization curve (*B*–*H* curve) of the core material of the machine. Fig. 4.10 shows the magnetization curve of the core material of the machine that later on will be used in the experimental tests. Fig. 4.11 shows the variation of the magnetic permeability as a function of the flux density in the core material.

Since the flux distribution in the machine is non-uniform, each tooth will have a different μ compared to others, and due to rotation of the magnetic field inside the machine, each tooth will also have a time-varying μ.

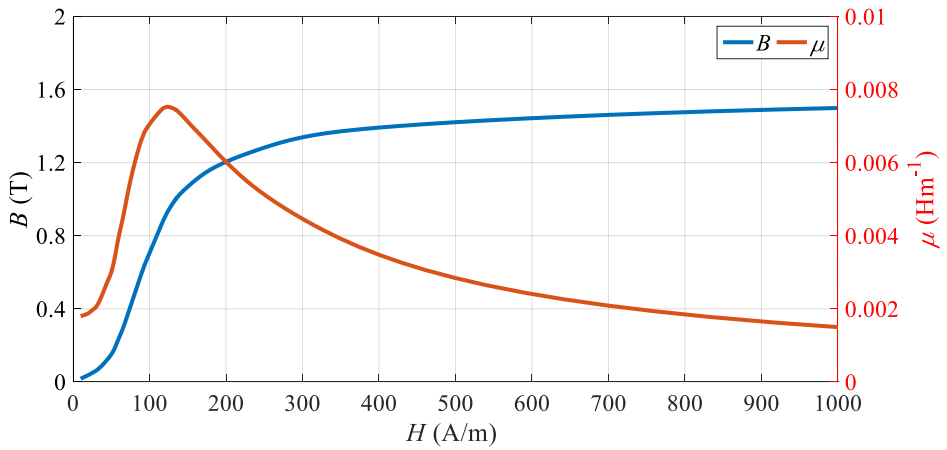

Fig. 4.10. Magnetization curve of the core material used in the experimental WRIM.

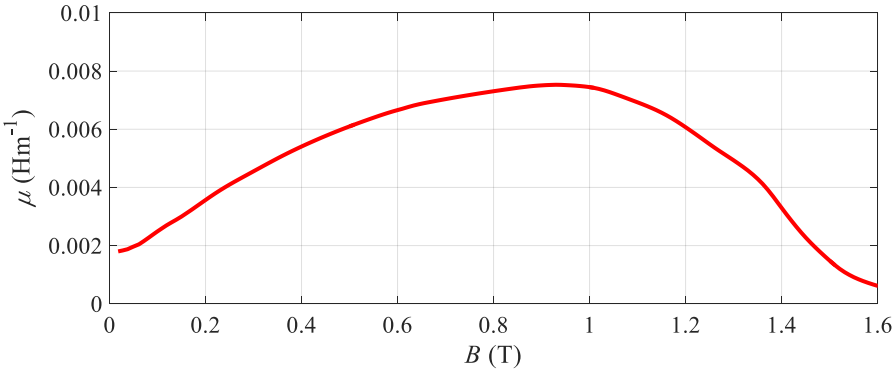

Fig. 4.11. Magnetic permeability versus flux density of the core material.

The magnetic reluctance of tooth *i* is calculated by

$$R_i = \frac{h_i}{\mu_i A_i}, \tag{4.20}$$

where h_i is the height of tooth *i*.

Now, the magnetic reluctance of tooth *i* is emulated by a proper decrement of its height. The height decrement of tooth *i* is given by

$$\Delta h_i = \frac{\mu_0}{\mu_i} h_i. \tag{4.21}$$

The equivalent height of tooth *i* is given by

$$h_i' = h_i - \Delta h_i. \tag{4.22}$$

The equivalent height of all stator and rotor teeth is updated at the end of every simulation step. The decrement of the height of the saturated teeth is schematically illustrated in Fig. 4.12.

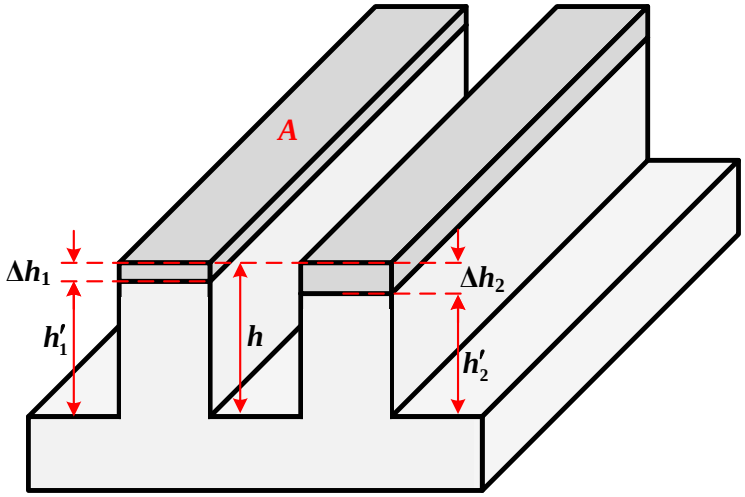

Fig. 4.12. Decrease of the height of the saturated teeth.

4.3.4 Inductances calculation using rectangular integration

According to the rotor position, at the end of every simulation step, the turns functions of the rotor windings as well as the inverse air-gap function are updated. Then, the definite integrals presented in (4.3), (4.2) and (4.8) are calculated by

$$\left\langle g^{-1}(\rho,\theta)\right\rangle = \frac{1}{N}\sum_{k=1}^{N} g^{-1}(k,\theta) \tag{4.23}$$

$$\left\langle M(\rho,\theta)\right\rangle = \frac{1}{N\left\langle g^{-1}(\rho,\theta)\right\rangle}\sum_{k=1}^{N} n(k,\theta)g^{-1}(k,\theta) = \frac{\sum_{k=1}^{N} n(k,\theta)g^{-1}(k,\theta)}{\sum_{k=1}^{N} g^{-1}(k,\theta)} \tag{4.24}$$

$$L_{BA}(\theta) = \mu_0 rl\left[\rho_N \sum_{k=1}^{N}\left[n_A(k,\theta)n_B(k,\theta)g^{-1}(k,\theta)\right] - 2\pi\left\langle M_A(\rho,\theta)\right\rangle\left\langle M_B(\rho,\theta)\right\rangle\left\langle g^{-1}(\rho,\theta)\right\rangle\right]. \tag{4.25}$$

The self-inductance of winding *A* is given by

$$L_{AA}(\theta) = L_{lA} + \mu_0 rl\left[\rho_N \sum_{k=1}^{N}\left[n_A(k,\theta)n_A(k,\theta)g^{-1}(k,\theta)\right] - 2\pi\left\langle M_A(\rho,\theta)\right\rangle\left\langle M_A(\rho,\theta)\right\rangle\left\langle g^{-1}(\rho,\theta)\right\rangle\right], \tag{4.26}$$

where L_{lA} is the leakage inductance of winding *A*.

For a given value of θ (θ is the rotor angular position), two nearby sample positions, floor sample (θ_F) and ceil sample (θ_C) are given by

$$\theta_F = \left\lfloor \frac{\theta}{\rho_N} \right\rfloor \rho_N \tag{4.27}$$

$$\theta_C = \theta_F + \rho_N. \tag{4.28}$$

The definition of θ_F and θ_C for a given θ is schematically illustrated in Fig. 4.13.

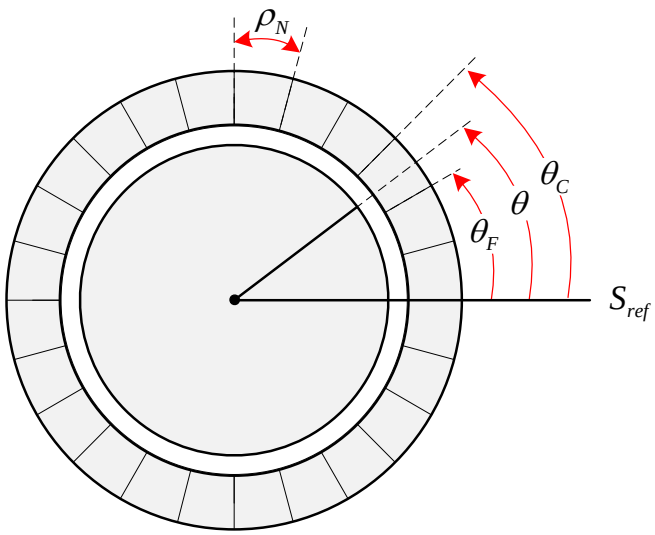

Fig. 4.13. Definition of θ_F and θ_C for a given θ.

At the end of each simulation step, all inductances are calculated for both rotor angular positions θ_F and θ_C. Then, the partial derivative of inductances with respect to the rotor angular position is given by

$$\frac{\partial L(\theta)}{\partial \theta} = \frac{L(\theta_C) - L(\theta_F)}{(\theta_C - \theta_F)}. \tag{4.29}$$

Finally, the inductances for the position θ are given by

$$L(\theta) = L(\theta_F) + \frac{\partial L(\theta)}{\partial \theta}(\theta - \theta_F). \tag{4.30}$$

Fig. 4.14 shows the inductances of the machine obtained with the simulation model.

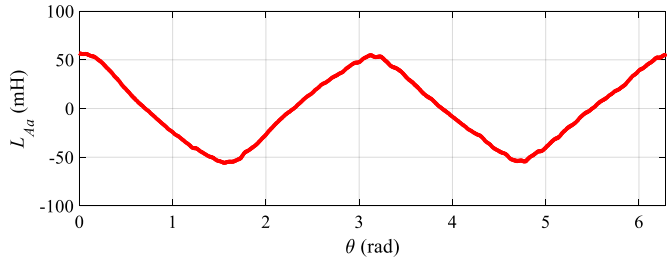

(a) Mutual inductance between the stator winding *A* and the rotor winding *a*

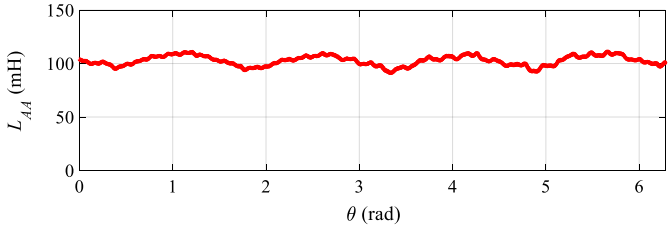

(b) Self-inductance of the stator winding *A*

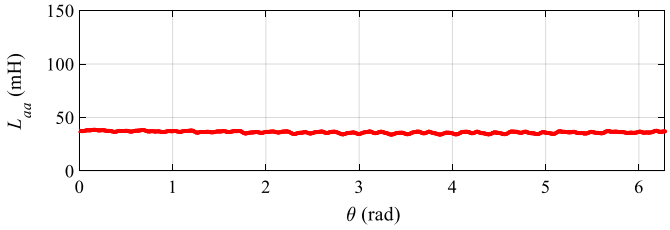

(c) Self-inductance of the rotor winding *a*

Fig. 4.14. Inductances of the machine obtained with the developed simulation model.

4.3.5 Modeling of ITSC faults

For the purpose of the mathematical modeling of ITSC faults in the windings of the machine, the affected winding is divided into two parts, healthy part and faulty part. Then, according to the position and number of the short-circuited turns, the turns function, resistance and inductances of the healthy and faulty parts of the affected winding are recalculated.

As an example, according to Fig. 4.15, 15 turns out of 180 turns of the stator winding *A* are short-circuited through an external short-circuit resistance R_{sc}. The turns function of the healthy and faulty parts of the stator winding *A* are shown in Fig. 4.16. The subscripts *h* and *f* are used for the healthy and faulty parts of the winding.

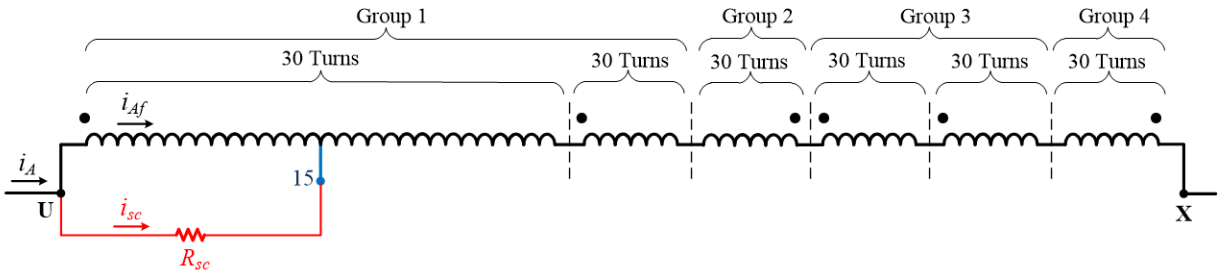

Fig. 4.15. Schematic representation of stator winding A with 15 short-circuited turns.

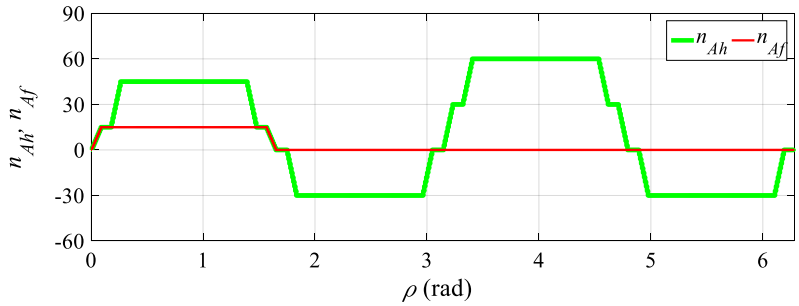

Fig. 4.16. Turns function of the healthy and faulty parts of the stator winding A.

According to the number of short-circuited turns, the resistance of the healthy and faulty parts of the affected winding is calculated by

$$\begin{cases} R_{Af} = \dfrac{N_{Af}}{N_A} R_A \\ R_{Ah} = \dfrac{N_A - N_{Af}}{N_A} R_A, \end{cases} \tag{4.31}$$

where R_A is the total resistance of winding A, N_A is the total number of turns of winding A and N_{Af} is the number of turns of the faulty part of winding A.

The leakage inductance of the healthy and faulty parts of the affected winding is calculated by [109]

$$\begin{cases} L_{lAf} \cong \left(\dfrac{N_{Af}}{N_A} \right)^2 L_{lA} \\ L_{lAh} \cong \left(\dfrac{N_A - N_{Af}}{N_A} \right)^2 L_{lA}. \end{cases} \tag{4.32}$$

After the recalculation of the turns function and the leakage inductance of the healthy and faulty parts of the affected winding, the MWFA is used to compute the self-inductances of the healthy and faulty parts of the affected winding as well as the mutual inductances between these parts and the rest of the stator and rotor windings of the machine.

The equivalent electric circuit of the stator winding *A* with an ITSC fault is presented in Fig. 4.17, where ψ_{Ah} and ψ_{Af} are the flux linkages of the healthy and faulty parts of the affected winding and u_A is the voltage applied to winding *A*.

From Loop 1 and Loop 2, marked in Fig. 4.17, the voltage equations of the windings healthy and faulty parts are given by

$$\begin{cases} u_A = R_{Ah} i_A + \dfrac{d\psi_{Ah}}{dt} + R_{sc} i_{sc} \\ 0 = R_{Af} i_{Af} + \dfrac{d\psi_{Af}}{dt} - R_{sc} i_{sc}. \end{cases} \tag{4.33}$$

Replacing $i_{sc} = i_A - i_{Af}$ in (4.33) leads to

$$\begin{cases} u_A = \left(R_{Ah} + R_{sc}\right) i_A - R_{sc} i_{Af} + \dfrac{d\psi_{Ah}}{dt} \\ 0 = -R_{sc} i_A + \left(R_{Af} + R_{sc}\right) i_{Af} + \dfrac{d\psi_{Af}}{dt}. \end{cases} \tag{4.34}$$

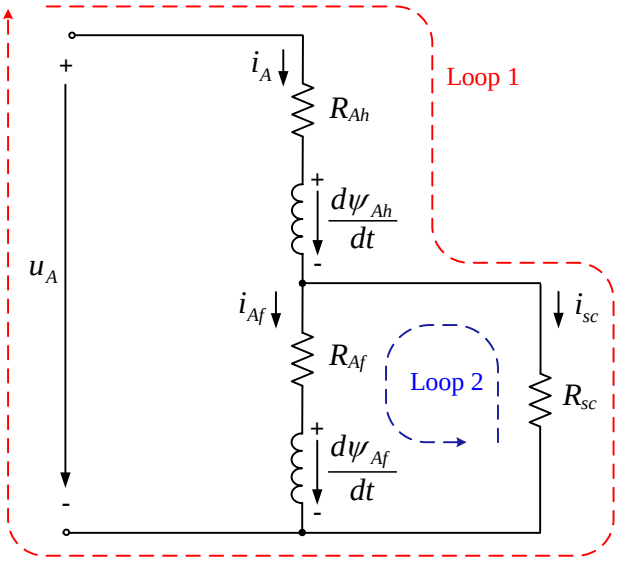

Fig. 4.17. Equivalent electric circuit of the stator winding A with an ITSC fault.

4.3.6 State-space model

The voltage equations for the stator and rotor circuits are expressed in the state-space form by [109]

$$\begin{bmatrix} [U_s] \\ [U_r] \end{bmatrix} = \begin{bmatrix} [R_s] & [0] \\ [0] & [R_r] \end{bmatrix} \begin{bmatrix} [I_s] \\ [I_r] \end{bmatrix} + \frac{d}{dt} \begin{bmatrix} [\psi_s] \\ [\psi_r] \end{bmatrix}, \tag{4.35}$$

where, for the healthy machine,

$$[U_s] = [u_A \quad u_B \quad u_C]^T \tag{4.36}$$

$$[U_r] = [u_a \quad u_b \quad u_c]^T \tag{4.37}$$

$$[I_s] = [i_A \quad i_B \quad i_C]^T \tag{4.38}$$

$$[I_r] = [i_a \quad i_b \quad i_c]^T \tag{4.39}$$

$$[\psi_s] = [\psi_A \quad \psi_B \quad \psi_C]^T \tag{4.40}$$

$$[\psi_r] = [\psi_a \quad \psi_b \quad \psi_c]^T \tag{4.41}$$

$$[R_s] = \begin{bmatrix} R_A & 0 & 0 \\ 0 & R_B & 0 \\ 0 & 0 & R_C \end{bmatrix} \tag{4.42}$$

$$[R_r] = \begin{bmatrix} R_a & 0 & 0 \\ 0 & R_b & 0 \\ 0 & 0 & R_c \end{bmatrix}, \tag{4.43}$$

where u_A, u_B and u_C are the voltages of the stator windings, u_a, u_b and u_c are the voltages of the rotor windings, i_A, i_B and i_C are the stator currents, i_a, i_b and i_c are the rotor currents,

ψ_A, ψ_B and ψ_C are the stator fluxes linkages, ψ_a, ψ_b and ψ_c are the rotor flux linkages, R_A, R_B and R_C are the resistance of the stator windings, and R_a, R_b and R_c are the resistance of the rotor windings.

The stator and rotor flux linkages are calculated by

$$\begin{bmatrix} [\psi_s] \\ [\psi_r] \end{bmatrix} = \begin{bmatrix} [L_{ss}] & [L_{sr}] \\ [L_{rs}] & [L_{rr}] \end{bmatrix} \begin{bmatrix} [I_s] \\ [I_r] \end{bmatrix}, \tag{4.44}$$

where, for the healthy machine,

$$[L_{ss}] = \begin{bmatrix} L_{AA} & L_{AB} & L_{AC} \\ L_{BA} & L_{BB} & L_{BC} \\ L_{CA} & L_{CB} & L_{CC} \end{bmatrix} \tag{4.45}$$

$$[L_{rr}] = \begin{bmatrix} L_{aa} & L_{ab} & L_{ac} \\ L_{ba} & L_{bb} & L_{bc} \\ L_{ca} & L_{cb} & L_{cc} \end{bmatrix} \tag{4.46}$$

$$[L_{sr}] = [L_{rs}]^T = \begin{bmatrix} L_{Aa} & L_{Ab} & L_{Ac} \\ L_{Ba} & L_{Bb} & L_{Bc} \\ L_{Ca} & L_{Cb} & L_{Cc} \end{bmatrix}, \tag{4.47}$$

where L_{AA}, L_{BB} and L_{CC} are the self-inductances of the stator windings, $L_{AB} = L_{BA}$, $L_{AC} = L_{CA}$ and $L_{BC} = L_{CB}$ are the mutual inductances between the stator windings, L_{aa}, L_{bb} and L_{cc} are the self-inductances of the rotor windings, $L_{ab} = L_{ba}$, $L_{ac} = L_{ca}$ and $L_{bc} = L_{cb}$ are the mutual inductances between the rotor windings, and L_{Aa}, L_{Ab}, L_{Ac}, L_{Ba}, L_{Bb}, L_{Bc}, L_{Ca}, L_{Cb} and L_{Cc} are the mutual inductances between the stator and rotor windings.

Replacing (4.44) in (4.35) leads to

$$\begin{bmatrix} [U_s] \\ [U_r] \end{bmatrix} = \begin{bmatrix} [R_s] & [0] \\ [0] & [R_r] \end{bmatrix} \begin{bmatrix} [I_s] \\ [I_r] \end{bmatrix} + \frac{d}{dt}\left(\begin{bmatrix} [L_{ss}] & [L_{sr}] \\ [L_{rs}] & [L_{rr}] \end{bmatrix} \begin{bmatrix} [I_s] \\ [I_r] \end{bmatrix} \right), \tag{4.48}$$

To introduce the ITSC fault in the stator windings, taking into account the voltage equations of the healthy and faulty parts of the affected winding presented in (4.34), the matrices $[U_s]$, $[I_s]$, $[R_s]$, $[L_{ss}]$ and $[L_{sr}]$ should be modified. As an example, to introduce the ITSC fault in the stator winding *A*, (4.36), (4.38), (4.42), (4.45) and (4.47) are modified as

$$[U_s]=[u_A \quad u_B \quad u_C \quad 0]^T \tag{4.49}$$

$$[I_s]=[i_A \quad i_B \quad i_C \quad i_{Af}]^T \tag{4.50}$$

$$[R_s]=\begin{bmatrix} R_{Ah}+R_{sc} & 0 & 0 & -R_{sc} \\ 0 & R_B & 0 & 0 \\ 0 & 0 & R_C & 0 \\ -R_{sc} & 0 & 0 & R_{Af}+R_{sc} \end{bmatrix} \tag{4.51}$$

$$[L_{ss}]=\begin{bmatrix} L_{AhAh} & L_{AhB} & L_{AhC} & L_{AhAf} \\ L_{BAh} & L_{BB} & L_{BC} & L_{BAf} \\ L_{CAh} & L_{CB} & L_{CC} & L_{CAf} \\ L_{AfAh} & L_{AfB} & L_{AfC} & L_{AfAf} \end{bmatrix} \tag{4.52}$$

$$[L_{sr}]=[L_{rs}]^T=\begin{bmatrix} L_{Aha} & L_{Ahb} & L_{Ahc} \\ L_{Ba} & L_{Bb} & L_{Bc} \\ L_{Ca} & L_{Cb} & L_{Cc} \\ L_{Afa} & L_{Afb} & L_{Afc} \end{bmatrix}, \tag{4.53}$$

where L_{AhAh} and L_{AfAf} are the self-inductances of the healthy and faulty parts of winding *A*, $L_{AhB}=L_{BAh}$ and $L_{AhC}=L_{CAh}$ are the mutual inductances between the healthy part of winding *A* and the stator windings *B* and *C*, $L_{AfB}=L_{BAf}$ and $L_{AfC}=L_{CAf}$ are the mutual inductances between the faulty part of winding *A* and the stator windings *B* and *C*, $L_{AhAf}=L_{AfAh}$ are the mutual inductances between the healthy and faulty parts of winding *A*, L_{Aha}, L_{Ahb} and L_{Ahc} are the mutual inductances between the healthy part of winding *A* and the rotor windings, and L_{Afa}, L_{Afb} and L_{Afc} are the mutual inductances between the faulty part of winding *A* and the rotor windings.

To introduce the ITSC fault in the rotor winding *a*, (4.37), (4.39), (4.43), (4.46) and (4.47) are modified as

$$\left[U_r\right]=\left[u_a \quad u_b \quad u_c \quad 0\right]^T \tag{4.54}$$

$$\left[I_r\right]=\left[i_a \quad i_b \quad i_c \quad i_{af}\right]^T \tag{4.55}$$

$$\left[R_r\right]=\begin{bmatrix} R_{ah}+R_{sc} & 0 & 0 & -R_{sc} \\ 0 & R_b & 0 & 0 \\ 0 & 0 & R_c & 0 \\ -R_{sc} & 0 & 0 & R_{af}+R_{sc} \end{bmatrix} \tag{4.56}$$

$$\left[L_{rr}\right]=\begin{bmatrix} L_{ahah} & L_{ahb} & L_{ahc} & L_{ahaf} \\ L_{bah} & L_{bb} & L_{bc} & L_{baf} \\ L_{cah} & L_{cb} & L_{cc} & L_{caf} \\ L_{afah} & L_{afb} & L_{afc} & L_{afaf} \end{bmatrix} \tag{4.57}$$

$$\left[L_{sr}\right]=\left[L_{rs}\right]^T=\begin{bmatrix} L_{Aah} & L_{Ab} & L_{Ac} & L_{Aaf} \\ L_{Bah} & L_{Bb} & L_{Bc} & L_{Baf} \\ L_{Cah} & L_{Cb} & L_{Cc} & L_{Caf} \end{bmatrix}, \tag{4.58}$$

where L_{ahah} and L_{afaf} are the self-inductances of the healthy and faulty parts of rotor winding *a*, $L_{ahb}=L_{bah}$ and $L_{ahc}=L_{cah}$ are the mutual inductances between the healthy part of winding *a* and the rotor windings *b* and *c*, $L_{afb}=L_{baf}$ and $L_{afc}=L_{caf}$ are the mutual inductances between the faulty part of winding *a* and the rotor windings *b* and *c*, $L_{ahaf}=L_{afah}$ are the mutual inductances between the healthy and faulty parts of winding *a*, L_{Aah}, L_{Bah} and L_{Cah} are the mutual inductances between the healthy part of winding *a* and the stator windings, and L_{Aaf}, L_{Baf} and L_{Caf} are the mutual inductances between the faulty part of winding *a* and the stator windings.

To introduce simultaneous ITSC faults in the stator winding *A* and the rotor winding *a*, (4.36), (4.38), (4.42) and (4.45) are modified as (4.49)-(4.52); (4.37), (4.39), (4.43) and (4.46) are modified as (4.54)-(4.57); and (4.47) is modified as

$$\left[L_{sr}\right]=\left[L_{rs}\right]^T=\begin{bmatrix} L_{Ahah} & L_{Ahb} & L_{Ahc} & L_{Ahaf} \\ L_{Bah} & L_{Bb} & L_{Bc} & L_{Baf} \\ L_{Cah} & L_{Cb} & L_{Cc} & L_{Caf} \\ L_{Afah} & L_{Afb} & L_{Afc} & L_{Afaf} \end{bmatrix}, \tag{4.59}$$

where L_{Ahah} is the mutual inductance between the healthy part of stator winding *A* and the healthy part of rotor winding *a*, L_{Afaf} is the mutual inductance between the faulty part of stator winding *A* and the faulty part of rotor winding *a*, L_{Ahaf} is the mutual inductance between the healthy part of stator winding *A* and the faulty part of rotor winding *a* and L_{Afah} is the mutual inductance between the faulty part of stator winding *A* and the healthy part of rotor winding *a*.

The second term on the second hand of (4.48) is equivalent to

$$\frac{d}{dt}\left(\left[\begin{array}{c|c}[L_{ss}] & [L_{sr}]\\ \hline [L_{rs}] & [L_{rr}]\end{array}\right]\left[\begin{array}{c}[I_s]\\ \hline [I_r]\end{array}\right]\right)=\frac{d}{dt}\left(\left[\begin{array}{c|c}[L_{ss}] & [L_{sr}]\\ \hline [L_{rs}] & [L_{rr}]\end{array}\right]\right)\left[\begin{array}{c}[I_s]\\ \hline [I_r]\end{array}\right]+\left[\begin{array}{c|c}[L_{ss}] & [L_{sr}]\\ \hline [L_{rs}] & [L_{rr}]\end{array}\right]\frac{d}{dt}\left(\left[\begin{array}{c}[I_s]\\ \hline [I_r]\end{array}\right]\right). \quad (4.60)$$

Replacing (4.60) in (4.48) leads to

$$\left[\begin{array}{c}[U_s]\\ \hline [U_r]\end{array}\right]=\left(\left[\begin{array}{c|c}[R_s] & [0]\\ \hline [0] & [R_r]\end{array}\right]+\frac{d}{dt}\left(\left[\begin{array}{c|c}[L_{ss}] & [L_{sr}]\\ \hline [L_{rs}] & [L_{rr}]\end{array}\right]\right)\right)\left[\begin{array}{c}[I_s]\\ \hline [I_r]\end{array}\right]+\left[\begin{array}{c|c}[L_{ss}] & [L_{sr}]\\ \hline [L_{rs}] & [L_{rr}]\end{array}\right]\frac{d}{dt}\left(\left[\begin{array}{c}[I_s]\\ \hline [I_r]\end{array}\right]\right). \quad (4.61)$$

The electromagnetic torque of the machine is calculated by [109]

$$T_{em}=\frac{1}{2}\left[\begin{array}{c}[I_s]\\ \hline [I_r]\end{array}\right]^T\frac{\partial}{\partial\theta}\left(\left[\begin{array}{c|c}[L_{ss}] & [L_{sr}]\\ \hline [L_{rs}] & [L_{rr}]\end{array}\right]\right)\left[\begin{array}{c}[I_s]\\ \hline [I_r]\end{array}\right]. \quad (4.62)$$

The mechanical equation of the system is given by

$$T_{em}-T_L=J_m\frac{d\Omega_m}{dt}+B_m\Omega_m, \quad (4.63)$$

where T_L is the load torque, J_m is the moment of inertia of the rotating parts of the machine, B_m is the viscous friction coefficient and Ω_m is the mechanical angular speed, given by

$$\Omega_m=\frac{d\theta}{dt}. \quad (4.64)$$

Combining the voltage equations presented in (4.61) with the mechanical equations presented in (4.63) and (4.64), the final set of equations of the machine model is given by

$$[A] = ([B] + [C])[X] + [D]\frac{d}{dt}[X], \tag{4.65}$$

where

$$[X] = \left[[I_s] \;\vdots\; [I_r] \;\vdots\; \Omega_m \;\vdots\; \theta \right]^T \tag{4.66}$$

$$[A] = \left[[U_s] \;\vdots\; [U_r] \;\vdots\; 0 \;\vdots\; T_{em} - T_L \right]^T \tag{4.67}$$

$$[B] = \left[\begin{array}{c:c:c} [R_s] & [0] & [0] \\ \hdashline [0] & [R_r] & [0] \\ \hdashline [0] & [0] & \begin{bmatrix} -1 & 0 \\ B_m & 0 \end{bmatrix} \end{array}\right] \tag{4.68}$$

$$[C] = \frac{d}{dt}\left[\begin{array}{c:c:c} [L_{ss}] & [L_{sr}] & [0] \\ \hdashline [L_{rs}] & [L_{rr}] & [0] \\ \hdashline [0] & [0] & \begin{bmatrix} 0 & 0 \\ 0 & 0 \end{bmatrix} \end{array}\right] \tag{4.69}$$

$$[D] = \left[\begin{array}{c:c:c} [L_{ss}] & [L_{sr}] & [0] \\ \hdashline [L_{rs}] & [L_{rr}] & [0] \\ \hdashline [0] & [0] & \begin{bmatrix} 0 & 1 \\ J_m & 0 \end{bmatrix} \end{array}\right]. \tag{4.70}$$

The equation (4.65) is implemented in the Matlab/Simulink environment using an *S*-function block. The block diagram of the developed model of the WRIM is schematically represented in Fig. 4.18. As observed in this figure, the inputs of the *S*-function block are the stator and rotor voltages, the difference value between T_{em} and T_L, and the time derivative of the inductances. The

outputs of the *S*-function block consist of electrical quantities (stator and rotor currents) and mechanical quantities (position and mechanical speed of the rotor).

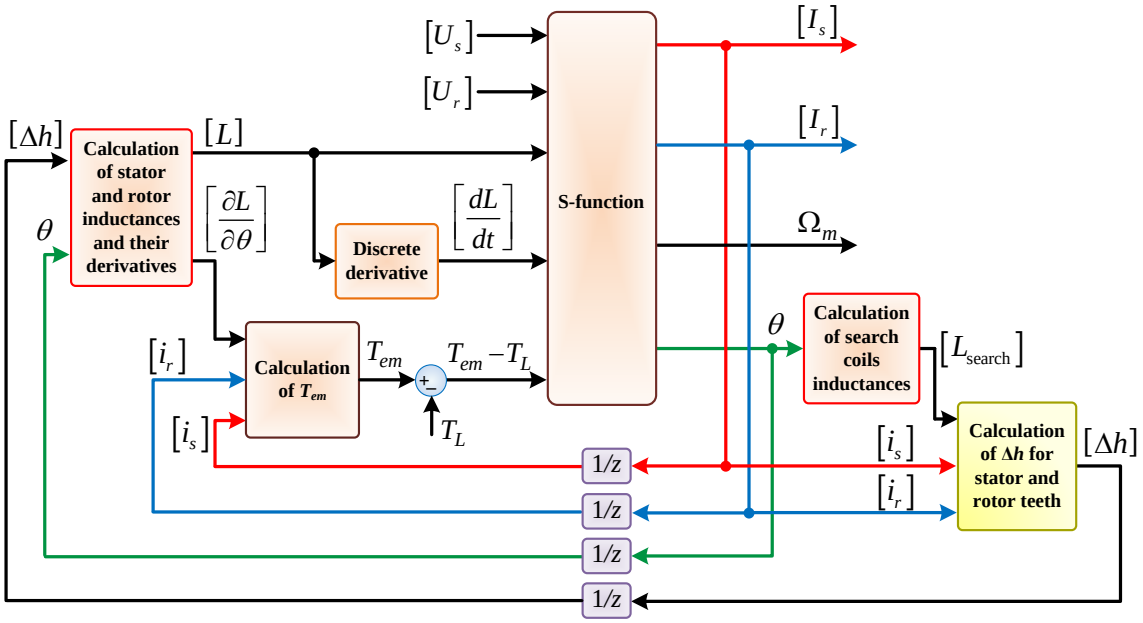

Fig. 4.18. Block diagram of the developed model of WRIM.

4.4 Model validation

To experimentally validate the developed model of the WRIM, an experimental test rig was prepared. In this test rig, a WRIM, with the specifications given in Appendix *C*, is mechanically coupled to a 7.5 kW three-phase IM drive as the mechanical load. Both the stator and rotor windings of the WRIM are star-connected with an isolated neutral point. The stator windings are connected to the grid, while the rotor windings are short-circuited. To compare the results obtained with the simulation model of the WRIM with the experimental ones, the stator and rotor currents, the short-circuit current, the grid voltages and the rotor speed were measured by the sensors mounted in the test rig.

Before presenting the results, the harmonic components in the stator and rotor currents and electromagnetic torque of the machine are analyzed. Then, the results obtained by the experimental tests along with the simulation results for both healthy and faulty conditions of the WRIM are presented.

4.4.1 Harmonic analysis

For the healthy operation of the WRIM, considering the grid voltage harmonics, the expected frequency components in the stator currents are given by [110]

$$f_{s.c}^{i,k} = |i \pm 6k(1-s)|\, f_s, \tag{4.71}$$

where f_s is the fundamental supply frequency, s is rotor slip, i=1, 2, 3,… is the order of the grid supply induced current harmonic components, and k=0, 1, 2, 3...

The expected frequency components in the electromagnetic torque are given by [110]

$$f_{\text{torque}}^{\vartheta,i,k} = |[\vartheta \pm i \pm 6k(1-s)]|\, f_s, \tag{4.72}$$

where ϑ is the supply harmonic order.

According to the simulation and experimental results obtained for different operating conditions of the WRIM, which will be presented in the next subsections, the magnetic saturation gives rise to some new components in the stator current at frequencies given by

$$f_{s.c}^{sat} = (1 \pm 6s)\, f_s. \tag{4.73}$$

These frequencies can also be obtained by considering i=5, k=1 and i=7, k=1 in (4.71) which confirms that the origin of these components is also related with the 5th and 7th grid voltage harmonics. However, if these grid voltage harmonics were not included in the simulation model of the WRIM, these components still found in the stator currents. When these grid voltage harmonics were not included in the model and magnetic saturation was not included as well, these components did not appear in the spectra of the stator currents. Therefore, these simulation tests confirm that the dominant origin of these current harmonics is the interaction between supply harmonics and magnetic saturation. However, the theory behind such analysis is still unknown and beyond the main scope of this work.

The magnetic saturation gives rise to the appearance of some components in the rotor currents at frequencies of

$$f_{r.c}^{sat} = ksf_s, \quad k = 5,\ 7,\ 11. \tag{4.74}$$

Finally, the frequency of the dominant component related to the magnetic saturation in the electromagnetic torque is given by

$$f_{\text{torque}}^{sat} = 6sf_s. \tag{4.75}$$

Besides, ITSC faults (or any electrical asymmetry) in the stator and rotor windings of WRIMs induce a series of harmonic components in the stator currents, rotor currents, and electromagnetic torque. The frequency of the components produced in the stator currents, rotor currents, and electromagnetic torque due to stator ITSC faults are given by (4.76), (4.77) and (4.78), respectively [111].

$$f_{s.c}^{sf} = \pm kf_s, \quad k = 1, 3, 5, ... \tag{4.76}$$

$$f_{r.c}^{sf} = (2k \pm s) f_s, \quad k = 1, 2, 3, ... \tag{4.77}$$

$$f_{\text{torque}}^{sf} = 2kf_s, \quad k = 1, 2, 3, ... \tag{4.78}$$

The frequency of the components produced in the stator currents, rotor currents, and electromagnetic torque due to rotor ITSC faults are given by (4.79), (4.80) and (4.81), respectively [111].

$$f_{s.c}^{rf} = (1 \pm 2ks) f_s, \quad k = 1, 2, 3, ... \tag{4.79}$$

$$f_{r.c}^{rf} = \pm ksf_s, \quad k = 1, 3, 5, ... \tag{4.80}$$

$$f_{\text{torque}}^{rf} = 2ksf_s, \quad k = 1, 2, 3, ... \tag{4.81}$$

4.4.2 Healthy conditions

The simulation and experimental results concerning the operation of the WRIM in healthy conditions and for three levels of the mechanical load are presented in this subsection. Fig. 4.19 shows the waveforms and spectrum of the grid voltages in the experimental tests. The amplitudes of the fundamental component, the 5^{th} and 7^{th} harmonics of the grid voltages were 347 V, 4.8 V and 4.7 V, respectively.

Due to the influence of the grid voltage harmonics on the spectra of currents [110], the 5th and 7th harmonics were also considered in the simulation model.

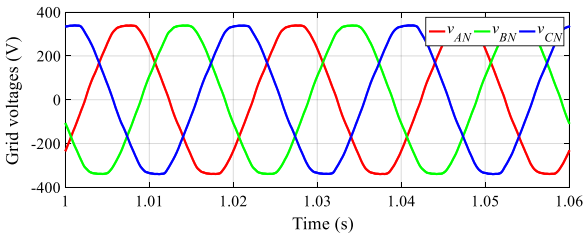

(a) Time waveforms

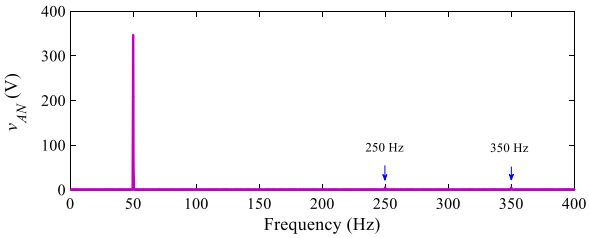

(b) Spectrum

Fig. 4.19. Grid voltages in the experimental tests.

The simulation and the experimental results for the operation of the WRIM in healthy conditions, when the stator is supplied with the rated voltage and the WRIM running at no-load, are presented in Fig. 4.20 and Fig. 4.21, respectively. As shown in Fig. 4.20(a), Fig. 4.20(b), Fig. 4.21(a) and Fig. 4.21(b), the stator and rotor currents are distorted. The main reason for the distortion of the stator and rotor currents is the structure of the WRIM under study that has non-skewed open slots in both stator and rotor sides. This leads to a severe non-uniform path for the air-gap flux which generates the currents distortions [41]. As seen in these figures, the stator and rotor currents waveforms are balanced and the amplitude and period of the stator and rotor currents obtained with the simulation model are identical to the experimental results.

As presented in Fig. 4.20(c) and Fig. 4.21(c), the rotor speed at no-load is 1490 rpm, which corresponds to a rotor slip of s=0.006. The waveform of the machine electromagnetic torque from simulation model (obtained by (4.62)) is shown in Fig. 4.20(d). The reason for the torque oscillations is by the non-skewed open slots in both stator and rotor sides of the WRIM under study, in addition to the big space harmonics generated by the stator and rotor windings.

It is worthy to mention that the fundamental values of the stator and rotor currents for this operating conditions of WRIM are listed in Table 4.1, at the end of this subsection.

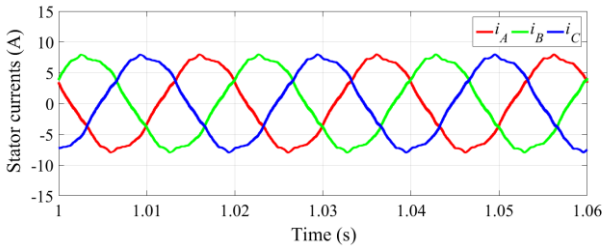

(a) Stator currents waveforms

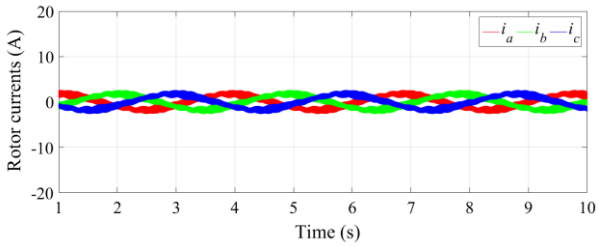

(b) Rotor currents waveforms

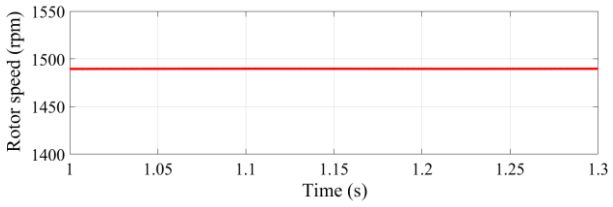

(c) Rotor speed waveform

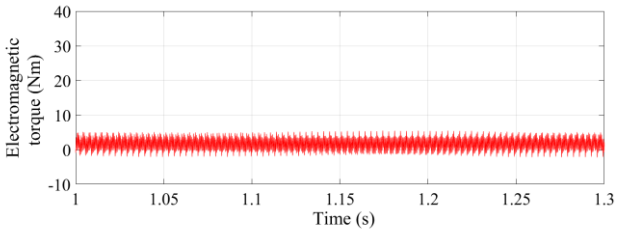

(d) Electromagnetic torque waveform

Fig. 4.20. Simulation results for the healthy operation of the WRIM at no-load condition.

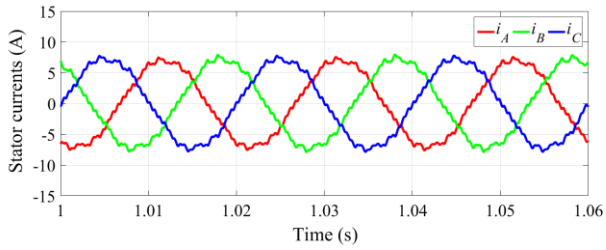

(a) Stator currents waveforms

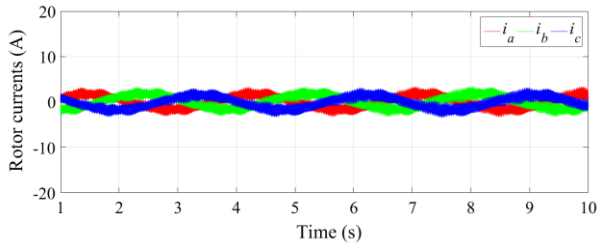

(b) Rotor currents waveforms

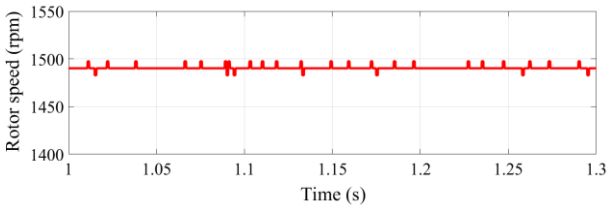

(c) Rotor speed waveform

Fig. 4.21. Experimental results for the healthy operation of the WRIM at no-load condition.

A zoom of the spectra for the operation of the WRIM in healthy conditions and running at no-load is presented in Fig. 4.22 and Fig. 4.23. From now on, all components related to faults are labeled with arrows in red color in the spectra, while all other components are indicated in blue. According to (4.71), the components at frequencies of 250 Hz (i=5, k=0) and 350 Hz (i=7, k=0) are observed in the stator current spectra presented in Fig. 4.22(a) and Fig. 4.23(a). The amplitudes of these components in the stator currents obtained with the simulation model are in good agreement with the experimental results.

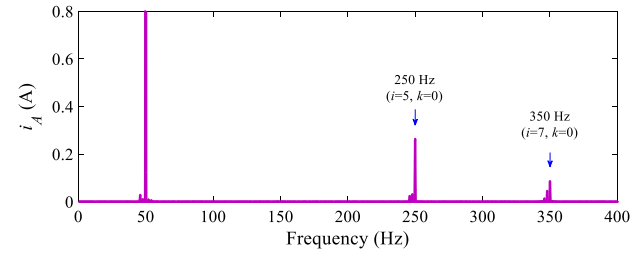

(a) Spectrum of the stator current i_A

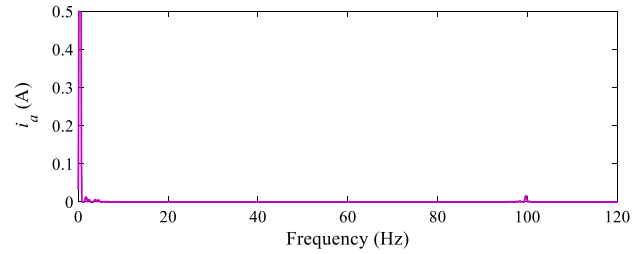

(b) Spectrum of the rotor current i_a

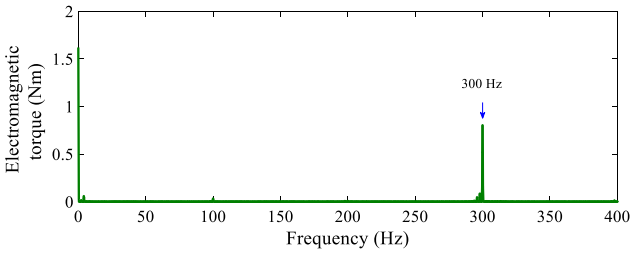

(c) Spectrum of the electromagnetic torque

Fig. 4.22. Simulation spectra for the healthy operation of the WRIM at no-load condition.

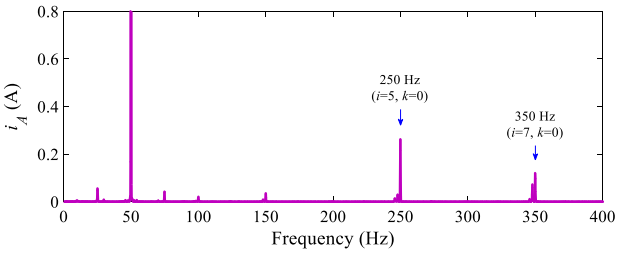

(a) Spectrum of the stator current i_A

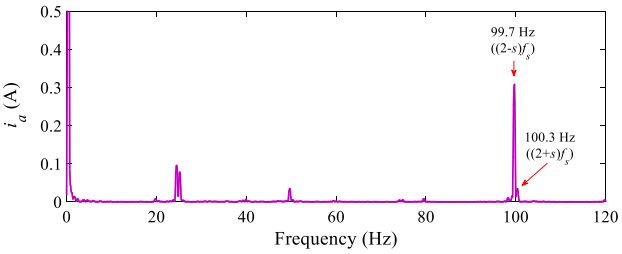

(b) Spectrum of the rotor current i_a

Fig. 4.23. Experimental spectra for the healthy operation of the WRIM at no-load condition.

Due to the addition of the extra taps in the stator and rotor windings, there is a small degree of inherent electrical unbalance in the stator and rotor of the WRIM which it is not considered in the simulation model. Therefore, unlike the simulation result presented in Fig. 4.22(b), two components related to the stator fault at frequencies of 99.7 Hz $((2-s)f_s)$ and 100.3 Hz $((2+s)f_s)$ are observed in the experimental rotor current spectrum, presented in Fig. 4.23(b).

The spectrum of the electromagnetic torque is presented in Fig. 4.22(c), where the component at a frequency of 300 Hz [(ϑ=5, i=1, k=0) and (ϑ=7, i=1, k=0)] is labeled.

The simulation and experimental spectra for the healthy operating of the WRIM at half-load (13.5 Nm) are presented in Fig. 4.24 and Fig. 4.25, respectively. For this operating condition of the WRIM, the rotor speed is 1457 rpm that leads to a rotor slip of s=0.029. According to (4.71),

the components at frequencies of 250 Hz (i=5, k=0), 350 Hz (i=7, k=0), 242 Hz and 342 Hz (i=1, k=1) are observed in the stator current spectra presented in Fig. 4.24(a) and Fig. 4.25(a). The amplitude of the components at frequencies of 250 Hz and 350 Hz are almost identical in the simulation and experimental results while the amplitude of the components at frequencies of 242 Hz and 342 Hz in the experimental results are larger than in the simulation results. According to (4.73), the components related to the magnetic saturation at frequencies of 41.5 Hz $((1-6s)f_s)$ and 58.5 Hz $((1+6s)f_s)$ are also labeled in these figures.

In Fig. 4.24(a), the components related to the faults do not appear in the stator current spectrum, which is revealing the fact that the WRIM has no faults. However, as shown in Fig. 4.25(a), due to the inherent electrical unbalance of the WRIM, the components related to rotor fault, at frequencies of 47.2 Hz and 52.8 Hz, exist in the stator current spectrum obtained in the experimental test.

The components related to the magnetic saturation in the rotor currents spectra (7.2 Hz, 10 Hz and 15.8 Hz) are labeled in Fig. 4.24(b) and Fig. 4.25(b). As shown in Fig. 4.25(b), due to the inherent electrical unbalance of the WRIM, the components related to the stator fault, at frequencies of 98.6 Hz and 101.4 Hz (referring to (4.77)), and the component related to the rotor fault, at a frequency of 4.3 Hz (referring to (4.80)), are not zero.

The spectrum of the electromagnetic torque is presented in Fig. 4.21(c). As shown in this figure, two components at frequencies of 292 Hz (ϑ=1, i=1, k=1) and 300 Hz [(ϑ=5, i=1, k=0) and (ϑ=7, i=1, k=0)] - referring to (4.72) - and the component related to the magnetic saturation at a frequency of 8.4 Hz - referring to (4.75) - are labeled.

The simulation and experimental results for the healthy operating of the WRIM at full-load (27 Nm) are presented in Fig. 4.26 and Fig. 4.27, respectively. As seen in these figures, the stator and rotor currents waveforms are balanced. Moreover, the amplitude and the period of the stator and rotor currents obtained with the simulation model are in good agreement with the experimental results.

As presented in Fig. 4.26(c) and Fig. 4.27(c), the rotor speed at full-load condition is 1428 rpm, which corresponds to a rotor slip of s=0.048. The waveform of the electromagnetic torque obtained with the simulation model is shown in Fig. 4.26(d).

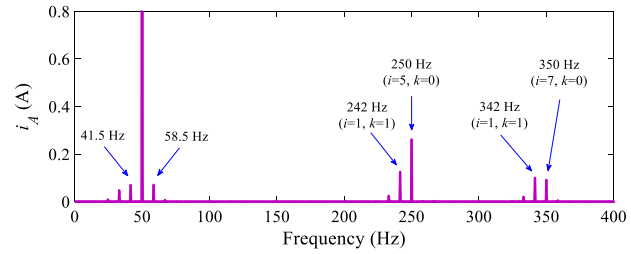

(a) Spectrum of the stator current i_A

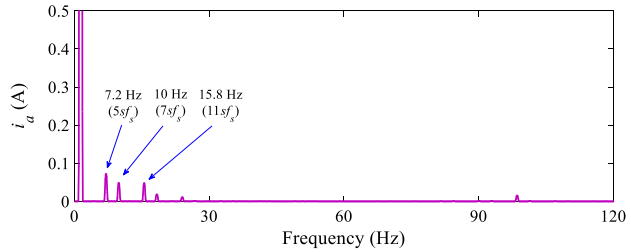

(b) Spectrum of the rotor current i_a

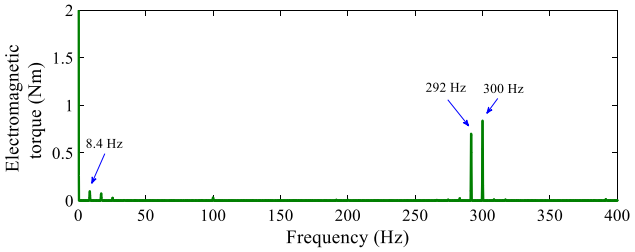

(c) Spectrum of the electromagnetic torque

Fig. 4.24. Simulation spectra for the healthy operation of the WRIM at half-load condition.

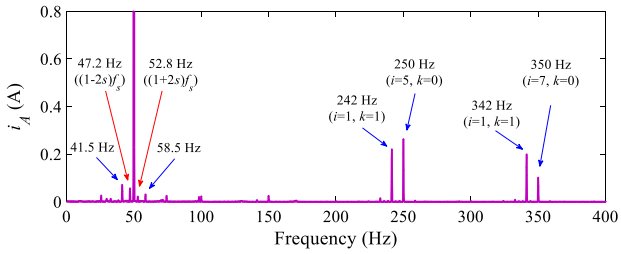

(a) Spectrum of the stator current i_A

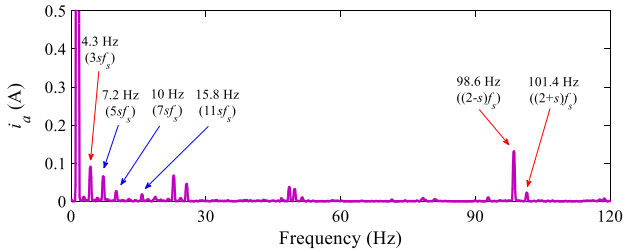

(b) Spectrum of the rotor current i_a

Fig. 4.25. Experimental spectra for the healthy operation of the WRIM at half-load condition.

The simulation and experimental spectra under these circumstances are presented in Fig. 4.28 and Fig. 4.29, respectively. Fig. 4.28(a) and Fig. 4.29(a) show the stator current spectra. According to (4.71), the components at frequencies of 250 Hz (i=5, k=0), 350 Hz (i=7, k=0), 236 Hz and 336 Hz (i=1, k=1) are labeled in the stator current spectrum presented in Fig. 4.28(a) and Fig. 4.29(a). According to (4.73), the components related to the magnetic saturation at frequencies of 35.5 Hz $((1-6s)f_s)$ and 64.5 Hz $((1+6s)f_s)$ are also labeled in these figures. As shown in Fig. 4.29(a), due to the inherent electrical unbalance of the WRIM, the components related to the rotor fault at frequencies of 45.1 Hz $((1-2s)f_s)$ and 54.9 Hz $((1+2s)f_s)$ exist in the stator current spectrum obtained in the experimental test.

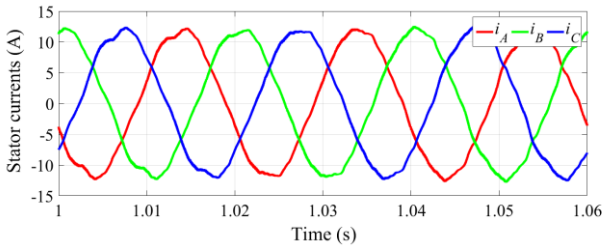

(a) Stator currents waveforms

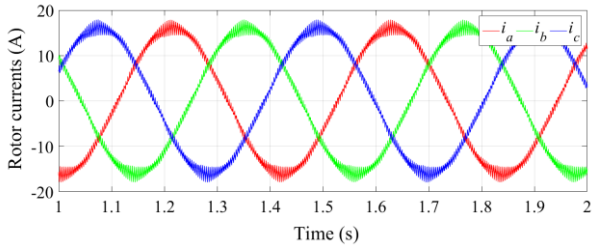

(b) Rotor currents waveforms

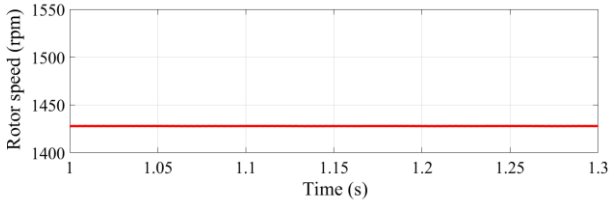

(c) Rotor speed waveform

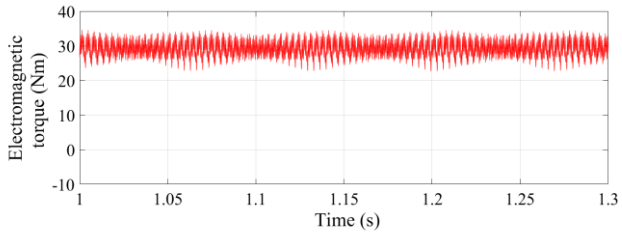

(d) Electromagnetic torque waveform

Fig. 4.26. Simulation results for the healthy operation of the WRIM at full-load condition.

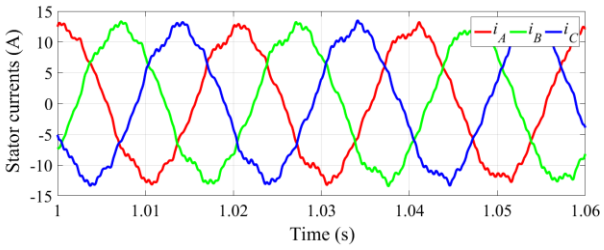

(a) Stator currents waveforms

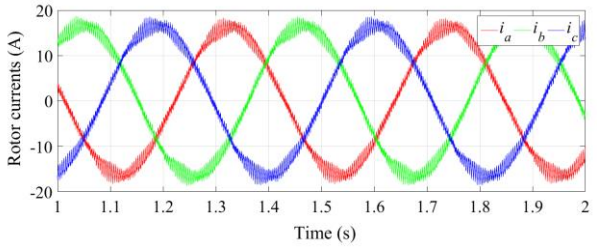

(b) Rotor currents waveforms

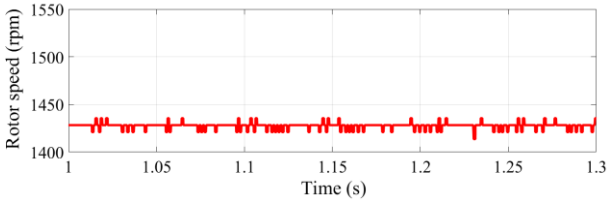

(c) Rotor speed waveform

Fig. 4.27. Experimental results for the healthy operation of the WRIM at full-load condition.

The components related to the magnetic saturation in the rotor currents spectra (12 Hz, 16.8 Hz and 26.2 Hz) are labeled in Fig. 4.28(b) and Fig. 4.29(b). Due to the inherent electrical unbalance of the WRIM, the components related to the stator fault (97.6 Hz and 102.4 Hz) and the component related to the rotor fault (7.2 Hz) exist in the rotor current (see Fig. 4.29(b)).

The spectrum of the electromagnetic torque is presented in Fig. 4.28(c). Referring to (4.72), two components at frequencies of 286 Hz (ϑ=1, i=1, k=1) and 300 Hz [(ϑ=5, i=1, k=0) and (ϑ=7, i=1, k=0)] are labeled in this figure. The component related to the magnetic saturation at a frequency of 14.5 Hz ($6sf_s$) is also labeled in this figure.

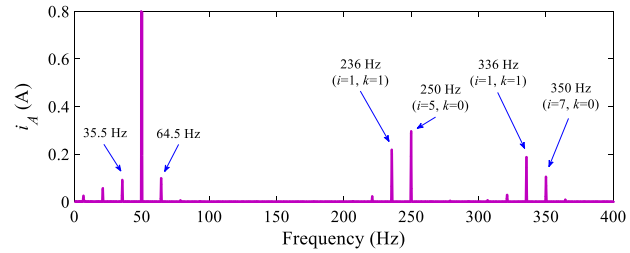

(a) Spectrum of the stator current i_A

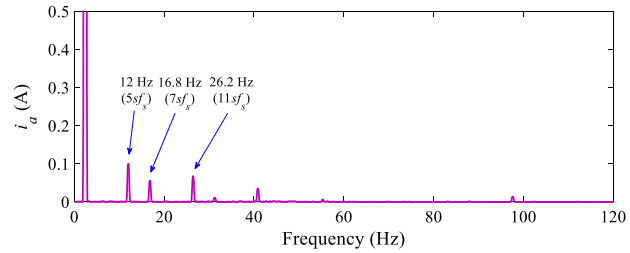

(b) Spectrum of the rotor current i_a

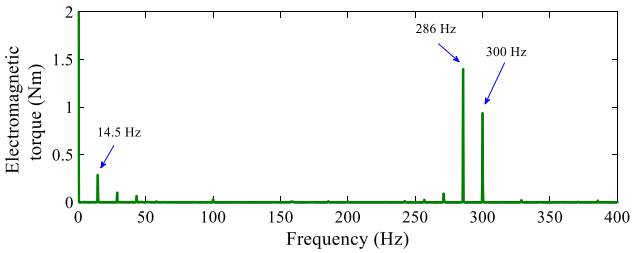

(c) Spectrum of the electromagnetic torque

Fig. 4.28. Simulation spectra for the healthy operation of the WRIM at full-load condition.

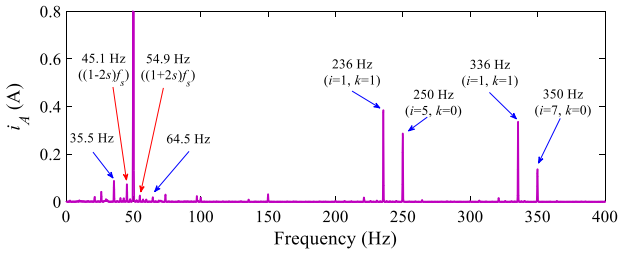

(a) Spectrum of the stator current i_A

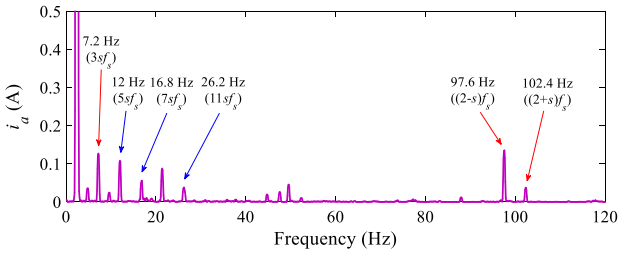

(b) Spectrum of the rotor current i_a

Fig. 4.29. Experimental spectra for the healthy operation of the WRIM at full-load condition.

For a complete comparison of the simulation and experimental results, the amplitude of the fundamental component of the stator and rotor currents under the three operating conditions of the WRIM are listed in Table 4.1. The simulation and experimental results are similar, demonstrating the good agreement between the simulation and experimental results.

Table 4.1. Comparison of the amplitude of the fundamental component of the currents obtained with the simulation model and by the experimental tests.

		No-load	Half-load	Full-load
i_s (A)	Simulation	7.2	9	12.1
	Experimental	7.1	9.1	12.3
i_r (A)	Simulation	1.8	9.5	16.2
	Experimental	1.7	9.6	16.2

4.4.3 Faulty conditions

4.4.3.1 Stator fault

According to Fig. 4.15, 15 turns out of 180 turns of the stator phase *A* are short-circuited. To avoid any damage to the windings, the short-circuit current (i_{sc}) is limited by a resistor R_{sc}=1.1 Ω. The simulation and experimental results under this faulty operating condition of the WRIM at full-load are presented in Fig. 4.30 and Fig. 4.31, respectively. As seen in Fig. 4.30(a) and Fig. 4.31(a), due to the fault in the stator winding of phase *A*, the stator currents are slightly unbalanced. In this case, the faulty phase *A* has a maximum current followed by the currents in phases *B* and *C*.

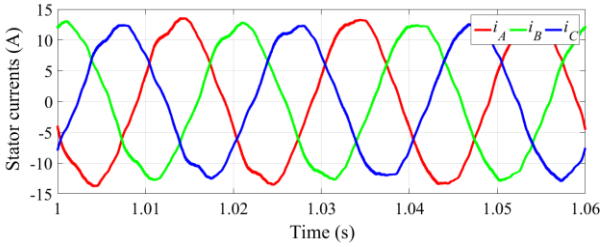

(a) Stator currents waveforms

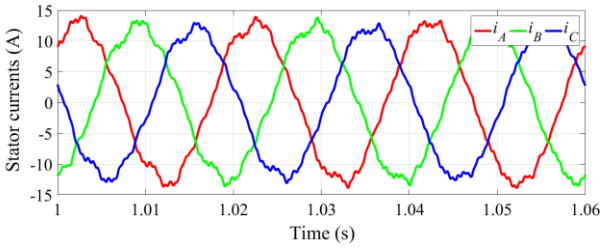

(a) Stator currents waveforms

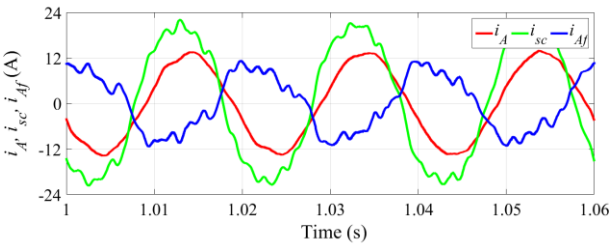

(b) Currents waveforms in the faulty winding

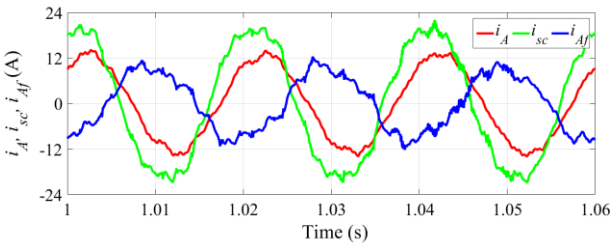

(b) Currents waveforms in the faulty winding

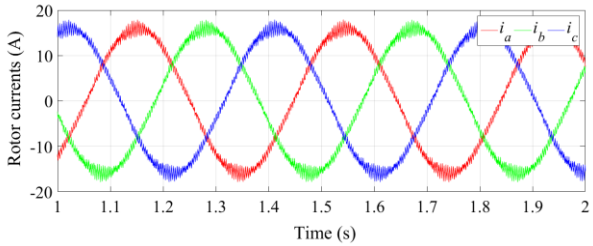

(c) Rotor currents waveforms

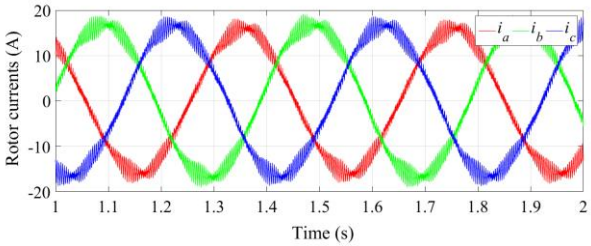

(c) Rotor currents waveforms

Fig. 4.30. Simulation results for the operation of the WRIM at full-load and with 15 turns short-circuited in phase *A* of the stator windings.

Fig. 4.31. Experimental results of the operation of the WRIM at full-load and with 15 turns short-circuited in phase *A* of the stator windings.

The time waveforms of the current in stator phase A (i_A) along with the short-circuit current (i_{sc}) and the current of the faulty turns are presented in Fig. 4.30(b) and Fig. 4.31(b). As seen in these figures, the amplitude of i_{sc} and i_{Af} as well as the phase shift between i_A, i_{sc} and i_{Af} obtained with the simulation model are identical to the experimental results.

As seen in in Fig. 4.30(c) and Fig. 4.31(c) (i_{Af}), in the presence of the stator fault, the rotor currents waveforms are still balanced.

The simulation and experimental spectra under these circumstances are presented in Fig. 4.32 and Fig. 4.33, respectively. Referring to (4.71) and for s=0.048, the components at frequencies of 250 Hz (i=5, k=0), 350 Hz (i=7, k=0), 236 Hz and 336 Hz (i=1, k=1) are labeled in the stator current spectra presented in Fig. 4.32(a) and Fig. 4.33(a). The components related to the magnetic saturation at frequencies of 35.5 Hz $((1-6s)f_s)$ and 64.5 Hz $((1+6s)f_s)$ are also labeled in these figures. Referring to (4.76), the presence of the stator fault gives rise to the component at the frequency of 150 Hz (k=3) in the stator currents, as labeled in Fig. 4.32(a) and Fig. 4.33(a).

The spectra of the rotor current are presented in Fig. 4.32(b) and Fig. 4.33(b). The components related to the magnetic saturation in the rotor currents spectra (12.8 Hz, 17.9 Hz and 28 Hz) are labeled in these figures. According to (4.77), the presence of the stator fault gives rise to two components at frequencies of 97.5 Hz and 102.5 Hz (k=1) in the rotor current. Due to the inherent electrical unbalance of the WRIM, the amplitude of these components in the experimental result is larger than in simulation.

The spectrum of the electromagnetic torque is presented in Fig. 4.32(c). Referring to (4.72), two components at frequencies of 285 Hz (ϑ=1, i=1, k=1) and 300 Hz [(i=5, ϑ=1, k=0) and (i=7, ϑ=1, k=0)] are labeled in this figure. The component related to the magnetic saturation at a frequency of 14.5 Hz $(6sf_s)$ is also labeled in this figure. Referring to (4.78), the presence of the stator fault gives rise to two components at frequencies of 100 Hz (k=1) and 200 Hz (k=2) in the electromagnetic torque.

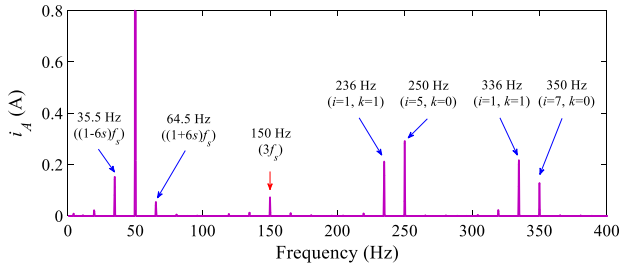

(a) Spectrum of the stator current i_A

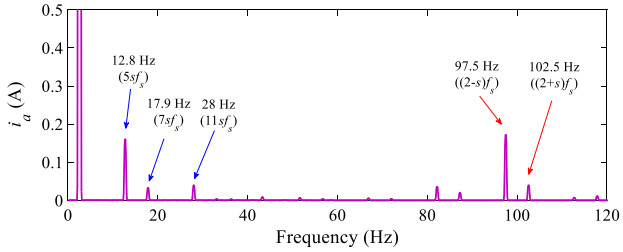

(b) Spectrum of the rotor current i_a

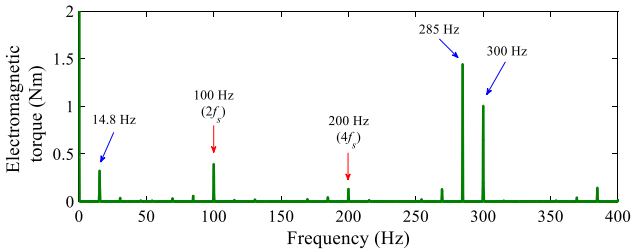

(c) Spectrum of the electromagnetic torque

Fig. 4.32. Simulation spectra for the operation of the WRIM at full-load condition and with 15 turns short-circuited in phase A of the stator windings.

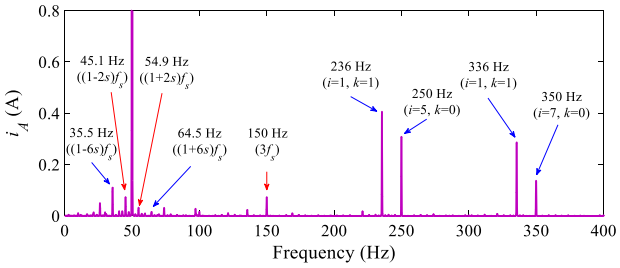

(a) Spectrum of the stator current i_A

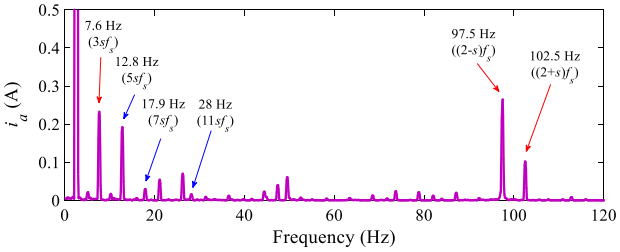

(b) Spectrum of the rotor current i_a

Fig. 4.33. Experimental spectra for the operation of the WRIM at full-load condition and with 15 turns short-circuited in phase A of the stator windings.

4.4.3.2 Rotor fault

According to Fig. 4.34, 17 turns out of 108 turns of the rotor phase *a* are short-circuited where $R_{sc} = 0.1\,\Omega$ is the total resistance of the slip ring, brushes and current sensor involved in the short-circuit loop.

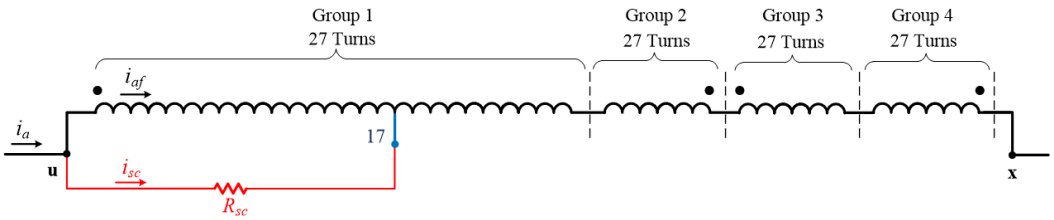

Fig. 4.34. Schematic representation of an ITSC fault in phase a of the rotor windings.

Fig. 4.35 and Fig. 4.36 show the simulation and experimental results for the operation of the WRIM at rated load with 17 turns short-circuited in the rotor phase *a*. As shown in these figures, the impact of the rotor ITSC fault upon the stator and rotor currents is not significant. Fig. 4.35(c) and Fig. 4.36(c) show the time waveforms of the rotor phase *a* current (i_a) along with i_{sc} and i_{af} which show the current of the short-circuited turns has no significant difference compared the rotor phase current.

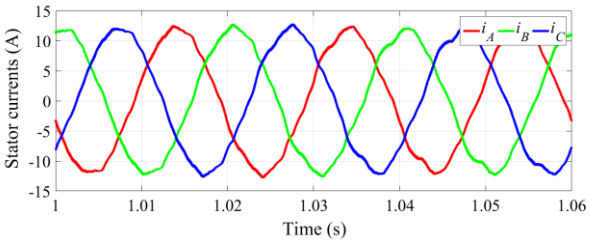

(a) Stator currents waveforms

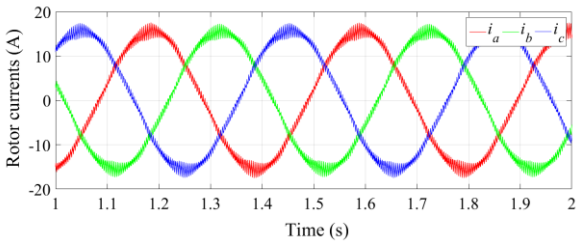

(b) Rotor currents waveforms

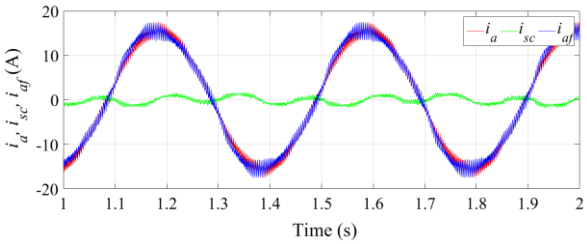

(c) Currents waveforms of the faulty winding

Fig. 4.35. Simulation results for the operation of the WRIM at full-load and with 17 turns short-circuited in phase *a* of the rotor windings.

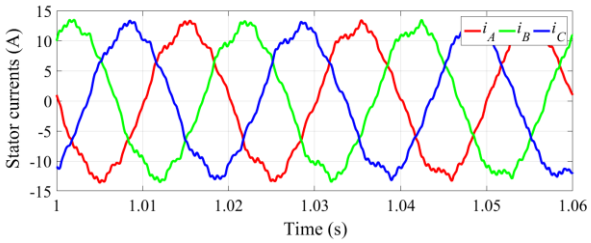

(a) Stator currents waveforms

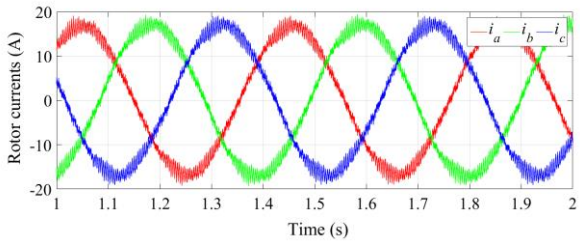

(b) Rotor currents waveforms

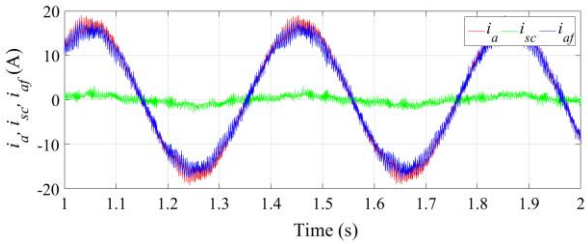

(c) Currents waveforms of the faulty winding

Fig. 4.36. Experimental results for the operation of the WRIM at full-load and with 17 turns short-circuited in phase *a* of the rotor windings.

This phenomenon is explained by the fact that the induced voltage in the rotor windings is proportional to the rotor slip. Therefore, since the value of the slip in induction motors is small, *e.g.* in the WRIM under study at full-load s=0.048, the induced voltage in the short-circuited turns of the rotor is small. This low voltage means a low short-circuit current [41]. Another factor that contributes for this situation is the fact that the three rotor phases are short-circuited at the rotor terminals of the WRIM. Hence, in the ideal conditions, the fault current would be zero. In practice, due to several phenomena, the short-circuit current is not null but very small. Fig. 4.37 and Fig. 4.38 show the spectra for this operating condition of the WRIM. The stator current spectra are presented in Fig. 4.37(a) and Fig. 4.38(a), where the components at frequencies of 250 Hz, 350 Hz, 236 Hz, 336 Hz, 35.5 Hz and 64.5 Hz are labeled. Referring to (4.79), the presence of the rotor fault gives rise to two components at frequencies of 45.1 Hz $((1-2s)f_s)$ and 54.9 Hz $((1+2s)f_s)$, as labeled in Fig. 4.37(a) and Fig. 4.38(a).

The simulation and experimental spectra of the rotor current are presented in Fig. 4.37(b) and Fig. 4.38(b), respectively. According to (4.77), the presence of the rotor fault gives rise to a component at a frequency of 7.5 Hz in the rotor current. Due to the inherent electrical unbalance of the WRIM, the amplitude of this component in the experimental result is larger than in the simulation result.

The spectrum of the electromagnetic torque obtained with the simulation model is presented in Fig. 4.37(c). Similarly to the healthy operating condition (see Fig. 4.28(c)), the components at frequencies of 285 Hz, 300 Hz and 14.5 Hz are labeled in this figure. Referring to (4.81), the presence of the rotor fault gives rise to a component at a frequency of 5 Hz in the electromagnetic torque.

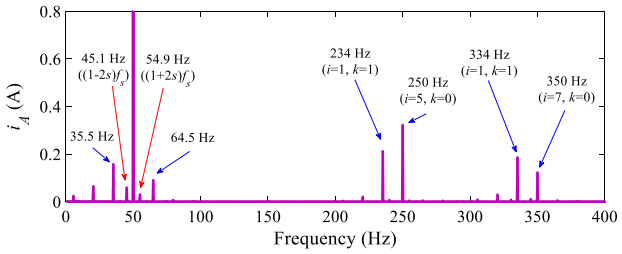

(a) Spectrum of the stator current i_A

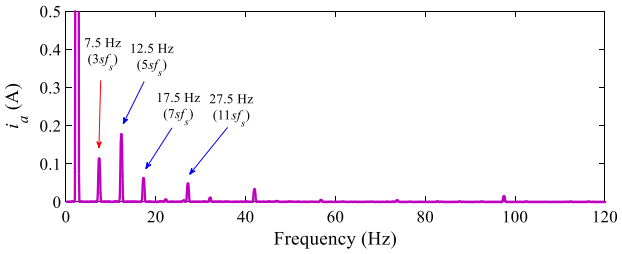

(b) Spectrum of the rotor current i_a

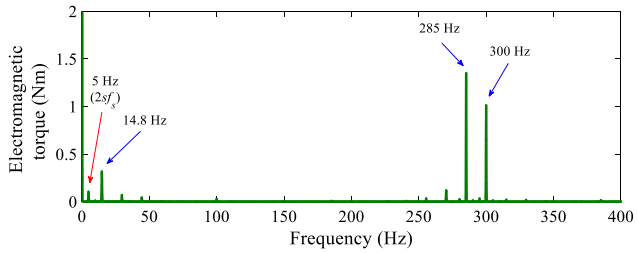

(c) Spectrum of the electromagnetic torque

Fig. 4.37. Simulation spectra for the operation of the WRIM at full-load condition and with 17 turns short-circuited in phase a of the rotor windings.

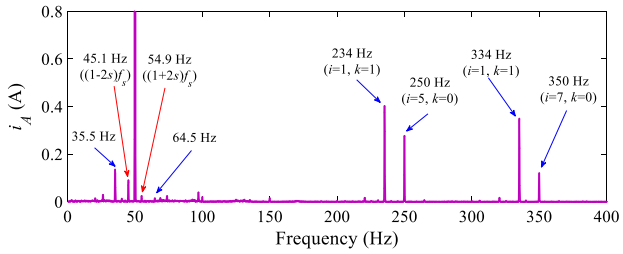

(a) Spectrum of the stator current i_A

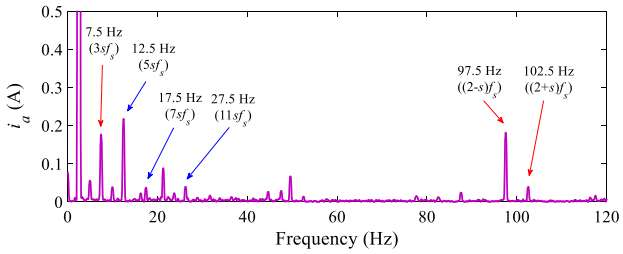

(b) Spectrum of the rotor current i_a

Fig. 4.38. Experimental spectra for the operation of the WRIM at full-load condition and with 17 turns short-circuited in phase a of the rotor windings.

Chapter 5

Doubly-fed induction generator

This chapter starts with the steady-state analysis of the doubly-fed induction generator (DFIG) system. Then, the space vector model of the DFIG system is outlined. Finally, the employed control strategy for the DFIG system is presented.

5.1 Steady-state analysis of the DFIG

The stator angular supply frequency is given by $\omega_s = 2\pi f_s$. The relation between the stator angular supply frequency and the rotor angular supply frequency (ω_r) is given by

$$\omega_r = \omega_s - \omega_m, \tag{5.1}$$

where ω_m is the electrical angular speed of the machine, which is given by

$$\omega_m = p\Omega_m, \tag{5.2}$$

where Ω_m and p are the mechanical angular speed of the machine and the number of pole-pairs, respectively.

The rotor slip is given by

$$s = \frac{\omega_s - \omega_m}{\omega_s}. \tag{5.3}$$

Replacing (5.3) into (5.1), the rotor angular frequency is given by

$$\omega_r = s\omega_s. \tag{5.4}$$

Three different operating regions for the DFIG can be defined:

- Subsynchronous operation $(\omega_m < \omega_s \Rightarrow s > 0)$
- Synchronous operation $(\omega_m = \omega_s \Rightarrow s = 0)$
- Supersynchronous operation $(\omega_m > \omega_s \Rightarrow s < 0)$

The active power balance of the DFIG is given by [84]

$$P_s + P_r = P_{mec} + P_{cu.s} + P_{cu.r}, \tag{5.5}$$

where P_s, P_r, P_{mec}, $P_{cu.s}$ and $P_{cu.r}$ are stator active power, rotor active power, mechanical power, stator copper losses and rotor copper losses, respectively.

The active power balance of the DFIG is schematically represented in Fig. 5.1 [84].

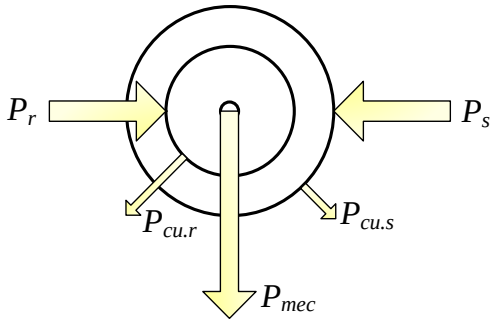

Fig. 5.1. Schematic representation of the DFIG active power balance.

The mechanical power is given by

$$P_{mec} = T_{em}\Omega_m = T_{em}\frac{\omega_m}{p}, \tag{5.6}$$

where T_{em} is electromagnetic torque developed by the DFIG.

The approximate relation between the stator and rotor powers (neglecting the stator and rotor copper power losses in the stator and rotor windings) is given by [84]

$$P_r \cong -sP_s. \tag{5.7}$$

Replacing (5.7) into (5.5) and neglecting the stator and rotor copper losses in the stator and rotor windings leads to

$$P_{mec} \cong P_s - sP_s = (1-s)P_s. \tag{5.8}$$

Table 5.1 presents the direction of the mechanical power, the stator active power and the rotor active power in the three different operating regions of the DFIG [84]. This table shows that at supersynchronous speeds, the DFIG delivers active power through the rotor while at subsynchronous speeds, the DFIG receives active power through the rotor.

In the real application of the wind turbine, the slip is confined to a range of ±30%. According to (5.7), this slip range indicates that the rated rotor active power exchange is ±30% of the rated stator active power.

Table 5.1. Different operating conditions of DFIG attending to the speed and powers.

Speed	Mechanical power	Stator active power	Rotor active power
$\omega_m > \omega_s$ (Supersynchronous)	$P_{mec} < 0$ (Machine receives mechanical power)	$P_s < 0$ (Machine delivers active power through the stator)	$P_r < 0$ (Machine delivers active power through the rotor)
$\omega_m = \omega_s$ (Synchronous)	$P_{mec} < 0$ (Machine receives mechanical power)	$P_s < 0$ (Machine delivers active power through the stator)	$P_r \cong 0$
$\omega_m < \omega_s$ (Subsynchronous)	$P_{mec} < 0$ (Machine receives mechanical power)	$P_s < 0$ (Machine delivers active power through the stator)	$P_r > 0$ (Machine receives active power through the rotor)

5.2 Space vector model of the DFIG

This subsection explains the model of the DFIG based on the space vector theory. The space vector model is needed for the purpose of the presentation of the vector control system of the DFIG, which is presented in the next subsection.

Fig. 5.2 shows the space vector model of the DFIG in synchronous coordinates, with the quantities of the rotor-side referred to the stator side [84].

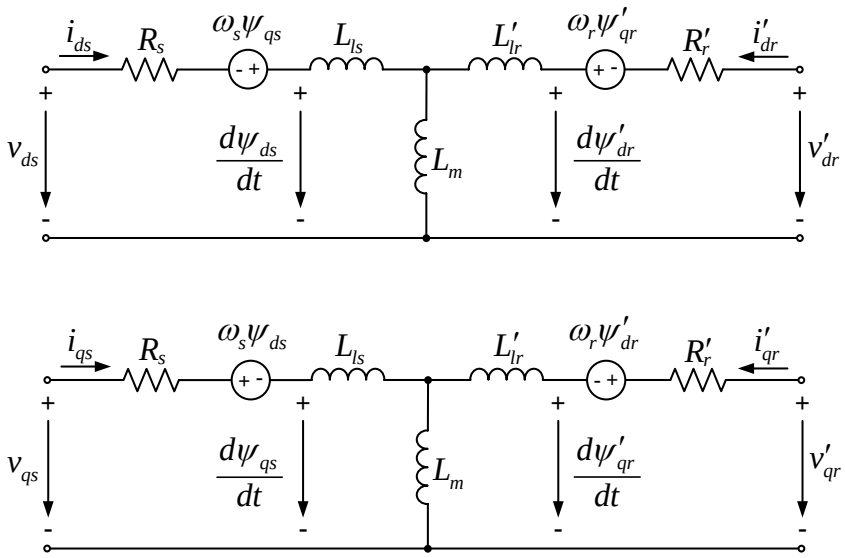

Fig. 5.2. *dq* model of the DFIG in synchronous coordinates.

The description of the parameters of the model is as bellow.

v_{ds} and v_{qs} : *dq* components of the stator voltage.

v'_{dr} and v'_{qr} : *dq* components of the rotor voltage, referred to the stator side.

i_{ds} and i_{qs} : *dq* components of the stator current.

i'_{dr} and i'_{qr} : *dq* components of the rotor current, referred to the stator side.

ψ_{ds} and ψ_{qs} : *dq* components of the stator flux.

ψ'_{dr} and ψ'_{qr} : *dq* components of the rotor flux, referred to the stator side.

R_s : Stator resistance.

R'_r : Rotor resistance, referred to the stator side.

L_{ls} : Stator leakage inductance.

L'_{lr} : Rotor leakage inductance, referred to the stator side.

L_m : Magnetizing inductance.

In the synchronous reference frame, the stator and rotor fluxes are given by [84]

$$\begin{cases} \psi_{ds} = L_s i_{ds} + L_m i'_{dr} \\ \psi_{qs} = L_s i_{qs} + L_m i'_{qr} \end{cases} \tag{5.9}$$

$$\begin{cases} \psi'_{dr} = L'_r i'_{dr} + L_m i_{ds} \\ \psi'_{qr} = L'_r i'_{qr} + L_m i_{qs}, \end{cases} \tag{5.10}$$

where L_s and L'_r are the stator and rotor inductances according to

$$\begin{cases} L_s = L_{ls} + L_m \\ L'_r = L'_{lr} + L_m. \end{cases} \tag{5.11}$$

The stator and rotor voltages in the *dq* reference frame rotating at ω_s are given by

$$\begin{cases} v_{ds} = R_s i_{ds} + \dfrac{d\psi_{ds}}{dt} - \omega_s \psi_{qs} \\ v_{qs} = R_s i_{qs} + \dfrac{d\psi_{qs}}{dt} + \omega_s \psi_{ds} \end{cases} \tag{5.12}$$

$$\begin{cases} v'_{dr} = R'_r i'_{dr} + \dfrac{d\psi'_{dr}}{dt} - \omega_r \psi'_{qr} \\ v'_{qr} = R'_r i'_{qr} + \dfrac{d\psi'_{qr}}{dt} + \omega_r \psi'_{dr}. \end{cases} \tag{5.13}$$

The active and reactive powers of the stator and rotor windings of the DFIG are given by

$$\begin{cases} P_s = \dfrac{3}{2}(v_{ds} i_{ds} + v_{qs} i_{qs}) \\ Q_s = \dfrac{3}{2}(v_{qs} i_{ds} - v_{ds} i_{qs}) \end{cases} \tag{5.14}$$

$$\begin{cases} P_r = \dfrac{3}{2}(v_{dr} i_{dr} + v_{qr} i_{qr}) \\ Q_r = \dfrac{3}{2}(v_{qr} i_{dr} - v_{dr} i_{qr}). \end{cases} \tag{5.15}$$

The electromagnetic torque is given by [112]

$$T_{em} = \frac{3}{2} p(\psi_{ds} i_{qs} - \psi_{qs} i_{ds}). \tag{5.16}$$

5.3 Control system for the DFIG system

DFIGs are usually controlled using vector control techniques [84, 113-115]. Vector control techniques allow a decoupled control of both the active and reactive powers of the DFIG. These techniques use a *dq* model of DFIG, in the synchronous reference frame, where the current and the voltage are decomposed into distinct components related to the active and reactive powers of the DFIG [116].

In the category of vector control techniques, there are two methods for the orientation of the synchronous reference frame: (1) the stator flux-orientation, where the *d*-axis of the synchronous reference frame is aligned with the stator flux vector [116, 117]; (2) the grid voltage-orientation, where the *q*-axis of the synchronous reference frame is aligned with the grid voltage space vector [118, 119]. The stator flux-orientation and the grid voltage-orientation are schematically represented in Fig. 5.3 [84].

When the stator flux-orientation is employed, the control system becomes unstable when the *d*-axis component of the rotor current is high. Such stability problem does not exist when the grid voltage-orientation is employed [84, 113, 120]. Moreover, if the stator flux-oriented reference frame is employed, the performance of the vector control system will be highly dependent on the accurate estimation of the stator flux position. This can be a critical problem under distorted supply voltage conditions or varying machine parameters [115].

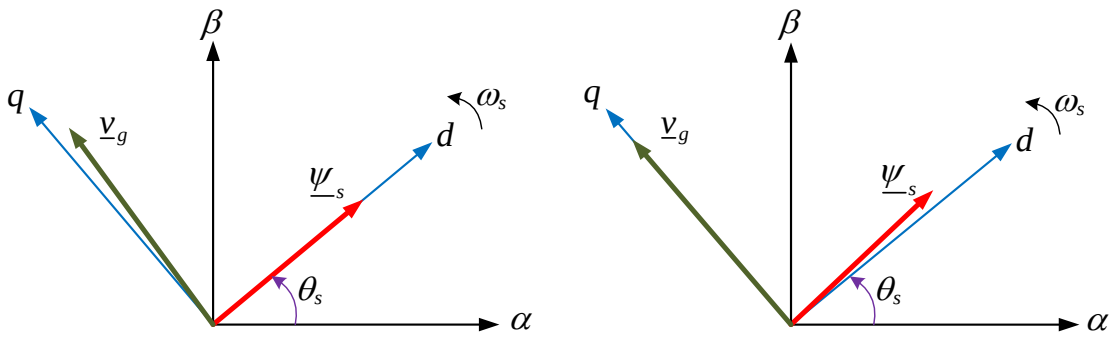

(a) Stator flux-orientation (b) Grid voltage-orientation

Fig. 5.3. Reference frame orientation.

Therefore, in this work, the grid voltage-oriented vector control scheme is employed to control the DFIG. This control system comprises two outer control loops, one to control the stator active power (injected into the grid) and the other one to control the stator reactive power. By using these loops, the rotor reference currents can be obtained from the reference values of the stator active and reactive powers. The control system also comprises two inner rotor current control loops which generate the reference voltages that will be applied to the rotor of the DFIG by the rotor-side converter.

To explain the control system, firstly the relationship between the stator powers and the rotor current components in a synchronous reference frame is obtained. Then, the closed control loops for the currents and powers are presented. Finally, the general overview of the employed control system is presented.

5.3.1 Analysis of the DFIG in the synchronous reference frame

In a synchronous reference frame with the *q*-axis aligned with the grid voltage, one has

$$\begin{cases} v_{ds} = 0 \\ v_{qs} = \left|\underline{v}_g\right|, \end{cases} \tag{5.17}$$

where $\left|\underline{v}_g\right|$ is the magnitude of the grid voltage space vector.

Since the *q*-axis of the reference frame is aligned with the grid voltage, and by neglecting the stator windings resistance, the stator flux is aligned with the *d*-axis. Therefore,

$$\begin{cases} \psi_{ds} = \left|\underline{\psi}_s\right| \cong \dfrac{\left|\underline{v}_g\right|}{\omega_s} \\ \psi_{qs} = 0, \end{cases} \tag{5.18}$$

where $\left|\underline{\psi}_s\right|$ is the magnitude of the stator flux space vector.

Combining (5.9) with (5.18), the relationship between the stator and rotor current components is given by

$$\begin{cases} i_{ds} = \dfrac{\psi_{ds}}{L_s} - \dfrac{L_m}{L_s} i'_{dr} \\ i_{qs} = -\dfrac{L_m}{L_s} i'_{qr}. \end{cases} \tag{5.19}$$

Combining (5.10) with (5.19), the relationship between the rotor flux and the rotor currents is given by

$$\begin{cases} \psi'_{dr} = \sigma L'_r i'_{dr} + \dfrac{L_m}{L_s}\psi_{ds} \\ \psi'_{qr} = \sigma L'_r i'_{qr}, \end{cases} \tag{5.20}$$

where σ is the leakage coefficient of the machine, being given by

$$\sigma = 1 - \frac{L_m^2}{L_s L_r}. \tag{5.21}$$

Combining (5.13) with (5.20), the relationship between the rotor voltages and the rotor currents is given by

$$\begin{cases} v'_{dr} = R'_r i'_{dr} - \omega_r \sigma L'_r i'_{qr} + \sigma L'_r \dfrac{d}{dt} i'_{dr} + \dfrac{L_m}{L_s}\dfrac{d}{dt}\psi_{ds} \\ v'_{qr} = R'_r i'_{qr} + \omega_r \sigma L'_r i'_{dr} + \sigma L'_r \dfrac{d}{dt} i'_{qr} + \omega_r \dfrac{L_m}{L_s}\psi_{ds}. \end{cases} \tag{5.22}$$

Equation (5.22) is equivalent to

$$\begin{cases} v'_{dr} = R'_r i'_{dr} + \sigma L'_r \dfrac{d}{dt} i'_{dr} - u'_{drc} \\ v'_{qr} = R'_r i'_{qr} + \sigma L'_r \dfrac{d}{dt} i'_{qr} + u'_{qrc}, \end{cases} \tag{5.23}$$

where

$$\begin{cases} u'_{drc} = \omega_r \sigma L'_r i'_{qr} - \dfrac{L_m}{L_s}\dfrac{d}{dt}\psi_{ds} \\ u'_{qrc} = \omega_r \sigma L'_r i'_{dr} + \omega_r \dfrac{L_m}{L_s}\psi_{ds}. \end{cases} \tag{5.24}$$

When the grid voltage is constant in amplitude, the derivative of ψ_{ds} is zero and therefore, the last term of the first equation in (5.24) disappears.

The active and reactive powers of the stator windings will then be given by

$$\begin{cases} P_s = \frac{3}{2} v_{qs} i_{qs} \\ Q_s = \frac{3}{2} v_{qs} i_{ds}. \end{cases} \tag{5.25}$$

Combining (5.25) with (5.17), (5.18) and (5.19), one obtains

$$\begin{cases} P_s = -\frac{3}{2} |\underline{v}_g| \frac{L_m}{L_s} i'_{qr} \\ Q_s = -\frac{3}{2} |\underline{v}_g| \frac{L_m}{L_s} i'_{dr} + \frac{3}{2} \frac{|\underline{v}_g|^2}{\omega_s L_s}. \end{cases} \tag{5.26}$$

The above equations show that under the grid voltage-oriented vector control, the stator active and reactive powers are decoupled and can be controlled independently by i_{qr} and i_{dr}, respectively.

5.3.2 Rotor current control loops

The control system comprises two inner rotor current control loops of high bandwidth (hundreds of Hertz). The current control loops must be incorporated to ensure that the rotor currents effectively follow their reference values. Proportional-integral (PI) controllers are employed in these control loops.

Based on the relationship between the rotor voltage and the rotor currents presented in (5.23) and (5.24), the transfer functions of the rotor current loops are given by

$$\frac{i'_{dr}(s)}{v'_{dr}(s) + u'_{drc}(s)} = \frac{1}{R'_r + \sigma L'_r s} \tag{5.27}$$

$$\frac{i'_{qr}(s)}{v'_{qr}(s) - u'_{qrc}(s)} = \frac{1}{R'_r + \sigma L'_r s}. \tag{5.28}$$

To obtain an effective system response to transients, the compensation terms in (5.24) have to be calculated and included in the control loops.

The rotor current control loops of the DFIG are graphically represented in Fig. 5.4, where u is the ratio between the stator and rotor effective turns number of the DFIG and K_{pi} and T_{ii} are the proportional gain and integral time of the employed PI controllers, respectively.

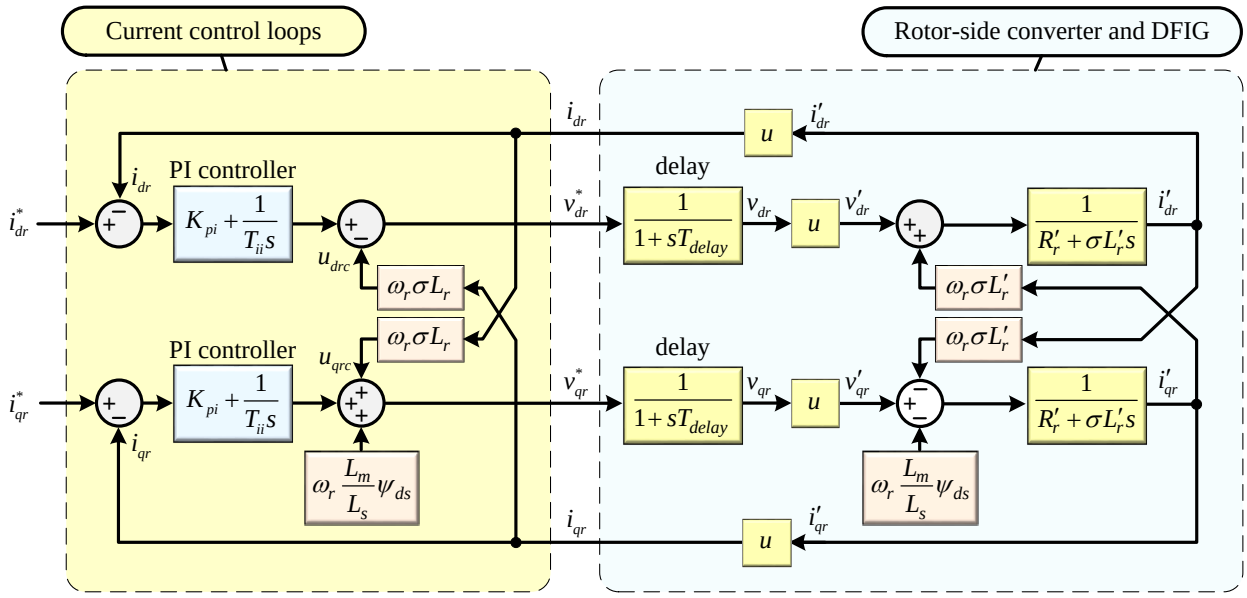

Fig. 5.4. Rotor current control loops of the DFIG.

The implementation of the control system implies several delays namely the analog to digital conversion (ADC) time, the zero-order hold (ZOH) considered in the sampling of the analog quantities and the time taken by the processor to run the control system and also in the power converter feeding the rotor of the DFIG. All these delays affect the dynamic behavior of the system. Since all added delays are much smaller compared to the dominant time constant of the system, they are considering as a single delay block, as shown in Fig. 5.4.

In this work, the Amplitude Optimum method is used to tune the parameters of the PI controllers of the control system [121, 122]. According to this tuning procedure, for a transfer function given by

$$G(s) = \frac{K}{(1+sT_1)(1+sT_2)},\ T_1 > T_2, . \tag{5.29}$$

the integral time and proportional gain of the PI controller are given by

$$\begin{cases} T_i = 2KT_2 \\ K_p = \dfrac{T_1}{2KT_2}. \end{cases} \cdot \tag{5.30}$$

The parameters of the transfer function of the rotor current loops are given by

$$\begin{cases} K^i = \dfrac{1}{R'_r} \\ T_1^i = \sigma \dfrac{L'_r}{R'_r} \\ T_2^i = T_{delay}, \end{cases} . \tag{5.31}$$

where T_{delay} is the total delay time considered in the employed control system.

Referring to (5.29)-(5.31) and considering $T_{delay} = 0.00013$ s, the parameters of the PI controllers of rotor current control loops are obtained as $T_{ii} \approx 0.0002$ s and $K_{pi} \approx 75$.

5.3.3 Stator active and reactive powers control loops

According to (5.26), the stator active and reactive powers can be controlled independently by regulating i_{qr} and i_{dr}, respectively. The control system of the DFIG comprises two outer control loops to control the stator active and reactive powers. By using these loops, the rotor reference currents can be obtained from the reference values of both stator powers.

The transfer functions of the stator active and reactive powers control loops can be obtained by (5.26). The power control loops are presented in Fig. 5.5. In this figure, α_i is the bandwidth of the rotor current control loops, being given by

$$\alpha_i \cong \frac{1.8}{t_r}, \tag{5.32}$$

where t_r is the rise time of the rotor current control loops subjected to a unit step function, as shown in Fig. 5.6 [112]. In the control system employed in this work, $t_r = 0.0008$ s and $\alpha_i = 2250$ rad/s.

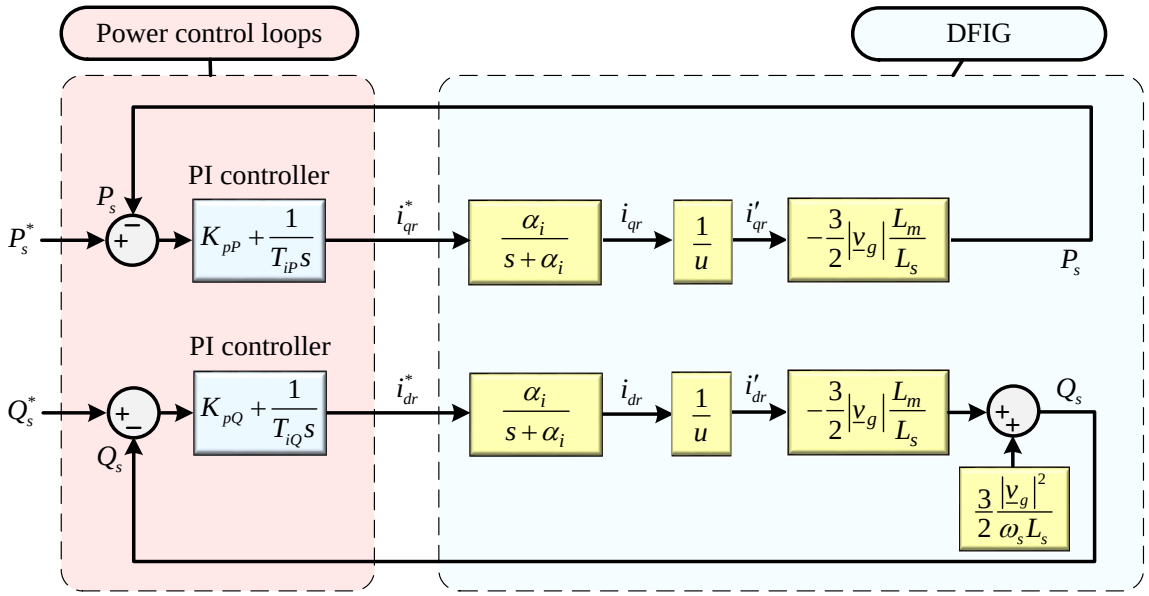

Fig. 5.5. Stator power control loops.

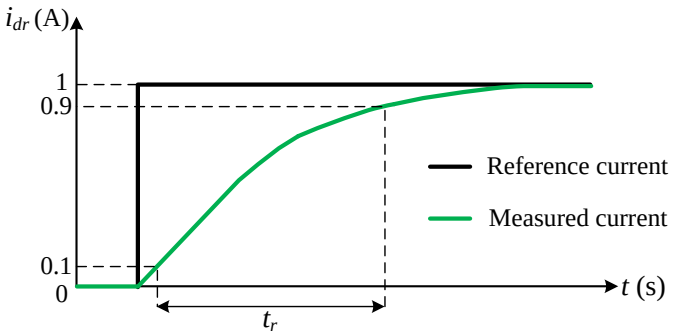

Fig. 5.6. Rotor current control loop dynamic response.

The parameters of the transfer function of the power loops are given by

$$\begin{cases} K^p = \dfrac{3}{2}|\underline{v}_g|\dfrac{L_m}{L_s} \\ T_1^p = \dfrac{1}{\alpha_i} \\ T_2^p = \dfrac{0.7}{\omega_p}, \end{cases} . \tag{5.33}$$

where ω_p is the expected bandwidth of the power control loops.

Combining (5.30) with (5.33) and considering $\omega_p = 100$ rad/s and $|\underline{v}_g| = 350\sqrt{2}/\sqrt{3}$ V, the parameters of the parameters of the PI controllers of power control loops are obtained as $T_{ip} \approx 5.8$ s and $K_{pp} \approx 0.000083$.

5.3.4 Overview of the employed control system

The entire control system of the DFIG is schematically illustrated in Fig. 5.7. The implementation of the control system involves the measurement of the stator voltages and currents, the rotor currents and the DC-bus voltage, according to the diagram shown in Fig. 5.7.

The angle of the fundamental component of the grid voltages (θ_g) is obtained with a phase locked loop (PLL). The angle needed for the transformations of the stator voltages and currents to the synchronous reference frame (θ_s) is calculated as $\theta_s=\theta_g - \pi/2$. The angle of the rotor position (θ) is measured by an encoder mounted on the shaft of the DFIG. The angle needed for the transformations of the rotor currents to the synchronous reference frame is calculated by $\theta_r=\theta_s - \theta$.

The reference values of the stator active and reactive powers are compared to the respective calculated values and the corresponding errors are passed through the PI controllers of the power control loops. The *dq* components of the rotor currents references in the synchronous frame (i_{dr}^* and i_{qr}^*) are obtained from these PI controllers. The values of i_{dr}^* and i_{qr}^* are then compared with the values of i_{dr} and i_{qr} and the errors are passed through the PI controllers of the current control loops. The values of the rotor voltage references in the synchronous frame (v_{dr}^* and v_{qr}^*) are obtained by adding the compensation terms in (5.24) to the output values of these PI controllers. Using the *dq/abc* transformation block, the values of the rotor reference voltages in the *abc* reference frame (v_a^*, v_b^* and v_c^*) are obtained from the values of v_{dr}^* and v_{qr}^*. According to the values of v_a^*, v_b^* and v_c^*, the modulator generates the gating signals for the 12 IGBTs of the 3LNPC converter.

Concerning the modulation technique, despite the numerous advantages of the space vector modulation (SVM) technique (covered in Chapter 2), its implementation needs a huge number of calculations that would increase the required sampling time for running the control system. Nevertheless, the SVM technique was initially implemented in the control system, which led to a not satisfactory performance. Consequently, in the control system of the DFIG, the sinusoidal pulse width modulation (SPWM) technique[2] (presented in Chapter 2) was adopted for the modulator. This technique resulted in very satisfying results for DFIG systems in the whole operating range.

[2] Since the value of V_{DC} was high enough, the peak value of the reference voltage was always lower than $V_{DC}/2$ and, therefore, it was not necessary to use the THIPWM technique.

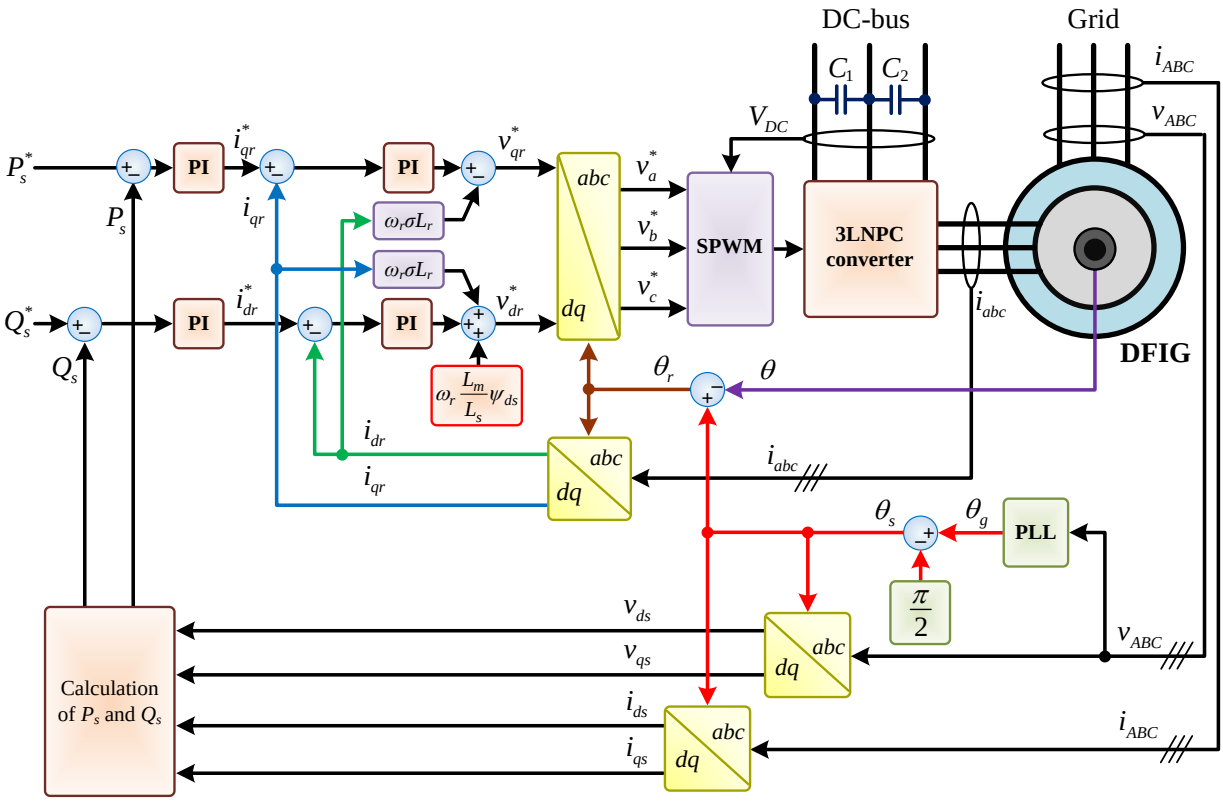

Fig. 5.7. Schematic diagram of the control system of the DFIG system.

5.4 DFIG model validation

The DFIG system, including the model of the generator (presented in Chapter 4), the model of the 3LNPC converter along with its modulator, and the control system of the DFIG that was previously presented in Subsection 5.3, was implemented in Matlab/Simulink environment. The aspects regarding the implementation of the DFIG model are presented in Appendix *D*.

To validate experimentally the simulation model of the entire DFIG system, an experimental test rig was prepared. In this test rig, the machine with specifications given in Appendix *C* was mechanically coupled to a variable speed drive based on an IM that emulates the wind turbine (Fig. 5.8). The stator windings were connected to a three-phase autotransformer (whose output emulates the grid) through a circuit breaker, while an *L*-filter (L_{filter}=2.6 mH) was used between the connection of the 3LNPC converter (with the specifications given in Appendix A) to the rotor windings of the DFIG.

In a real DFIG system, there is a rotor-side converter and a grid-side converter in a back-to-back configuration. Since the purpose of this work is the analysis and diagnosis of ITSC faults in the DFIG windings as well as the diagnosis of OC faults in the rotor-side 3LNPC converter, the grid-side converter was not included neither in the simulation model nor in the experimental test rig.

Since the grid-side converter is usually used with the purpose of the DC-bus voltage regulation, instead of a grid-side converter, two three-phase diode rectifiers were employed to supply the DC-bus of the rotor-side converter. Furthermore, to dissipate the energy sent by the DFIG to the DC-bus when it runs at supersynchronous speeds, a load resistance was connected in parallel with the DC-bus. With this test rig, the DFIG can operate at both subsynchronous and supersynchronous speeds.

The stator and rotor currents, the short-circuit current, the grid voltages, the converter pole voltages and the DC-bus voltage were measured by appropriate sensors built-in the test rig. The rotor position was measured by an incremental encoder with 2048 pulses per revolution. The data acquisition was performed with *ControlDesk* software. The control strategy of the DFIG system was implemented in a *dSPACE* 1103 digital controller board, with a sampling frequency of 18 kHz.

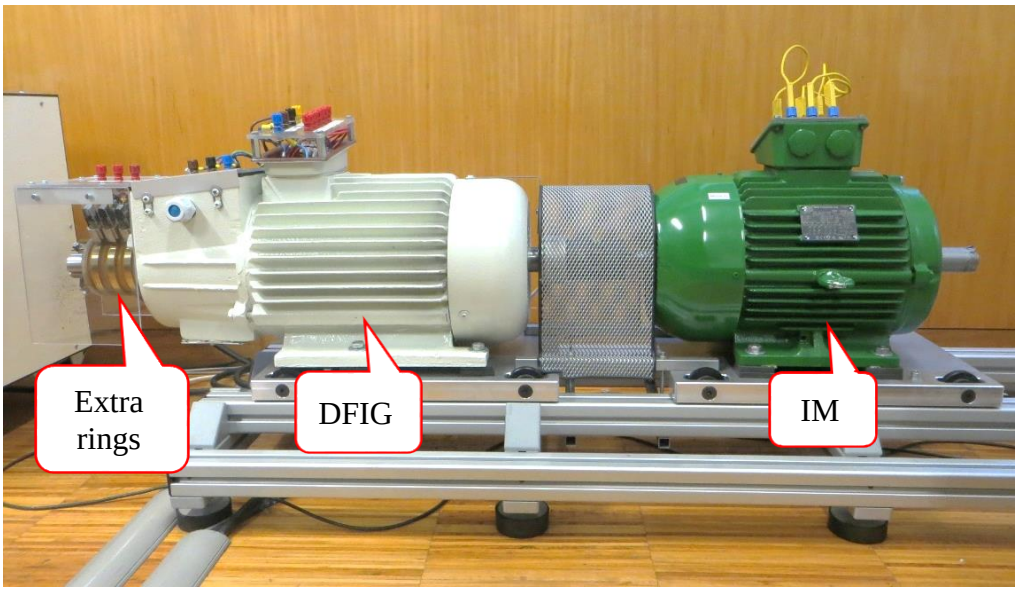

Fig. 5.8. DFIG mechanically coupled to an IM drive.

For the evaluation of the simulation model of the DFIG system, several experimental tests were performed at different DFIG operating conditions. The different operating conditions were based on different values of the active and reactive power injected into the grid and different values of the rotor speed when the generator operates in subsynchronous, synchronous and supersynchronous modes.

The machine employed in the experimental test is essentially a WRIM and it was designed to be used as a single-fed induction motor. When this machine was used as a DFIG, it was not possible to supply the stator windings with the rated voltage (400 V) because at this voltage level, the rotor currents were above the nominal value. Therefore, due to the limitation of the rotor current, the grid voltage was set to 350 V. Considering the maximum modulation rotor voltages, the DC-bus voltage was set to 200 V.

For the healthy operation of the DFIG, considering the grid voltage harmonics, the expected frequency components in the stator currents are given by [110]

$$f_{s.c}^{i,k} = |i \pm 6k(1-s)|\, f_s, \tag{5.34}$$

where i=1, 2, 3,… is the order of the grid supply induced current harmonic components and k=0, 1, 2, 3...

As presented in Chapter 4, the magnetic saturation gives rise to some new components in the stator current at frequencies given by

$$f_{s.c}^{sat} = (1 \pm 6s)\, f_s. \tag{5.35}$$

The expected frequency components in the stator active and reactive powers are given by [123]

$$f_{\text{power}}^{\vartheta,i,k} = |[\vartheta \pm i \pm 6k(1-s)]|\, f_s, \tag{5.36}$$

where ϑ is the supply harmonic orders and k=0, 1, 2, 3...

Moreover, the interaction of the stator current components related to the magnetic saturation given by (4.73) and the fundamental component of the supply voltage gives rise to a component in both the stator active and reactive powers, at a frequency given by

$$f_{\text{power}}^{sat} = 6sf_s. \tag{5.37}$$

Fig. 5.9 shows the waveforms and spectrum of the grid voltages used in the experimental tests. The amplitudes of the fundamental component, the 5th and 7th harmonics of the grid voltages were 302 V, 7.2 V and 4.2 V, respectively. These harmonics were also considered in the simulation tests performed in this subsection to compare the results obtained under identical operating conditions of the DFIG.

Fig. 5.10 and Fig. 5.11 show the simulation and experimental results obtained for the DFIG operating in healthy conditions, with a rotor speed of 1350 rpm, and with the reference values for the stator active and reactive powers (P_s^* and Q_s^*) of -2000 W and 0 VAr, respectively. The spectra obtained are presented in Fig. 5.12 and Fig. 5.13. From now on, all components related to the faults are highlighted in red in the spectra, while the other components are indicated in blue.

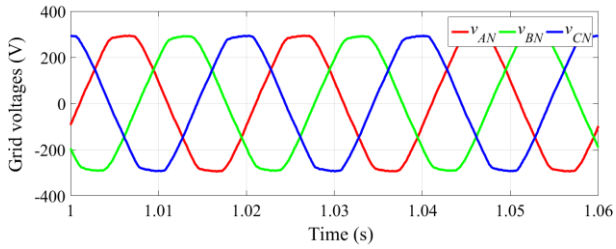

(a) Waveforms

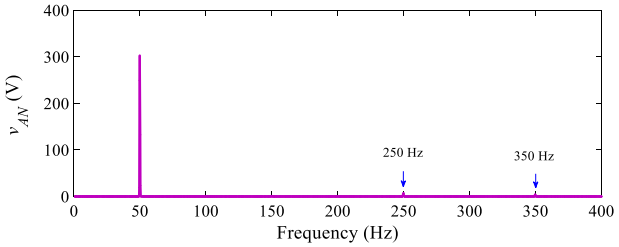

(b) Spectrum

Fig. 5.9. Grid voltages of the experimental tests.

As seen in these figures, the stator and rotor currents waveforms are balanced and the amplitude and period of the stator and rotor currents obtained with the simulation model are identical to those obtained in the experimental tests.

According to (5.34) and for s=0.1, the components at frequencies of 220 Hz and 320 Hz (i=1, k=1), 250 Hz (i=5, k=0) and 350 Hz (i=7, k=0) are observed in the stator current spectra. Referring to (4.73), two components related to the magnetic saturation at frequencies of 20 Hz and 80 Hz are also labeled in the stator current spectra. Due to the addition of the extra taps in the stator and

rotor windings, there is a small degree of inherent electrical unbalance in the machine that it is not considered in the simulation model. Therefore, unlike the simulation result presented in Fig. 5.12 (a), two components related to the rotor fault at frequencies of 40 Hz $((1-2s)f_s)$ and 60 Hz $((1+2s)f_s)$ are observed in the stator current spectrum, as presented in Fig. 5.13 (a). The results match well with the exception of the amplitude of the components at frequencies of 20 Hz, 80 Hz and 320 Hz that are slightly different in the simulation results compared to the experimental results.

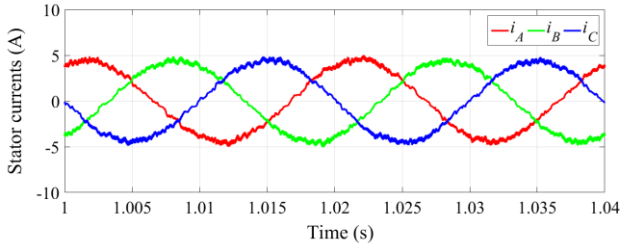

(a) Stator currents waveforms

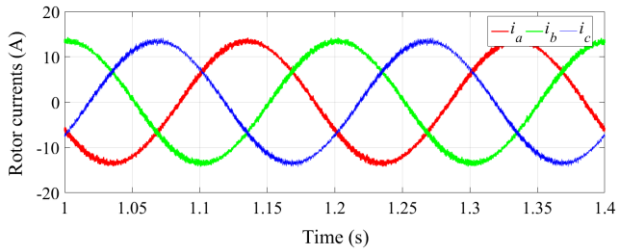

(b) Rotor currents waveforms

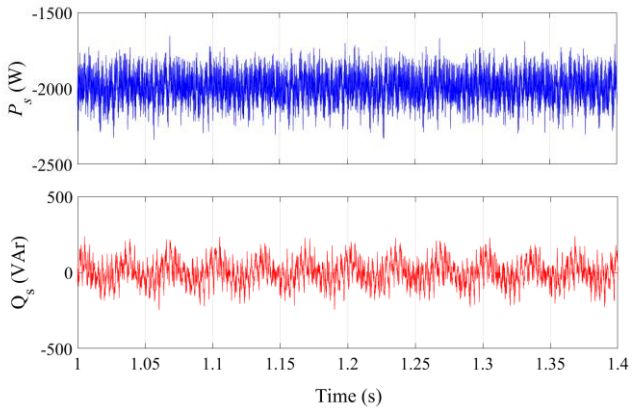

(c) Time waveforms of the stator active and reactive powers

Fig. 5.10. Simulation results for the DFIG system in healthy conditions ($n = 1350$ rpm, $P_s^* = -2000$ W, $Q_s^* = 0$ VAr) .

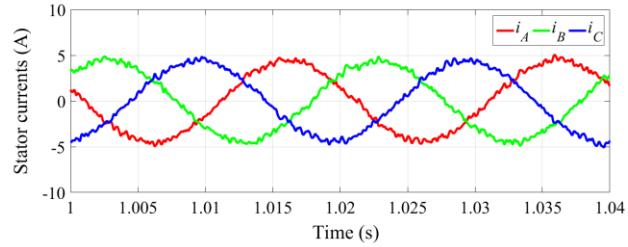

(a) Stator currents waveforms

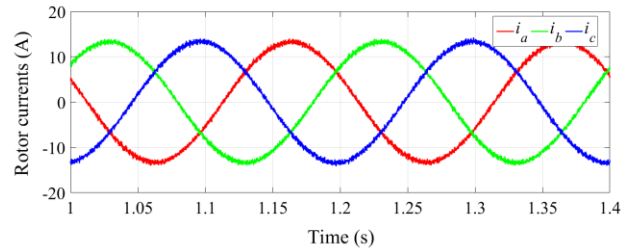

(b) Rotor currents waveforms

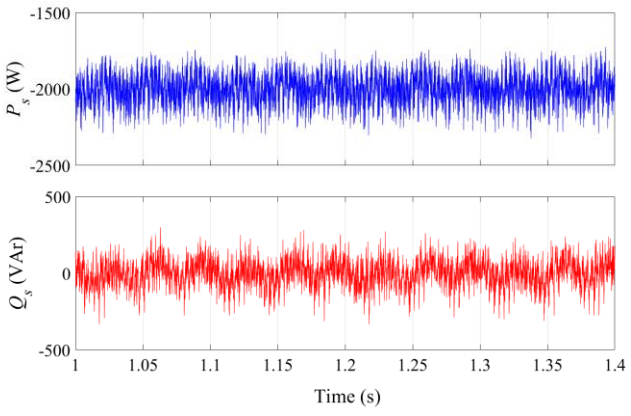

(c) Time waveforms of the stator active and reactive powers

Fig. 5.11. Experimental results for the DFIG system in healthy conditions ($n = 1350$ rpm, $P_s^* = -2000$ W, $Q_s^* = 0$ VAr) .

The interaction of the aforementioned components in the stator currents and the fundamental component of the supply voltage leads to significant oscillations in both the stator active and reactive power waveforms. However, the average values of the stator active and reactive powers follow the corresponding reference values.

Fig. 5.12 (b), Fig. 5.12 (c), Fig. 5.13 (b) and Fig. 5.13 (c) show the spectra of the stator active and reactive powers. Referring to (5.36), the components at frequencies of 270 Hz (i=1, ϑ=1, k=1) and 300 Hz [(i=5, ϑ=1, k=0) and (i=7, ϑ=1, k=0)] are labeled in these figures. Referring to (5.37), the component related to the magnetic saturation at the frequency of 30 Hz is also labeled in both the stator active and reactive power spectra. Furthermore, due to the inherent electrical unbalance of the machine, two components, at frequencies of 10 Hz and 100 Hz, appear in the spectra of the stator active and reactive powers (obtained by experimental test) whose origin will be discussed in the next chapter. In general, these simulation and experimental results match very well.

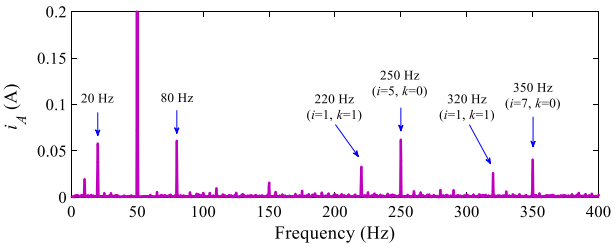

(a) Spectrum of stator current i_A

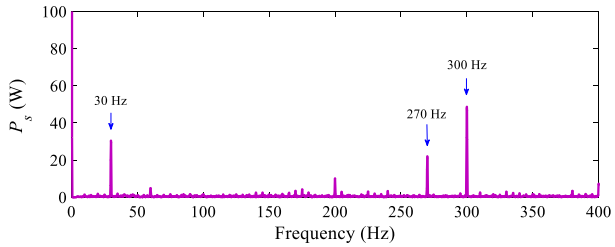

(b) Spectrum of stator active power

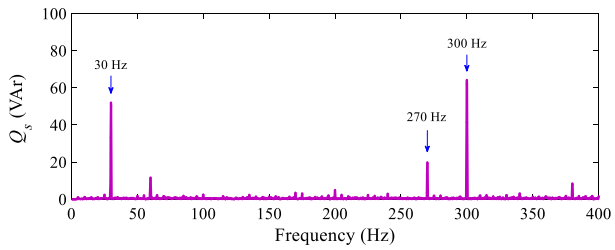

(c) Spectrum of stator reactive power

Fig. 5.12. Spectra for the DFIG system in healthy conditions, obtained with the simulation model (n = 1350 rpm, P_s^* = –2000 W, Q_s^* = 0 VAr) .

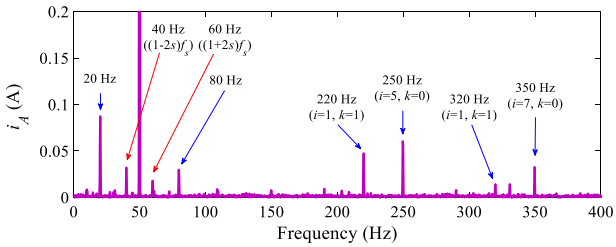

(a) Spectrum of stator current i_A

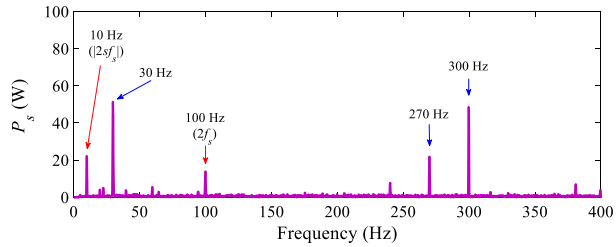

(b) Spectrum of stator active power

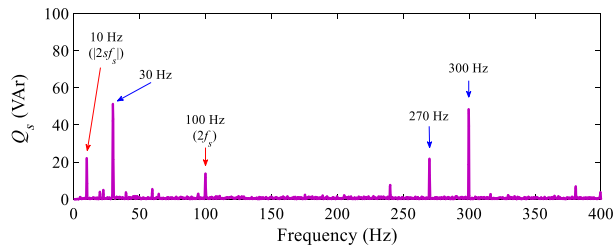

(c) Spectrum of stator reactive power

Fig. 5.13. Spectra for the DFIG system in healthy conditions, obtained by experimental test (n = 1350 rpm, P_s^* = –2000 W, Q_s^* = 0 VAr) .

Fig. 5.14 and Fig. 5.15 show the results for the DFIG operating at a supersynchronous speed of 1650 rpm (s=-0.1), and when the reference values of the active and reactive powers were set to -2000 W and 0 VAr, respectively. As seen in these figures, the stator and rotor currents waveforms are balanced and the amplitude and period of the stator and rotor currents obtained with the simulation model are identical to the experimental results. Due to the negative slip, the rotor currents now constitute a negative sequence component.

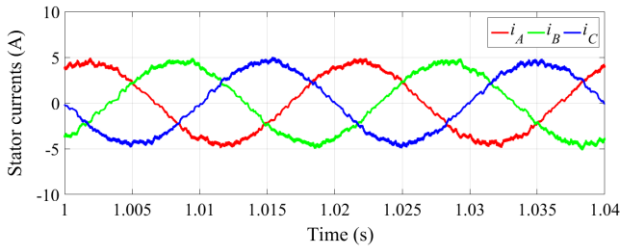

(a) Time waveforms of stator currents

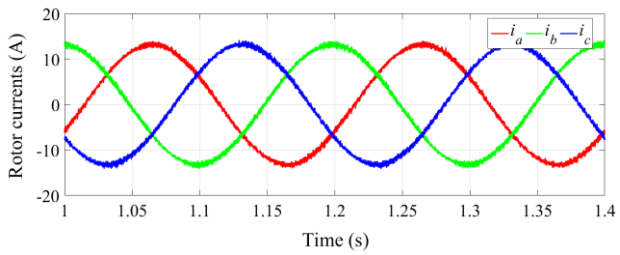

(b) Time waveforms of rotor currents

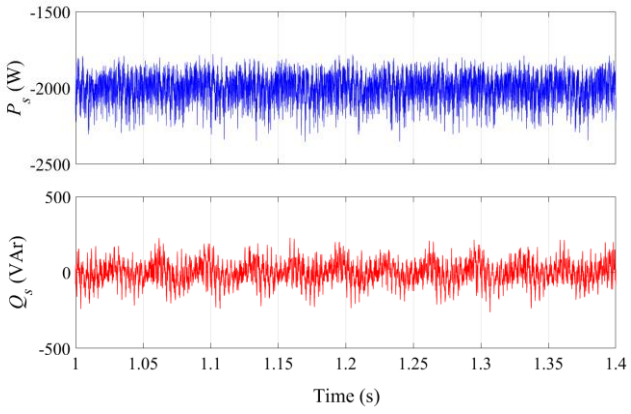

(c) Time waveforms of stator active and reactive powers

Fig. 5.14. Simulation results for the DFIG system in healthy conditions ($n = 1650$ rpm, $P_s^* = -2000$ W, $Q_s^* = 0$ VAr) .

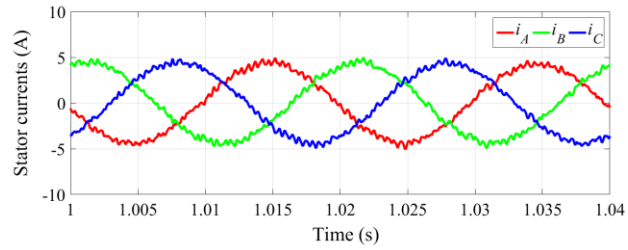

(a) Time waveforms of stator currents

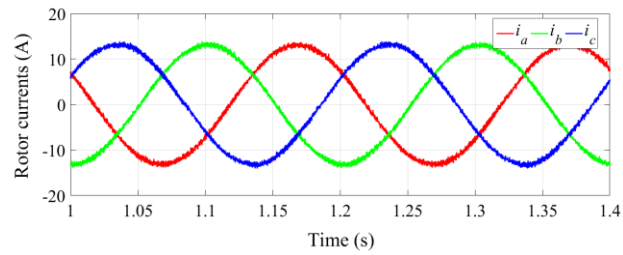

(b) Time waveforms of rotor currents

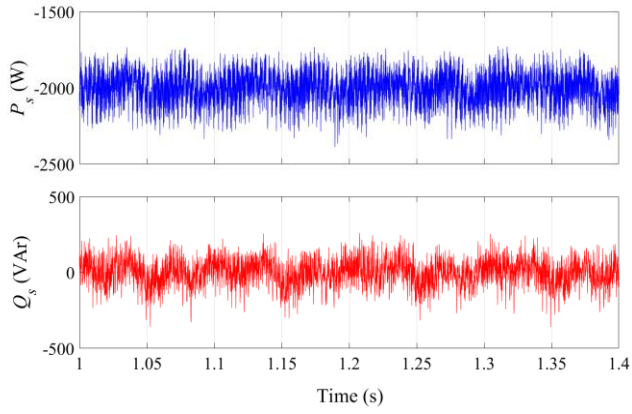

(c) Time waveforms of stator active and reactive powers

Fig. 5.15. Experimental results for the DFIG system in healthy conditions ($n = 1650$ rpm, $P_s^* = -2000$ W, $Q_s^* = 0$ VAr) .

The spectra of the stator current and stator active and reactive powers, for the same operating conditions are presented in Fig. 5.16 and Fig. 5.17. Referring to (5.34) and for s=-0.1, the components at frequencies of 250 Hz (i=5, k=0), 350 Hz (i=7, k=0), 220 Hz and 320 Hz (i=1, k=1) are labelled in the stator current spectra. Referring to (4.73), two components related to the magnetic saturation at frequencies of 20 Hz and 80 Hz are also observed in the stator current spectra.

Referring to (5.36), the components at frequencies of 300 Hz [(i=5, ϑ=1, k=0) and (i=7, ϑ=1, k=0)] and 330 Hz (i=1, ϑ=1, k=1) are observed in the stator active and reactive powers spectra. The component related to the magnetic saturation at a frequency of 30 Hz is also labeled in these figures. The amplitudes of these components in the results obtained with the simulation model match well with the experimental results.

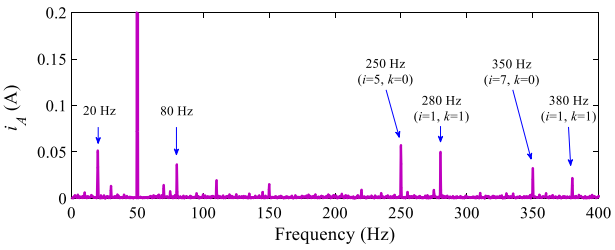

(a) Spectrum of stator current i_A

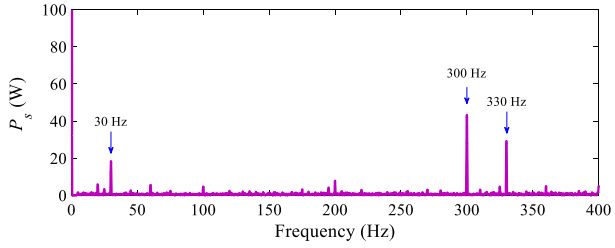

(b) Spectrum of stator active power

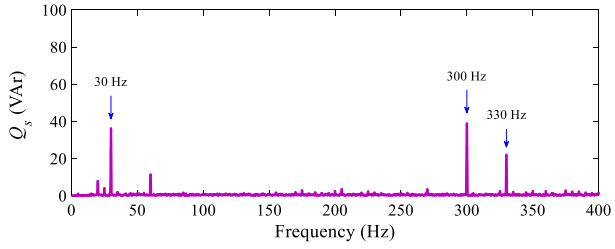

(c) Spectrum of stator reactive power

Fig. 5.16. Spectra for the DFIG system in healthy conditions, obtained with the simulation model (n = 1650 rpm, P_s^* = –2000 W, Q_s^* = 0 VAr) .

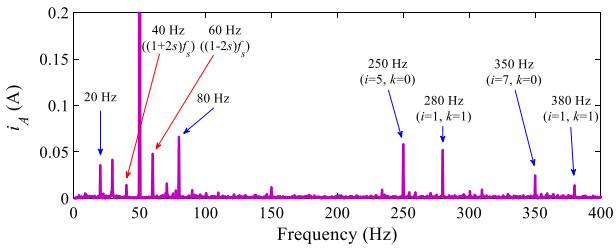

(a) Spectrum of stator current i_A

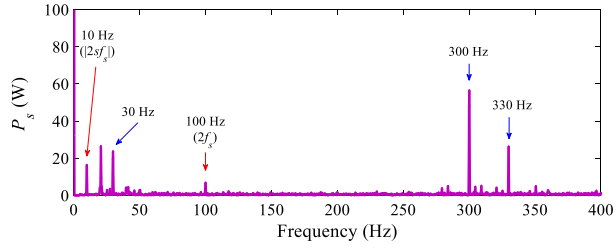

(b) Spectrum of stator active power

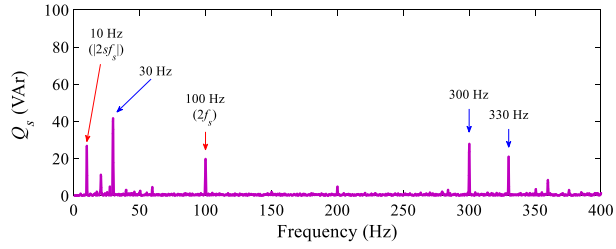

(c) Spectrum of stator reactive power

Fig. 5.17. Spectra for the DFIG system in healthy conditions, obtained by experimental tests (n = 1650 rpm, P_s^* = –2000 W, Q_s^* = 0 VAr) .

Similar results were obtained for other operating speeds, and different values of the active and reactive powers injected into the grid. For comparison of the simulation and experimental results, the fundamental values of the stator and rotor currents under various operating conditions of the DFIG (different rotor speeds and different values of the active and reactive powers injected into the grid) are listed in Table 5.2. It should be mentioned that for the DFIG operating at synchronous speed, since the rotor currents are dc quantities, the average value of the space vector of the rotor currents was used in the table. The simulation and experimental results are similar, thus validating the simulation model of the DFIG system.

Table 5.2. Amplitudes of the stator and rotor currents, in different DFIG operating conditions.

n (rpm)		1350		1500		1650	
P_s^* (W)		-2000	-1000	-2000	-1000	-2000	-1000
Q_s^* (VAr)		0	-500	0	-500	0	-500
i_s (A)	Simulation	4.43	2.47	4.5	2.53	4.44	2.48
	Experimental	4.46	2.48	4.42	2.5	4.41	2.51
i_r (A)	Simulation	13.43	13.41	13.46	12.95	13.5	13.44
	Experimental	13.26	13.13	13.22	12.78	13.19	13.03

Chapter 6

Fault diagnosis of inter-turn short-circuit faults

6.1 Introduction

Winding ITSC faults are one of the common faults in electric machines, being caused by many reasons such as high temperature in the windings or core, mechanical stress, insulation damage and transient overvoltages [124-126].

ITSC faults normally begin with an undetected turn-to-turn fault which then progresses to a more serious fault [125, 127]. In this type of fault, the short-circuited turns create an additional circuit loop coupled to the other windings of the machine. Since the impedance of the short-circuited turns is small, a large current flows there. Consequently, this current generates heat which will generally lead to the damage of the insulation system of the adjacent conductors [128, 129].

When the windings of a machine are fed from a power electronic converter, the insulation lifetime decreases due to an increase of the thermal and electrical stresses to which the turns insulation material is subjected to [130-132]. Hence, ITSC faults are a probable fault in rotor windings of DFIGs [133].

Several techniques can be found in the literature for the detection of faults in the windings of DFIGs. In [134], the detection of ITSC faults in the stator windings of DFIGs operating under time-varying operating conditions was achieved by using the rotor current signals in conjunction with the voltage of a rotor mounted search coil. In this case, the installation of the rotor search coil is an invasive procedure, hence limiting the applicability of this diagnostic approach.

In [135], the cumulative sum algorithm has been proposed for the detection of ITSC faults in the stator windings of DFIGs. The implementation of this method is easy and provides a rapid fault detection capability. However, it is necessary to study the method for different operating points to select the proper threshold value for fault detection.

Another method for the detection of ITSC faults in the stator and rotor windings of DFIGs is proposed in [136]. In this method, when the stator windings of the DFIG are short-circuited, short voltage pulses, with a duration of around hundreds of μs, are applied to the rotor windings. Measuring the rotor current response provides the knowledge of the transient leakage inductance of the DFIG. Then, using a special signal processing procedure, a fault indicator is developed to identify ITSC faults. However, since a short-circuited stator is needed, this method can not be applied during the normal operation of the DFIG.

In some research works, ITSC faults have been emulated by an additional resistance connected in series with one phase of the stator or rotor windings of the DFIG, called increased phase resistance (IPR) faults.

To identify IPR faults in the stator and rotor of a DFIG, different techniques such as the spectrum analysis of the stator currents, rotor currents, and rotor modulating signals inside the DFIG control system are investigated in [111]. The presented results show that the performance of the rotor modulating signals analysis is better than the analysis of both rotor and stator currents. The embedment of this method in the control system is easy and does not need any additional equipment.

For the detection of rotor IPR faults, two different techniques, the spectrum analysis of the stator currents and the spectrum analysis of the instantaneous stator active power has been investigated in [137]. The results presented in [137] reveal that the instantaneous active power spectrum contains more potential fault-specific information than the stator current spectrum.

For the detection of IPR faults in the rotor windings of DFIGs, in [138], the frequency analysis of the *dq* components of the rotor error current signals inside the DFIG control system is used. According to the presented results, the spectral component at the frequency of $2sf$ in the *dq* components of the rotor error current signals is an indicator for the detection of rotor IPR faults. This diagnostic technique is simple and embedding it in the DFIG system is easy.

In [139], fault in the stator windings of a DFIG was emulated by placing a resistor in parallel with the stator winding. The fast Fourier transform **(**FFT) and the Extended Park's Vector Approach (EPVA) of the stator currents are used in a first stage for the detection of ITSC faults in the stator windings of the DFIG operating in steady-state. For the detection of that specific fault under time-varying load conditions, the authors proposed a technique based on the combination of the EPVA and the wavelet transform (WT).

Although a wide range of diagnostic techniques is proposed in the literature, in the majority of those studies, the faults in the windings of the DFIG are emulated by inserting an additional resistance in series with the rotor phase windings [111, 137, 138]. Although it creates a winding unbalance, this does not emulate the true condition of the generator due to ITSC faults. As clarified in Chapter 4, for the modeling of ITSC faults, the structure of the equations is changed by increasing the number of state variables. Only two authors developed a simulation model that allow the capability of introducing ITSC faults in the windings of DFIG [134, 135]. What's more, in the majority of the published works, the experimental setup was not adapted to introduce the ITSC faults in the stator and rotor windings of the DFIG.

In the current work, a technique based on the spectrum analysis of the stator instantaneous reactive power is introduced to detect ITSC faults in the stator and rotor windings of DFIG. As it will be further clarified in the following, both the active and reactive powers can be used for the detection of ITSC faults in the stator and rotor windings of DFIG. The use of the active power for the detection of ITSC faults has already been proposed in [137]. However, considering the fact that compared to the reactive power, the stator active power changes in a much wider range and in a faster way, in this work the spectrum analysis of the stator reactive power is used for fault diagnostic purposes.

6.2 Analysis of the stator reactive power for the diagnosis of ITSC faults

6.2.1 Analysis of an ITSC fault in the stator windings

In ideal conditions and with no faults the three stator and rotor impedances are identical. Hence, neglecting stator and rotor slots harmonics, saturation harmonics and high-frequency harmonics, only the normal frequency components at f_s and sf_s exist in stator and rotor current spectra.

In the presence of an ITSC fault in the stator windings of the DFIG, due to the resulting asymmetry, the stator currents will contain a positive and a negative sequence component, at frequencies of f_s and $-f_s$, respectively [111].

The positive sequence component of the stator currents is given by

$$\begin{cases} i_A^+ = I_m^+ cos\left(\omega_s t + \theta_i^+\right) \\ i_B^+ = I_m^+ cos\left(\omega_s t - \dfrac{2\pi}{3} + \theta_i^+\right) \\ i_C^+ = I_m^+ cos\left(\omega_s t + \dfrac{2\pi}{3} + \theta_i^+\right), \end{cases} \tag{5.38}$$

where I_m^+ is the peak value of the positive sequence component of the stator currents and θ_i^+ is the initial phase angle of i_A^+.

The negative sequence component of the stator currents is given by

$$\begin{cases} i_A^- = I_m^- cos\left(\omega_s t + \theta_i^-\right) \\ i_B^- = I_m^- cos\left(\omega_s t + \dfrac{2\pi}{3} + \theta_i^-\right) \\ i_C^- = I_m^- cos\left(\omega_s t - \dfrac{2\pi}{3} + \theta_i^-\right), \end{cases} \tag{5.39}$$

where I_m^- is the peak value of the negative sequence component of the stator currents and θ_i^- is the initial phase angle of i_A^-.

The three-phase current components presented before can be transformed to a synchronous reference frame, according to [140]

$$\begin{bmatrix} x_d \\ x_q \end{bmatrix} = \frac{2}{3} \begin{bmatrix} \cos(\theta_s) & \cos\left(\theta_s - \dfrac{2\pi}{3}\right) & \cos\left(\theta_s + \dfrac{2\pi}{3}\right) \\ -\sin(\theta_s) & -\sin\left(\theta_s - \dfrac{2\pi}{3}\right) & -\sin\left(\theta_s + \dfrac{2\pi}{3}\right) \end{bmatrix} \begin{bmatrix} x_A \\ x_B \\ x_C \end{bmatrix}, \tag{5.40}$$

where θ_s is the angle between the *d*-axis of the synchronous reference frame with respect to the stationary reference frame, given by

$$\theta_s = \omega_s t. \tag{5.41}$$

Using (5.40) and (5.41), the *d*-axis component of the positive sequence component of the stator currents is calculated by

$$i_{ds}^{+}=\frac{2}{3}I_{m}^{+}[\cos\left(\theta_s+\theta_i^{+}\right)\cos\left(\theta_s\right)+\cos\left(\theta_s-\frac{2\pi}{3}+\theta_i^{+}\right)\cos\left(\theta_s-\frac{2\pi}{3}\right)+\cos\left(\theta_s+\frac{2\pi}{3}+\theta_i^{+}\right)\cos\left(\theta_s+\frac{2\pi}{3}\right)], \tag{5.42}$$

which is equivalent to

$$i_{ds}^{+}=\frac{2}{3}I_{m}^{+}[\frac{1}{2}\left(\cos\left(2\theta_s+\theta_i^{+}\right)+\cos\left(\theta_i^{+}\right)\right)+\frac{1}{2}\left(\cos\left(2\theta_s-\frac{4\pi}{3}+\theta_i^{+}\right)+\cos\left(\theta_i^{+}\right)\right)+\frac{1}{2}\left(\cos\left(2\theta_s+\frac{4\pi}{3}+\theta_i^{+}\right)+\cos\left(\theta_i^{+}\right)\right)]=I_{m}^{+}\cos\left(\theta_i^{+}\right). \tag{5.43}$$

The *q*-axis component of the positive sequence component of the stator currents is calculated by

$$i_{qs}^{+}=-\frac{2}{3}I_{m}^{+}[\cos\left(\theta_s+\theta_i^{+}\right)\sin\left(\theta_s\right)+\cos\left(\theta_s-\frac{2\pi}{3}+\theta_i^{+}\right)\sin\left(\theta_s-\frac{2\pi}{3}\right)+\cos\left(\theta_s+\frac{2\pi}{3}+\theta_i^{+}\right)\sin\left(\theta_s+\frac{2\pi}{3}\right)], \tag{5.44}$$

which is equivalent to

$$i_{qs}^{+}=-\frac{2}{3}I_{m}^{+}[\frac{1}{2}\left(\sin\left(2\theta_s+\theta_i^{+}\right)-\sin\left(\theta_i^{+}\right)\right)+\frac{1}{2}\left(\sin\left(2\theta_s-\frac{4\pi}{3}+\theta_i^{+}\right)-\sin\left(\theta_i^{+}\right)\right)+\frac{1}{2}\left(\sin\left(2\theta_s+\frac{4\pi}{3}+\theta_i^{+}\right)-\sin\left(\theta_i^{+}\right)\right)]=I_{m}^{+}\sin\left(\theta_i^{+}\right). \tag{5.45}$$

The *d*-axis component of the negative sequence component of the stator currents is calculated by

$$i_{ds}^{-}=\frac{2}{3}I_{m}^{-}[\cos\left(\theta_s+\theta_i^{-}\right)\cos\left(\theta_s\right)+\cos\left(\theta_s+\frac{2\pi}{3}+\theta_i^{-}\right)\cos\left(\theta_s-\frac{2\pi}{3}\right)+\cos\left(\theta_s-\frac{2\pi}{3}+\theta_i^{-}\right)\cos\left(\theta_s+\frac{2\pi}{3}\right)], \tag{5.46}$$

which is equivalent to

$$\begin{aligned} i_{ds}^{-} = \frac{2}{3} I_m^{-} [\frac{1}{2}\left(\cos\left(2\theta_s + \theta_i^{-}\right) + \cos\left(\theta_i^{-}\right)\right) + \frac{1}{2}\left(\cos\left(2\theta_s + \theta_i^{-}\right) + \cos\left(\frac{4\pi}{3} + \theta_i^{-}\right)\right) \\ + \frac{1}{2}\left(\cos\left(2\theta_s + \theta_i^{-}\right) + \cos\left(-\frac{4\pi}{3} + \theta_i^{-}\right)\right)] = I_m^{-} \cos\left(2\theta_s + \theta_i^{-}\right). \end{aligned} \tag{5.47}$$

The *q*-axis component of the negative sequence component of the stator currents is calculated by

$$\begin{aligned} i_{qs}^{-} = -\frac{2}{3} I_m^{-} [\cos\left(\theta_s + \theta_i^{-}\right) \sin\left(\theta_s\right) + \cos\left(\theta_s + \frac{2\pi}{3} + \theta_i^{-}\right) \sin\left(\theta_s - \frac{2\pi}{3}\right) \\ + \cos\left(\theta_s - \frac{2\pi}{3} + \theta_i^{-}\right) \sin\left(\theta_s + \frac{2\pi}{3}\right)], \end{aligned} \tag{5.48}$$

which is equivalent to

$$\begin{aligned} i_{qs}^{-} = -\frac{2}{3} I_m^{-} [\frac{1}{2}\left(\sin\left(2\theta_s + \theta_i^{-}\right) - \sin\left(\theta_i^{-}\right)\right) + \frac{1}{2}\left(\sin\left(2\theta_s + \theta_i^{-}\right) - \sin\left(\frac{4\pi}{3} + \theta_i^{-}\right)\right) \\ + \frac{1}{2}\left(\sin\left(2\theta_s + \theta_i^{-}\right) - \sin\left(-\frac{4\pi}{3} + \theta_i^{-}\right)\right)] = -I_m^{-} \sin\left(2\theta_s + \theta_i^{-}\right). \end{aligned} \tag{5.49}$$

Therefore, in a synchronous reference frame, i_{ds}^{+} and i_{qs}^{+} are dc quantities, while i_{ds}^{-} and i_{qs}^{-} are ac quantities with a frequency of $2 f_s$.

Replacing the *dq*-axis components of the positive sequence component of the stator currents into (5.25), the positive sequence component of the active and reactive powers of the stator are given by

$$\begin{cases} P_s^{+} = \frac{3}{2} v_{qs} i_{qs}^{+} \\ Q_s^{+} = \frac{3}{2} v_{qs} i_{ds}^{+}. \end{cases} \tag{5.50}$$

Since v_{qs}, i_{ds}^{+} and i_{qs}^{+} are dc quantities, P_s^{+} and Q_s^{+} are dc quantities and represent the active and reactive power injected by the stator of the DFIG into the grid.

The negative sequence component of the stator currents and the stator voltages will give rise to a new spectral component in both the stator active and reactive powers, given by

$$\begin{cases} \Delta P_s^{sf} = \dfrac{3}{2} v_{qs} i_{qs}^{-} \\ \Delta Q_s^{sf} = \dfrac{3}{2} v_{qs} i_{ds}^{-}. \end{cases} \tag{5.51}$$

Taking into account the fact that i_{ds}^{-} and i_{qs}^{-} are ac quantities with a frequency of $2f_s$, ΔP_s^{sf} and ΔQ_s^{sf} are ac quantities with a frequency of $2f_s$ and they are a direct consequence of the stator fault. Therefore, the appearance of ΔP_s^{sf} and ΔQ_s^{sf} in the stator active and reactive powers spectra can be used as an indicator of stator faults in the DFIG.

In theory, in the considered reference frame, both the active and reactive powers could be used for the detection of the stator fault, because the stator currents i_{ds}^{-} and i_{qs}^{-} have the same amplitude. Considering that the stator active power changes in a much wider range and in a faster way when compared to the reactive power, in this study, the spectrum analysis of the stator reactive power is used for diagnostic purposes.

In the fault diagnostic field, it is important not only to detect the faults but also to quantify their extension. For this purpose, severity factors (*SFs*) are usually defined, giving a measure of how serious those faults are.

For the case of a stator fault, a possible severity factor SF_{sf} is obtained as [60]

$$SF_{sf}(\%) = \frac{\left|\Delta Q_s^{sf}\right|}{Q_n} \times 100\%, \tag{5.52}$$

where $\left|\Delta Q_s^{sf}\right|$ is the amplitude of the oscillating component in the stator reactive power at a frequency of $2f_s$ and Q_n is the rated reactive power of the DFIG.

6.2.2 Analysis of an ITSC fault in the rotor windings

In case the DFIG develops a rotor fault and considering for now that $s>0$, an inverse sequence component appears in the rotor currents, at the frequency of $-sf$. This component produces a primary fault-related spectral component (lower sideband) in all stator currents, at a frequency of [111]

$$f_{lsb} = (1-2s) f_s. \tag{5.53}$$

The interaction of this stator current component with the fundamental component of the stator flux will originate torque oscillations in the generator at a frequency of $2sf_s$ which, in turn, will create speed oscillations at the same frequency. These speed oscillations will give rise to the appearance of a second spectral component (upper sideband) in the stator currents, at a frequency given by [111]

$$f_{usb} = (1+2s)\, f_s. \tag{5.54}$$

Due to the high inertia of the drive train associated with a wind generator, which includes the gearbox, rotor hub and rotor blades, these speed oscillations will be reduced and, consequently, the amplitude of the current spectral component given by (5.54) will be smaller than the amplitude of the stator current component given by (5.53).

The lower sideband component of the stator currents is given by

$$\begin{cases} i_A^{lsb} = I_m^{lsb}\, cos\left((1-2s)\,\omega_s t + \theta_i^{lsb}\right) \\ i_B^{lsb} = I_m^{lsb}\, cos\left((1-2s)\,\omega_s t - \dfrac{2\pi}{3} + \theta_i^{lsb}\right) \\ i_C^{lsb} = I_m^{lsb}\, cos\left((1-2s)\,\omega_s t + \dfrac{2\pi}{3} + \theta_i^{lsb}\right), \end{cases} \tag{5.55}$$

where I_m^{lsb} is the peak value of the lower sideband component of the stator currents and θ_i^{lsb} is the phase angle of i_A^{lsb} with respect to *d*-axis of the synchronous reference frame at *t*=0 s.

The upper sideband component of the stator currents is given by

$$\begin{cases} i_A^{usb} = I_m^{usb}\, cos\left((1+2s)\,\omega_s t + \theta_i^{usb}\right) \\ i_B^{usb} = I_m^{usb}\, cos\left((1+2s)\,\omega_s t - \dfrac{2\pi}{3} + \theta_i^{usb}\right) \\ i_C^{usb} = I_m^{usb}\, cos\left((1+2s)\,\omega_s t + \dfrac{2\pi}{3} + \theta_i^{usb}\right), \end{cases} \tag{5.56}$$

where I_m^{usb} is the peak value of the lower sideband component of the stator currents and θ_i^{usb} is the phase angle of i_A^{usb} with respect to *d*-axis of the synchronous reference frame at *t*=0 s.

The *d*-axis component of the lower sideband component of the stator currents is calculated by

$$i_{ds}^{lsb}=\frac{2}{3}I_m^{lsb}[\cos\left(\theta_s-2s\theta_s+\theta_i^{lsb}\right)\cos\left(\theta_s\right)+\cos\left(\theta_s-2s\theta_s-\frac{2\pi}{3}+\theta_i^{lsb}\right)\cos\left(\theta_s-\frac{2\pi}{3}\right)+\cos\left(\theta_s-2s\theta_s+\frac{2\pi}{3}+\theta_i^{lsb}\right)\cos\left(\theta_s+\frac{2\pi}{3}\right)], \tag{5.57}$$

which is equivalent to

$$\begin{aligned}i_{ds}^{lsb}=\frac{2}{3}I_m^{lsb}[&\frac{1}{2}\left(\cos\left(2\theta_s-2s\theta_s+\theta_i^{lsb}\right)+\cos\left(-2s\theta_s+\theta_i^{lsb}\right)\right)\\&+\frac{1}{2}\left(\cos\left(2\theta_s-2s\theta_s-\frac{4\pi}{3}+\theta_i^{lsb}\right)+\cos\left(-2s\theta_s+\theta_i^{lsb}\right)\right)\\&+\frac{1}{2}\left(\cos\left(2\theta_s-2s\theta_s+\frac{4\pi}{3}+\theta_i^{lsb}\right)+\cos\left(-2s\theta_s+\theta_i^{lsb}\right)\right)]=I_m^{lsb}\cos\left(-2s\theta_s+\theta_i^{lsb}\right).\end{aligned} \tag{5.58}$$

The *q*-axis component of the lower sideband component of the stator currents is calculated by

$$i_{qs}^{lsb}=-\frac{2}{3}I_m^{lsb}[\cos\left(\theta_s-2s\theta_s+\theta_i^{lsb}\right)\sin\left(\theta_s\right)+\cos\left(\theta_s-2s\theta_s-\frac{2\pi}{3}+\theta_i^{lsb}\right)\sin\left(\theta_s-\frac{2\pi}{3}\right)+\cos\left(\theta_s-2s\theta_s+\frac{2\pi}{3}+\theta_i^{lsb}\right)\sin\left(\theta_s+\frac{2\pi}{3}\right)], \tag{5.59}$$

which is equivalent to

$$\begin{aligned}i_{qs}^{lsb}=-\frac{2}{3}I_m^{lsb}[&-\frac{1}{2}\left(\sin\left(2\theta_s-2s\theta_s+\theta_i^{lsb}\right)-\sin\left(-2s\theta_s+\theta_i^{lsb}\right)\right)\\&-\frac{1}{2}\left(\sin\left(2\theta_s-2s\theta_s-\frac{4\pi}{3}+\theta_i^{lsb}\right)-\sin\left(-2s\theta_s+\theta_i^{lsb}\right)\right)\\&-\frac{1}{2}\left(\sin\left(2\theta_s-2s\theta_s+\frac{4\pi}{3}+\theta_i^{lsb}\right)-\sin\left(-2s\theta_s+\theta_i^{lsb}\right)\right)]=I_m^{lsb}\sin\left(-2s\theta_s+\theta_i^{lsb}\right).\end{aligned} \tag{5.60}$$

The *d*-axis component of the upper sideband component of the stator currents is calculated by

$$i_{ds}^{usb}=\frac{2}{3}I_m^{usb}[\cos\left(\theta_s+2s\theta_s+\theta_i^{usb}\right)\cos\left(\theta_s\right)+\cos\left(\theta_s+2s\theta_s-\frac{2\pi}{3}+\theta_i^{usb}\right)\cos\left(\theta_s-\frac{2\pi}{3}\right)+\cos\left(\theta_s+2s\theta_s+\frac{2\pi}{3}+\theta_i^{usb}\right)\cos\left(\theta_s+\frac{2\pi}{3}\right)], \tag{5.61}$$

which is equivalent to

$$\begin{aligned} i_{ds}^{usb} = \frac{2}{3} I_m^{usb} [& \frac{1}{2}\left(\cos\left(2\theta_s + 2s\theta_s + \theta_i^{usb}\right) + \cos\left(2s\theta_s + \theta_i^{usb}\right)\right) \\ & + \frac{1}{2}\left(\cos\left(2\theta_s + 2s\theta_s - \frac{4\pi}{3} + \theta_i^{usb}\right) + \cos\left(2s\theta_s + \theta_i^{usb}\right)\right) \\ & + \frac{1}{2}\left(\cos\left(2\theta_s + 2s\theta_s + \frac{4\pi}{3} + \theta_i^{usb}\right) + \cos\left(2s\theta_s + \theta_i^{usb}\right)\right)] = I_m^{usb} \cos\left(2s\theta_s + \theta_i^{usb}\right). \end{aligned} \tag{5.62}$$

The *q*-axis component of the upper sideband component of the stator currents is calculated by

$$\begin{aligned} i_{qs}^{usb} = -\frac{2}{3} I_m^{usb} [& \cos\left(\theta_s + 2s\theta_s + \theta_i^{usb}\right)\sin\left(\theta_s\right) + \cos\left(\theta_s + 2s\theta_s - \frac{2\pi}{3} + \theta_i^{usb}\right)\sin\left(\theta_s - \frac{2\pi}{3}\right) \\ & + \cos\left(\theta_s + 2s\theta_s + \frac{2\pi}{3} + \theta_i^{usb}\right)\sin\left(\theta_s + \frac{2\pi}{3}\right)], \end{aligned} \tag{5.63}$$

which is equivalent to

$$\begin{aligned} i_{ds}^{usb} = -\frac{2}{3} I_m^{usb} [& -\frac{1}{2}\left(\sin\left(2\theta_s + 2s\theta_s + \theta_i^{usb}\right) - \sin\left(2s\theta_s + \theta_i^{usb}\right)\right) \\ & - \frac{1}{2}\left(\sin\left(2\theta_s + 2s\theta_s - \frac{4\pi}{3} + \theta_i^{usb}\right) - \sin\left(2s\theta_s + \theta_i^{usb}\right)\right) \\ & - \frac{1}{2}\left(\sin\left(2\theta_s + 2s\theta_s + \frac{4\pi}{3} + \theta_i^{usb}\right) - \sin\left(2s\theta_s + \theta_i^{usb}\right)\right)] = I_m^{usb} \sin\left(2s\theta_s + \theta_i^{usb}\right). \end{aligned} \tag{5.64}$$

According to (5.57)-(5.64), in a synchronous reference frame, the stator current components at frequencies given by (5.53) and (5.54) appear as spectral components at a frequency of $2sf_s$.

The lower sideband component of the stator currents and the stator voltages will give rise to a spectral component in both the stator active and reactive powers, given by

$$\begin{cases} P_s^{lsb} = \frac{3}{2} v_{qs} i_{qs}^{lsb} \\ Q_s^{lsb} = \frac{3}{2} v_{qs} i_{ds}^{lsb}. \end{cases} \tag{5.65}$$

Taking into account the fact that i_{ds}^{lsb} and i_{qs}^{lsb} are ac quantities with a frequency of $2sf_s$, P_s^{lsb} and Q_s^{lsb} are also ac quantities with a frequency of $2sf_s$.

The upper sideband component of the stator currents and the stator voltages will give rise to a spectral component at a frequency of $2sf_s$ in both the stator active and reactive powers, given by

$$\begin{cases} P_s^{usb} = \dfrac{3}{2} v_{qs} i_{qs}^{usb} \\ Q_s^{usb} = \dfrac{3}{2} v_{qs} i_{ds}^{usb}. \end{cases} \tag{5.66}$$

Hence, the total rotor fault-related components in the stator active and reactive powers are given by

$$\begin{cases} \Delta P_s^{rf} = P_s^{lsb} + P_s^{usb} \\ \Delta Q_s^{rf} = Q_s^{lsb} + Q_s^{usb}. \end{cases} \tag{5.67}$$

In the general case, where s may be positive or negative, the quantities ΔP_s^{rf} and ΔQ_s^{rf} are ac quantities with a frequency of $|2sf_s|$. The rotor fault can then be detected by the identification of a spectral component at a frequency of $|2sf_s|$ in the total stator active and reactive powers of the DFIG.

A word of caution should be given: if the DFIG operates exactly at synchronous speed, the possibility of detection of the rotor fault will be compromised. In that case, the fault may remain unnoticed until the generator operates at speed different from this value.

It can be shown that the stator and rotor reactive powers of a DFIG operating in healthy conditions and in steady-state (neglecting the copper losses) are given by [60]

$$\begin{cases} Q_r \cong s\left(K_Q - Q_s\right) \\ K_Q = \dfrac{3}{2}\dfrac{\omega_s \psi_{ds}^2}{L_s} = \dfrac{3}{2}\dfrac{\left|\underline{v}_g\right|^2}{\omega_s L_s}, \end{cases} \tag{5.68}$$

where Q_r is the reactive power injected into the rotor of the DFIG, $\left|\underline{v}_g\right|$ is the magnitude of the grid voltage space vector and L_s is the self-inductance of the stator windings. Since the grid voltages are imposed by the grid, K_Q will be a constant value.

Neglecting the rotor transient inductance, if there is a variation in the rotor reactive power, the following relation will apply

$$\Delta Q_s \cong -\frac{\Delta Q_r}{s}. \tag{5.69}$$

For the case of a rotor fault, and inspired in the relation (5.69), the severity factor SF_{rf} is given by [60]

$$SF_{rf}(\%) = \frac{\left|\Delta Q_s^{rf}\right|}{|s| \times Q_n} \times 100\%, \tag{5.70}$$

where $\left|\Delta Q_s^{rf}\right|$ is the oscillating component in the stator reactive power at a frequency of $\left|2sf_s\right|$.

6.3 Diagnostic results

6.3.1 Diagnosis of ITSC faults in the stator windings

To evaluate the proposed diagnostic approach, several simulation and experimental tests for various operating conditions of the DFIG system and with different severity levels of the ITSC fault in the stator windings were carried out.

Fig. 6.1 and Fig. 6.2 show the simulation and experimental results for the DFIG operating at a subsynchronous speed of 1350 rpm, with the reference values of the active and reactive powers set to -2000 W and 0 VAr, respectively. In this test, 1 turn out of 180 turns of the stator winding of phase *A* is short-circuited through a resistance $R_{sc} = 0.08\ \Omega$. The spectra obtained are presented in Fig. 6.3 and Fig. 6.4.

The time waveforms of the current in stator phase *A* along with the short-circuit current (i_{sc}) and the current of the faulty turns (i_{Af}) are presented in Fig. 6.1(a) and Fig. 6.2(a). As seen in these figures, the amplitudes of i_A, i_{sc} and i_{Af} as well as the phase shift between i_A, i_{sc} and i_{Af} obtained with the simulation model are identical to the experimental results.

Despite the stator fault, the time waveforms and spectra of the stator currents are almost identical to the results obtained for the healthy machine, presented in Fig. 5.10 and Fig. 5.11.

As shown in Fig. 6.1(c) and Fig. 6.2(c), the waveforms of both the stator active and reactive powers for this faulty condition have no significant differences when compared to the results obtained for the DFIG operating in the healthy condition. However, as shown in Fig. 6.3(c) and Fig. 6.4(c), the presence of the stator fault causes a component at a frequency of $2f_s$ (100 Hz) in the spectra of the stator active and reactive powers. These results show that even with the limited

short-circuit current, the proposed diagnostic method is able to detect a ITSC fault involving 1 shorted turn.

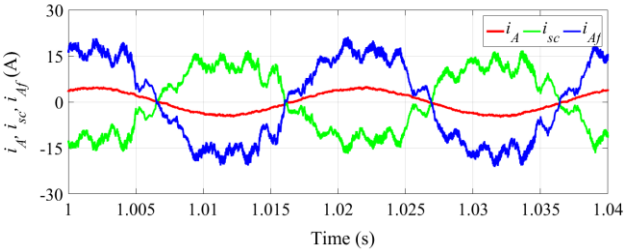

(a) Currents waveforms of the faulty winding

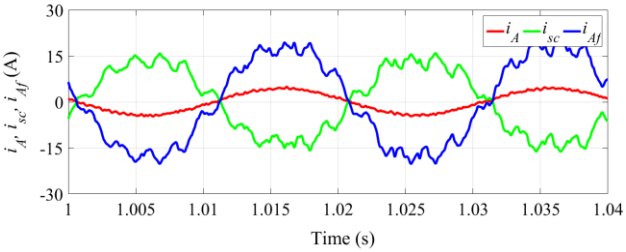

(a) Currents waveforms of the faulty winding

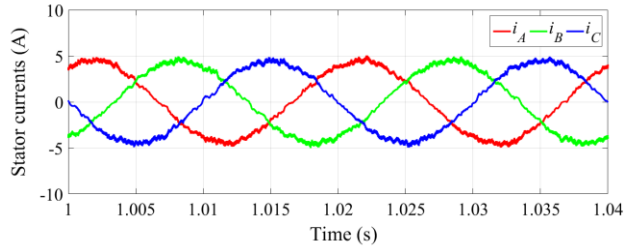

(b) Stator currents waveforms

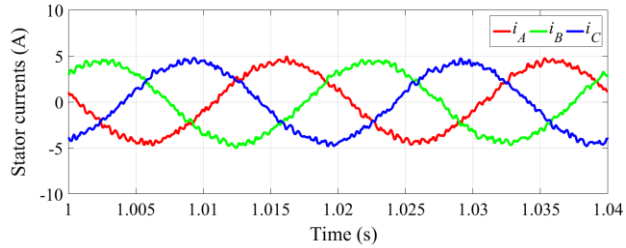

(b) Stator currents waveforms

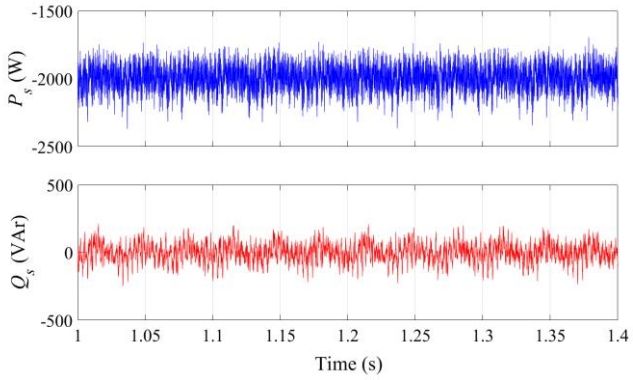

(c) Time waveforms of the stator active and reactive powers

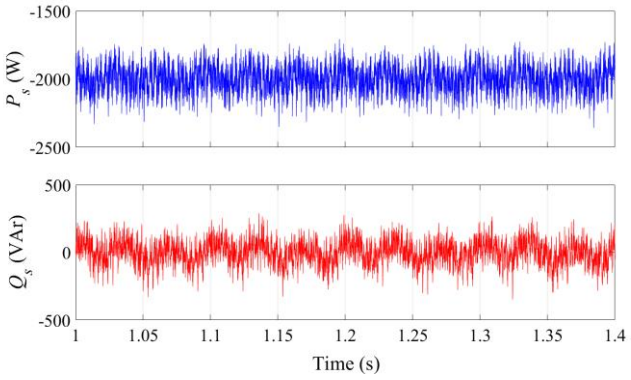

(c) Time waveforms of the stator active and reactive powers

Fig. 6.1. Simulation results for the DFIG operating with 1 short-circuited turn in phase A of the stator windings ($n = 1350$ rpm, $P_s^* = -2000$ W, $Q_s^* = 0$ VAr).

Fig. 6.2. Experimental results for the DFIG operating with 1 short-circuited turn in phase A of the stator windings ($n = 1350$ rpm, $P_s^* = -2000$ W, $Q_s^* = 0$ VAr).

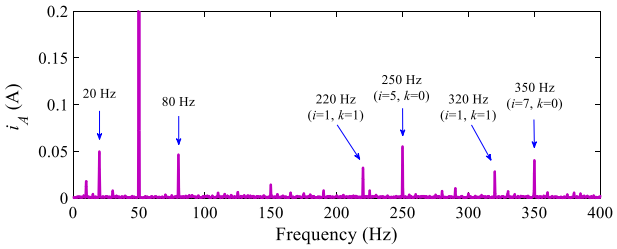

(a) Spectrum of stator current i_A

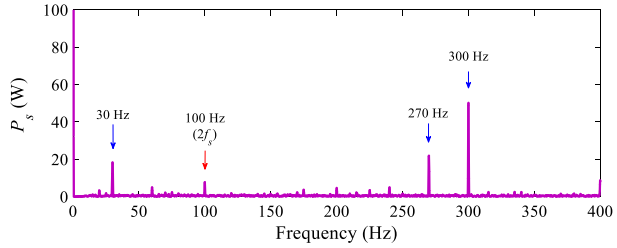

(b) Spectrum of stator active power

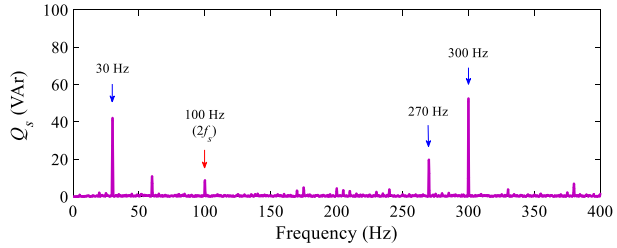

(c) Spectrum of stator reactive power

Fig. 6.3. Simulation spectra for the DFIG operating with 1 short-circuited turn in phase A of the stator windings ($n = 1350$ rpm, $P_s^* = -2000$ W, $Q_s^* = 0$ VAr).

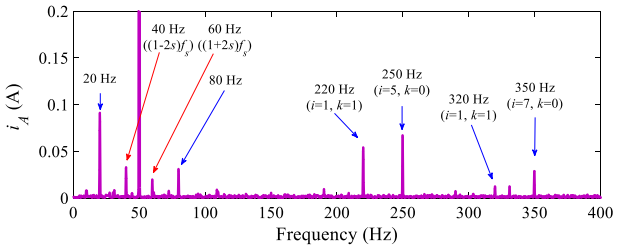

(a) Spectrum of stator current i_A

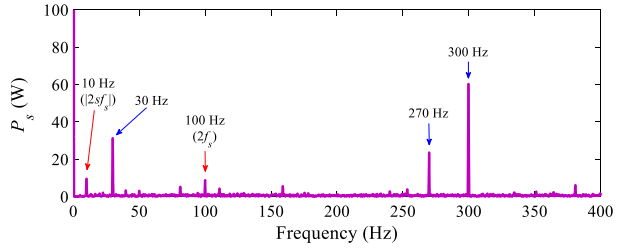

(b) Spectrum of stator active power

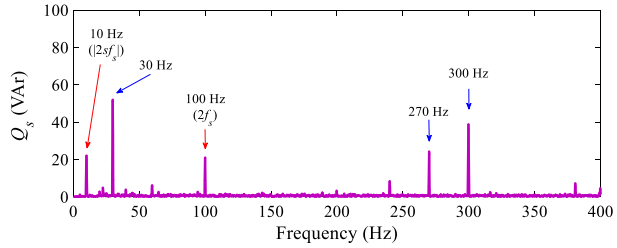

(c) Spectrum of stator reactive power

Fig. 6.4. Experimental spectra for the DFIG operating with 1 short-circuited turn in phase A of the stator windings ($n = 1350$ rpm, $P_s^* = -2000$ W, $Q_s^* = 0$ VAr).

Table 6.1 contains experimental results covering the amplitudes of the stator active and reactive power components at a frequency of $2f_s$ ($|\Delta Q_s^{sf}|$ and $|\Delta P_s^{sf}|$) for the DFIG operating with 1 short-circuited turn in stator phase A and for various values of P_s^*, Q_s^* and rotor speed. The values of $|\Delta Q_s^{sf}|$ and $|\Delta P_s^{sf}|$ for the DFIG operating with 1 short-circuited turn in phase A of the stator windings and for different values of the rotor speed are listed in Table 6.2. These results show that for these operating conditions, the values of $|\Delta Q_s^{sf}|$ are larger than $|\Delta P_s^{sf}|$. Therefore, the value of $|\Delta Q_s^{sf}|$ is more appropriate for the detection of ITSC faults in the stator windings of the DFIG.

According to (5.52), and taking into account that Q_n=4294 VAr, the severity factor related to the stator fault was calculated and the obtained results are also listed in Table 6.1 and Table 6.2. These results reveal that this severity factor is highly independent of the different operating

conditions of the DFIG, thus being a good indicator about the presence of ITSC faults in the stator windings of the DFIG.

Table 6.1. Evolution of $|\Delta Q_s^{sf}|$ and $|\Delta P_s^{sf}|$ for different values of P_s^* and Q_s^*, obtained by experimental tests ($n = 1350$ rpm and $N_{SC} = 1$).

P_s^* (W)	0	0	-1000	-2000
Q_s^* (VAr)	0	-1000	-500	0
$\|\Delta P_s^{sf}\|$ (W)	10	8.5	9	9
$\|\Delta Q_s^{sf}\|$ (VAr)	19	18	18	21
SF_{sf} (%)	0.44	0.42	0.42	0.49

Table 6.2. Evolution of $|\Delta Q_s^{sf}|$ and $|\Delta P_s^{sf}|$ for different values of rotor speed, obtained by experimental tests (P_s^*=-2000 W, $Q_s^* = 0$ VAr and $N_{SC} = 1$).

n (rpm)	1350	1500	1650
$\|\Delta P_s^{sf}\|$ (W)	9	10.5	11
$\|\Delta Q_s^{sf}\|$ (VAr)	21	23	24
SF_{sf} (%)	0.49	0.53	0.55

Fig. 6.5 and Fig. 6.6 show the results for the DFIG operating at a subsynchronous speed of 1350 rpm, when 7 turns out of 180 turns of the stator phase *A* are short-circuited through a limiting resistor $R_{sc} = 0.6\ \Omega$. The reference values of the active and reactive powers were set to -2000 W and 0 VAr, respectively. The spectra obtained are presented in Fig. 6.7 and Fig. 6.8.

The time waveforms of the stator phase *A* current along with the short-circuit current and the current of the faulty turns are shown in Fig. 6.5(a) and Fig. 6.6(a). It is worthy to mention that in both the simulation and experimental tests i_{Af} was limited to almost 150% of the machine rated current. Without the limitating resistance, i_{Af} would be around 800% of rated current, very likely damaging permanently the machine.

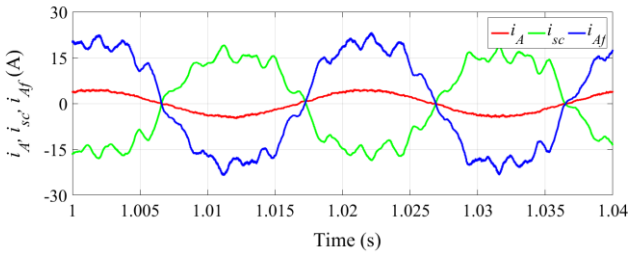

(a) Currents waveforms of the faulty winding

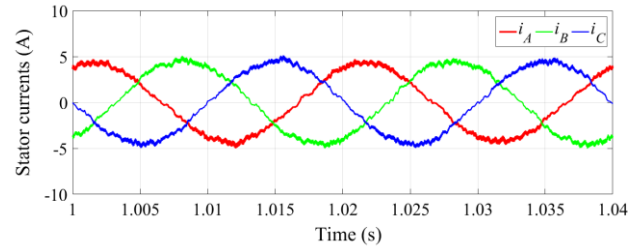

(b) Stator currents waveforms

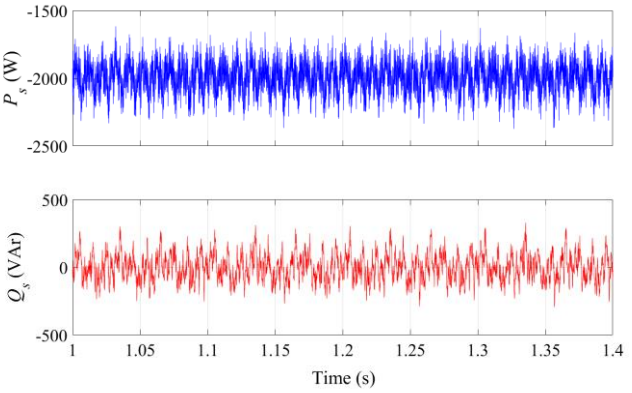

(c) Time waveforms of stator active and reactive powers

Fig. 6.5. Simulation results for the DFIG operating with 7 short-circuited turns in phase A of the stator windings ($n = 1350$ rpm, $P_s^* = -2000$ W, $Q_s^* = 0$ VAr).

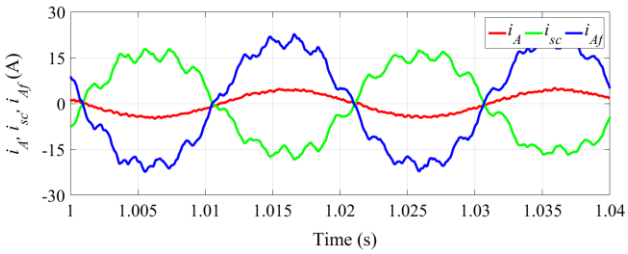

(a) Currents waveforms of the faulty winding

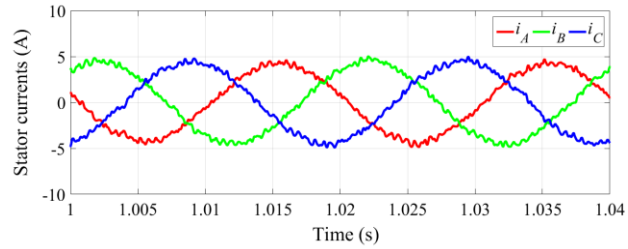

(b) Stator currents waveforms

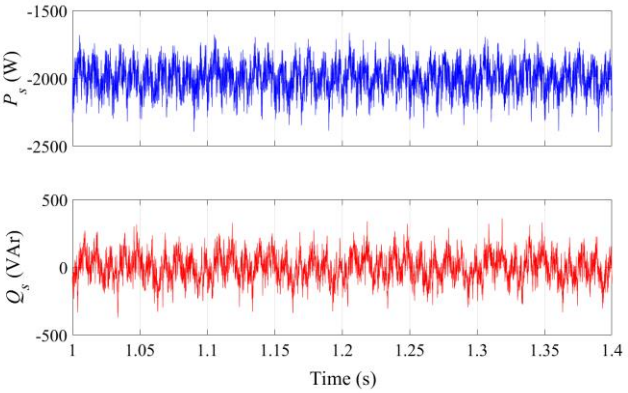

(c) Time waveforms of stator active and reactive powers

Fig. 6.6. Experimental results for the DFIG operating with 7 short-circuited turns in phase A of the stator windings ($n = 1350$ rpm, $P_s^* = -2000$ W, $Q_s^* = 0$ VAr).

As shown in Fig. 6.5(b) and Fig. 6.6(b), due to the stator fault, the stator current waveforms become slightly unbalanced. The spectrum of the stator current shows that the stator fault leads to the appearance of a third harmonic in the stator currents. Analyzing the phase of the third harmonic in the stator currents proves that they have a negative sequence component. However, this harmonic may exist even in the healthy machine when it is fed by an unbalanced supply system. Furthermore, it is very difficult to quantify the extension of the fault using this spectral component, because there is not a direct relationship between this component and the extension of the fault

[131]. Therefore, in this work, the third harmonic of the stator currents is not used for diagnostic purposes.

Comparing the results for the healthy operation of the DFIG (see Fig. 5.10 and Fig. 5.11) with the results herein under analysis, the waveforms of both the stator active and reactive powers have more oscillations. These oscillations also manifest themselves in the spectra of the stator active and reactive powers as a component at the frequency of $2f_s$ (100 Hz), as presented in Fig. 6.7(b), Fig. 6.7(c), Fig. 6.8(b) and Fig. 6.8(c). Moreover, the interaction of the third harmonic with a negative sequence component present in the three stator currents with the fundamental component of stator supply voltages gives rise to a component at a frequency of 200 Hz in both the stator active and reactive powers.

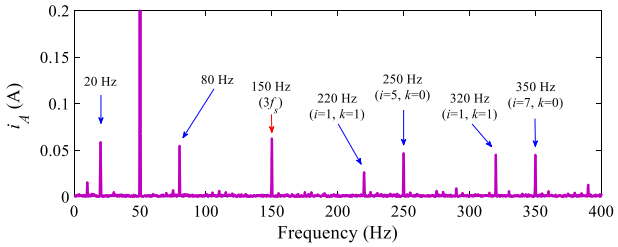

(a) Spectrum of stator current i_A

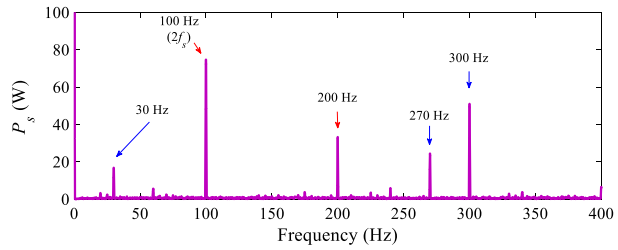

(b) Spectrum of stator active power

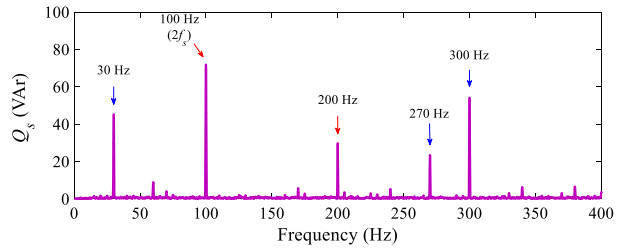

(c) Spectrum of stator reactive power

Fig. 6.7. Simulation spectra for the DFIG operating with 7 short-circuited turns in phase A of the stator windings ($n = 1350$ rpm, $P_s^* = -2000$ W, $Q_s^* = 0$ VAr).

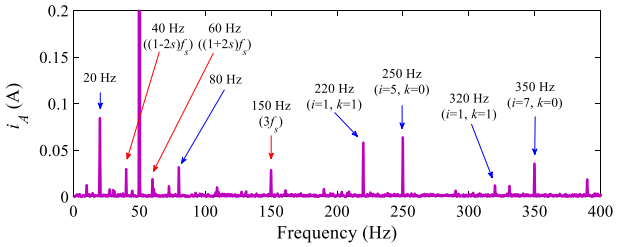

(a) Spectrum of stator current i_A

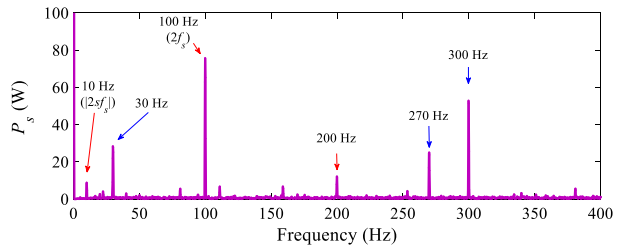

(b) Spectrum of stator active power

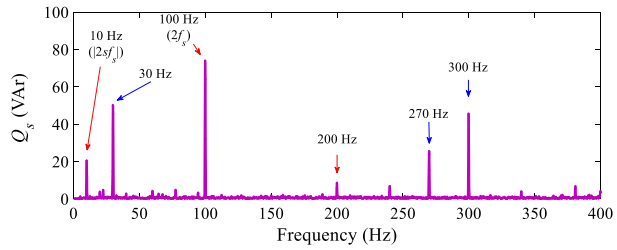

(c) Spectrum of stator reactive power

Fig. 6.8. Experimental spectra for the DFIG operating with 7 short-circuited turns in phase A of the stator windings ($n = 1350$ rpm, $P_s^* = -2000$ W, $Q_s^* = 0$ VAr).

The spectra of the stator active and reactive powers for the DFIG operating at a supersynchronous speed of 1650 rpm and with 7 short-circuited turns in phase *A* of the stator windings are presented in Fig. 6.9 and Fig. 6.10, respectively. Similarly to the subsynchronous operation of the DFIG, the stator fault gives rise to the component at the frequency of $2f_s$ in the spectra of the stator active and reactive powers. In addition, the interaction of the fundamental component of the supply voltage and the third harmonic component of the stator currents generates a component at a frequency of 200 Hz in both the stator active and reactive powers.

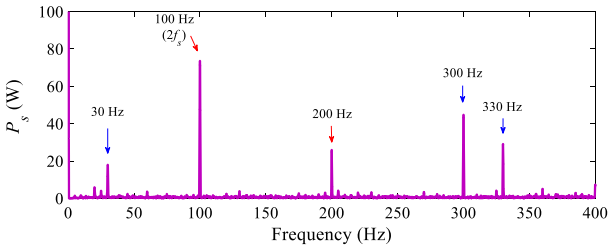

(a) Spectrum of stator active power

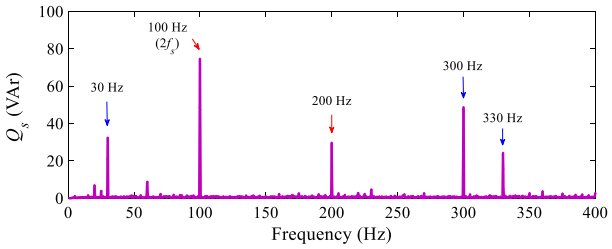

(b) Spectrum of stator reactive power

Fig. 6.9. Simulation spectra for the DFIG operating with 7 short-circuited turns in phase *A* of the stator windings ($n = 1650$ rpm, $P_s^* = -2000$ W, $Q_s^* = 0$ VAr).

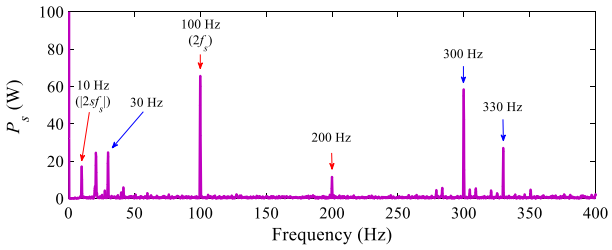

(a) Spectrum of stator active power

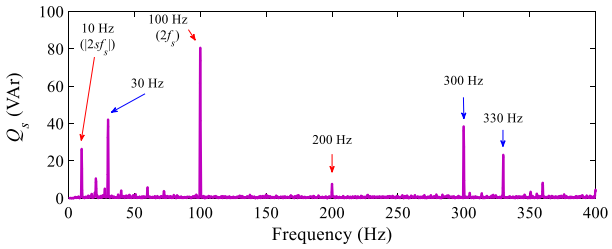

(b) Spectrum of stator reactive power

Fig. 6.10. Experimental spectra for the DFIG operating with 7 short-circuited turns in phase *A* of the stator windings ($n = 1650$ rpm, $P_s^* = -2000$ W, $Q_s^* = 0$ VAr).

Several experimental tests were also carried out for other DFIG operating conditions, namely for different values of the injected active and reactive powers and different values of the rotor speed. The values of $|\Delta Q_s^{sf}|$ and $|\Delta P_s^{sf}|$ for the DFIG operating with 7 short-circuited turns in phase *A* of the stator windings and for various values of P_s^* and Q_s^*, obtained by experimental tests, are listed in Table 6.3. Table 6.4 presents the values of $|\Delta Q_s^{sf}|$ and $|\Delta P_s^{sf}|$ for the DFIG

operating with 7 short-circuited turns in phase *A* of the stator windings and for different values of the rotor speed. These results show that the values of $|\Delta Q_s^{sf}|$ and $|\Delta P_s^{sf}|$ are highly independent for different operating conditions of the DFIG. In all tests, the variation of $|\Delta Q_s^{sf}|$ and $|\Delta P_s^{sf}|$ was in the range [73.5 83.1] VAr and [65.6 79.3] W.

According to the data listed in these tables, both the active and reactive powers can be used for the detection of ITSC faults in the stator windings of DFIG. However, considering the fact that compared to the active power, the stator reactive power changes in a much narrower range and in a slower way, the spectrum analysis of the stator reactive power is more suitable for fault diagnostic purposes.

Table 6.3. Evolution of $|\Delta Q_s^{sf}|$ and $|\Delta P_s^{sf}|$ for various values of P_s^* and Q_s^*, obtained by experimental tests ($n = 1350$ rpm and $N_{SC} = 7$).

P_s^* (W)	0	0	0	-500	-1000	-1000	-1500	-2000	-2500
Q_s^* (VAr)	0	-500	-1000	0	0	-500	0	0	0
$\|\Delta P_s^{sf}\|$ (W)	76.4	76.3	76.6	78	79.3	76.7	74	74.9	72.8
$\|\Delta Q_s^{sf}\|$ (VAr)	80.2	78	81.2	80.5	81.2	75.3	73.5	74.1	77.2

Table 6.4. Evolution of $|\Delta Q_s^{sf}|$ and $|\Delta P_s^{sf}|$ for various values of rotor speed, obtained by experimental tests (P_s^* =-2000 W, $Q_s^* = 0$ VAr and $N_{SC} = 7$).

n (rpm)	1275	1350	1425	1500	1575	1650	1725
$\|\Delta P_s^{sf}\|$ (W)	72.5	74.9	67.7	71.6	66.3	65.6	70.4
$\|\Delta Q_s^{sf}\|$ (VAr)	73.7	74.1	73.7	79.2	75.9	80.5	83.1

According to (5.52), the severity factor related to the stator fault was calculated for these operating conditions of the DFIG. The evolution of the severity factor as a function of different generator operating conditions, namely, active and reactive powers injected into the grid and rotor

speed is shown in Fig. 6.11. These results clearly show that this severity factor is highly independent of all operating conditions of the DFIG, thus constituting a good indicator about the presence of stator ITSC faults in the DFIG.

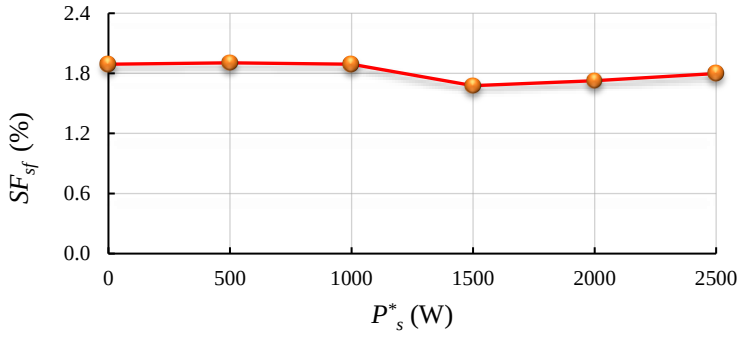

(a) As a function of the stator active power ($n = 1350$ rpm and $Q^*_s = 0$ VAr)

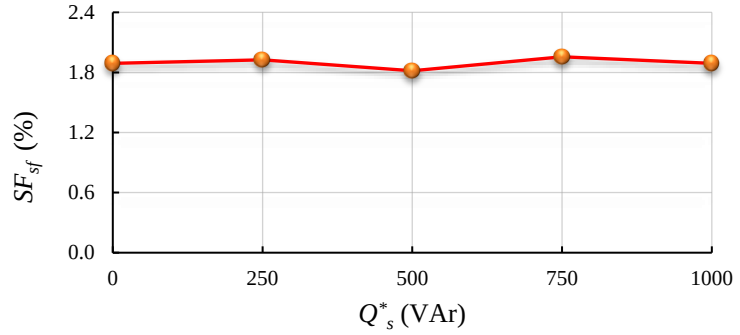

(b) As a function of the stator reactive power ($n = 1350$ rpm and $P^*_s = 0$ W)

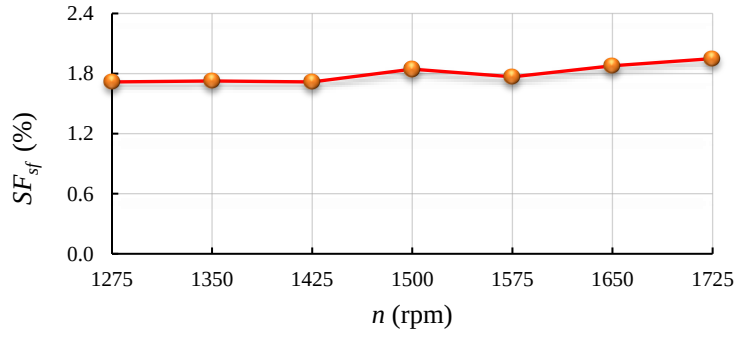

(c) As a function of the rotor speed ($P^*_s = -2000$ W and $Q^*_s = 0$ VAr)

Fig. 6.11. Evolution of SF_{sf} with 7 short-circuited turns in phase A of the stator windings, obtained from the experimental tests.

The evolution of $|\Delta Q_s^{sf}|$ and $|\Delta P_s^{sf}|$ as a function of the number of stator short-circuited turns, when $P_s^* = -2000$ W and $Q_s^* = 0$ VAr and for three different values of the rotor speed, is listed in Table 6.5. It is worthy mentioning that the current in the short-circuited turns for all results in this table was limited to around 150% of rated current. The value of R_{sc} for each severity of the fault is inserted in this table. The results show that by increasing the severity of the fault, the amplitudes of the faulty components also increase.

Table 6.5. Evolution of $|\Delta Q_s^{sf}|$ and $|\Delta P_s^{sf}|$ as a function of N_{SC}, obtained by experimental tests ($P_s^* = -2000$ W and $Q_s^* = 0$ VAr).

Short-circuited turns number		0	1	2	4	7	15
R_{sc} (Ω)		--	0.08	0.16	0.31	0.6	1.4
n=1350 rpm (s=0.1)	$\|\Delta P_s^{sf}\|$ (W)	10.3	9	16.2	42.6	74.9	152.2
	$\|\Delta Q_s^{sf}\|$ (VAr)	13.8	21	31	45.2	74.1	165
n=1500 rpm (s=0)	$\|\Delta P_s^{sf}\|$ (W)	9	10.5	19.7	41.9	71.6	148.6
	$\|\Delta Q_s^{sf}\|$ (VAr)	9.1	23	33.8	58	79.2	167
n=1650 rpm (s=-0.1)	$\|\Delta P_s^{sf}\|$ (W)	6.9	11	21.1	42.1	65.6	150.6
	$\|\Delta Q_s^{sf}\|$ (VAr)	17	24	36.2	59	80.5	179

The evolution of the severity factor as a function of the number of short-circuited turns and for three different values of the rotor speed is shown in Fig. 6.11. These results substantiate that the obtained severity factor is a good indicator for detection and qualification of ITSC faults in the stator windings of the DFIG.

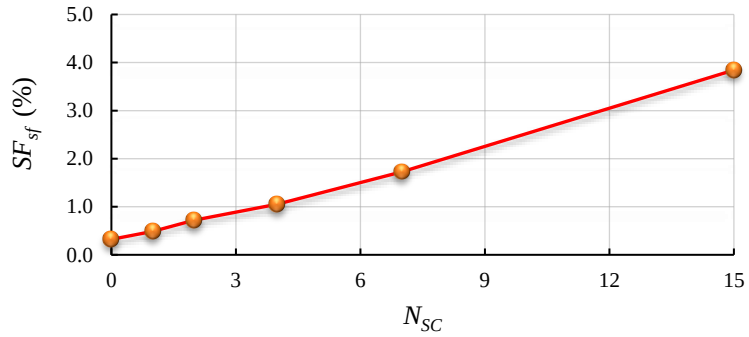

(a) n=1350 rpm

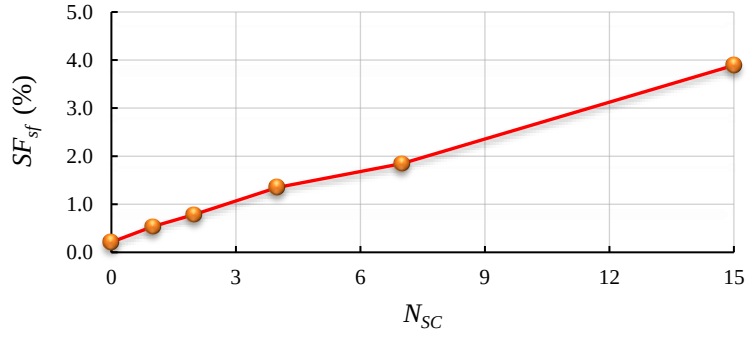

(b) n=1500 rpm

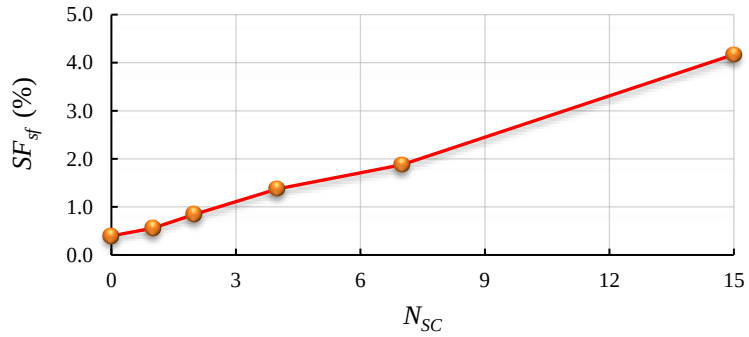

(c) n=1650 rpm

Fig. 6.12. Evolution of the severity factor for stator ITSC faults as a function of N_{SC}, obtained from the experimental tests (P_s^* = –2000 W and Q_s^*=0 VAr).

6.3.2 Diagnosis of ITSC faults in the rotor windings

In this subsection, diagnostic results for ITSC faults in the rotor windings of the DFIG are presented. On the contrary to the stator windings, the induced voltage in the rotor windings is proportional to the rotor slip. Taking into account that in the real application of the DFIG system,

the slip is confined to a range of ±0.3, the induced voltage in the short-circuited turns in the case of a rotor fault is smaller than that for a stator fault. This will also lead to significant changes in the amplitude of the short-circuit current which will have a huge influence on the detectability of the fault in the rotor windings.

In the experimental tests, with the DFIG operating with 1 short-circuited turn in the rotor windings, due to the resistance of the ring and brushes ($R_{sc} = 0.1\,\Omega$), the amplitude of i_{sc} was small. Therefore, the amplitudes of the components related to the rotor fault in both the stator active and reactive power spectra at a frequency of $|2sf_s|$ ($|\Delta P_s^{rf}|$ and $|\Delta Q_s^{rf}|$) were negligible. Of course, the values of $|i_{sc}|$, $|\Delta P_s^{rf}|$ and $|\Delta Q_s^{rf}|$ are dependent on the value of R_{sc}. For example, when $R_{sc} = 0\ \Omega$ (in the simulation model) and with the DFIG operating at a speed of 1350 rpm, the values of $|i_{sc}|$, $|\Delta P_s^{rf}|$ and $|\Delta Q_s^{rf}|$ were estimated as 39 A, 21 W and 22 VAr, respectively.

Fig. 6.13 and Fig. 6.14 show the results for the DFIG operating at a subsynchronous speed of 1350 rpm, when 7 turns out of 108 turns of rotor phase *a* were short-circuited. The reference values of the active and reactive powers were set to -2000 W and 0 VAr, respectively. The spectra obtained for this circumstances are presented in Fig. 6.15 and Fig. 6.16. As shown in these figures, despite the presence of the rotor ITSC fault, the stator and rotor currents waveforms are almost balanced. Since the DFIG is operating at a rotor speed of 1350 rpm (s=0.1), the induced voltage in the short-circuited turns in the rotor is small making the short-circuit current in the affected turns much lower than the one corresponding to a stator fault, at identical situation.

As shown in Fig. 6.15(a) and Fig. 6.16(a), the existence of the rotor ITSC fault gives rise to two components at frequencies of $(1-2s)f_s$ (40 Hz) and $(1+2s)f_s$ (60 Hz) in the stator current spectrum. The waveforms of the stator active and reactive powers for this faulty condition have more oscillations when compared to the results obtained for the DFIG operating in healthy conditions. As shown in these figures, the existence of the rotor ITSC fault produces a component related to the rotor fault in both the stator active and reactive power spectra at a frequency of $|2sf_s|$ (10 Hz). Once again, the simulation results are in good agreement with the experimental results.

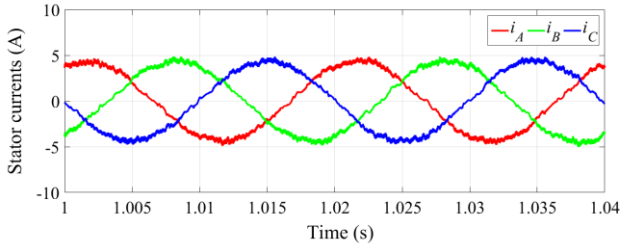

(a) Stator currents waveforms

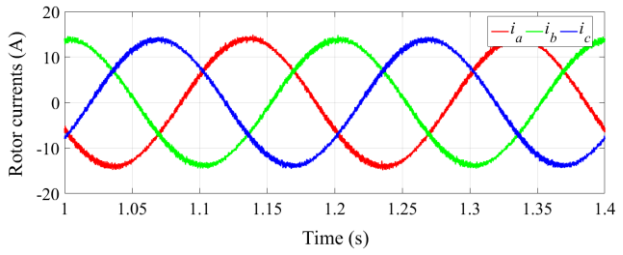

(b) Rotor currents waveforms

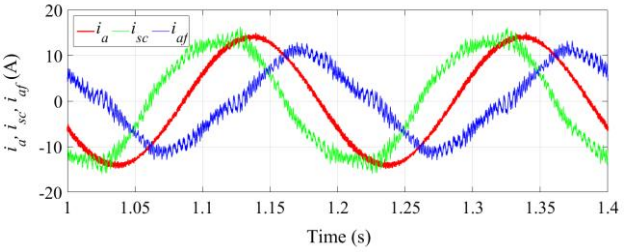

(c) Currents waveforms of the faulty winding

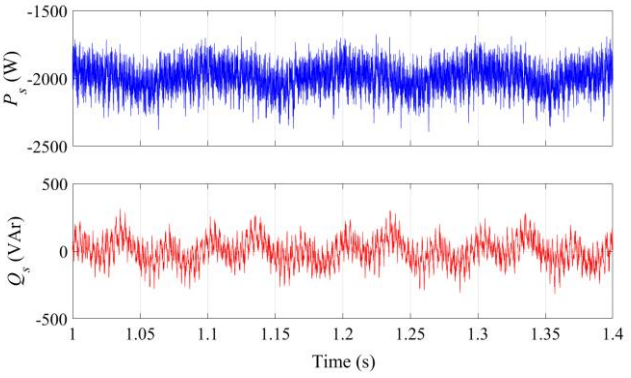

(d) Time waveforms of stator active and reactive powers

Fig. 6.13. Simulation results for the DFIG operating with 7 short-circuited turns in phase a of the rotor windings ($n = 1350$ rpm, $P_s^* = -2000$ W, $Q_s^* = 0$ VAr) .

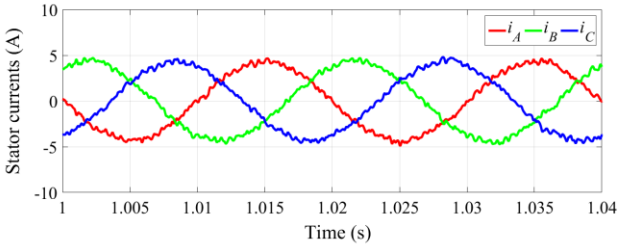

(a) Stator currents waveforms

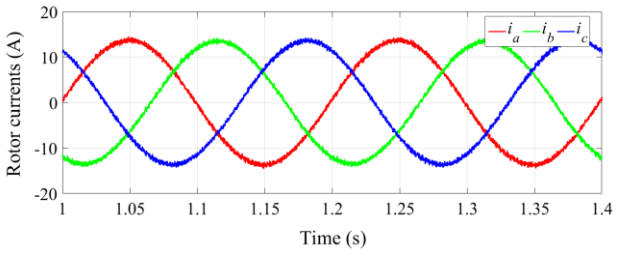

(b) Rotor currents waveforms

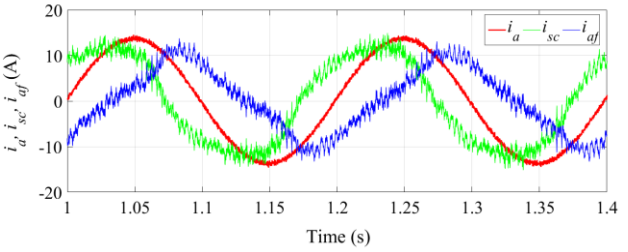

(c) Currents waveforms of the faulty winding

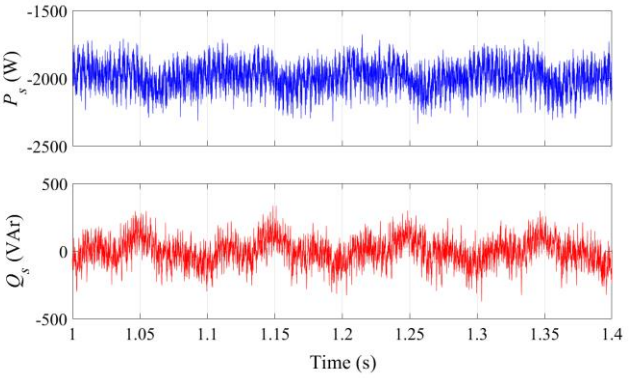

(d) Time waveforms of stator active and reactive powers

Fig. 6.14. Experimental results for the DFIG operating with 7 short-circuited turns in phase a of the rotor windings ($n = 1350$ rpm, $P_s^* = -2000$ W, $Q_s^* = 0$ VAr) .

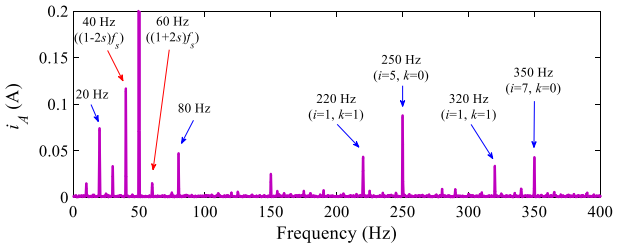

(a) Spectrum of stator current i_A

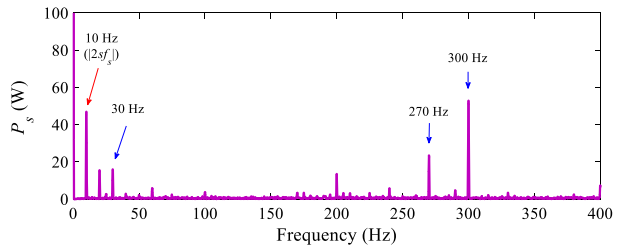

(c) Spectrum of stator active power

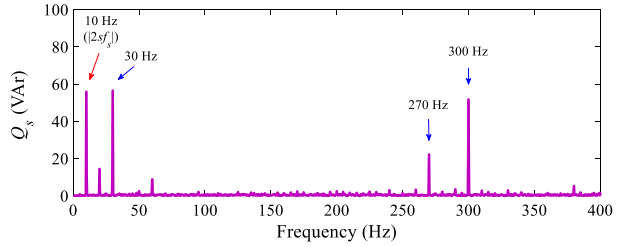

(d) Spectrum of stator reactive power

Fig. 6.15. Simulation spectra for the DFIG operating with 7 short-circuited turns in phase a of the rotor windings ($n = 1350$ rpm, $P_s^* = -2000$ W, $Q_s^* = 0$ VAr).

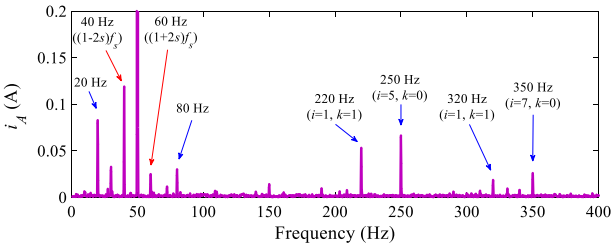

(a) Spectrum of stator current i_A

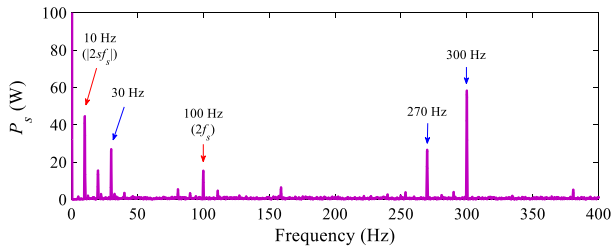

(c) Spectrum of stator active power

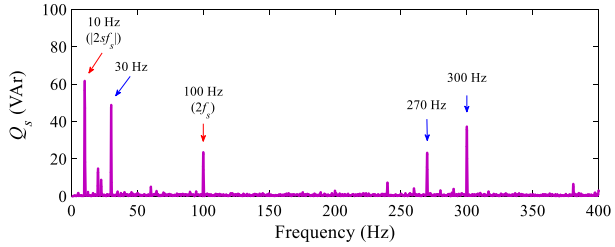

(d) Spectrum of stator reactive power

Fig. 6.16. Experimental spectra for the DFIG operating with 7 short-circuited turns in phase a of the rotor windings ($n = 1350$ rpm, $P_s^* = -2000$ W, $Q_s^* = 0$ VAr).

The spectra for the DFIG operating at a supersynchronous speed of 1650 rpm, obtained from the simulation model and experimental tests, are presented in Fig. 6.17 and Fig. 6.18, respectively. Similarly to the subsynchronous case, the presence of the rotor fault gives rise to the appearance of the component at a frequency of $|2sf_s|$ (10 Hz) in the spectra of both stator powers.

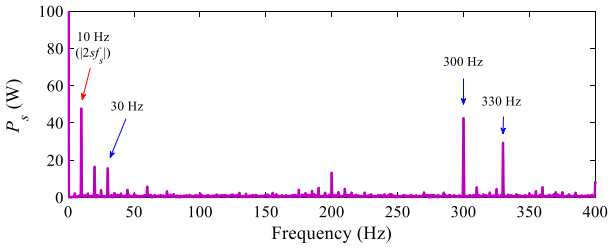

(a) Spectrum of stator active power

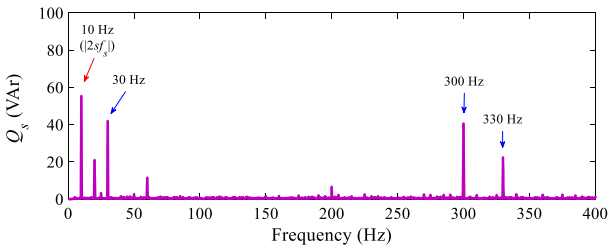

(b) Spectrum of stator reactive power

Fig. 6.17. Simulation spectra for the DFIG operating with 7 short-circuited turns in phase a of the rotor windings ($n = 1650$ rpm, $P_s^* = -2000$ W, $Q_s^* = 0$ VAr) .

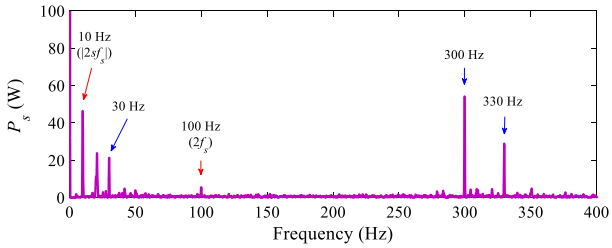

(a) Spectrum of stator active power

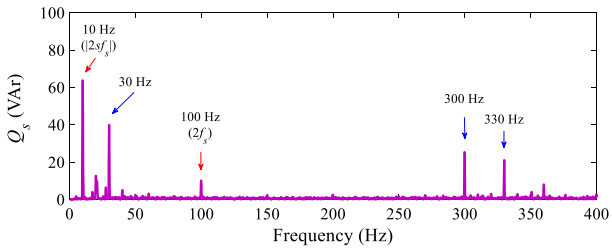

(b) Spectrum of stator reactive power

Fig. 6.18. Experimental spectra for the DFIG operating with 7 short-circuited turns in phase a of the rotor windings ($n = 1650$ rpm, $P_s^* = -2000$ W, $Q_s^* = 0$ VAr) .

Various experimental tests were also carried out for other DFIG operating conditions, namely for different values of the injected active and reactive powers and different values of the rotor speed and with different fault severity.

Table 6.6 presents the values of $|\Delta P_s^{rf}|$ and $|\Delta Q_s^{rf}|$ for the DFIG operating with 7 short-circuited turns in phase *a* of the rotor windings and for various values of P_s^* and Q_s^*, obtained by experimental tests. As can be seen, the values of $|\Delta P_s^{rf}|$ and $|\Delta Q_s^{rf}|$ are almost independent of the values of active and reactive power injected into the grid. Table 6.4 presents the values of $|\Delta P_s^{rf}|$ and $|\Delta Q_s^{rf}|$ for the DFIG operating with 7 short-circuited turns in the rotor winding and for different rotor speeds. As stated before, the values of $|\Delta P_s^{rf}|$ and $|\Delta Q_s^{rf}|$ at rotor speeds close to the synchronous speed are very small. Therefore, the rotor speed influences the values of $|\Delta P_s^{rf}|$ and $|\Delta Q_s^{rf}|$.

Table 6.6. Evolution of $|\Delta Q_s^{rf}|$ and $|\Delta P_s^{rf}|$ for various values of P_s^* and Q_s^*, obtained by experimental tests ($n = 1350$ rpm and $N_{SC} = 7$).

P_s^* (W)	0	0	0	-500	-1000	-1000	-1500	-2000	-2500
Q_s^* (VAr)	0	-500	-1000	0	0	-500	0	0	0
$\|\Delta P_s^{rf}\|$ (W)	48	45.8	47.4	48.2	46.5	47.1	47.1	44.7	44.6
$\|\Delta Q_s^{rf}\|$ (VAr)	61.4	62	66	63	62.1	64.6	64.2	62	63.1

Table 6.7. Evolution of $|\Delta Q_s^{rf}|$ and $|\Delta P_s^{rf}|$ for various values of rotor speed, obtained by experimental tests (P_s^*=-2000 W, $Q_s^* = 0$ VAr and $N_{SC} = 7$).

n (rpm)	1275	1350	1425	1575	1650	1725
$\|\Delta P_s^{rf}\|$ (W)	66.9	44.7	25.7	21.1	46.4	65.9
$\|\Delta Q_s^{rf}\|$ (VAr)	87	62	50	41	63.7	89.5

The behavior of the severity factor defined by (5.70), as a function of different DFIG operating conditions, namely rotor speed and active and reactive powers injected into the grid, is shown in Fig. 6.19. As can be seen, this severity factor is almost independent of the values of active and reactive power injected into the grid. Nevertheless, as stated before, the rotor speed influences the obtained results. The closer the rotor speed is of the synchronous speed, the minor are the effects of the rotor ITSC faults in all stator quantities (currents, active power, reactive power, *etc.*). Therefore, in such operating conditions of the DFIG, the ITSC fault in the rotor windings cannot be detected by the proposed method. Considering that the value of $|i_{af}|$ in such operating conditions is small, the rotor ITSC fault does not pose any serious heat for the rotor windings of the DFIG when it operates close to the synchronous speed. Hence, the diagnosis of the rotor fault can be performed when the DFIG is operating at a speed different from the synchronous one, thus not invalidating the use of the proposed diagnostic approach.

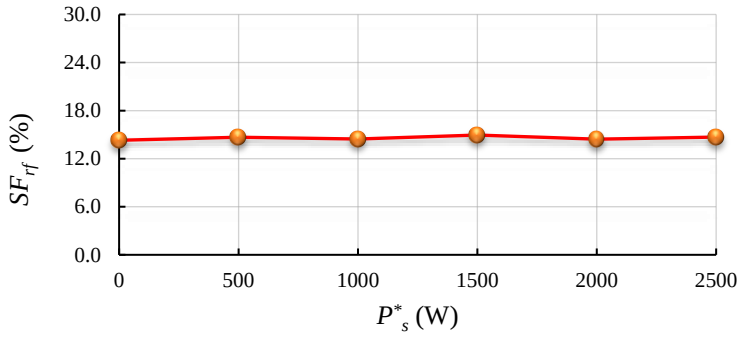

(a) As a function of the stator active power ($n = 1350$ rpm and $Q_s^* = 0$ VAr)

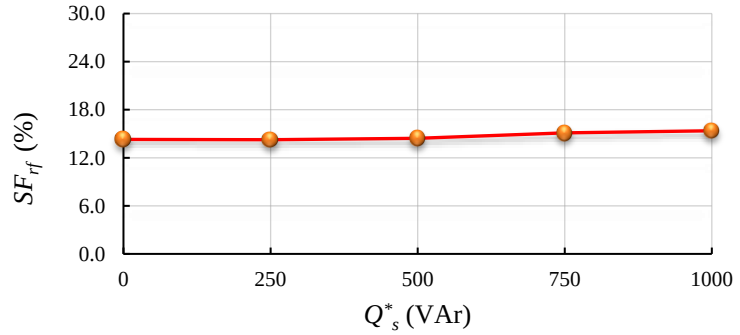

(b) As a function of the stator reactive power ($n = 1350$ rpm and $P_s^* = 0$ W)

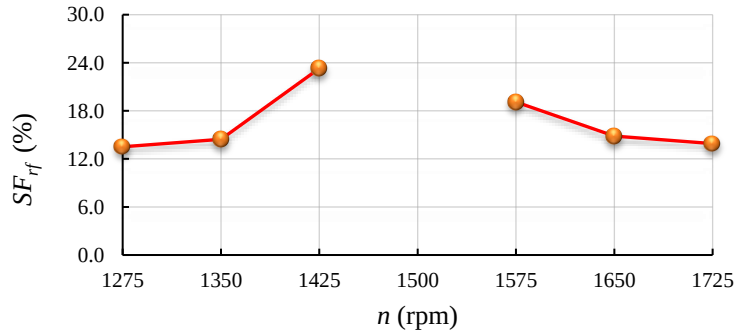

(c) As a function of the rotor speed ($P_s^* = -2000$ W and $Q_s^* = 0$ VAr)

Fig. 6.19. Evolution of the severity factor for rotor ITSC faults with 7 short-circuited turns in phase a, obtained from experimental tests.

Table 6.8 presents the values of $|\Delta P_s^{rf}|$ and $|\Delta Q_s^{rf}|$ for different numbers of rotor short-circuited turns, for two different values of the rotor speed. According to the results presented in this table, by increasing the severity of the fault, the amplitudes of these components also increase.

The behavior of the severity factor defined in (5.70), as a function of the number of the short-circuited turns and for three different values of the rotor speed, is shown in Fig. 6.20. These results substantiate that the severity factor defined is a good indicator of ITSC faults in the rotor windings of the DFIG.

Table 6.8. Evolution of $|\Delta Q_s^{rf}|$ and $|\Delta P_s^{rf}|$ as a function of N_{SC} ($P_s^* = -2000$ W and $Q_s^*=0$ VAr).

Short-circuited turns number		0	1	7	17
n=1350 rpm (s=0.1)	$\|\Delta P_s^{rf}\|$ (W)	9.3	9.4	44.7	139.8
	$\|\Delta Q_s^{rf}\|$ (VAr)	21.6	21.8	62	172.3
n=1650 rpm (s=-0.1)	$\|\Delta P_s^{rf}\|$ (W)	16.3	17.3	46.4	113.3
	$\|\Delta Q_s^{rf}\|$ (VAr)	26	29.2	63.7	156

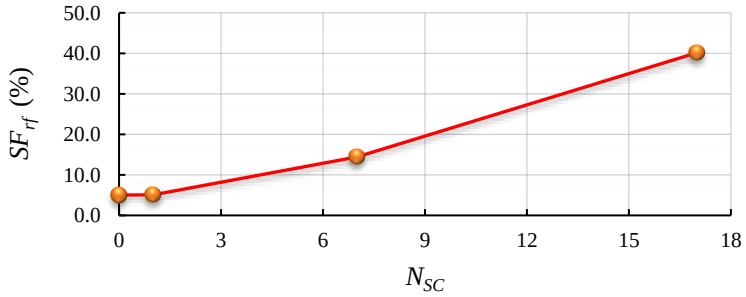

(a) n=1350 rpm

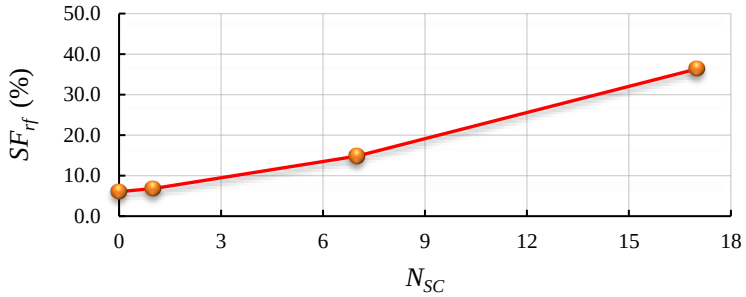

(b) n=1650 rpm

Fig. 6.20. Evolution of SF_{rf} as a function of N_{SC}, obtained from experimental tests ($P_s^* = -2000$ W and $Q_s^*=0$ VAr).

6.4 Final remarks

In this chapter, a literature review related to the existing methods for detection of ITSC faults in the stator and rotor windings of DFIG systems was presented.

Then, the stator reactive power was proposed as a diagnostic method for the detection and identification of ITSC faults in the stator and rotor windings of a DFIG. For the case of a stator fault, the detection of a spectral component at two times the grid frequency ($2f_s$) is an indicator of the presence of this type of the fault, while a rotor fault can be detected by the identification of a spectral component at a frequency of $|2sf_s|$. Furthermore, for each type of fault, a severity factor that indicates the extension of the fault was defined.

The effectiveness of the proposed diagnostic method to detect ITSC faults in the stator and rotor windings of a DFIG was evaluated by extensive experimental tests that were performed for different DFIG operating conditions, namely for different values of the active and reactive power injected into the grid and different values of the rotor speed.

The results obtained from the simulation model and experimental tests prove that the value of the severity factor related to the stator fault is highly independent of several DFIG operating conditions namely active and reactive power injected into the grid and rotor speed. The simulation and experimental results also show that by increasing the number of the short-circuited turns in the stator windings, the value of the severity factor value related to the stator fault increases. Furthermore, the obtained results demonstrate that this severity factor is a good indicator for detection and quantification of ITSC faults in the stator windings of the DFIG.

In the case of an ITSC fault in the rotor windings of the DFIG, the results obtained from the simulation model and experimental tests prove that the value of the severity factor related to the rotor fault is highly independent of the values of active and reactive power injected into the grid. The simulation and experimental results also show that by increasing the number of short-circuited turns in the rotor windings, the value the severity factor related to the rotor fault increases. The only exception is the detection of the rotor fault in the vicinity of the synchronous speed which was not possible by using this approach. Considering that the amplitude of the current on the affected turns in such DFIG operating conditions is very small, the rotor ITSC fault would not impose any serious problem to the rotor windings of the DFIG. Hence, the diagnosis of a rotor fault can be performed when the DFIG is operating at a speed different and, preferably, far apart, the synchronous speed.

Chapter 7

Fault diagnosis in the 3LNPC rotor-side converter of the DFIG system

7.1 Introduction

The state-of-the-art in the field of fault diagnosis in 3LNPC converters (presented in Chapter 3) shows that there is no systematic previously report on OC fault diagnosis in 3LNPC converters used in DFIG systems.

The operating conditions of the 3LNPC converter in the DFIG system are different from those in the IM drive system. These differences rely on the fact that the converter delivers active power to the motor (inverter mode), whereas in the DFIG system, the direction of active power is bidirectional. At subsynchronous speeds, the converter delivers active power to the rotor while at supersynchronous speeds, the converter receives active power from the rotor (see Table 5.1). Furthermore, as it was already demonstrated in this study, the employed modulation techniques used in the IM drive system and in the DFIG system are different.

In this chapter, OC faults in the IGBTs and clamp-diodes of the rotor-side 3LNPC converter of a DFIG system are investigated. A fault diagnostic approach with the capability to detect and locate OC faults in the IGBTs, as well as in the clamp-diodes of the converter is developed. It provides a very fast and reliable diagnostic result for different operating conditions of the DFIG system, including the subsynchronous and supersynchronous regions. This diagnostic approach is similar to the method proposed for IM drives (in Section 3.5). However, for the simplification of the method, a smaller number of diagnostic variables are used (in this approach, diagnostic variables ε_x^o are used instead of diagnostic variables δ_x and ε_x^z).

7.2 Diagnostic approach

The topology of the DFIG rotor-side 3LNPC converter under analysis is shown in Fig. 7.1. For the explanation of the proposed diagnostic approach, the components of each inverter leg are classified into four groups g_{x1}, g_{x2}, g_{x3} and g_{x4}.

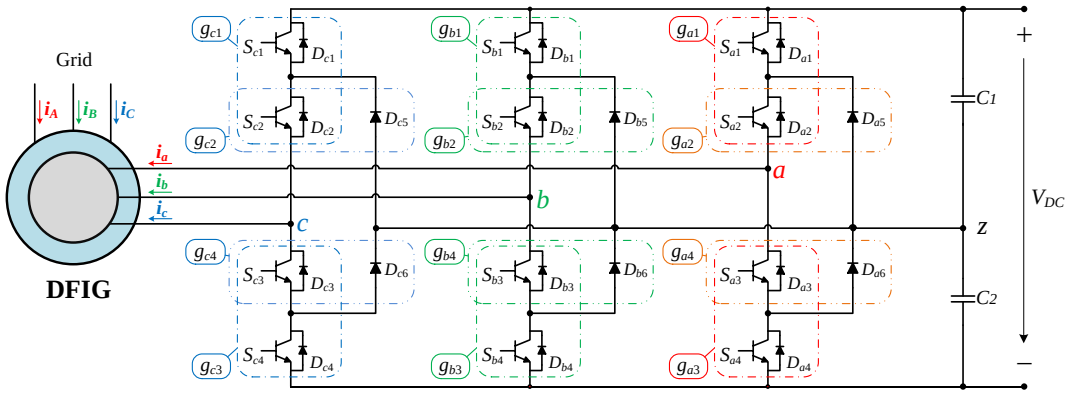

Fig. 7.1. Schematic representation of the rotor-side 3LNPC converter of the DFIG system.

For the implementation of the diagnostic approach, three converter pole voltages are measured between the converter output terminals *a*, *b*, *c* and the DC-bus middle point "z" (v_{xz}, $x \in a,b,c$). Similarly to the diagnostic approach presented in Section 3.5, the values of the pole voltages are normalized according to (3.18) and the variables LS_x are defined by (3.19).

The diagnostic process is developed in two steps. The first step involves the detection of the OC fault and identification of the group where the faulty power device is located, while the second step involves the identification of the faulty power device among the two potential candidates located in the faulty group.

For both steps, diagnostic variables ε_x^+, ε_x^- and ε_x^o are needed, being defined by (6.1), (6.2) and (6.3), respectively.

$$\varepsilon_x^+[k]=\begin{cases}-1 \Leftarrow CS_x[k-1]\neq 1\\ 0 \Leftarrow LS_x[k]=1 \ \wedge \ CS_x[k-1]=1\\ 1 \Leftarrow LS_x[k]\neq 1 \ \wedge \ CS_x[k-1]=1.\end{cases} \tag{6.1}$$

$$\varepsilon_x^-[k]=\begin{cases}-1 \Leftarrow CS_x[k-1]\neq -1\\ 0 \Leftarrow LS_x[k]=-1 \ \wedge \ CS_x[k-1]=-1\\ 1 \Leftarrow LS_x[k]\neq -1 \ \wedge \ CS_x[k-1]=-1.\end{cases} \tag{6.2}$$

$$\varepsilon_x^o[k]=\begin{cases}-1 \Leftarrow \ CS_x[k-1]\neq 0\\ 0 \Leftarrow LS_x[k]=0 \ \wedge CS_x[k-1]=0\\ 1 \Leftarrow LS_x[k]=-1 \ \wedge CS_x[k-1]=0\\ 2 \Leftarrow LS_x[k]=1 \ \wedge CS_x[k-1]=0\\ 3 \Leftarrow LS_x[k]=2 \ \wedge CS_x[k-1]=0.\end{cases} \tag{6.3}$$

The variables ε_x^+ and ε_x^- show the condition of the power devices located in groups g_{x1} and g_{x3}, respectively. The variables ε_x^o indicate the condition of the power devices in groups g_{x2} and g_{x4}. When the inverter operates in healthy conditions, diagnostic variables ε_x^+, ε_x^- and ε_x^o change between -1 and 0.

After obtaining these diagnostic variables, Table 7.1 allows the identification of the faulty group. In this table, the symbol "--" means that the variable is irrelevant for the diagnostic process.

Table 7.1. Lookup table for identification of the faulty group.

Diagnostic variables									Faulty leg	Faulty group		Faulty devices
ε_a^+	ε_a^-	ε_a^o	ε_b^+	ε_b^-	ε_b^o	ε_c^+	ε_c^-	ε_c^o		Name	Number	
1	--	--	--	--	--	--	--	--	*a*	g_{a1}	1	S_{a1} or S_{a2}
--	--	1	--	--	--	--	--	--		g_{a2}	2	S_{a2} or D_{a5}
--	1	--	--	--	--	--	--	--		g_{a3}	3	S_{a3} or S_{a4}
--	--	2	--	--	--	--	--	--		g_{a4}	4	S_{a3} or D_{a6}
--	--	--	1	--	--	--	--	--	*b*	g_{b1}	5	S_{b1} or S_{b2}
--	--	--	--	--	1	--	--	--		g_{b2}	6	S_{b2} or D_{b5}
--	--	--	--	1	--	--	--	--		g_{b3}	7	S_{b3} or S_{b4}
--	--	--	--	--	2	--	--	--		g_{b4}	8	S_{b3} or D_{b6}
--	--	--	--	--	--	1	--	--	*c*	g_{c1}	9	S_{c1} or S_{c2}
--	--	--	--	--	--	--	--	1		g_{c2}	10	S_{c2} or D_{c5}
--	--	--	--	--	--	--	1	--		g_{c3}	11	S_{c3} or S_{c4}
--	--	--	--	--	--	--	--	2		g_{c4}	12	S_{c3} or D_{c6}

Once the faulty group is identified by Table 7.1 and stored in the variable faulty group, the second step of the diagnostic procedure is applied. In this step, the diagnostic variables γ_x (given by (3.24)), ε_x^+, ε_x^- and ε_x^o are calculated. Finally, Table 7.2 allows the identification of the faulty device, based on the knowledge of the faulty group and the values of the diagnostic variables.

Table 7.2. Lookup table for the identification of the faulty device.

Faulty group	Diagnostic variables												Faulty device	
	ε_a^o	γ_a	ε_a^+	ε_a^-	ε_b^o	γ_b	ε_b^+	ε_b^-	ε_c^o	γ_c	ε_c^+	ε_c^-	Name	Number
g_{a1}	0	1	--	--	--	--	--	--	--	--	--	--	S_{a1}	1
	≥1	--	--	--	--	--	--	--	--	--	--	--	S_{a2}	2
g_{a2}	--	--	1	--	--	--	--	--	--	--	--	--	S_{a2}	2
	--	1	0	--	--	--	--	--	--	--	--	--	D_{a5}	5
g_{a3}	≥1	--	--	--	--	--	--	--	--	--	--	--	S_{a3}	3
	0	-1	--	--	--	--	--	--	--	--	--	--	S_{a4}	4
g_{a4}	--	--	--	1	--	--	--	--	--	--	--	--	S_{a3}	3
	--	-1	--	0	--	--	--	--	--	--	--	--	D_{a6}	6
g_{b1}	--	--	--	--	0	1	--	--	--	--	--	--	S_{b1}	7
	--	--	--	--	≥1	--	--	--	--	--	--	--	S_{b2}	8
g_{b2}	--	--	--	--	--	--	1	--	--	--	--	--	S_{b2}	8
	--	--	--	--	--	1	0	--	--	--	--	--	D_{b5}	11
g_{b3}	--	--	--	--	≥1	--	--	--	--	--	--	--	S_{b3}	9
	--	--	--	--	0	-1	--	--	--	--	--	--	S_{b4}	10
g_{b4}	--	--	--	--	--	--	--	1	--	--	--	--	S_{b3}	9
	--	--	--	--	--	-1	--	0	--	--	--	--	D_{b6}	12
g_{c1}	--	--	--	--	--	--	--	--	0	1	--	--	S_{c1}	13
	--	--	--	--	--	--	--	--	≥1	--	--	--	S_{c2}	14
g_{c2}	--	--	--	--	--	--	--	--	--	--	1	--	S_{c2}	14
	--	--	--	--	--	--	--	--	--	1	0	--	D_{c5}	17
g_{c3}	--	--	--	--	--	--	--	--	≥1	--	--	--	S_{c3}	15
	--	--	--	--	--	--	--	--	0	-1	--	--	S_{c4}	16
g_{c4}	--	--	--	--	--	--	--	--	--	--	--	1	S_{c3}	15
	--	--	--	--	--	--	--	--	--	-1	--	0	D_{c6}	18

The block diagram and flowchart of the diagnostic process is schematically illustrated in Fig. 7.2 and Fig. 7.3, respectively.

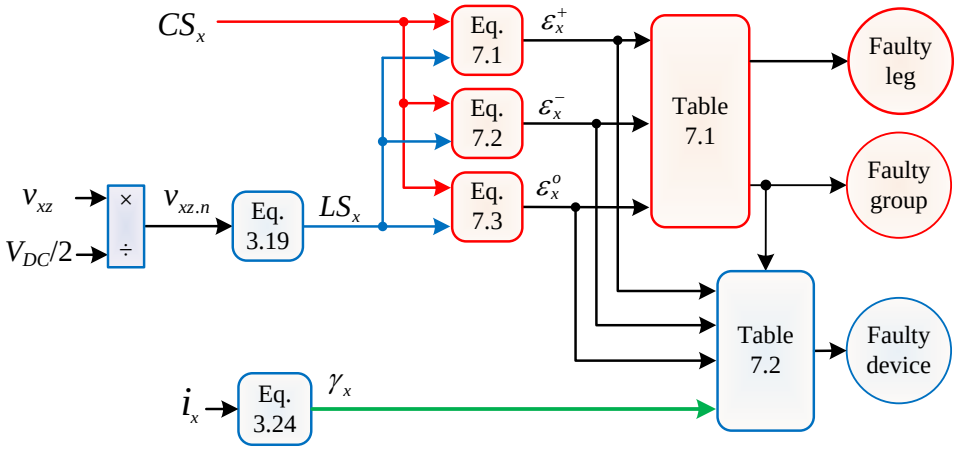

Fig. 7.2. Block diagram of the diagnostic technique.

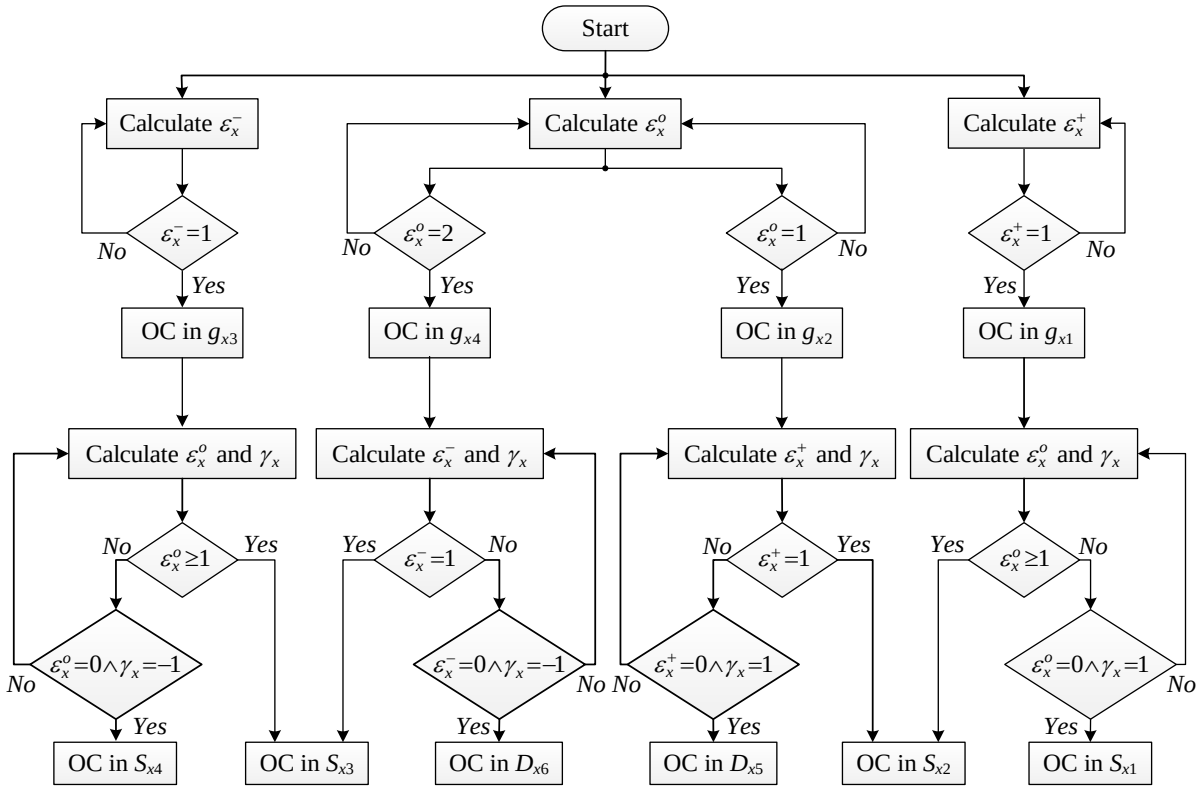

Fig. 7.3. Flowchart of the diagnostic technique.

7.3 Simulation and experimental results

The results obtained for the DFIG operating with different OC faults introduced in the power switches of the rotor-side converter as well as the fault diagnostic results are presented in this section. Each faulty situation was conducted at different values of the injected power into the grid and at different rotor speeds, including subsynchronous and supersynchronous speeds. The results presented in this section were obtained for a DC-bus voltage of 200 V. In order to avoid any damage to the DFIG system during the operation with OC faults in the converter, the value of the stator (grid) voltage was set to 200 V.

7.3.1 Subsynchronous operation of the DFIG

This subsection presents the diagnostic results obtained under DFIG subsynchronous operation and for four different faulty conditions, including two single IGBT OC faults, one clamp-diode OC fault and one double IGBT OC fault. The rotor speed for all results presented in this subsection is 1350 rpm.

The first test is performed for the DFIG operating with an OC fault in IGBT S_{a1}, and when the values of the stator active and reactive power were set to -2000 W and 0 VAr, respectively. The simulation and the experimental results for this test are shown in Fig. 7.4 and Fig. 7.5, respectively. The time instant when the fault was applied (t=2 s) is marked with a vertical line labeled F_T. The results presented in this figure are for both healthy operating condition (t<2 s) and with a fault in S_{a1} (t≥2 s).

As shown in Fig. 7.4(a) and Fig. 7.5(a), after the occurrence of the OC fault in IGBT S_{a1}, the rotor currents waveforms are slightly distorted. These distortions in the rotor currents are reflected in the dq-axes components of the rotor currents in the synchronous reference frame (i_{dr}, i_{qr}), presented in Fig. 7.4(b) and Fig. 7.5(b). Referring to (5.26), the variations in i_{dr} and i_{qr} are converted into stator active and reactive power variations, as presented in Fig. 7.4(c) and Fig. 7.5(c). It is not shown here, but the stator currents and electromagnetic torque are also affected by the OC fault.

These results show that despite that the effect of the fault on the rotor currents are not significant, the stator active and reactive powers are significantly affected by this fault. If the DFIG system continues to run with the OC fault in S_{a1}, this malfunction can then be the source of

secondary problems in other components of the DFIG system. These results also show that the diagnostic approaches based on the rotor currents analysis are unable to detect OC faults in the outer IGBTs. This limitation does not exist in the proposed diagnostic approach as shown in the following.

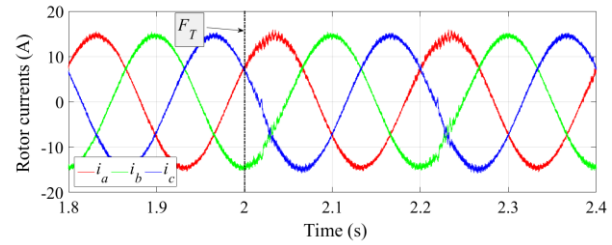

(a) Rotor currents waveforms

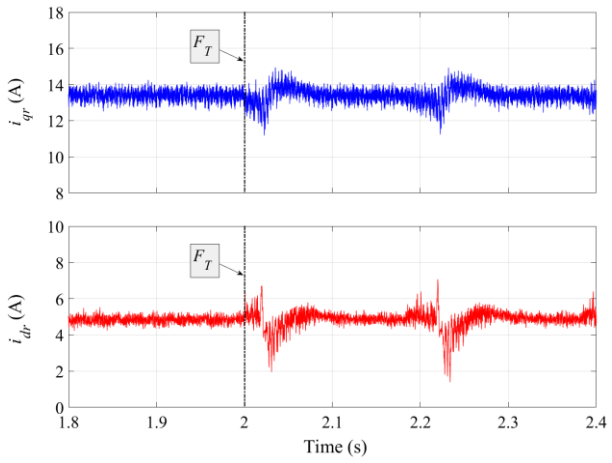

(b) *dq*-axes components of rotor currents

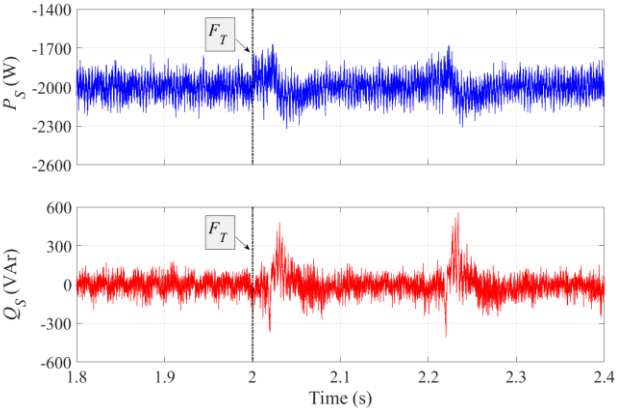

(c) Stator active and reactive powers

Fig. 7.4. Simulation results for the DFIG operating in healthy conditions ($t < 2$ s) and with an OC fault in S_{a1} ($t \geq 2$ s) ($n = 1350$ rpm, $P_s^* = -2000$ W, $Q_s^* = 0$ VAr).

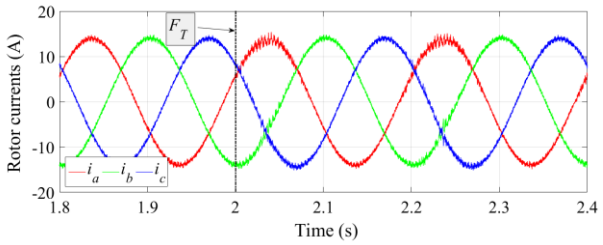

(a) Rotor currents waveforms

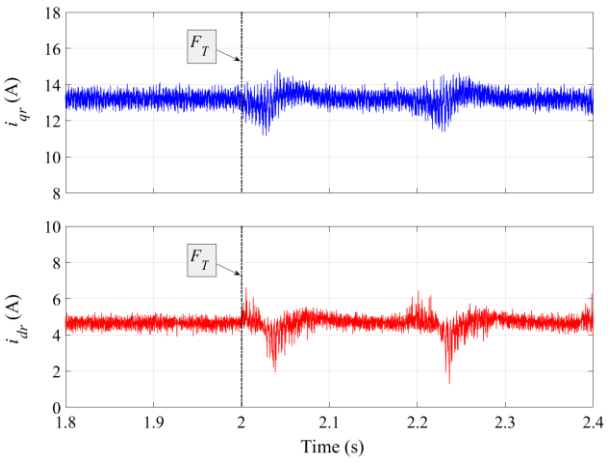

(b) *dq*-axes components of rotor currents

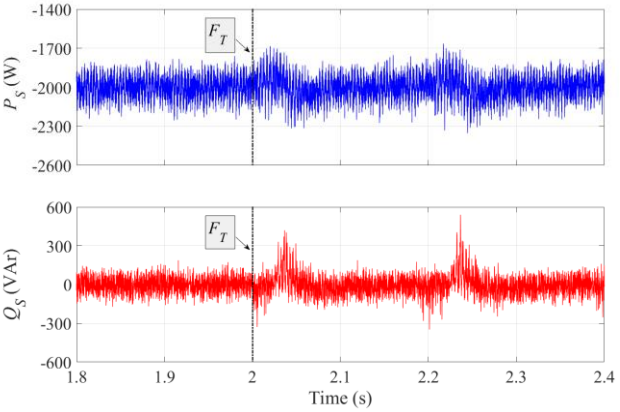

(c) Stator active and reactive powers

Fig. 7.5. Experimental results for the DFIG operating in healthy conditions ($t < 2$ s) and with an OC fault in S_{a1} ($t \geq 2$ s) ($n = 1350$ rpm, $P_s^* = -2000$ W, $Q_s^* = 0$ VAr).

The diagnostic results for this faulty condition, obtained with the simulation model are shown in Fig. 7.6. The normalized pole voltage and the control state of the leg *a* are shown in Fig. 7.6(a) while the variables and diagnostic results are presented in Fig. 7.6(b). After the occurrence of the fault, the positive parts of $v_{az.n}$ and CS_a are different and therefore, ε_a^+ changed to 1. As shown in Fig. 7.6(b), once ε_a^+ takes value 1 (t=2 s), Table 7.1 allows the identification of g_{a1} as the faulty group.

To identify the faulty device, according to Table 7.2, it is necessary to read the value of ε_a^+ and γ_a, presented in Fig. 7.6(b). Since $\gamma_a = 1$, the first time that $\varepsilon_a^o = 0$ (t=2.000278 s), Table 7.2 allows to identify S_{a1} as the faulty device.

A similar analysis can be conducted for the experimental diagnostic results presented in Fig. 7.7.

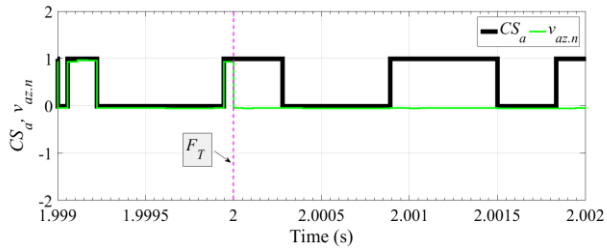

(a) Normalized pole voltage and control state of leg *a*

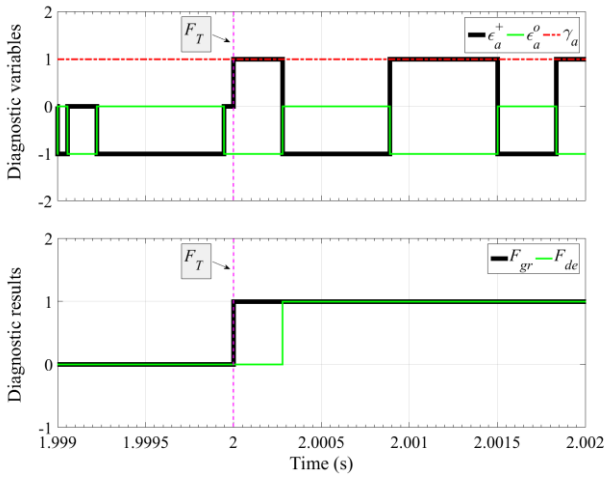

(b) Diagnostic results

Fig. 7.6. Diagnostic results for the DFIG operating with an OC fault in S_{a1}, obtained with the simulation model (n = 1350 rpm, P_s^* = –2000 W, Q_s^* = 0 VAr).

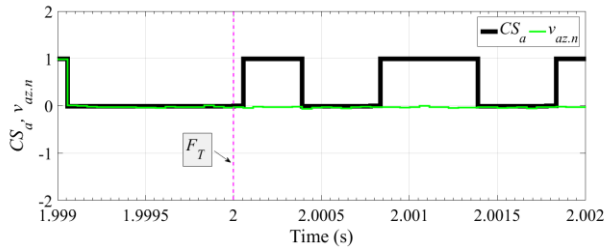

(a) Normalized pole voltage and control state of leg *a*

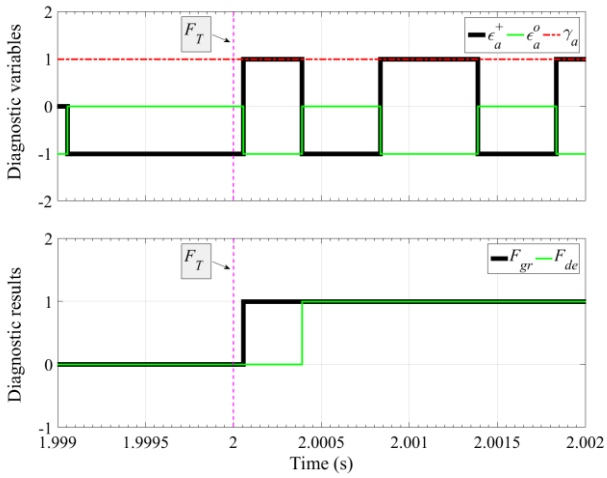

(b) Diagnostic results

Fig. 7.7. Diagnostic results for the DFIG operating with an OC fault in S_{a1}, obtained by experimental test (n = 1350 rpm, P_s^* = –2000 W, Q_s^* = 0 VAr).

Another faulty condition was considered with an OC fault in S_{a2}, introduced at t=2 s. For this faulty condition, due to the limitation of the rotor currents, the values of the stator active and reactive powers were set to -800 W and 0 VAr, respectively. The simulation and experimental results for this circumstances are presented in Fig. 7.8 and Fig. 7.9, respectively.

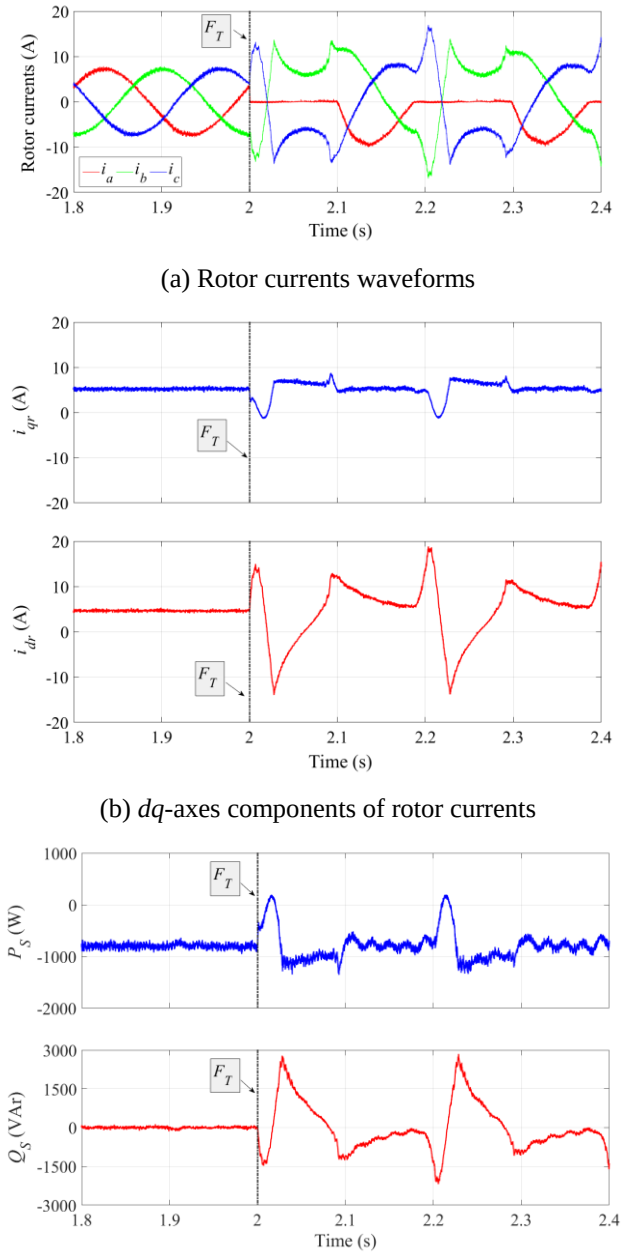

(a) Rotor currents waveforms

(b) *dq*-axes components of rotor currents

(c) Stator active and reactive powers

Fig. 7.8. Simulation results for the DFIG operating in healthy conditions ($t < 2$ s) and with a S_{a2} OC fault ($t \geq 2$ s) ($n = 1350$ rpm, $P_s^* = -800$ W, $Q_s^* = 0$ VAr).

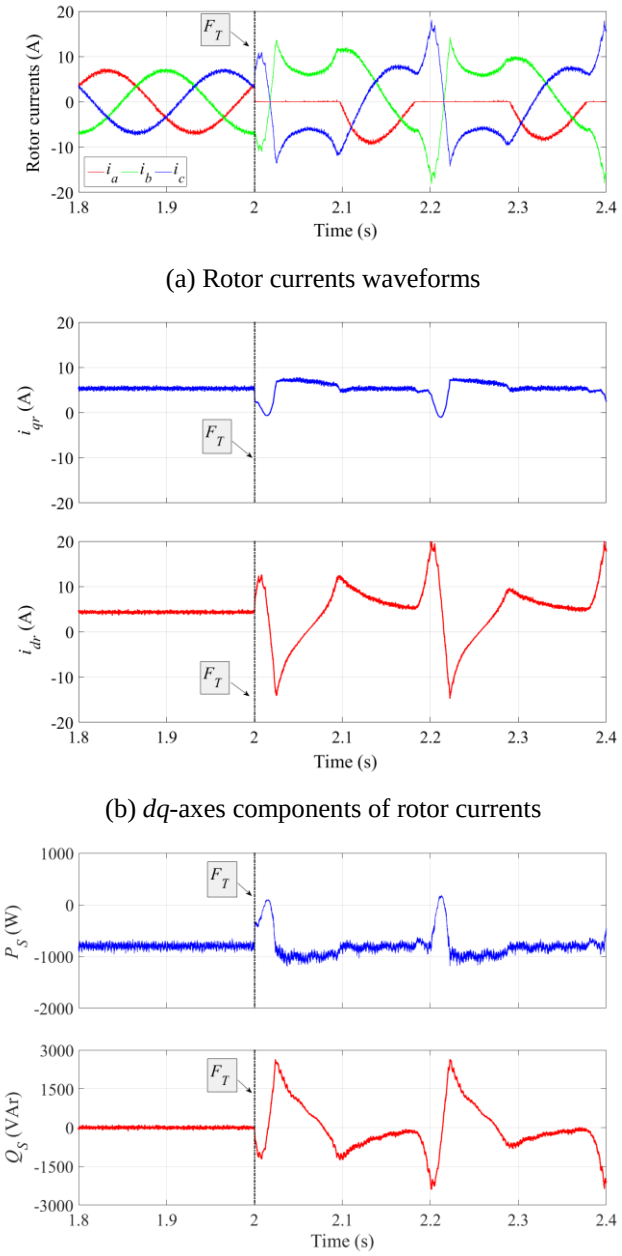

(a) Rotor currents waveforms

(b) *dq*-axes components of rotor currents

(c) Stator active and reactive powers

Fig. 7.9. Experimental results for the DFIG operating in healthy conditions ($t < 2$ s) and with a S_{a2} OC fault ($t \geq 2$ s) ($n = 1350$ rpm, $P_s^* = -800$ W, $Q_s^* = 0$ VAr).

As shown in Fig. 7.8(a) and Fig. 7.9(a), after the fault occurrence at t=2 s, the positive part of i_a is eliminated and therefore, a huge distortion appears in both i_{dr} and i_{qr}. Consequently, these distortions lead to the appearance of large oscillations in the stator active and reactive powers of the DFIG. The oscillations of the stator active and reactive powers in this faulty condition are much higher than in a S_{a1} fault. Once more, there is a good agreement between the simulation and experimental results.

Fig. 7.10 shows the simulation diagnostic results obtained for OC fault in S_{a2}. To analyze the fault, CS_a and $v_{az.n}$ are presented in Fig. 7.10(a). After the occurrence of the fault, $v_{az.n}$ is different from CS_a and this difference is shown by ε_a^+, presented in Fig. 7.10(b). According to Table 7.1, once ε_a^+ takes value 1 (t=2 s), the faulty group is identified as g_{a1}. As shown in Fig. 7.10(b), the first time after the faulty group identification that ε_a^o takes value 1 (t=2.0000556 s), Table 7.2 allows identifying the faulty device as S_{a2}. A similar analysis can be conducted for the experimental diagnostic results presented in Fig. 7.11.

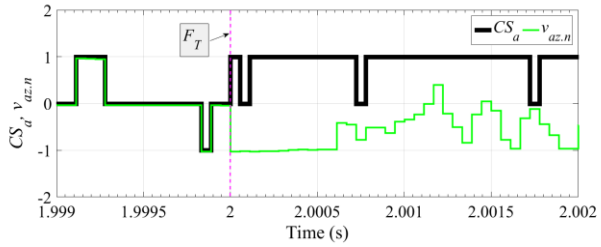

(a) Normalized pole voltage and control state of leg *a*

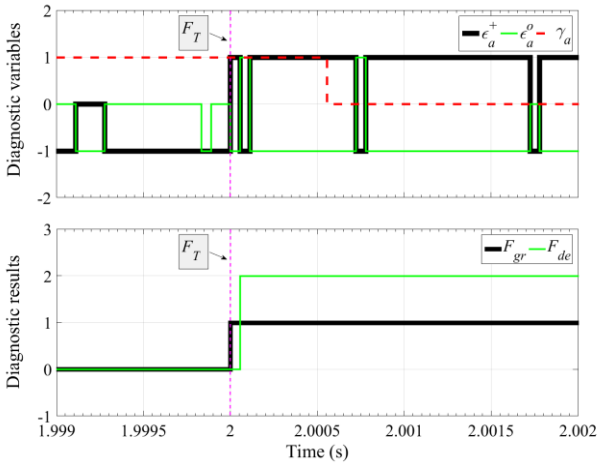

(b) Diagnostic results

Fig. 7.10. Diagnostic results for the DFIG operating with an OC fault in S_{a2}, obtained with the simulation model (n = 1350 rpm, P_s^* = –800 W, Q_s^* = 0 VAr).

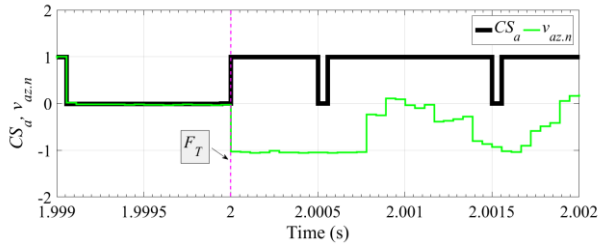

(a) Normalized pole voltage and control state of leg *a*

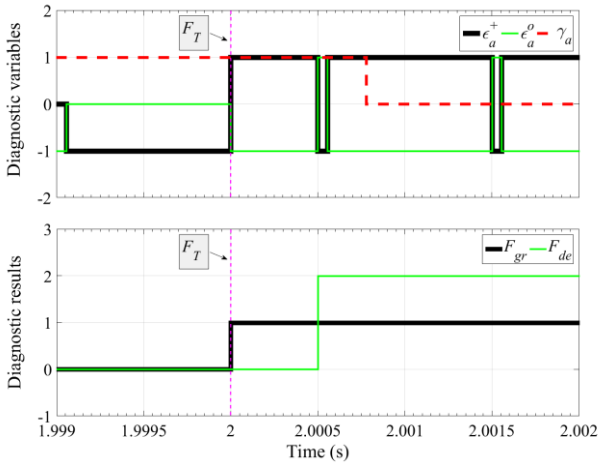

(b) Diagnostic results

Fig. 7.11. Diagnostic results for the DFIG operating with an OC fault in S_{a2}, obtained by experimental test (n = 1350 rpm, P_s^* = –800 W, Q_s^* = 0 VAr).

Fig. 7.12 and Fig. 7.13 show the results for the DFIG operating with an OC fault in the clamp-diode D_{a5} and when the values of the stator active and reactive power injected into the grid were set to -2000 W and 0 VAr, respectively. As can be observed in Fig. 7.12(a), the positive part of i_a is slightly affected by the OC fault in D_{a5}. The effect of the fault is also observable in the *d*-axis and *q*-axis components of the rotor currents, presented in Fig. 7.12(b). Consequently, according to (5.26), the stator active and reactive powers are affected by the OC fault in the clamp-diode D_{a5}.

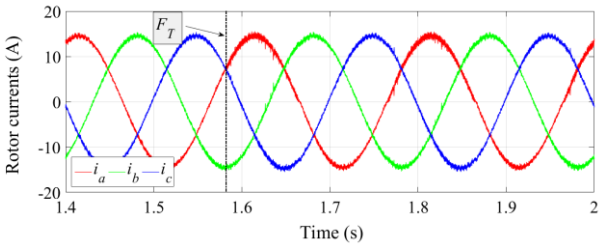

(a) Rotor currents waveforms

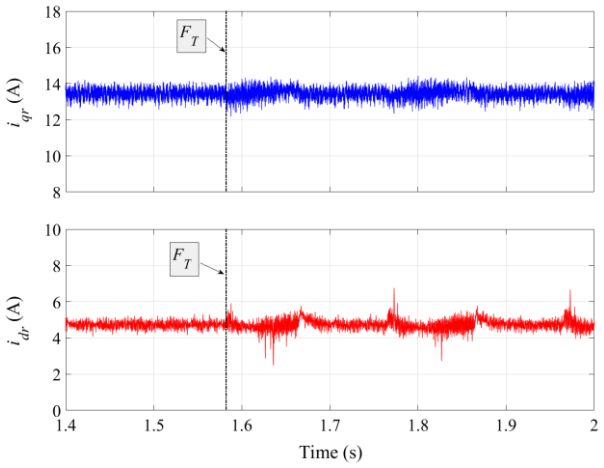

(b) *dq*-axes components of rotor currents

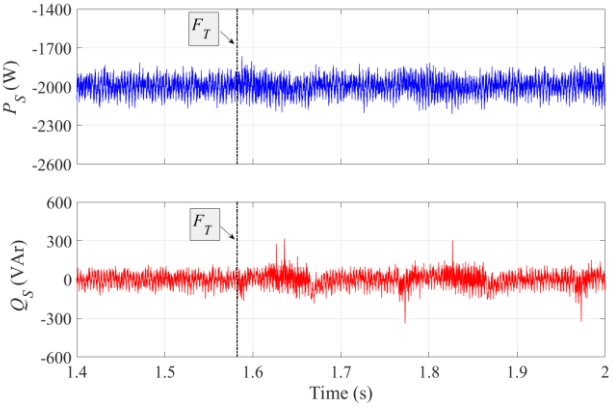

(c) Stator active and reactive powers

Fig. 7.12. Simulation results for the DFIG operating in healthy conditions (t <1.581 s) and with an OC fault in D_{a5} (t ≥1.581 s) (n = 1350 rpm, P_s^* = –2000 W, Q_s^* = 0 VAr).

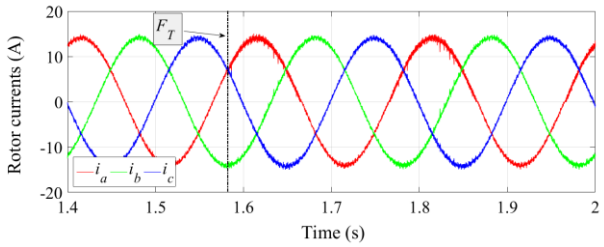

(a) Rotor currents waveforms

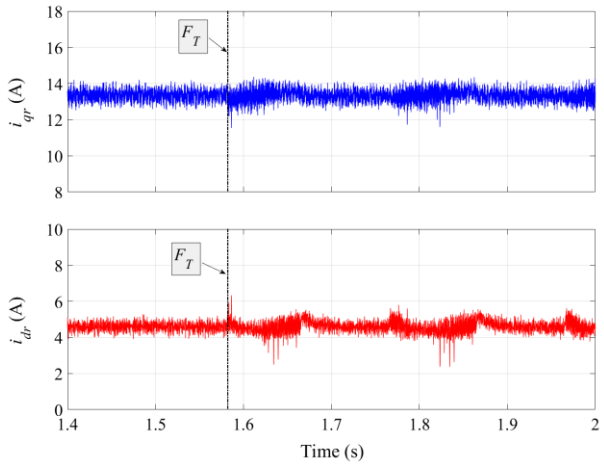

(b) *dq*-axes components of rotor currents

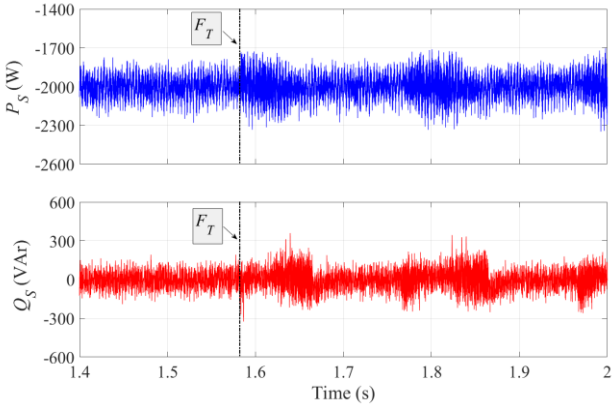

(c) Stator active and reactive powers

Fig. 7.13. Experimental results for the DFIG operating in healthy conditions (t <1.581 s) and with an OC fault in D_{a5} (t ≥1.581 s) (n = 1350 rpm, P_s^* = –2000 W, Q_s^* = 0 VAr).

The diagnostic results for an OC fault in clamp-diode D_{a5}, obtained by simulation, are presented in Fig. 7.14. As shown in Fig. 7.14(a), after the occurrence of the fault, the zero parts of CS_a and $v_{az.n}$ are different and this difference is reflected in ε_a^o, presented in Fig. 7.14(b). The first time that ε_a^o takes value 1 (t=1.581 s), Table 7.1 allows the identification of g_{a2} as the faulty group.

After the identification of the faulty group, the first time that $\varepsilon_a^+ = 0$ while $\gamma_a = 1$ (t=1.5810556 s), Table 7.2 allows to identify the faulty device as D_{a5} (Fig. 7.14(b)). The diagnostic timeline is presented in Fig. 7.14(b), where the faulty group number 2 and the faulty device number 5 are identified by the diagnostic algorithm.

The analysis performed to the simulations results is also valid for the experimental diagnostic results presented in Fig. 7.15.

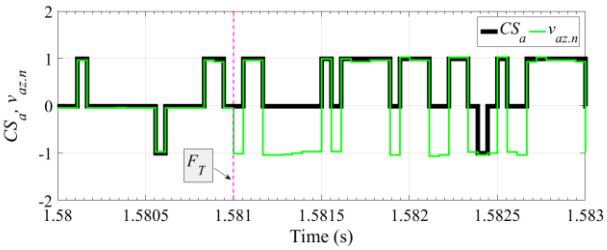

(a) Normalized pole voltage and control state of leg *a*

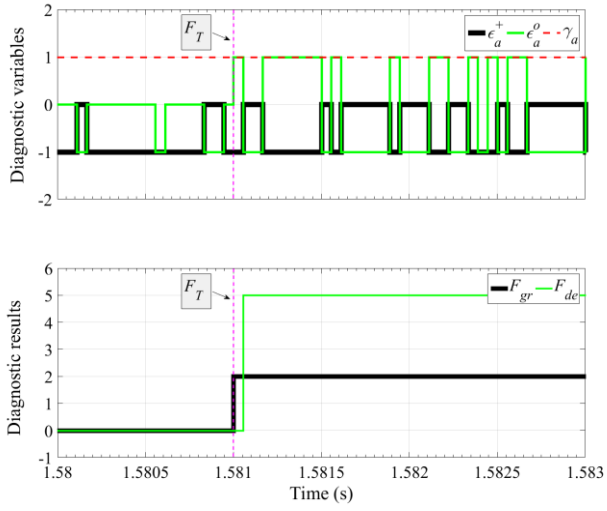

(b) Diagnostic results

Fig. 7.14. Diagnostic results for the DFIG operating with an OC fault in D_{a5}, obtained with the simulation model (n = 1350 rpm, P_s^* = –2000 W, Q_s^* = 0 VAr).

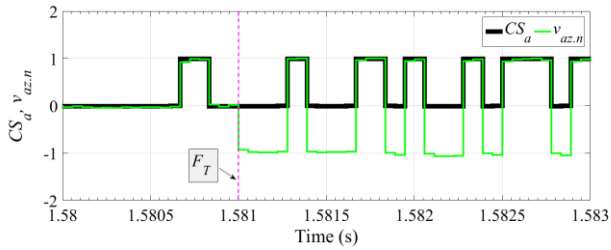

(a) Normalized pole voltage and control state of leg *a*

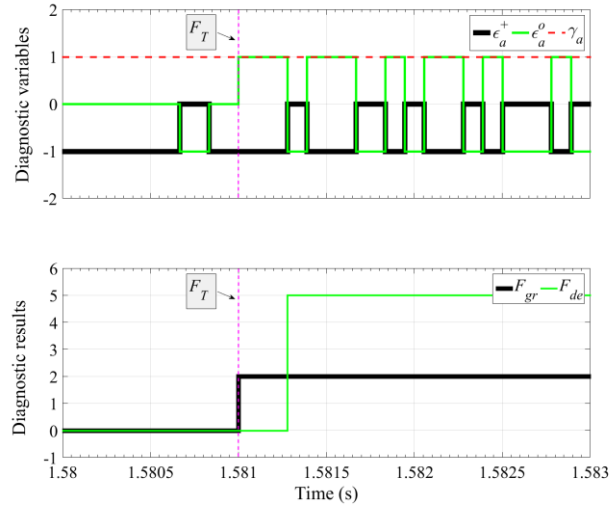

(b) Diagnostic results

Fig. 7.15. Diagnostic results for the DFIG operating with an OC fault in D_{a5}, obtained by experimental test (n = 1350 rpm, P_s^* = –2000 W, Q_s^* = 0 VAr).

To evaluate the capability of the diagnostic approach for the detection of double IGBT OC faults, simulation and experimental results for a combination of double IGBT OC faults are presented in Fig. 7.16 and Fig. 7.17, respectively. The first OC fault is applied to IGBT S_{b4} at t=2 s and the second one is applied to IGBT S_{c2} at t=2.001 s, being these time instants labeled as F_T^1 and F_T^2.

The rotor current waveforms presented in Fig. 7.16(a) and Fig. 7.17(a) show that after the occurrence of the faults, some negative values of i_b and all positive values of i_c are eliminated.

The control state and the normalized converter pole voltage together with the diagnostic variables of legs *b* and *c* are presented in Fig. 7.16(b) and Fig. 7.16 (c), respectively.

Considering the results of the first fault (Fig. 7.16(b)), the first time that ε_b^- takes value 1 (t=2.00017 s), Table 7.1 allows to identify the first faulty group as g_{b3}. Then, knowing that the faulty device is located in g_{b3}, it is necessary to know the values of ε_b^o and γ_b. As shown in Fig. 7.16(b), while $\gamma_b = -1$, $\varepsilon_b^o = 0$ at t=2.000278 s. Thus, Table 7.2 allows to identify S_{b4} as the first faulty device.

As far as the second fault is concerned, after the occurrence of the fault, the zero parts of CS_c and $v_{cz.n}$ are different and this difference is reflected in ε_c^o, presented in Fig. 7.16(c). According to Table 7.1, the first time that ε_c^o takes value 1 (t=2.001 s), it is possible to identify the second faulty group as g_{c2}. Afterwards, combining this information with the fact that at t=2.001111 s $\varepsilon_c^+ = 1$, and using Table 7.2, it is possible to identify S_{c2} as the second faulty device.

The diagnostic timeline is shown in Fig. 7.16(d), where the diagnostic algorithm identifies the first faulty group as number 7, the first faulty device as number 10, the second faulty group as number 10 and the second faulty device as number 14.

The experimental diagnostic results for this combination of double IGBT OC faults are shown in Fig. 7.17. The procedure of the identification of the faulty device for the first fault is similar to the one already presented for the simulation results. For the second fault, as shown in Fig. 7.17(c), the positive parts of CS_c and $v_{cz.n}$ are different and this difference is reflected in ε_c^+. According to Table 7.1, once ε_c^+ takes value 1 (t=2.001 s), the faulty group is identified as g_{c1}. Then, the first time that ε_a^o takes value 1 (t=2.001222 s), Table 7.2 allows to identify the faulty device as S_{c2}.

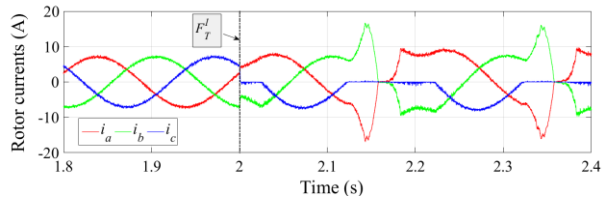

(a) Rotor current waveforms

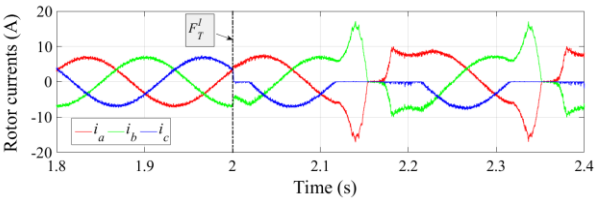

(a) Rotor current waveforms

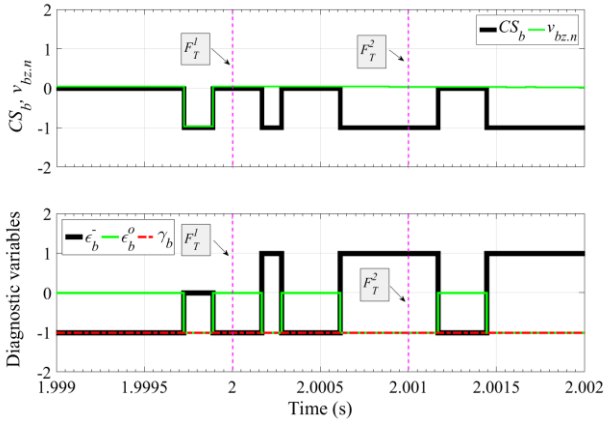

(b) Diagnostic variables of leg *b*

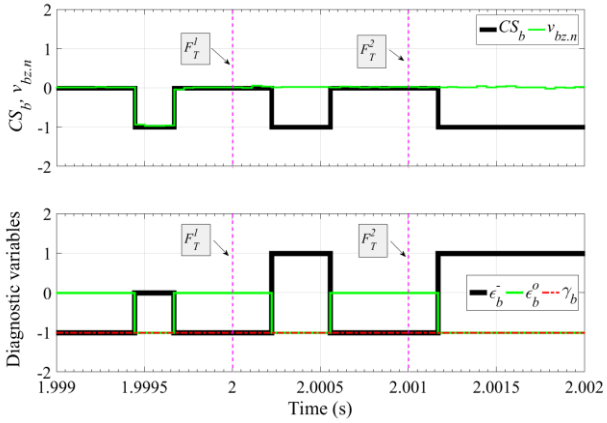

(b) Diagnostic variables of leg *b*

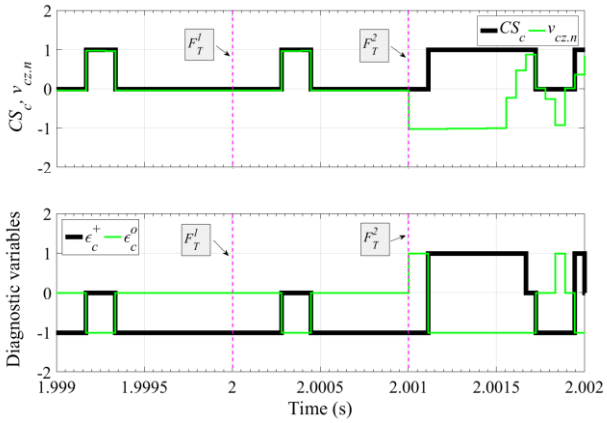

(c) Diagnostic variables of leg *c*

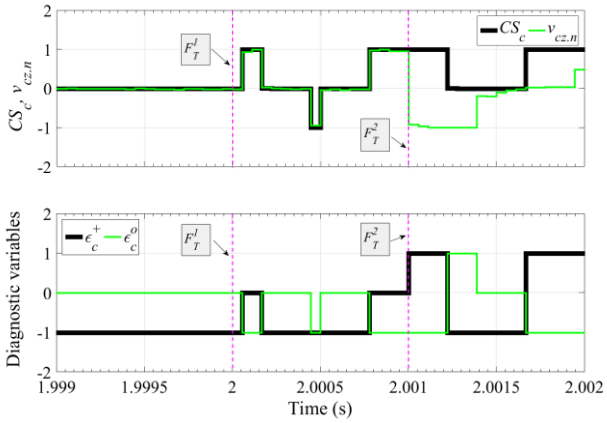

(c) Diagnostic variables of leg *c*

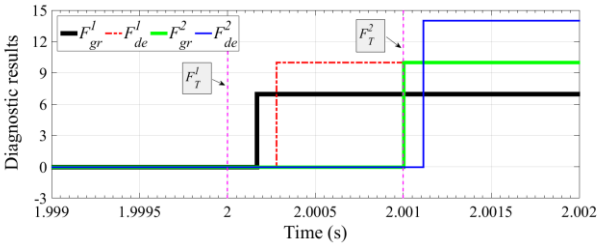

(d) Final diagnostic results

Fig. 7.16. Simulation results for the DFIG operating with OC faults in S_{b4} and S_{c2} ($n = 1350$ rpm, $P_s^* = -800$ W, $Q_s^* = 0$ VAr).

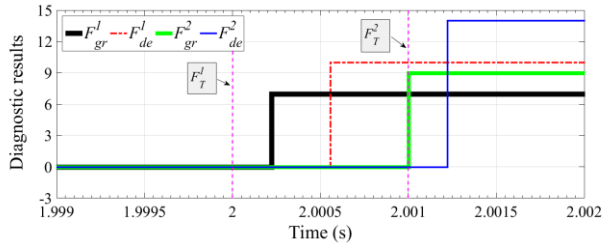

(d) Final diagnostic results

Fig. 7.17. Experimental results for the DFIG operating with OC faults in S_{b4} and S_{c2} ($n = 1350$ rpm, $P_s^* = -800$ W, $Q_s^* = 0$ VAr).

7.3.2 Supersynchronous operation of the DFIG

This subsection presents results for the DFIG operating at a supersynchronous speed of 1650 rpm. Fig. 7.18 and Fig. 7.19 show the results for the DFIG operating with an OC fault in S_{a1}, and the values of the stator active and reactive power are set to -2000 W and 0 VAr, respectively.

As seen in these figures, the effect of the OC fault in S_{a1} is almost indistinguishable in the rotor currents and the stator active and reactive powers.

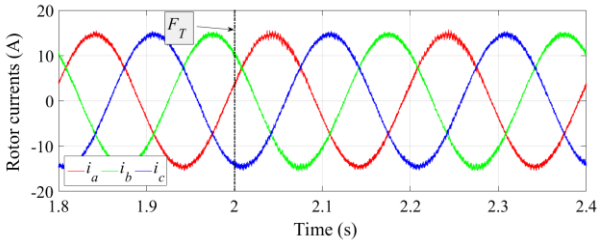

(a) Rotor currents waveforms

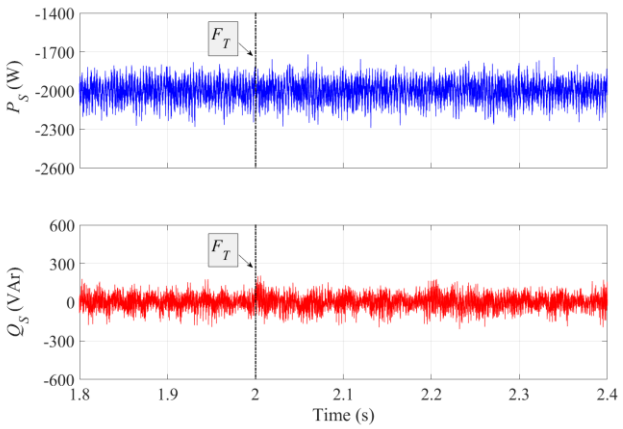

(b) Stator active and reactive powers

Fig. 7.18. Simulation results for the DFIG operating in healthy conditions ($t < 2$ s) and with an OC fault in S_{a1} ($t \geq 2$ s) ($n = 1650$ rpm, $P_s^* = -2000$ W, $Q_s^* = 0$ VAr).

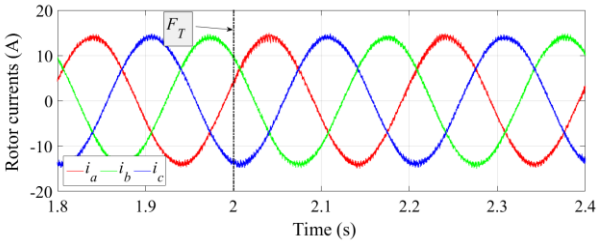

(a) Rotor currents waveforms

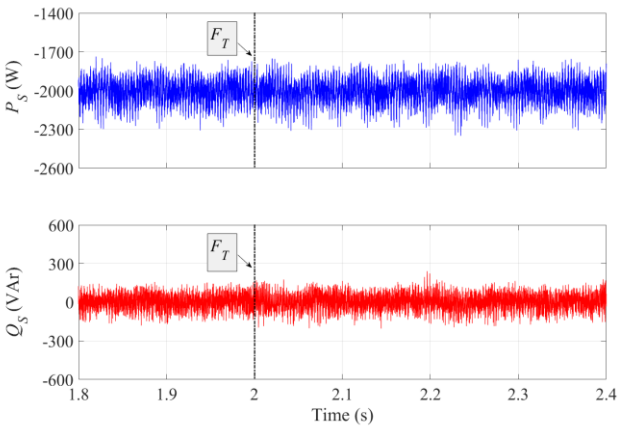

(b) Stator active and reactive powers

Fig. 7.19. Experimental results for the DFIG operating in healthy conditions ($t < 2$ s) and with an OC fault in S_{a1} ($t \geq 2$ s) ($n = 1650$ rpm, $P_s^* = -2000$ W, $Q_s^* = 0$ VAr).

Fig. 7.20 shows the diagnostic results for this faulty condition, obtained with the simulation model. As shown in Fig. 7.20(a), after the occurrence of the fault, the positive parts of $v_{az.n}$ and CS_a are different and therefore, ε_a^+ changed to 1. As shown in Fig. 7.20(b), once ε_a^+ takes value 1 (t=2.0000556 s), Table 7.1 allows the identification of the faulty group as g_{a1}.

In the next step, since the faulty device is located in g_{a1}, it is necessary to read the value of ε_a^o and γ_a, presented in Fig. 7.20(b). Since $\gamma_a = 1$, the first time that $\varepsilon_a^o = 0$ (t=2.000278 s), Table 7.2 allows to identify S_{a1} as the faulty device. A similar analysis can be done for the experimental diagnostic results, presented in Fig. 7.21.

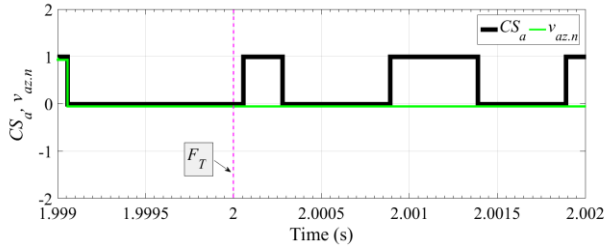

(a) Normalized pole voltage and control state of leg *a*

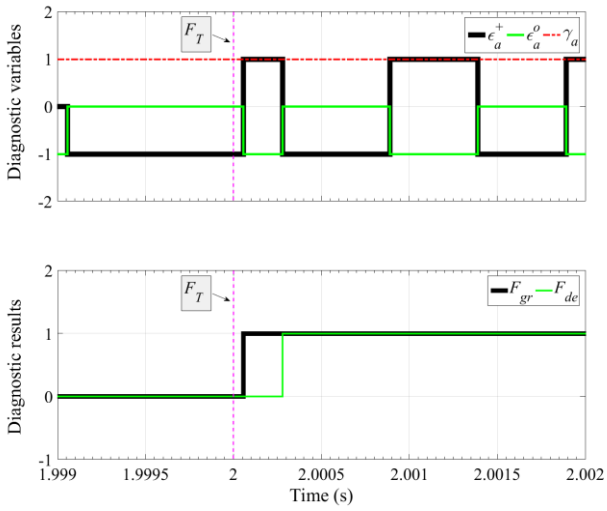

(b) Diagnostic results

Fig. 7.20. Diagnostic results for the DFIG operating with an OC fault in S_{a1}, obtained with the simulation model (n = 1650 rpm, P_s^* = –2000 W, Q_s^* = 0 VAr).

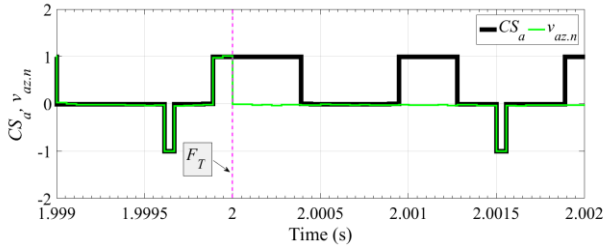

(a) Normalized pole voltage and control state of leg *a*

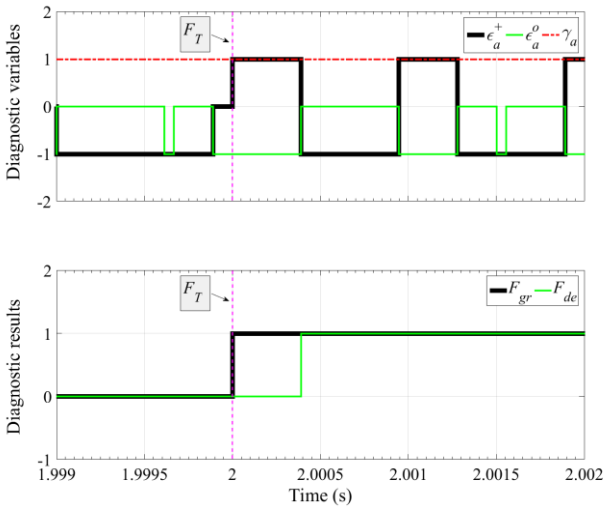

(b) Diagnostic results

Fig. 7.21. Diagnostic results for the DFIG operating with an OC fault in S_{a1}, obtained by experimental test (n = 1650 rpm, P_s^* = –2000 W, Q_s^* = 0 VAr).

Another faulty condition was carried out for the supersynchronous operation of the DFIG and with an OC fault in S_{a2}, introduced at t=2 s. Fig. 7.22(a) and Fig. 7.23(a) show the rotor currents waveforms, which show that after the fault occurrence at t=2 s, the positive part of i_a is eliminated. As a consequence, the waveforms of the stator active and reactive powers shown in Fig. 7.22(b) and Fig. 7.23(b) exhibit a large oscillation.

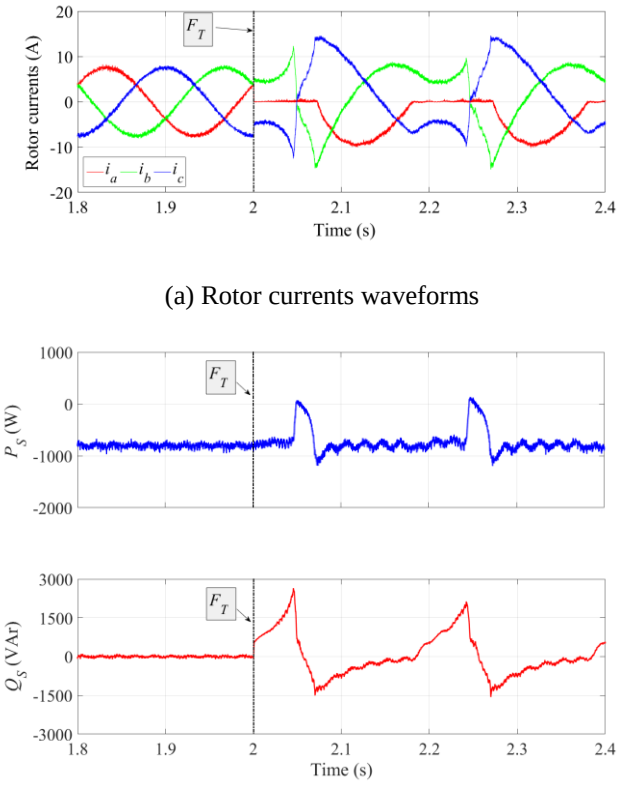

(a) Rotor currents waveforms

(b) Stator active and reactive powers

Fig. 7.22. Simulation results for the DFIG operating in healthy conditions ($t < 2$ s) and with an OC fault in S_{a2} ($t \geq 2$ s) ($n = 1650$ rpm, $P_s^* = -800$ W, $Q_s^* = 0$ VAr).

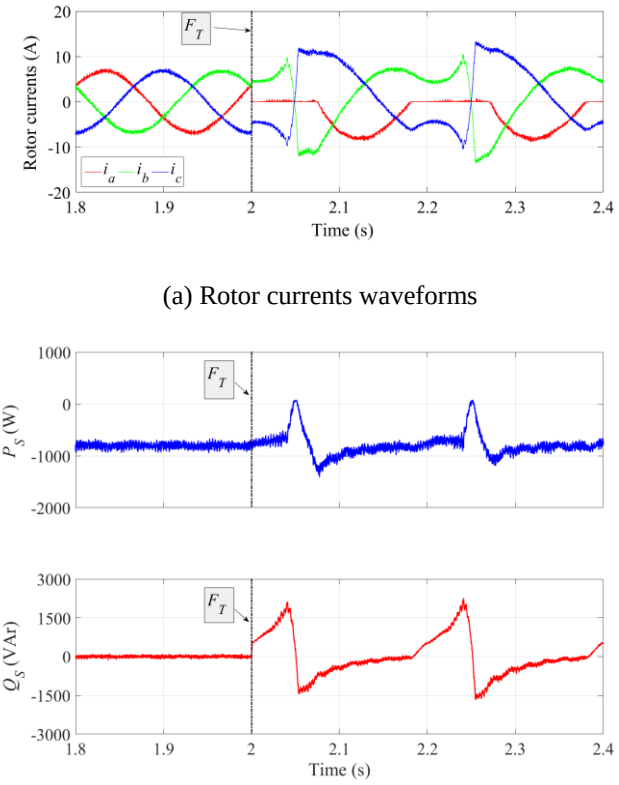

(a) Rotor currents waveforms

(b) Stator active and reactive powers

Fig. 7.23. Experimental results for the DFIG operating in healthy conditions ($t < 2$ s) and with an OC fault in S_{a2} ($t \geq 2$ s) ($n = 1650$ rpm, $P_s^* = -800$ W, $Q_s^* = 0$ VAr).

The diagnostic results for this faulty condition, obtained with the simulation model, are presented in Fig. 7.24. As presented in Fig. 7.24(a), after the occurrence of the fault, $v_{az.n}$ is different from CS_a. This difference is shown by ε_a^o, presented in Fig. 7.24(b). The first time that ε_a^O takes value 1 (t=2 s), the faulty group is identified as g_{a2} from Table 7.1.

Taking into account that the faulty device is located in g_{a2}, the first time that ε_a^+ takes value 1 (t=2.000167 s), Table 7.2 allows to identify S_{a2} as the faulty device, as shown in Fig. 7.24(b).

The analysis performed for the simulations results is also valid for the experimental diagnostic results presented in Fig. 7.25.

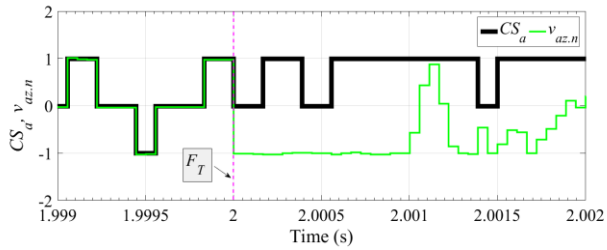

(a) Normalized pole voltage and control state of leg *a*

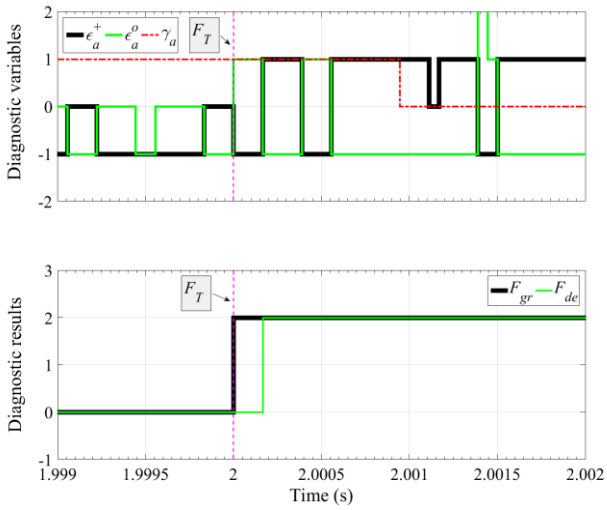

(b) Diagnostic results

Fig. 7.24. Diagnostic results for the DFIG operating with an OC fault in S_{a2}, obtained with the simulation model ($n = 1650$ rpm, $P_s^* = -800$ W, $Q_s^* = 0$ VAr).

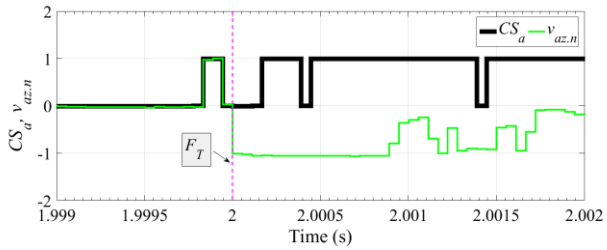

(a) Normalized pole voltage and control state of leg *a*

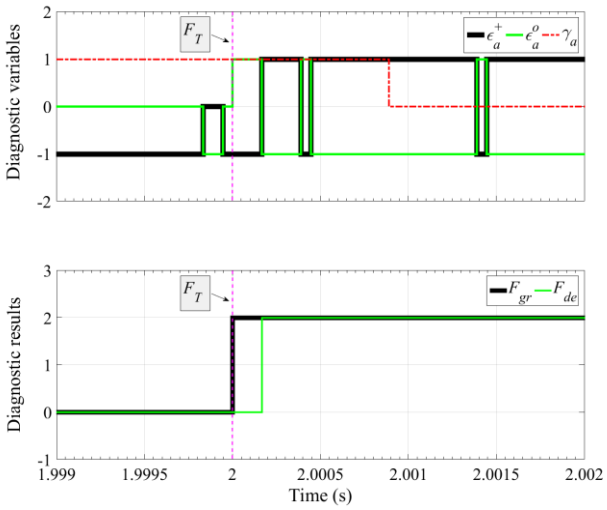

(b) Diagnostic results

Fig. 7.25. Diagnostic results for the DFIG operating with an OC fault in S_{a2}, obtained by experimental test ($n = 1650$ rpm, $P_s^* = -800$ W, $Q_s^* = 0$ VAr).

7.4 Final remarks

The performance of the DFIG system under different semiconductor OC faults in the rotor-side converter was analyzed. It was demonstrated that the DFIG rotor currents are slightly affected by the OC faults in the outer IGBTs as well as in the clamp-diodes of the rotor-side converter. Consequently, these current distortions reduce the system performance and lead to distortions in the injected power into the grid.

Since in this particular application the effect of OC faults in the outer IGBTs, as well as in the clamp-diodes, is barely visible in the rotor currents, the analysis of the rotor currents is not effective for diagnostic purposes. Therefore, a diagnostic approach based on the analysis of the pole voltages of the 3LNPC converter was developed.

The capability of detection and identification of multiple OC fault in all IGBTs and clamp-diodes of the 3LNPC converter, under all operating conditions of the DFIG system, as well as a quick and reliable performance are the main advantages of the proposed approach. The applicability and performance of the proposed diagnostic approach were demonstrated by various simulation and experimental results obtained for different operating conditions of the DFIG system.

Chapter 8

Conclusions and future work

8.1 Conclusions

The work reported in this thesis has been focused in two major topics:

- Diagnosis OC faults in 3LNPC converters for two applications: IM drives and DFIG systems;
- Diagnosis of inter-turn short-circuit faults in the stator and rotor windings of DFIGs.

With the aim to diagnose faults in 3LNPC converters used in IM drives, three novel algorithms for the real-time diagnosis of OC faults in the 3LNPC converter were developed:

- Approach I: Average Current Park's Vector;
- Approach II: Average values of positive and negative parts of output currents;
- Approach III: Pole voltage analysis.

The approach I is able to detect and identify the faulty IGBT while the approach II has the capability to diagnose multiple OC faults in all IGBTs of the converter. The diagnostic approaches I and II only need the converter output currents already used by the IM drive controller. Therefore, their implementation cost is low and their integration into the motor drive control system is easy. Typically, in both approaches, the faulty IGBT is identified within half of the fundamental converter output period. However, the diagnostic approaches I and II have a limitation for the diagnosis of OC faults in the outer IGBTs of 3LNPC converter, when the converter operates with a low modulation index.

The diagnostic approach III has several advantages such as the capability of detection and identification of multiple OC fault in all controlled power switches and clamp-diodes, the capability of detection and identification of OC faults in the outer IGBTs when the power converter

operates with a very low modulation index and it exhibits a reliable performance. Typically, the fault diagnostic process with this approach is accomplished within one modulation period (1 ms in this study). However, the implementation of this diagnostic approach requires the measurement of each converter leg pole voltage, which increases the overall system costs.

Thanks to the use of normalized quantities, the final diagnostic results obtained with the three diagnostic approaches are independent of the converter operating conditions. Furthermore, all these diagnostic methods present a reliable performance in steady-state and in transient conditions. Moreover, they just require basic mathematical operations as there is no need to use complex algorithms. Therefore, they are suitable to be easily integrated into the drive control system without significant effort.

Overall, as long as the implementation cost of the diagnostic approach is concerned and only diagnosis of the faulty IGBTs is required, the approach II would be the optimum choice. On the other hand, when the diagnosis of OC faults in IGBTs and clamp-diodes in very short period of time is concerned, the approach III is recommended.

In the context of generator faults, a method based on the spectrum analysis of the stator reactive power for the detection and identification of ITSC faults in the stator and rotor windings of the DFIG was proposed. Furthermore, for each type of fault, a severity factor that indicates the extension of the fault was defined.

The simulation and experimental results showed that the value of the severity factor defined for the stator fault is highly independent of the various operating conditions of the DFIG, namely rotor speed and active and reactive power injected into the grid.

The simulation and experimental results obtained for the DFIG operating with rotor ITSC faults showed that the value of the severity factor defined for this type of fault is highly independent of the values of the active and reactive powers injected into the grid. The only limitation of the proposed method is the detection of the rotor fault when the DFIG operates near synchronous speed. Considering that the amplitude of the current on the affected turns in such DFIG operating conditions is very small, the rotor ITSC fault cannot impose any serious threat to the integrity of the rotor windings. Hence, the diagnosis of an ITSC fault in the rotor windings can be accomplished when the DFIG is operating at a speed different than the synchronous speed.

At the end, the performance of the DFIG system, based on a 3LNPC converter, under different semiconductor OC faults in the rotor-side converter was analyzed. It was shown that OC faults in the IGBTs and clamp-diodes of the rotor-side converter reduce the system performance and lead to distortions in all stator quantities (active power, reactive power, *etc.*). It was also shown that the effects of OC faults in the outer IGBTs and clamp-diodes of the 3LNPC converter on the rotor currents is inappreciable and, consequently, the analysis of the rotor currents is not an effective solution for diagnostic purposes. A diagnostic approach based on the analysis of the pole voltages of the rotor-side converter was presented, which possesses the capability of diagnosing OC faults in all IGBTs and clamp-diodes of the 3LNPC converter.

As a concluding remark, it can be stated that the diagnostic methods proposed in this thesis for semiconductor faults and for DFIG winding faults can be readily integrated into the control system of the DFIG, therefore leading to an increase of the availability as well as a reduction of the maintenance cost of wind energy conversion systems based on DFIGs.

8.2 Future work

Following the investigations and developed work, some suggestions for future research are summarized in this subsection.

Firstly, this work can be extended by investigating of the OC faults in the DFIG grid-side converter. To do that, the DFIG test rig should be expanded in order to include the 3LNPC grid-side converter.

In addition, further work can be conducted to develop some methods for the diagnosis of faults in the DC bus capacitors and feedback sensors (namely current sensors).

Another research idea with this regard is to improve the reliability of the DFIG system by adding a fault-tolerant control strategy to the 3LNPC converters. The development and integration of a fault-tolerant technique for the two 3LNPC converters allows the DFIG system to keep running after the occurrence of a fault in its power switches, although with a degraded performance.

Regarding the method developed for the detection of ITSC, the proposed approach has a limitation in the detection of a rotor fault when the DFIG operates in the vicinity of the synchronous speed. Therefore, further study to improve the applicability of this diagnostic

approach to overcome this limitation is needed. In that case, the detection of the rotor fault should rely on second-order effects, like the use of space harmonics created by the currents circulating in the stator and rotor windings.

Finally, the development of some diagnostic methods for other types of faults in the generator such as rotor eccentricity and slip ring faults can also be other interesting topics for future research.

Bibliography

[1] M. Liserre, T. Sauter, and J. Y. Hung, "Future energy systems: integrating renewable energy sources into the smart power grid through industrial electronics," *IEEE Mag. Industrial Electronics*, vol. 4, no. 1, pp. 18-37, 2010.

[2] M. Liserre, R. Cardenas, M. Molinas, and J. Rodriguez, "Overview of Multi-MW Wind Turbines and Wind Parks," *IEEE Trans. Industrial Electronics*, vol. 58, no. 4, pp. 1081-1095, 2011.

[3] V. Yaramasu, B. Wu, P. C. Sen, S. Kouro, and M. Narimani, "High-power wind energy conversion systems: State-of-the-art and emerging technologies," *Proceedings of the IEEE*, vol. 103, no. 5, pp. 740-788, 2015.

[4] "Global wind statistics 2015, a report from Global Wind Energy Council (GWEC)," 2016.

[5] "Wind in power, 2015 European statistics, a report from European Wind Energy Association (EWEA)," 2016.

[6] "Wind energy and the electricity grid, a report from the European Wind Energy Association (EWEA)," 2010.

[7] T. Ackermann, *Wind Power in Power Systems, 2nd Edition*: John Wiley & Sons Ltd., 2012.

[8] C. Zhe, J. M. Guerrero, and F. Blaabjerg, "A Review of the State of the Art of Power Electronics for Wind Turbines," *IEEE Trans. Power Electronics*, vol. 24, no. 8, pp. 1859-1875, 2009.

[9] F. Blaabjerg and K. Ma, "Future on Power Electronics for Wind Turbine Systems," *IEEE Journal of Emerging and Selected Topics in Power Electronics*, vol. 1, no. 3, pp. 139-152, 2013.

[10] R. Cardenas, R. Pena, S. Alepuz, and G. Asher, "Overview of Control Systems for the Operation of DFIGs in Wind Energy Applications," *IEEE Trans. Industrial Electronics*, vol. 60, no. 7, pp. 2776-2798, 2013.

[11] B. Badrzadeh, "Qualitative performance assessment of semiconductor switching device, converter and generator candidates for 10 MW offshore wind turbine generators," *Wind Energy*, vol. 14, no. 3, pp. 425-448, 2011.

[12] F. Blaabjerg and K. Ma, "CHAPTER 6 - High Power Electronics: Key Technology for Wind Turbines," in *Power Electronics for Renewable Energy Systems, Transportation and Industrial Applications*, ed: John Wiley & Sons, Ltd, 2014, pp. 136-159.

[13] A. Calle-Prado, S. Alepuz, J. Bordonau, P. Cortes, and J. Rodriguez, "Predictive Control of a Back-to-Back NPC Converter-Based Wind Power System," *IEEE Trans. Industrial Electronics*, vol. 63, no. 7, pp. 4615-4627, 2016.

[14] L. G. Franquelo, J. Rodriguez, J. I. Leon, S. Kouro, R. Portillo, and M. A. M. Prats, "The age of multilevel converters arrives," *IEEE Mag. Industrial Electronics*, vol. 2, no. 2, pp. 28-39, 2008.

[15] J. Rodriguez, S. Bernet, P. K. Steimer, and I. E. Lizama, "A Survey on Neutral-Point-Clamped Inverters," *IEEE Trans. Industrial Electronics*, vol. 57, no. 7, pp. 2219-2230, 2010.

[16] C. Hochgraf, R. Lasseter, D. Divan, and T. A. Lipo, "Comparison of multilevel inverters for static VAr compensation," in *Proc. Industry Applications Society Annual Meeting*, 1994, pp. 921-928.

[17] A. Nabae, I. Takahashi, and H. Akagi, "A New Neutral-Point-Clamped PWM Inverter," *IEEE Trans. Industry Applications*, vol. 17, no. 5, pp. 518-523, 1981.

[18] T. A. Meynard and H. Foch, "Multi-level conversion: high voltage choppers and voltage-source inverters," in *Proc. PESC*, 1992, pp. 397-403.

[19] Y. Shakweh and E. A. Lewis, "Assessment of medium voltage PWM VSI topologies for multi-megawatt variable speed drive applications," in *Proc. PESC*, 1999, pp. 965-971.

[20] F. Blaabjerg, M. Liserre, and K. Ma, "Power Electronics Converters for Wind Turbine Systems," *IEEE Trans. Industry Applications*, vol. 48, no. 2, pp. 708-719, 2012.

[21] J. S. Lee and K. B. Lee, "Open-Circuit Fault-Tolerant Control for Outer Switches of Three-Level Rectifiers in Wind Turbine Systems," *IEEE Trans. Power Electronics*, vol. 31, no. 5, pp. 3806-3815, 2016.

[22] H. Abu-Rub, J. Holtz, J. Rodriguez, and B. Ge, "Medium-Voltage Multilevel Converters; State of the Art, Challenges, and Requirements in Industrial Applications," *IEEE Trans. Industrial Electronics*, vol. 57, no. 8, pp. 2581-2596, 2010.

[23] D. Krug, S. Bernet, S. S. Fazel, K. Jalili, and M. Malinowski, "Comparison of 2.3-kV Medium-Voltage Multilevel Converters for Industrial Medium-Voltage Drives," *IEEE Trans. Industrial Electronics*, vol. 54, no. 6, pp. 2979-2992, 2007.

[24] G. Abad, M. Rodriguez, and J. Poza, "Three-Level NPC Converter-Based Predictive Direct Power Control of the Doubly Fed Induction Machine at Low Constant Switching Frequency," *IEEE Trans. Industrial Electronics,* vol. 55, no. 12, pp. 4417-4429, 2008.

[25] S. K. Sharma, A. Chandra, and M. Saad, "Control of three-level NPC converters in DFIG based off-grid wind energy conversion systems," in *Proc. IECON*, 2015, pp. 1008-1013.

[26] M. E. Adabi and A. Vahedi, "A common-mode voltage reduction strategy for a DFIG with a three-level back-to-back converter," in *Proc. PEDSTC*, 2011, pp. 392-397.

[27] W. Srirattanawichaikul, Y. Kumsuwan, S. Premrudeepreechacharn, and B. Wu, "A vector control of a grid-connected 3L-NPC-VSC with DFIG drives," in *Proc. ECTI-CON*, 2010, pp. 828-832.

[28] Y. Park, D. Han, Y. Suh, and W. Choi, "Minimization of Active Power and Torque Ripple for a Doubly Fed Induction Generator in Medium Voltage Wind Power Systems under Unbalanced Grid Conditions," *Journal of Power Electronics,* vol. 13, no. 6, pp. 1032-1041, 2013.

[29] T. Ghennam, O. Bouhali, D. Maizi, E. M. Berkouk, and B. Francois, "Theoretical study and experimental validation of a Wind Energy Conversion System control with three-level NPC converters," in *Proc. ICEM*, 2012, pp. 2178-2183.

[30] M. Z. Sujod and I. Erlich, "Harmonics and common mode voltage in a DFIG with two-level and three-level NPC converter using standard PWM techniques," in *Proc. IECON*, 2013, pp. 1650-1655.

[31] O. S. Senturk, L. Helle, S. Munk-Nielsen, P. Rodriguez, and R. Teodorescu, "Power Capability Investigation Based on Electrothermal Models of Press-Pack IGBT Three-Level NPC and ANPC VSCs for Multimegawatt Wind Turbines," *IEEE Trans. Power Electronics,* vol. 27, no. 7, pp. 3195-3206, 2012.

[32] "Secure, clean and efficient energy, work programme 2016-2017, Horizon 2020," 2016.

[33] Z. Hameed, Y. S. Hong, Y. M. Cho, S. H. Ahn, and C. K. Song, "Condition monitoring and fault detection of wind turbines and related algorithms: A review," *Renewable and Sustainable Energy Reviews,* vol. 13, no. 1, pp. 1-39, 2009.

[34] Z. Daneshi-Far, G. A. Capolino, and H. Henao, "Review of failures and condition monitoring in wind turbine generators," in *Proc. ICEM*, 2010, pp. 1-6.

[35] F. Spinato, P. J. Tavner, G. J. W. v. Bussel, and E. Koutoulakos, "Reliability of wind turbine subassemblies," *IET Renewable Power Generation,* vol. 3, no. 4, pp. 387-401, 2009.

[36] J. Ribrant and L. M. Bertling, "Survey of Failures in Wind Power Systems With Focus on Swedish Wind Power Plants During 1997-2005," *IEEE Trans. Energy Conversion*, vol. 22, no. 1, pp. 167-173, 2007.

[37] K. Fischer, F. Besnard, and L. Bertling, "Reliability-Centered Maintenance for Wind Turbines Based on Statistical Analysis and Practical Experience," *IEEE Trans. Energy Conversion*, vol. 27, no. 1, pp. 184-195, 2012.

[38] J. Carroll, A. McDonald, and D. McMillan, "Reliability Comparison of Wind Turbines With DFIG and PMG Drive Trains," *IEEE Trans. Energy Conversion*, vol. 30, no. 2, pp. 663-670, 2015.

[39] Y. Amirat, V. Choqueuse, M. Benbouzid, and S. Turri, "Hilbert Transform-Based Bearing Failure Detection in DFIG-Based Wind Turbines," *International Review of Electrical Engineering*, vol. 6, no. 3, pp. 1249-1256, 2011.

[40] J. Faiz and S. M. M. Moosavi, "Eccentricity fault detection - From induction machines to DFIG - A review," *Renewable and Sustainable Energy Reviews*, vol. 55, pp. 169-179, 2016.

[41] J. Faiz, M. Keravand, M. Ghasemi-Bijan, S. M. Â. Cruz, and M. B. Abadi, "Impacts of rotor inter-turn short circuit fault upon performance of wound rotor induction machines," *Electric Power Systems Research*, vol. 135, pp. 48-58, 2016.

[42] W. Qiao and D. Lu, "A Survey on Wind Turbine Condition Monitoring and Fault Diagnosis; Part I: Components and Subsystems," *IEEE Trans. Industrial Electronics*, vol. 62, no. 10, pp. 6536-6545, 2015.

[43] Y. Amirat, M. E. H. Benbouzid, E. Al-Ahmar, B. Bensaker, and S. Turri, "A brief status on condition monitoring and fault diagnosis in wind energy conversion systems," *Renewable and Sustainable Energy Reviews*, vol. 13, no. 9, pp. 2629-2636, 2009.

[44] L. Ran, S. Konaklieva, P. McKeever, and P. Mawby, "Condition monitoring of power electronics for offshore wind," *IET Engineering and Technology Reference*, vol. 1, no. 1, pp. 1-10, 2014.

[45] U. Choi, F. Blaabjerg, and K. Lee, "Study and Handling Methods of Power IGBT Module Failures in Power Electronic Converter Systems," *IEEE Trans. Power Electronics*, vol. 30, no. 5, pp. 2517-2533, 2015.

[46] L. M. A. Caseiro and A. M. S. Mendes, "Real-Time IGBT Open-Circuit Fault Diagnosis in Three-Level Neutral-Point-Clamped Voltage-Source Rectifiers Based on Instant Voltage Error," *IEEE Trans. Industrial Electronics*, vol. 62, no. 3, pp. 1669-1678, 2015.

[47] A. K. Jain and V. T. Ranganathan, "Vce Sensing for IGBT Protection in NPC Three Level Converters; Causes For Spurious Trippings and Their Elimination," *IEEE Trans. Power Electronics*, vol. 26, no. 1, pp. 298-307, 2011.

[48] M. Salehifar, R. S. Arashloo, J. M. Moreno-Equilaz, V. Sala, and L. Romeral, "Fault Detection and Fault Tolerant Operation of a Five Phase PM Motor Drive Using Adaptive Model Identification Approach," *IEEE Journal of Emerging and Selected Topics in Power Electronics*, vol. 2, no. 2, pp. 212-223, 2014.

[49] P. Lezana, J. Pou, T. A. Meynard, J. Rodriguez, S. Ceballos, and F. Richardeau, "Survey on Fault Operation on Multilevel Inverters," *IEEE Trans. Industrial Electronics*, vol. 57, no. 7, pp. 2207-2218, 2010.

[50] S. Ceballos, J. Pou, J. Zaragoza, E. Robles, J. L. Villate, and J. L. Martin, "Fault-Tolerant Neutral-Point-Clamped Converter Solutions Based on Including a Fourth Resonant Leg," *IEEE Trans. Industrial Electronics*, vol. 58, no. 6, pp. 2293-2303, 2011.

[51] M. Boettcher and F. W. Fuchs, "Power electronic converters in wind energy systems-Considerations of reliability and strategies for increasing availability," in *Proc. EPE*, 2011, pp. 1-10.

[52] W. Zhang, D. Xu, P. N. Enjeti, H. Li, J. T. Hawke, and H. S. Krishnamoorthy, "Survey on Fault-Tolerant Techniques for Power Electronic Converters," *IEEE Trans. Power Electronics*, vol. 29, no. 12, pp. 6319-6331, 2014.

[53] U. M. Choi, J. S. Lee, F. Blaabjerg, and K. B. Lee, "Open-Circuit Fault Diagnosis and Fault-Tolerant Control for a Grid-Connected NPC Inverter," *IEEE Trans. Power Electronics*, vol. 31, no. 10, pp. 7234-7247, 2016.

[54] B. R. O. Baptista, M. B. Abadi, A. M. S. Mendes, and S. M. A. Cruz, "The performance of a three-phase induction motor fed by a three-level NPC converter with fault tolerant control strategies," in *Proc. SDEMPED*, 2013, pp. 497-504.

[55] A. M. S. Mendes, M. B. Abadi, and S. M. A. Cruz, "Fault diagnostic algorithm for three-level neutral point clamped AC motor drives, based on the average current Park's vector," *IET Power Electronics*, vol. 7, no. 5, pp. 1127-1137, 2014.

[56] M. B. Abadi, A. M. S. Mendes, and S. M. A. Cruz, "A Real-Time Method for the Diagnosis of Multiple Switch Faults in NPC Inverters Based on Output Currents Analysis," *Journal of Power Electronics*, vol. 16, no. 4, pp. 1415-1425, 2016.

[57] M. B. Abadi, A. M. S. Mendes, and S. M. A. Cruz, "A Method to Diagnose Open-Circuit Faults in IGBTs and Clamp-Diodes of Three-Level NPC Inverters," *IET Electric Power Applications*, vol. 10, no. 7, pp. 623-632, 2016.

[58] M. B. Abadi, A. M. S. Mendes, and S. M. A. Cruz, "Three-Level NPC Inverter Fault Diagnosis by the Average Current Park's Vector Approach," in *Proc. ICEM*, 2012, pp. 1893-1898.

[59] M. B. Abadi, S. M. A. Cruz, A. P. Gonçalves, A. M. S. Mendes, A. Ribeiro, and F. Silva, "Inter-turn fault detection in doubly-fed induction generators for wind turbine applications using the stator reactive power analysis," in *Proc. RPG*, 2014, pp. 1-6.

[60] M. B. Abadi, S. M. A. Cruz, A. P. Gonçalves, P. F. C. Gonçalves, A. M. S. Mendes, A. Ribeiro, *et al.*, "Detection of stator and rotor faults in a DFIG based on the stator reactive power analysis," in *Proc. IECON*, 2014, pp. 2037-2043.

[61] J. Rodriguez, L. Jih-Sheng, and P. Fang Zheng, "Multilevel inverters: a survey of topologies, controls, and applications," *IEEE Trans. Industrial Electronics*, vol. 49, no. 4, pp. 724-738, 2002.

[62] K. A. Corzine, M. W. Wielebski, F. Z. Peng, and W. Jin, "Control of cascaded multilevel inverters," *IEEE Trans. Power Electronics*, vol. 19, no. 3, pp. 732-738, 2004.

[63] H. Sepahvand, M. Khazarei, M. Ferdowsi, and K. Corzine, "Feasibility of capacitor voltage regulation and output voltage harmonic minimization in cascaded H-bridge converters," in *Proc. APEC*, 2010, pp. 452-457.

[64] R. C. Portillo, M. M. Prats, J. I. Leon, J. A. Sanchez, J. M. Carrasco, E. Galvan, *et al.*, "Modeling Strategy for Back-to-Back Three-Level Converters Applied to High-Power Wind Turbines," *IEEE Trans. Industrial Electronics*, vol. 53, no. 5, pp. 1483-1491, 2006.

[65] E. J. Bueno, S. C. breces, F. J. Rodr?guez, H. ndez, and F. Espinosa, "Design of a Back-to-Back NPC Converter Interface for Wind Turbines With Squirrel-Cage Induction Generator," *IEEE Trans. Energy Conversion*, vol. 23, no. 3, pp. 932-945, 2008.

[66] Z. Xiang-Jun, Y. Yongbing, Z. Hongtao, L. Ying, F. Luguang, and Y. Xu, "Modelling and control of a multi-phase permanent magnet synchronous generator and efficient hybrid 3L-converters for large direct-drive wind turbines," *IET Electric Power Applications*, vol. 6, no. 6, pp. 322-331, 2012.

[67] S. Alepuz, A. Calle, S. Busquets-Monge, S. Kouro, and B. Wu, "Use of Stored Energy in PMSG Rotor Inertia for Low-Voltage Ride-Through in Back-to-Back NPC Converter-Based Wind Power Systems," *IEEE Trans. Industrial Electronics*, vol. 60, no. 5, pp. 1787-1796, 2013.

[68] V. Yaramasu and W. Bin, "Predictive Control of a Three-Level Boost Converter and an NPC Inverter for High-Power PMSG-Based Medium Voltage Wind Energy Conversion Systems," *IEEE Trans. Power Electronics*, vol. 29, no. 10, pp. 5308-5322, 2014.

[69] M. Zabaleta, E. Burguete, D. Madariaga, I. Zubimendi, M. Zubiaga, and I. Larrazabal, "LCL Grid Filter Design of a Multi-Megawatt Medium-Voltage Converter for Offshore Wind Turbine using SHEPWM Modulation," *IEEE Trans. Power Electronics*, vol. 31, no. 3, pp. 1993-2001, 2015.

[70] G. Xiaoqiang, M. C. Cavalcanti, A. M. Farias, and J. M. Guerrero, "Single-Carrier Modulation for Neutral-Point-Clamped Inverters in Three-Phase Transformerless Photovoltaic Systems," *IEEE Trans. Power Electronics*, vol. 28, no. 6, pp. 2635-2637, 2013.

[71] W. Cui, H. Luo, Y. Gu, W. Li, B. Yang, and X. He, "Hybrid-bridge transformerless photovoltaic grid-connected inverter," *IET Power Electronics*, vol. 8, no. 3, pp. 439-446, 2015.

[72] H. R. Teymour, D. Sutanto, K. M. Muttaqi, and P. Ciufo, "Solar PV and Battery Storage Integration using a New Configuration of a Three-Level NPC Inverter With Advanced Control Strategy," *IEEE Trans. Energy Conversion*, vol. 29, no. 2, pp. 354-365, 2014.

[73] L. Tan, B. Wu, S. Rivera, and V. Yaramasu, "Comprehensive DC Power Balance Management in High-Power Three-Level DC-DC Converter for Electric Vehicle Fast Charging," *IEEE Trans. Power Electronics*, vol. 31, no. 1, pp. 89-100, 2016.

[74] I. Lopez, S. Ceballos, J. Pou, J. Zaragoza, J. Andreu, I. Kortabarria, *et al.*, "Modulation Strategy for Multiphase Neutral-Point-Clamped Converters," *IEEE Trans. Power Electronics*, vol. 31, no. 2, pp. 928-941, 2015.

[75] S. Payami, R. K. Behera, A. Iqbal, and R. Al-Ammari, "Common-Mode Voltage and Vibration Mitigation of a Five-Phase Three-Level NPC Inverter-Fed Induction Motor Drive System," *IEEE Journal of Emerging and Selected Topics in Power Electronics*, vol. 3, no. 2, pp. 349-361, 2015.

[76] O. Dordevic, E. Levi, and M. Jones, "A Vector Space Decomposition Based Space Vector PWM Algorithm for a Three-Level Seven-Phase Voltage Source Inverter," *IEEE Trans. Power Electronics*, vol. 28, no. 2, pp. 637-649, 2013.

[77] M. Saeedifard, H. Nikkhajoei, and R. Iravani, "A Space Vector Modulated STATCOM Based on a Three-Level Neutral Point Clamped Converter," *IEEE Trans. Power Delivery*, vol. 22, no. 2, pp. 1029-1039, 2007.

[78] T.-J. Kim, W.-C. Lee, and D.-S. Hyun, "Detection Method for Open-Circuit Fault in Neutral-Point-Clamped Inverter Systems," *IEEE Trans. Industrial Electronics*, vol. 56, no. 7, pp. 2754-2763, 2009.

[79] J. D. Barros and J. F. Silva, "Optimal Predictive Control of Three-Phase NPC Multilevel Converter for Power Quality Applications," *IEEE Trans. Industrial Electronics*, vol. 55, no. 10, pp. 3670-3681, 2008.

[80] R. K. Behera, T. V. Dixit, and S. P. Das, "Analysis of Experimental Investigation of Various Carrier-based Modulation Schemes for Three Level Neutral Point Clamped Inverter-fed Induction Motor Drive," in *Proc. PEDES*, 2006, pp. 1-6.

[81] B. P. McGrath and D. G. Holmes, "Multicarrier PWM strategies for multilevel inverters," *IEEE Trans. Industrial Electronics,* vol. 49, no. 4, pp. 858-867, 2002.

[82] A. Videt, P. L. Moigne, N. Idir, P. Baudesson, and X. Cimetiere, "A New Carrier-Based PWM Providing Common-Mode-Current Reduction and DC-Bus Balancing for Three-Level Inverters," *IEEE Trans. Industrial Electronics,* vol. 54, no. 6, pp. 3001-3011, 2007.

[83] B. Wu, *High-Power Converters and AC Drives*: John Wiley & Sons Ltd., 2006.

[84] G. Abad, J. Lopez, M. Rodriguez, L. Marroyo, and G. Iwanski, *Doubly fed induction machine: modeling and control for wind energy generation*: John Wiley & Sons Ltd., 2011.

[85] M. P. Kazmierkowski, L. G. Franquelo, J. Rodriguez, M. A. Perez, and J. I. Leon, "High-Performance Motor Drives," *IEEE Mag. Industrial Electronics,* vol. 5, no. 3, pp. 6-26, 2011.

[86] L. Yo-Han, K. Rae-Young, and H. Dong-Seok, "A novel SVPWM strategy considering DC-link balancing for a multi-level voltage source inverter," in *Proc. APEC*, 1999, pp. 509-514.

[87] M. A. S. Aneesh, A. Gopinath, and M. R. Baiju, "A Simple Space Vector PWM Generation Scheme for Any General n-Level Inverter," *IEEE Trans. Industrial Electronics,* vol. 56, no. 5, pp. 1649-1656, 2009.

[88] A. R. Beig, G. Narayanan, and V. T. Ranganathan, "Modified SVPWM Algorithm for Three Level VSI With Synchronized and Symmetrical Waveforms," *IEEE Trans. Industrial Electronics,* vol. 54, no. 1, pp. 486-494, 2007.

[89] J. Pou, D. Boroyevich, and R. Pindado, "New feedforward space vector PWM method to obtain balanced AC output voltages in a three-level neutral-point-clamped converter," *IEEE Trans. Industrial Electronics,* vol. 49, no. 5, pp. 1026-1034, 2002.

[90] A. K. Gupta and A. M. Khambadkone, "A Simple Space Vector PWM Scheme to Operate a Three-Level NPC Inverter at High Modulation Index Including Overmodulation Region, With Neutral Point Balancing," *IEEE Trans. Industry Applications,* vol. 43, no. 3, pp. 751-760, 2007.

[91] D. W. Feng, W. Bin, and W. X. Samnin, D., "Space vector modulation for neutral point clamped multilevel inverter with even order harmonic elimination," in *Proc. Electrical and Computer Engineering*, 2004, pp. 1471-1475.

[92] N. Celanovic and D. Boroyevich, "A fast space-vector modulation algorithm for multilevel three-phase converters," *IEEE Trans. Industry Applications,* vol. 37, no. 2, pp. 637-641, 2001.

[93] M. P. Kazmierkowski, "CHAPTER 5 - Control of PWM Inverter-Fed Induction Motors," in *Control in Power Electronics, Selected Problems*, ed Burlington: Academic Press, 2002, pp. 161-207.

[94] S. M. A. Cruz and A. J. M. Cardoso, "Fault Indicators for the Diagnosis of Rotor Faults in FOC Induction Motor Drives," in *Proc. IEMDC*, 2007, pp. 1136-1141.

[95] W. Fei, L. Rixin, Y. Xibo, L. Fang, R. Burgos, and D. Boroyevich, "Failure-Mode Analysis and Protection of Three-Level Neutral-Point-Clamped PWM Voltage Source Converters," *IEEE Trans. Industry Applications,* vol. 46, no. 2, pp. 866-874, 2010.

[96] E. R. C. Silva, C. B. Jacobina, R. L. Ribeiro, L. C. A. Melo, and H. Razik, "Compensation of Switch Faults in a Three-Level Inverter," in *Proc. IAS*, 2008, pp. 1-6.

[97] S. Farnesi, P. Fazio, and M. Marchesoni, "A new fault tolerant NPC converter system for high power induction motor drives," in *Proc. SDEMPED* 2011, pp. 337-343.

[98] C. Ui-Min, J. Hae-Gwang, L. Kyo-Beum, and F. Blaabjerg, "Method for Detecting an Open-Switch Fault in a Grid-Connected NPC Inverter System," *IEEE Trans. Power Electronics,* vol. 27, no. 6, pp. 2726-2739, 2012.

[99] L. June-Seok, L. Kyo-Beum, and F. Blaabjerg, "Open-Switch Fault Detection Method of a Back-to-Back Converter Using NPC Topology for Wind Turbine Systems," *IEEE Trans. Industry Applications,* vol. 51, no. 1, pp. 325-335, 2015.

[100] J. O. Estima and A. J. M. Cardoso, "A New Approach for Real-Time Multiple Open-Circuit Fault Diagnosis in Voltage-Source Inverters," *IEEE Trans. Industry Applications,* vol. 47, no. 6, pp. 2487-2494, 2011.

[101] W. Sleszynski, J. Nieznanski, and A. Cichowski, "Open-Transistor Fault Diagnostics in Voltage-Source Inverters by Analyzing the Load Currents," *IEEE Trans. Industrial Electronics,* vol. 56, no. 11, pp. 4681-4688, 2009.

[102] J. O. Estima and A. J. M. Cardoso, "A New Algorithm for Real-Time Multiple Open-Circuit Fault Diagnosis in Voltage-Fed PWM Motor Drives by the Reference Current Errors," *IEEE Trans. Industrial Electronics,* vol. 60, no. 8, pp. 3496 - 3505, 2012.

[103] F. Meinguet, P. Sandulescu, X. Kestelyn, and E. Semail, "A Method for Fault Detection and Isolation Based on the Processing of Multiple Diagnostic Indices: Application to Inverter Faults in AC Drives," *IEEE Trans. Vehicular Technology,* vol. 62, no. 3, pp. 995-1009, 2013.

[104] P. Jong-Je, K. Tae-Jin, and H. Dong-Seok, "Study of neutral point potential variation for three-level NPC inverter under fault condition," in *Proc. IECON*, 2008, pp. 983-988.

[105] A. M. S. Mendes and A. J. Marques Cardoso, "Voltage source inverter fault diagnosis in variable speed AC drives, by the average current Park's vector approach," in *Proc. IEMD*, 1999, pp. 704-706.

[106] H. A. Toliyat, S. Nandi, S. Choi, and H. Meshgin-Kelk, *Electric Machines: Modeling, Condition Monitoring, and Fault Diagnosis*: CRC Press 2012.

[107] S. Nandi, "A detailed model of induction machines with saturation extendable for fault analysis," *IEEE Trans. Industry Applications,* vol. 40, no. 5, pp. 1302-1309, 2004.

[108] M. Ojaghi and S. Nasiri, "Modeling Eccentric Squirrel-Cage Induction Motors With Slotting Effect and Saturable Teeth Reluctances," *IEEE Trans. Energy Conversion,* vol. 29, no. 3, pp. 619-627, 2014.

[109] S. M. A. Cruz, "Diagnosis and Analysis of the Fault in the Stator Windings of Three-phase Induction Motor by using Multiple References Method," PhD Thesis, Department of Electrical and Computer Engineering, University of Coimbra, Coimbra, 2004.

[110] S. Djurovi, x, D. S. Vilchis-Rodriguez, and A. C. Smith, "Supply Induced Interharmonic Effects in Wound Rotor and Doubly-Fed Induction Generators," *IEEE Trans. Energy Conversion,* vol. 30, no. 4, pp. 1397-1408, 2015.

[111] A. Stefani, A. Yazidi, C. Rossi, F. Filippetti, D. Casadei, and G. A. Capolino, "Doubly-fed induction machines diagnosis based on signature analysis of rotor modulating signals," *IEEE Trans. Industry Applications,* vol. 44, no. 6, pp. 1711-1721, 2008.

[112] A. P. Gonçalves, "Control of the doubly-fed induction machine, for the study of the impact of power systems faults on the behavior of wind generators," Master's thesis, Department of Electrical and Computer Engineering, Univesity of Coimbra, 2013.

[113] S. Chondrogiannis and M. Barnes, "Stability of doubly-fed induction generator under stator voltage orientated vector control," *IET Renewable Power Generation,* vol. 2, no. 3, pp. 170-180, 2008.

[114] M. Eremia and M. Shahidehpour, *Handbook of electrical power system dynamics : modeling, stability, and control*: John Wiley & Sons Ltd., 2012.

[115] J. Mohammadi, S. Vaez-Zadeh, S. Afsharnia, and E. Daryabeigi, "A Combined Vector and Direct Power Control for DFIG-Based Wind Turbines," *IEEE Trans. Sustainable Energy,* vol. 5, no. 3, pp. 767-775, 2014.

[116] A. D. Hansen, P. Sørensen, F. Iov, and F. Blaabjerg, "Control of Variable Speed Wind Turbines with Doubly-Fed Induction Generators," *Wind Engineering,* vol. 28, no. 4, pp. 411-432, 2004.

[117] R. Pena, J. C. Clare, and G. M. Asher, "Doubly fed induction generator using back-to-back PWM converts and its application to variable speed wind-energy generation," *IEEE Trans. Electrical Power Application,* vol. 143, no. 3, pp. 231-241, 1996.

[118] S. Muller, M. Deicke, and R. W. D. Doncker, "Doubly fed induction generator systems for wind turbines," *IEEE Mag. Industry Applications,* vol. 8, no. 3, pp. 26-33, 2002.

[119] H. Akagi and H. Sato, "Control and performance of a doubly-fed induction machine intended for a flywheel energy storage system," *IEEE Trans. Power Electronics,* vol. 17, no. 1, pp. 109-116, 2002.

[120] A. Petersson, L. Harnefors, and T. Thiringer, "Comparison between stator-flux and grid-flux-oriented rotor current control of doubly-fed induction generators," in *Proc. PESC*, 2004, pp. 482-486.

[121] A. O'Dwyer, *Handbook of PI and PID Controller Tuning Rules*, 3 ed.: Imperial College Press, 2009.

[122] V. Vodovozov and D. Vinnikov, *Electronic systems of motor drive,* 1 ed.: TUT Press, 2008.

[123] S. Djurović and S. Williamson, "Influence of supply harmonic voltages on DFIG stator current and power spectrum," in *Proc. ICEM*, 2010, pp. 1-6.

[124] S. Nandi, "Detection of Stator Faults in Induction Machines Using Residual Saturation Harmonics," *IEEE Trans. Industry Applications,* vol. 42, no. 5, pp. 1201-1208, 2006.

[125] R. M. Tallam, L. Sang-Bin, G. C. Stone, G. B. Kliman, Y. Ji-Yoon, T. G. Habetler, *et al.*, "A survey of methods for detection of stator-related faults in induction machines," *IEEE Trans. Industry Applications,* vol. 43, no. 4, pp. 920-933, 2007.

[126] A. Gandhi, T. Corrigan, and L. Parsa, "Recent advances in modeling and online detection of stator interturn faults in electrical motors," *IEEE Trans. Industrial Electronics,* vol. 58, no. 5, pp. 1564-1575, 2011.

[127] S. M. A. Cruz and A. J. M. Cardoso, "Stator winding fault diagnosis in three-phase synchronous and asynchronous motors, by the extended Park's vector approach," *IEEE Trans. Industry Applications,* vol. 37, no. 5, pp. 1227-1233, 2001.

[128] A. H. Bonnett and G. C. Soukup, "Cause and analysis of stator and rotor failures in three-phase squirrel-cage induction motors," *IEEE Trans. Industry Applications,* vol. 28, no. 4, pp. 921-937, 1992.

[129] B. G. Gu, "Study of IPMSM Interturn Faults Part I: Development and Analysis of Models With Series and Parallel Winding Connections," *IEEE Trans. Power Electronics,* vol. 31, no. 8, pp. 5931-5943, 2016.

[130] G. Stone, S. Campbell, and S. Tetreault, "Inverter-fed drives: which motor stators are at risk?," *IEEE Mag. Industry Applications*, vol. 6, no. 5, pp. 17-22, 2000.

[131] S. M. A. Cruz and A. J. M. Cardoso, "Diagnosis of stator inter-turn short circuits in DTC induction motor drives," *IEEE Trans. Industry Applications*, vol. 40, no. 5, pp. 1349-1360, 2004.

[132] J. Yang, S. B. Lee, J. Yoo, S. Lee, Y. Oh, and C. Choi, "A Stator Winding Insulation Condition Monitoring Technique for Inverter-Fed Machines," *IEEE Trans. Power Electronics*, vol. 22, no. 5, pp. 2026-2033, 2007.

[133] J. Faiz, S. M. M. Moosavi, M. B. Abadi, and S. M. A. Cruz, "Magnetic equivalent circuit modelling of doubly-fed induction generator with assessment of rotor inter-turn short-circuit fault indices," *IET Renewable Power Generation*, vol. 10, no. 9, pp. 1431-1440, 2016.

[134] D. Shah, S. Nandi, and P. Neti, "Stator-interturn-fault detection of doubly-fed induction generators using rotor-current and search-coil-voltage signature analysis," *IEEE Trans. Industry Applications*, vol. 45, no. 5, pp. 1831-1842, 2009.

[135] J. Zafar and J. Gyselinck, "CUSUM based fault detection of stator winding short circuits in doubly-fed induction generator based wind energy conversion systems," in *Proc. ICREPQ*, 2010, pp. 550-555.

[136] G. Stojcic, K. Pasanbegovic, and T. M. Wolbank, "Detecting Faults in Doubly Fed Induction Generator by Rotor Side Transient Current Measurement," *IEEE Trans. Industry Applications*, vol. 50, no. 5, pp. 3494-3502, 2014.

[137] S. Djurovic, C. J. Crabtree, P. J. Tavner, and A. C. Smith, "Condition monitoring of wind turbine induction generators with rotor electrical asymmetry," *IET Renewable Power Generation*, vol. 6, no. 4, pp. 207-216, 2012.

[138] M. Zaggout, P. Tavner, C. Crabtree, and L. Ran, "Detection of rotor electrical asymmetry in wind turbine doubly-fed induction generators," *IET Renewable Power Generation*, vol. 8, no. 8, pp. 878-886, 2014.

[139] H. Douglas, P. Pillay, and P. Barendse, "The detection of interturn stator faults in doubly-fed induction generators," in *Proc. IAS*, 2005, pp. 1097-1102.

[140] R. H. Park, "Two-reaction theory of synchronous machines generalized method of analysis-part I," *Transactions of the American Institute of Electrical Engineers*, vol. 48, no. 3, pp. 716-727, 1929.

Appendix A

Details of the 3LNPC converter prototype

Since there is no commercial available 3LNPC converter with the required specifications for this study, a 3LNPC converter prototype of an appropriate power was developed and constructed, so that faults (OC in all power switches of the converter) can be introduced in a controlled way (Fig. A.1). The constructed prototype comprises 6 Semix IGBT modules (each module includes 2 IGBTs), 6 SKYPER 32 PRO drivers, which constitute an interface between the IGBT modules and the controller, and 3 diode modules (each one includes two power diodes) as shown in Fig. A.2.

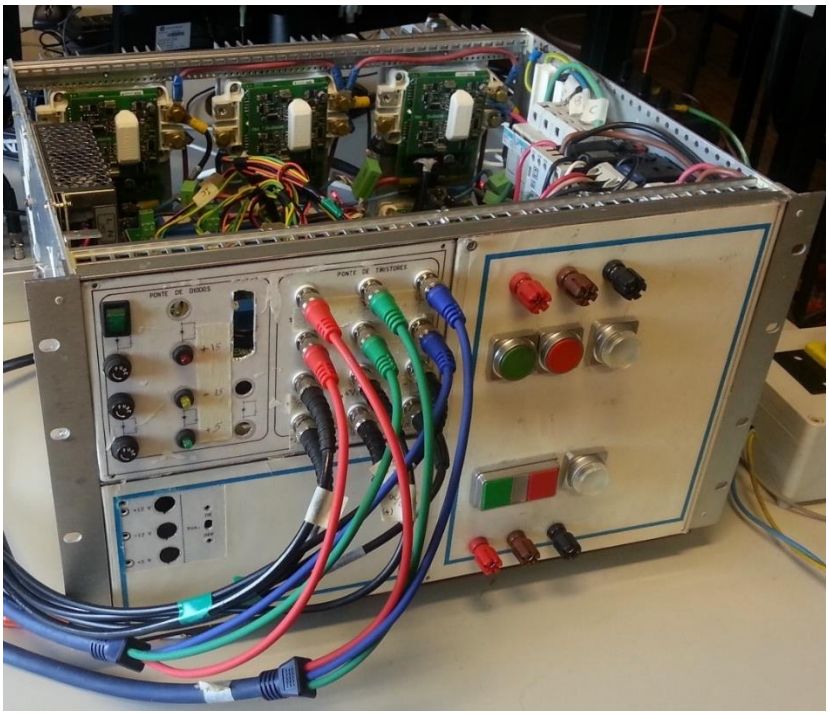

Fig. A.1. 3LNPC converter prototype.

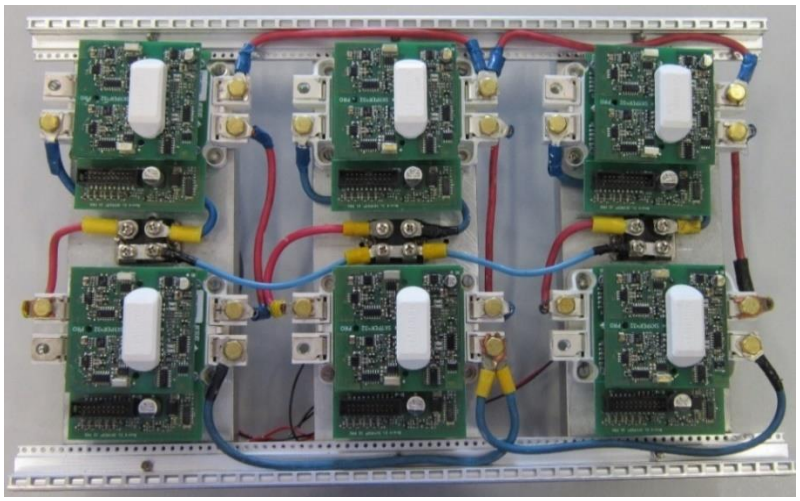

Fig. A.2. IGBT modules with the corresponding drivers and diode modules of the 3LNPC converter.

In order to provide an appropriate interface between the *dSPACE* terminals and the IGBT modules, three interface boards, including isolation board, delay board, and distribution board are used. The connection sequence of the interface boards is schematically shown in Fig. A.3.

The isolation board (Fig. A.4) is used to isolate the *dSPACE* terminals and also to increase the voltage level of the control signals. In order to generate the dead-time for the IGBTs of a given leg, the delay board (Fig. A.5) is employed. The distribution board (Fig. A.6) is used to distribute the control signals for the IGBT modules.

In addition, the prototype also includes several current and voltage sensors in order to measure the DC-bus voltage, converter pole voltages and converter output currents (Fig. A.7).

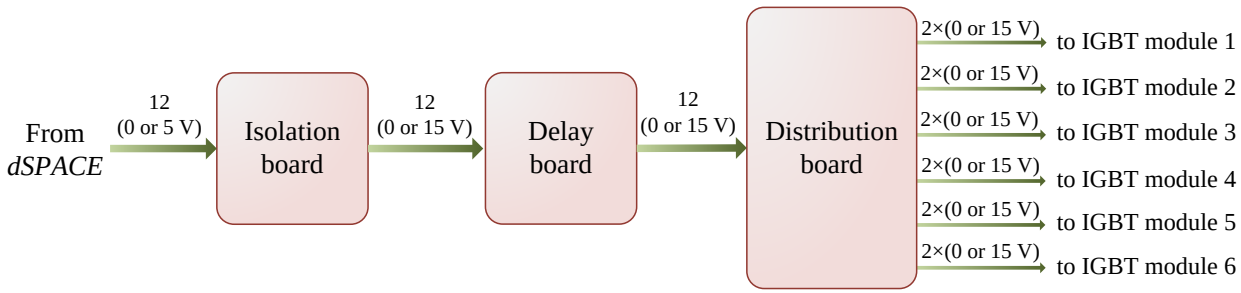

Fig. A.3. Connection of the gate signals, generated by the control platform, to the IGBTs.

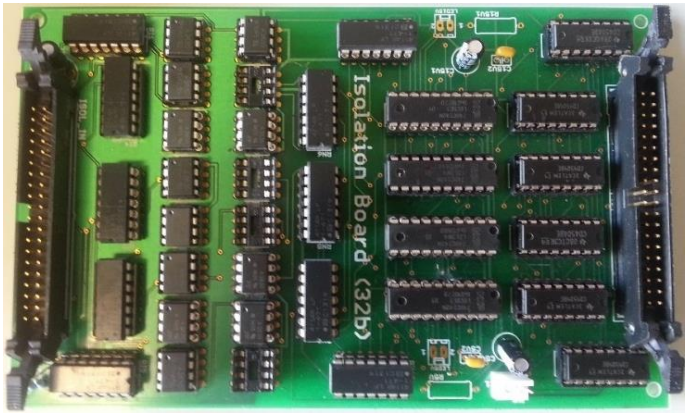

Fig. A.4. Isolation board.

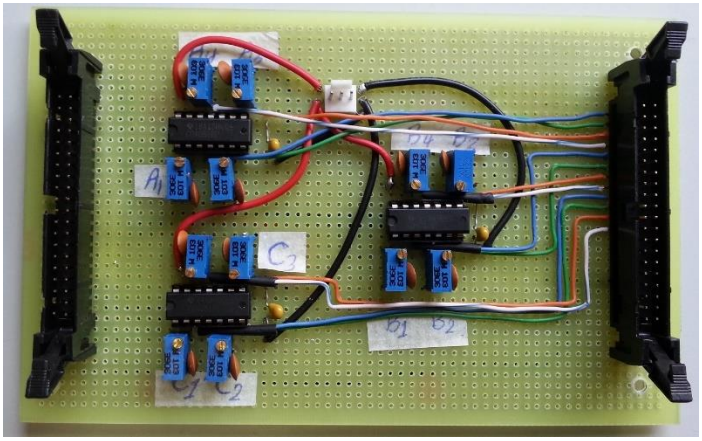

Fig. A.5. Delay board.

Fig. A.6. Distribution board.

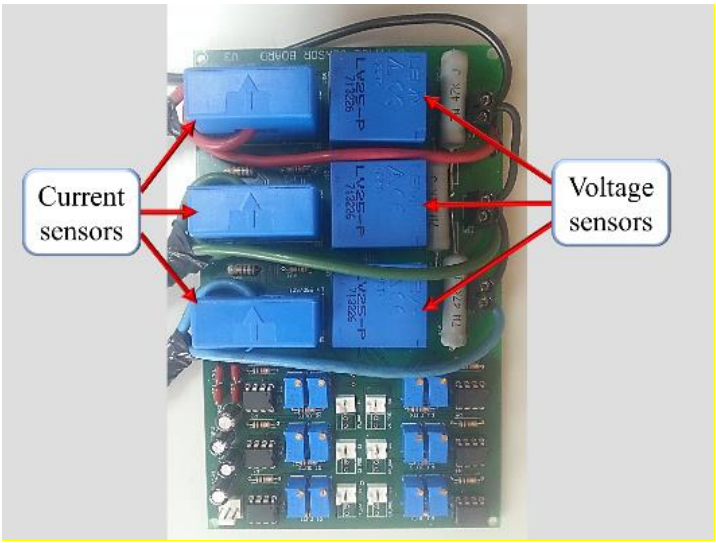

Fig. A.7. Measurement board.

Appendix B

IM drive test rig

To validate the techniques proposed for the diagnosis of the OC fault in the 3LNPC converter, an IM drive test rig was built, according to the block diagram shown in Fig. B.1. It comprises an IM fed by the 3LNPC converter, subjected to an IRFOC strategy. The mechanical load of the IM was a WEG 4 kW PMSG feeding a variable load resistor. The global overview of the experimental setup is shown in Fig. B.2. The main parameters of the IM under study are shown in Table B.1.

The whole control system was implemented in a *dSPACE* 1103 platform, where all quantities are measured and processed. A user interface was also developed in the *ControlDesk* environment from *dSPACE*, thus allows the real-time monitoring and control of the system (Fig. B.3).

In the experiments, the OC fault(s) were introduced by sending the zero state to a specific IGBT(s). To introduce OC faults in the clamp-diodes, extra mechanical switches were connected in series with these power switches.

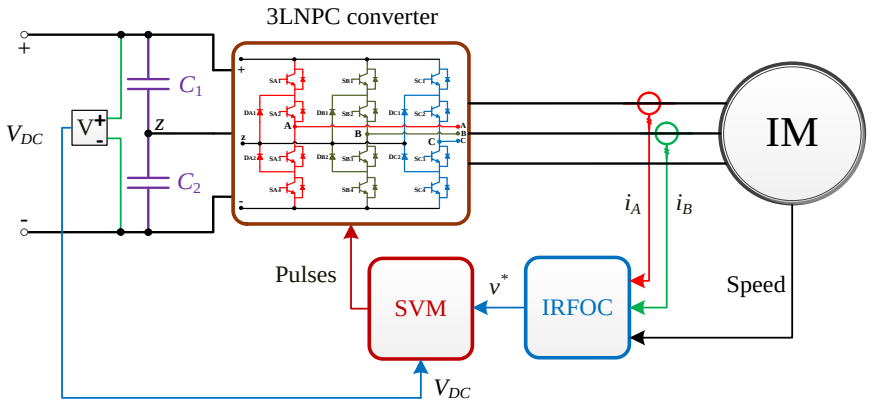

Fig. B.1. Schematic diagram of the IM drive test rig.

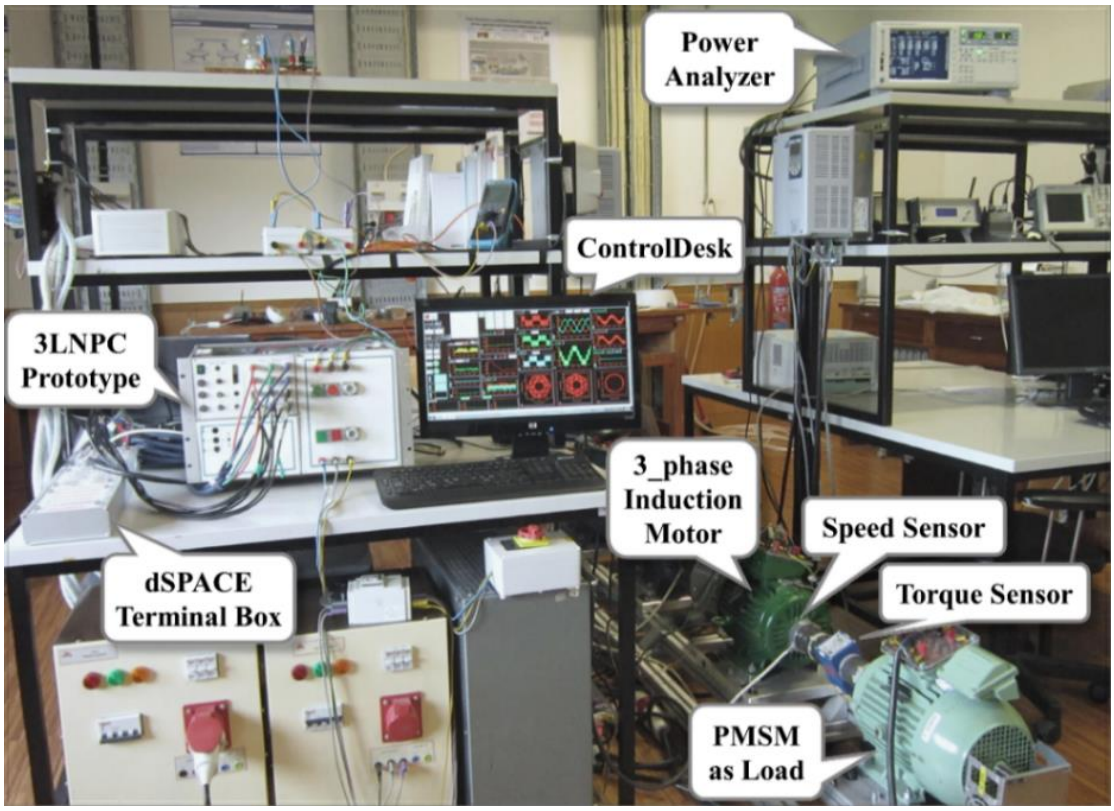

Fig. B.2. Global overview of the 3LNPC IM drive test rig.

Table B.1. Parameters of the IM used in the experimental tests.

Rated power	4 kW
Rated voltage	380 V
Rated frequency	50 Hz
Rated current	8.35 A
Rated speed	1435 rpm
Magnetizing inductance	163 mH
Stator leakage inductance	9.1 mH
Rotor leakage inductance	9.1 mH
Stator resistance	1.45 Ω
Rotor resistance	1.5 Ω

Appendix B

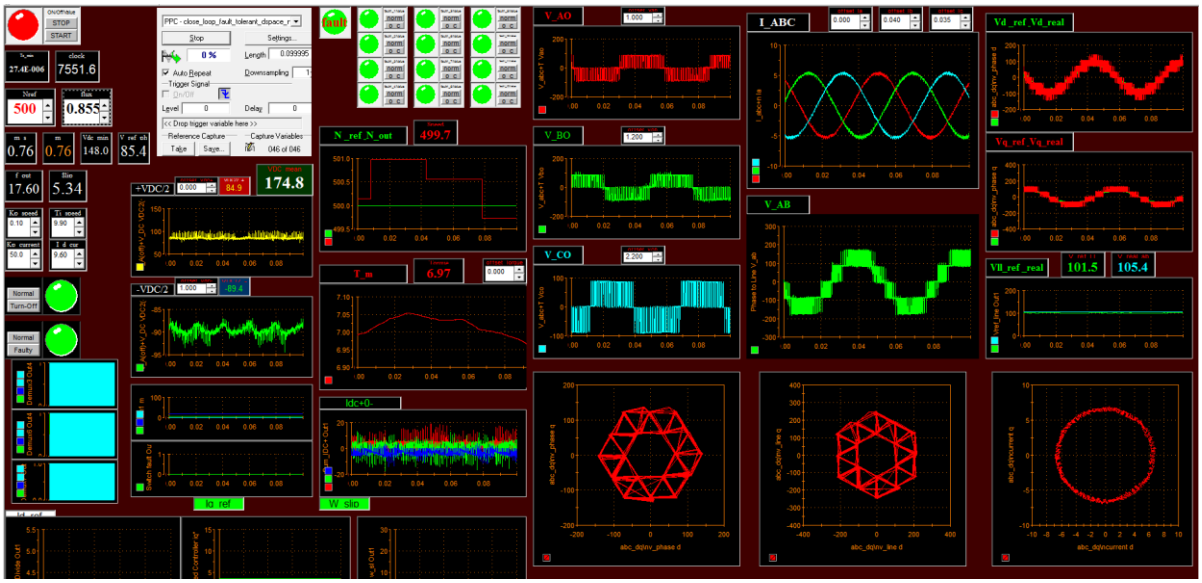

Fig. B.3. Screenshot of the user interface panel for real-time monitoring and control of the IM drive system.

Appendix C

Details of the WRIM used in the experimental tests

The specifications of the WRIM used in the experimental tests are listed in Table C.1. Both the stator and the rotor windings are star connected with an isolated neutral.

Table C.1. Specifications of the WRIM used in the experimental tests.

Rated Power	4 kW
Rated frequency	50 Hz
Rated stator voltage	400 V
Rated rotor voltage	230 V
Rated stator current	9.4 A
Rated rotor current	11.5 A
Rated speed	1420 rpm
Number of poles	4
Number of stator slots	36
Number of rotor slots	24
Inner diameter of stator	136 mm
Outer diameter of rotor	135.4 mm
Core length	114 mm
Stator winding type	One layer
Rotor winding type	One layer
Number of stator coil per phase	6
Number of rotor coil per phase	4
Stator conductors per coil	30
Rotor conductors per coil	27
Stator conductors per phase	180
Rotor conductors per phase	108
Stator resistance per phase	1.28 Ω
Rotor resistance per phase	0.5 Ω

Appendix C

To introduce the ITSC faults in the machine in a controlled manner, the stator and rotor windings were rewound with the necessary modifications in the machine (Fig. C.1).

For the stator windings, according to Fig. C.2(a), five extra taps from 1st, 3rd, 7th, 15th, and 30th turns of the first coil of stator phase *A* are expelled. Using these additional taps along with the stator terminal U, 11 different fault scenarios (1, 2, 3, 4, 6, 7, 8, 12, 14, 15, and 30 turns) can be easily accomplished by connecting some of these taps.

For the rotor windings, by adding three extra slip rings and brushes to the machine, three extra accessible taps from 17th, 24th, and 25th turns of the first coil of rotor phase *a* are provided (Fig. C.2(b)). Therefore, 6 different faulty cases (1, 7, 8, 17, 24 and 25 turns) for the rotor are available.

The detail of the terminals of the machine is presented in Fig. C.3.

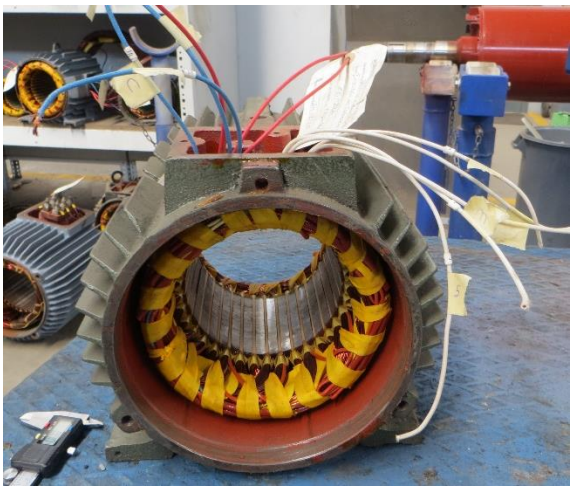

(a) Stator

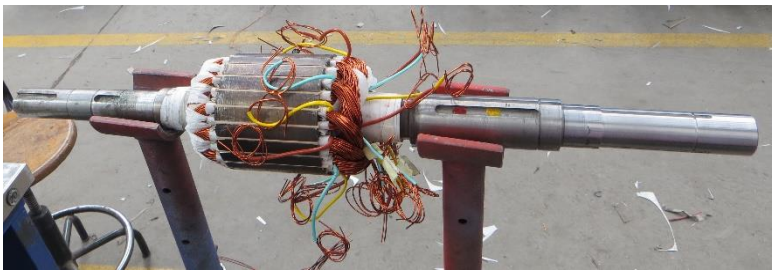

(b) Rotor

Fig. C.1. The rewound WRIM.

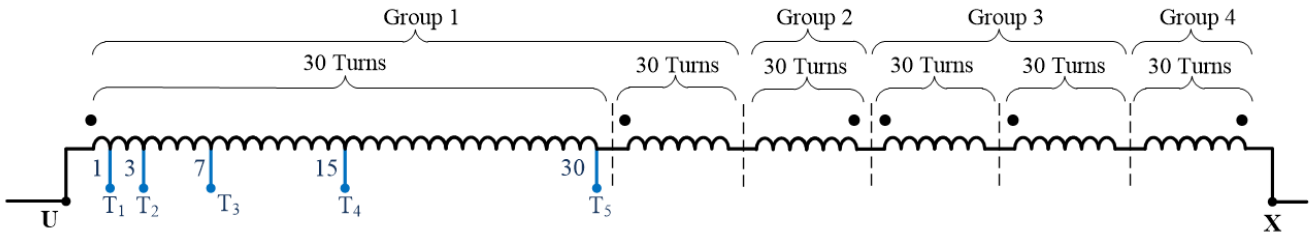

(a) Stator phase *A* with five extra taps

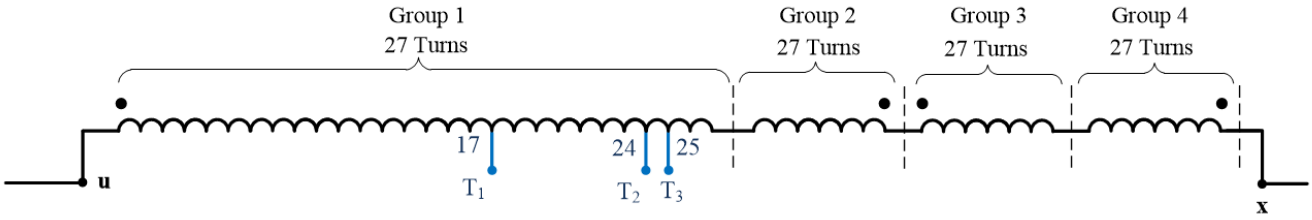

(b) Rotor phase *a* with three extra taps

Fig. C.2. Schematic representation of the windings of the machine.

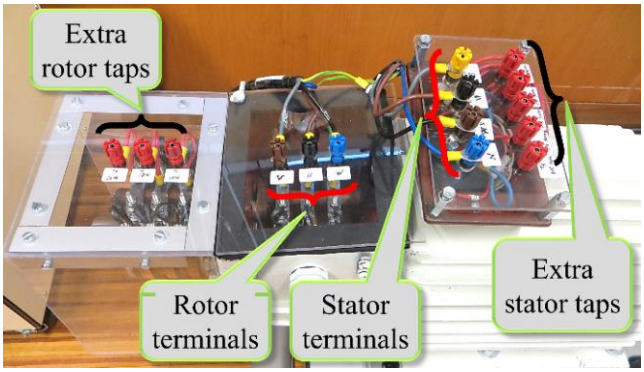

Fig. C.3. Detail of the machine terminals.

Appendix D

Details of the DFIG simulation model

This appendix presents some pictures regarding the implementation of the DFIG model using the software Matlab/Simulink. The general overview of the model of the DFIG system is shown in Fig. D.1. The model of the generator and the DFIG control system are presented in Fig. D.2 and Fig. D.3, respectively.

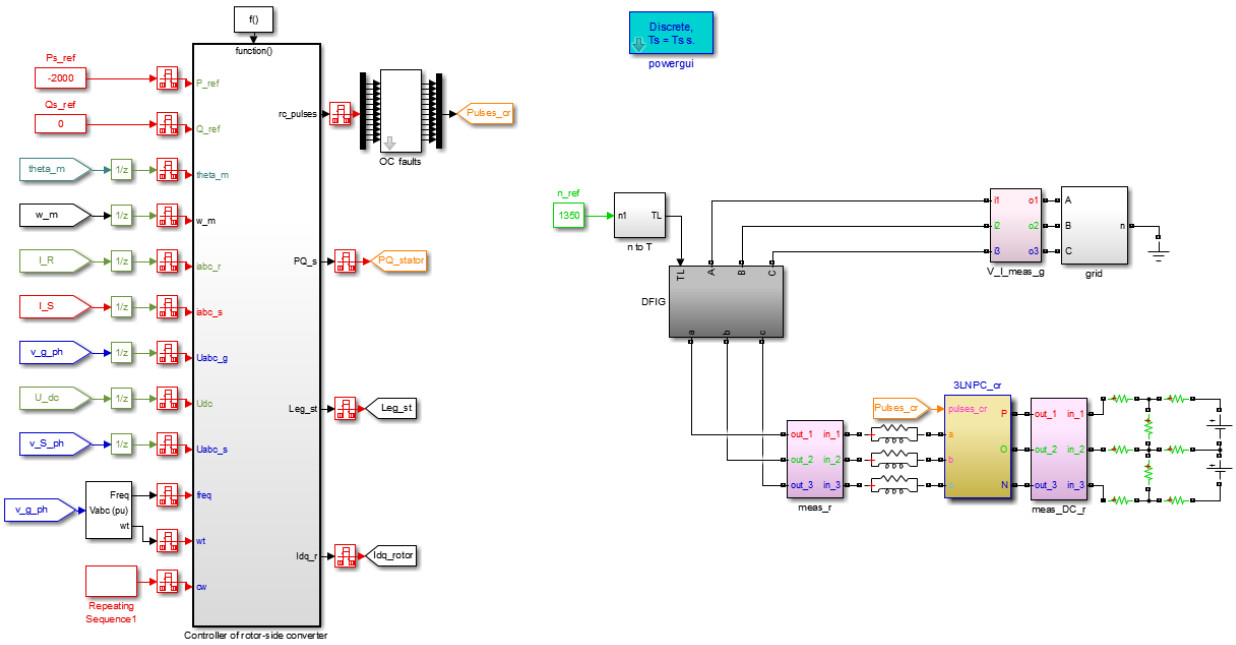

Fig. D.1. Overview of the model of the DFIG system.

Appendix D

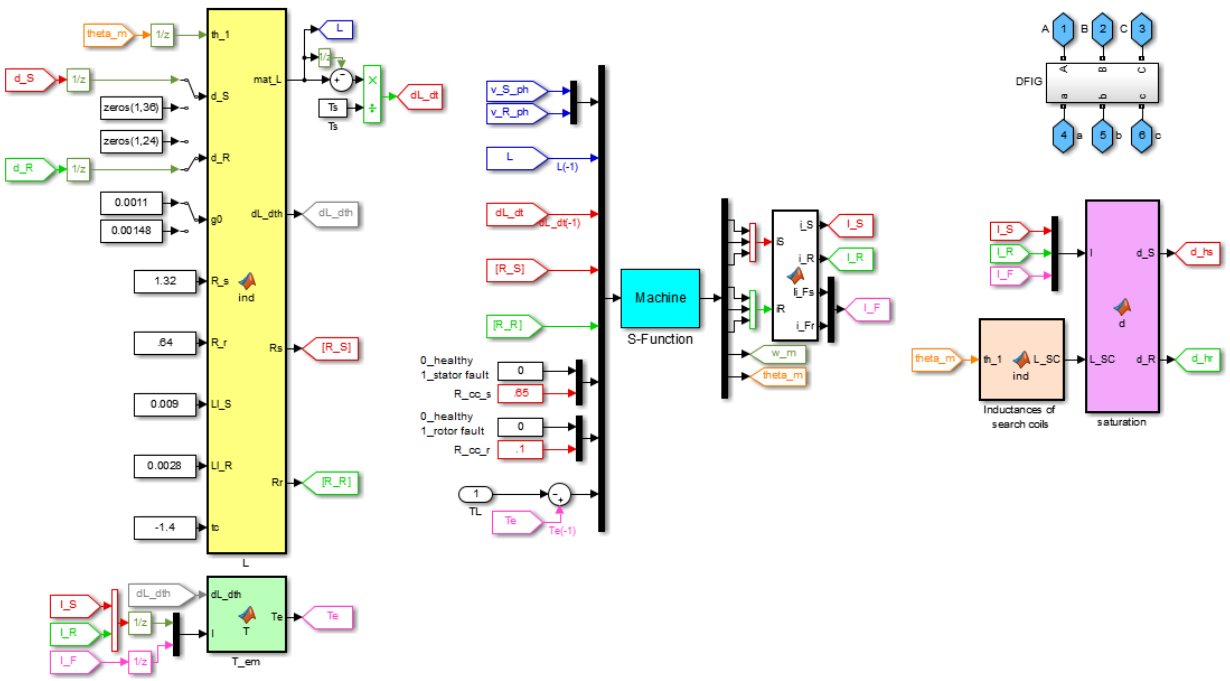

Fig. D.2. Model of the Machine.

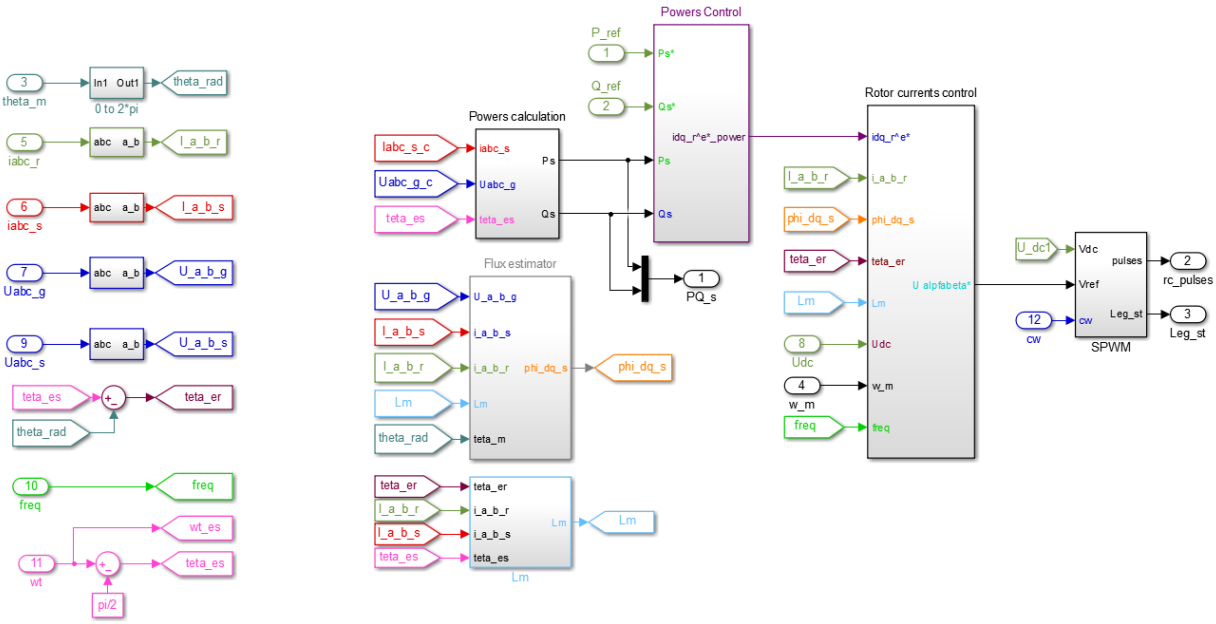

Fig. D.3. DFIG control system.